KU LEUVEN

INTERNATIONAL DOCTORAL PROGRAM
IN SCIENCE
Double doctoral degree

Mott materials out-of-equilibrium: from quantum simulations to control

Alessandra Milloch

Supervisors:
Prof. Dr. Claudio Giannetti
Prof. Dr. Jean-Pierre Locquet

Dissertation presented in partial
fulfillment of the requirements
for the degree of
Doctor of Science (PhD): Physics
Dottore di ricerca in Science
Ciclo XXXVI
S.S.D.: FIS/03

December 2024

Mott materials out-of-equilibrium: from quantum simulations to control

Alessandra MILLOCH

Examination committee:
Prof. Dr. Christ Glorieux, chair (KU Leuven)
Prof. Dr. Claudio Giannetti, supervisor (Università Cattolica del Sacro Cuore)
Prof. Dr. Jean-Pierre Locquet, supervisor (KU Leuven)
Prof. Dr. Michel Houssa (KU Leuven)
Prof. Dr. Stefania Pagliara (Università Cattolica del Sacro Cuore)
Prof. Dr. Stefano Dal Conte (Politecnico di Milano)

Dissertation presented in partial fulfillment of the requirements for the degree of
Doctor of Science (PhD): Physics
Dottore di ricerca in Science
Ciclo XXXVI
S.S.D.: FIS/03

December 2024

Acknowledgements

This PhD thesis represents the tip of the iceberg of the extraordinary journey of the past four years - a journey filled with challenges, growth, and discovery. I am very grateful for every step along the way and would like to express my heartfelt thanks to all those whose support, guidance, and collaboration made the work presented in these pages possible.

First and foremost, I thank Prof. Claudio Giannetti for the insightful mentorship and reliable support. Your dedication to science has been a constant source of inspiration, and I am profoundly grateful for your guidance, encouragement, and the opportunities you offered, which have shaped my growth as a researcher.
I also extend my sincere gratitude to Prof. Jean-Pierre Locquet for supervising my work, welcoming me in the group at KU Leuven, and fostering exciting scientific collaborations.
I would like to express my appreciation to all the members of the Examination Committee for dedicating their time to reviewing this manuscript and for providing valuable feedback and insightful comments.

Collaborators from external institutions also played an essential role in the projects and experiments discussed in this thesis. My sincere thanks go to:

- Liberato Manna, Dmitry Baranov and Umberto Filippi from IIT (Italian Institute of Technology , Genova) for all the work and collaboration related to lead halide perovskites nanocrystals;
- Giulio Cerullo, Cristian Manzoni, Stefano Dal Conte and Franco V. A. Camargo from Politecnico di Milano for the assistance and support in the development of the NOPA and 2D electronic spectroscopy setup;

- Mariela Menghini and Ignacio Figueruelo-Campanero from IMDEA Nanociencia for the preparation and electrical characterization of V_2O_3 devices, and for the collaboration for PEEM beamtimes;
- the Functional Oxides Coating Center group at KU Leuven, particularly Wei-Fan Hsu and Simon Mellaerts, for the growth and characterization of V_2O_3 samples and for the collaboration on PEEM experiments;
- the staff scientists from the i06 beamline at Diamond Light Source, especially Francesco Maccherozzi, for their invaluable support during PEEM experiments;
- Massimo Capone and Michele Fabrizio from SISSA (Scuola Internazionale Superiore di Studi Avanzati, Trieste) for providing theoretical support on several different research projects.

A big thank you to Paolo Franceschini for providing guidance on how to navigate PhD life (lab-, personal- and bureaucracy-wise) throughout these four years. Luckily, you always had a picture in your phone to answer my questions. Thank you also for reading this thesis and providing useful feedback.
To Mohammad, Francesco and Rizwan, thank you for disrupting the comfortable solitary darkness of lab F, and making lab life - yes, I admit it - even more fun. Thank you also to all other PhD students and postdocs, both in Brescia and in Leuven, as well as those met at conferences, summer schools and beamtimes, for sharing coffee breaks and lunches and, most importantly, for making me feel part of a community.

I owe a heartfelt thank you also to all those who have been part of my life outside of university during these years.
Thank you to all the friends who shared a climbing rope, a mountain hike, or a bike ride with me. Briefly switching off from research and enjoying some outdoors has been crucial to be able to return to the lab, week after week, with renewed energy and motivation.
To Stefano, thank you for always being by my side and supporting me through the ups and downs of this journey.
Last but not least, thank you to my family for all the love and support you have always shown me, despite the distance and little time together. In particular, thank you to my parents: to my dad, for instilling in me the values of dedication and hard work that have daily driven my work and reminded me of you; and to my mum, for being the best example of how to face life with resilience, positivity, and enthusiasm.

December 2024

Alessandra

Abstract

In strongly correlated materials, the occurrence of phase transitions and the existence of multiple competing orders arise from a delicate balance among many interacting degrees of freedom, such as charge, spin, and lattice. This intricate interplay makes these systems highly susceptible to external perturbations, which can induce large variations in the material properties and even change the macroscopic phase of the material. Because of the fragility to external control parameters, strongly correlated materials are ideal platforms for the development of novel technologies and devices based on emergent phenomena and exotic properties [281, 15]. Their richness and technological potential, however, is counterbalanced by an inherent complexity originating from the strong intertwining of many degrees of freedom. As a consequence, a comprehensive understanding and control of these systems still remains a major challenge.

In the first part of this thesis, we study prototypical Mott insulators to tackle open challenges in the development of strategies to achieve control over quantum materials. When light excitations are employed, one promising approach consists in exploiting quantum coherence, i.e. the phase coherence between electronic wave functions and the exciting electromagnetic field, which can lead to enhanced functionalities as well as ultrafast and reversible manipulation of material properties [93, 266]. In order to access quantum coherence and investigate the mechanisms that, instead, cause the loss of coherence in strongly correlated materials, we implement two dimensional coherent electronic spectroscopy, a three-pulse time-resolved technique that enables the measurement of decoherence times [57]. The light-induced out-of-equilibrium dynamics and loss of coherence is investigated in the prototypical Mott insulator lanthanum vanadate $LaVO_3$, where long range orders in the orbital and spin degrees of freedom strongly influence optical excitations and the evolution of excitonic states [172]. We

study how the interactions of the $LaVO_3$ excitonic resonance with the ordered background influence the exciton spectral linewidth and decoherence time.
A second control mechanism to manipulate the electronic and magnetic properties of quantum materials consists in the application of current or voltage. In Mott materials, for example, applying a current above a certain threshold can induce resistive switching, that is a sudden drop in resistance caused by a transition from an insulating to a metallic state [130]. Here, we investigate resistive switching in the prototypical Mott insulator vanadium sesquioxide (V_2O_3). We specifically combine transport measurements with an X-ray based microscopy technique to image the resistive switching process at the nanoscale. On this length scale, V_2O_3 displays spatial inhomogeneities resulting from the breaking of the crystal symmetry upon transitioning from the high temperature metallic phase to the low temperature insulating one. This experiment provides novel insights on the nature and mechanisms of resistive switching, as well as the role of the nanometric texture of the material, suggesting novel viable routes to control the current-induced insulator-metal transition.

The second part of the thesis is dedicated to the quantum simulation of the physics of strongly correlated materials using artificial platforms. This approach aims to overcome the inherent complexity of quantum materials by employing systems where the phenomena typical of correlated systems can take place in a controlled way, with the relevant parameters that can be tuned on demand [6, 52]. Within this framework, we here introduce synthetic lattices composed of lead halide perovskite nanocubes, which we propose as a suitable novel platform for quantum simulations. Time-resolved optical spectroscopies are then employed to study the excitonic dynamics in the superlattices. Pump-probe experiments on the inorganic perovskite cesium lead bromide ($CsPbBr_3$) reveal the emergence of several phases relevant for strongly correlated materials (collective superradiant state, exciton gas and electron-hole liquid phases) that can be accessed upon controlling the excitation intensity, thus making the system a suitable platform for the investigation of long range ordered phases in systems displaying insulator-metal Mott transitions. Nanocube superlattices of the hybrid organic-inorganic compound $CH(NH_2)_2PbI_3$ are also investigated; two dimensional coherent electronic spectroscopy is employed to trace the evolution of optical excitons in this artificial lattice, measure their decoherence time and address how the decoherence process is affected by the structural phase transition taking place in the system.

List of Abbreviations

2DES	2D electronic spectroscopy
BBO	Barium borate β-BaB_2O_4
CDW	Charge density wave
DMFT	Dynamical mean field theory
EG	Exciton gas
EHL	Electron-hole liquid
FA	Formamidinium
FAPI	Formamidinium lead iodide $CH(NH_2)_2PbI_3$
FWHM	Full width at half maximum
GVM	Group velocity mismatch
HE	Hubbard exciton
IMT	Insulator-to-metal transition
LHB	Lower Hubbard band
LO	Local oscillator
MA	Methylammonium
MAPI	Methylammonium lead iodide $CH_3NH_3PbI_3$
MBE	Molecular beam epitaxy
NC	Nanocube
NOPA	Non-collinear optical parametric amplifier
OPA	Optical parametric amplifier
PEEM	Photo-electron emission microscopy
PL	Photoluminescence
RWA	Rotating wave approximation
SHG	Second harmonic generation
SL	Superlattice
STE	Self-trapped exciton
SW	Spectral weight

TWINS	Translating-Wedge-Based Identical Pulses eNcoding System
UHB	Upper Hubbard band
WLG	White light generation
XLD	X-ray linear dichroism
XRD	X-ray diffraction
YAG	Yttrium aluminum garnet

Contents

CHAPTER 1

Introduction

In this chapter, we outline the general context of the out-of-equilibrium physics in strongly correlated materials within which the topics of this thesis are framed. First, by means of specific examples, we introduce Mott systems and their complex phase diagrams, and provide a brief overview of the phenomena that can be induced, upon excitation, in out-of-equilibrium conditions. We then discuss the open challenges in the investigation and exploitation of strongly correlated materials that will be addressed in this thesis: i) the measurement of the decoherence dynamics; ii) the role of spatial nanotexture and inherent topological defects in out-of-equilibrium phenomena; iii) the employment of quantum simulators to study phase transitions and collective phenomena in strongly correlated materials. Lastly, the structure of this thesis is presented.

1.1 Strongly correlated electron systems and Mott materials

Strongly correlated materials are systems displaying a rich physics characterized by phase transitions, collective orders and topological phenomena. These effects emerge from the strong electron-electron interactions that make the single-electron approximation fail and lead to the intertwining of all the degrees of freedom of the system, namely charge, orbital, spin and lattice [279].

One of the most important and outstanding effects of strong electron correlations is the occurrence of the insulator-to-metal Mott transition (IMT) [128]. When the Coulomb repulsion between electrons U is large, the single-particle

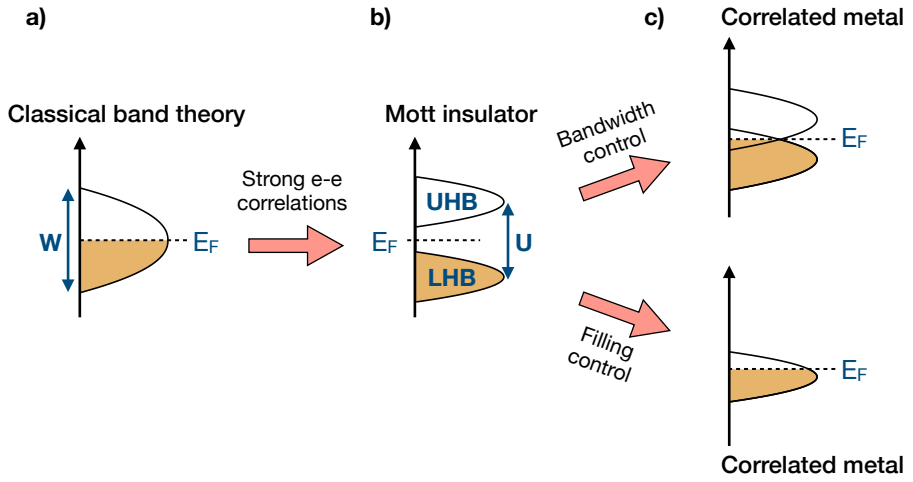

Figure 1.1: a) Sketch of the density of states of a material with partially filled orbitals according to the conventional band theory, predicting a metallic behavior. b) In a Mott insulator, due to the strong Coulomb repulsion U, a Mott gap is formed and separates the Lower Hubbard Band (LHB) and the Upper Hubbard Band (UHB). c) Two possible mechanism can lead to the transition from a Mott insulator to a correlated metal: bandwidth control (variation of the U/W ratio, where W is the one-electron bandwidth) and filling control. Adapted from Ref. 333.

description, which predicts a metallic behavior and partially-filled bands for systems with an odd number of electrons per unit cell, breaks down. For example, in a system with one electron per site but large U, the hopping of one electron to a neighboring site is hindered by the Coulomb repulsion that "freezes" the electrons on their site, thus preventing the metallic conductivity. In this case, two separate bands are formed: a completely filled Lower Hubbard Band (LHB) and an empty Upper Hubbard Band (UHB), separated by the Mott gap (see Fig. 1.1). It is, therefore, the competition between the Coulomb repulsion U and the kinetic energy, i.e. the one-electron bandwidth $W = 4t$ where t is the hopping, that determines the behavior of the material [128]. The outcome of such competition can be controlled by a number of parameters, including pressure, temperature and charge doping, which can determine the occurrence of IMTs. Mott transitions can in general be categorized into two types [128, 281]: bandwidth controlled and band-filling controlled (see Fig. 1.1). In the former case, the IMT is driven by the ratio U/W, describing the effective electron correlation strength, which can be changed by modifying the atomic spacing through strain; in the latter, carrier doping varies the number of electrons per atomic site. These effects are typical of many transition metal oxides. For example, in the family of oxide perovskites AMO_3, where M is a transition metal element, the size of the A-ion can control the bandwidth W by changing the

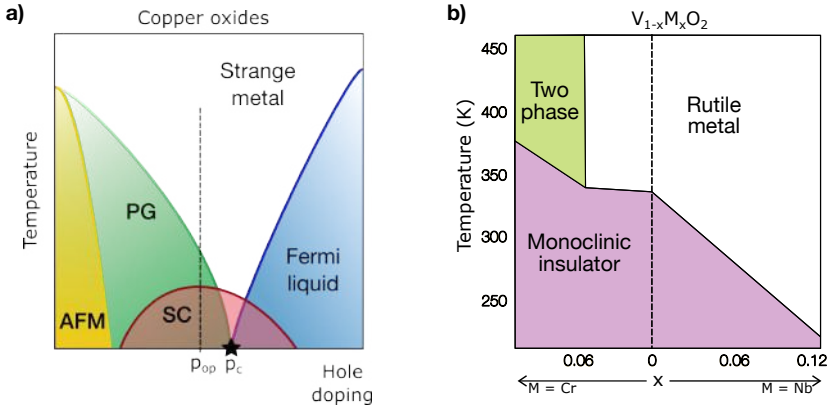

Figure 1.2: a) Sketch of the phase diagram of superconducting copper oxides. AFM = antiferromagnet; SC = superconductor; PG = pseudo-gap. p_{op} indicates the optimal doping where the superconducting transition temperature is the highest. The black star at the critical doping p_c indicates the quantum critical point. b) Phase diagram of vanadium oxide VO_2 as a function of chemical doping x and temperature. Adapted from Ref. 1.

O–M–O bond angle (bandwidth control) [281]. The most prominent example of filling controlled IMT is the case of copper-oxide superconductors, which are composed of CuO_2 square-lattice sheets sandwiched between layers of other chemical composition, acting as charge reservoir. The undoped compound has half filling (one hole per Cu) and is insulating; upon doping, achieved by changing the oxygen content or by partially substituting the cations of the reservoir layers, the system transitions into a metallic or high-temperature superconductor state (doped Mott insulator) [159], as shown by the phase diagram sketched in Fig. 1.2a.

Due to the correlation-driven suppression of the kinetic energy, strongly correlated materials are often characterized by the occurrence of symmetry-breaking phenomena and the establishment of long range orders in the charge, orbital or spin degrees of freedom. Most of the observed Mott transitions driven by temperature or pressure, for example, are accompanied by a magnetic transition and/or a lattice distortion changing the crystal symmetry. This is the case, for instance, of vanadium oxides VO_2 and V_2O_3 which are considered paradigmatic Mott system: VO_2 transitions from a paramagnetic high-temperature metal with rutile structure to paramagnetic monoclinic insulator below 340 K (see phase diagram in Fig. 1.2b) [9, 45]; V_2O_3 undergoes a transition from a rhombohedral paramagnetic metal to an antiferromagnetic insulator with a monoclinic structure that breaks the threefold rotational symmetry at 170 K [193, 64]. Charge and orbital degrees of freedom can also be affected, with the emergence of collective phases such as orbital orders [123], charge density waves [43] and high-temperature superconductivity [159, 138].

Orbital ordered phases are for example observed in manganites like $LaMnO_3$ and vanadates such as YVO_3 and $LaVO_3$, where an alternation in the occupation of the e_g ($d_{3x^2-r^2}$ and $d_{3y^2-r^2}$) or t_{2g} (d_{yz} and d_{zx}) orbitals on the Mn/V sites, respectively, spontaneously emerges [279, 141]. Several ordered phases are observed also in copper oxides, including charge-order and the elusive pseudogap that characterize the low-doping region of the phase diagram (see Fig. 1.2a) [138]. In the limit of zero temperature, a phase transition between such an ordered phase on the low doping side and a disordered one on the high doping side (Fermi liquid metallic phase) is believed to occur in copper oxides at a specific doping defining a *quantum critical point* [242]. This scenario has been questioned by the recent observation of an additional symmetry-breaking ordered phase on the high doping side, compatible with a ferroic-like order [133, 200]. Another example is given by charge density wave (CDW) phases, which are also typical of strongly correlated electron systems. In CDW systems, the energetically most favorable state is characterized by a periodic lattice distortion and a consequent static modulation of the conduction electrons [43]. These effects have been reported, for example, in transition metal chalcogenides MX_3 (M = Nb and Ta, X = S, Se, or Te), layered transition metal dichalcogenides and cuprates [43].

In many cases the physics of these materials is further complicated by the intertwining of multiple order parameters [269]. The onset of various symmetry-breaking orders is often observed at comparable temperatures within a wide range of materials parameters (e.g. doping, pressure) suggesting a complex interplay among the coexisting or competing orders [82]. For example, high-temperature superconductors show a competing behavior between charge order and superconductivity, suggested by the charge ordering appearing in the pseudogap region and being suppressed within the superconducting dome [82, 138]. Manganese oxides host a ferromagnetic metal phase and a charge–orbital ordered antiferromagnetic phase that compete with each other [280]. In perovskite transition metal oxides there is a close interplay between spin and orbital degrees of freedom, which manifests itself in the appearance of both orbital ordering and spin ordering phases. This coupling is particularly strong in vanadium oxides RVO_3 (R being a rare-earth ion or Y) where the energy scales of Jahn-Teller and exchange interactions are of the same order, resulting in the critical temperatures for the two transitions being very close to each other and depending on the radius of the R^{3+} ion [121].

Although the examples mentioned above do not provide an exhaustive overview, they illustrate the complexity and richness of the different orders emerging in strongly correlated systems. Within this scenario of intricate phase diagrams, we can assume that the phase of the material can be described by a global minimum of the free energy F of the system. Fig. 1.3 displays a sketch of a free energy landscape in phase space as a function of the order parameter η, which here collectively represents the possible degrees of freedom coming into play, such as lattice, charge and spin. Thermodynamic variables, such as temperature, pressure and doping, influence and control the free energy and determine which is the favored phase. The free energy in Fig. 1.3, for example,

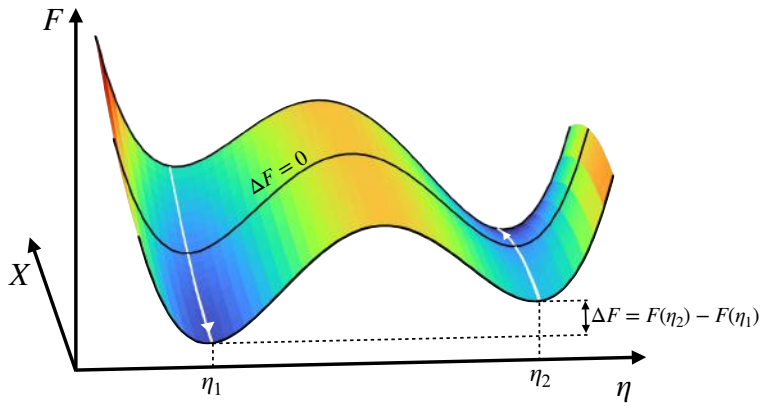

Figure 1.3: Sketch of the free energy functional F in Eq. 1.1 with $\alpha = 20$ and $\beta = 4 - X^2$, plotted as a function of the system variable η, which includes electronic, lattice and spin configurations, and the control parameter X, representing, for example, an applied voltage or the density of particle-hole excitations generated by an applied light pulse. As X is increased, the free energy difference $\Delta F > 0$ between the local minimum η_2 and the global one η_1, corresponding to two different phases of system, decreases until ΔF crosses zero and the phase transition occurs.

has the general form

$$F(\eta, X) = \alpha(X)(\eta^2 - 1)^2 + \beta(X)\eta \tag{1.1}$$

where α and β are parameters that can depend on thermodynamic variables or, more in general, on some external control parameter X. The first term in Eq. 1.1 provides the typical double-well structure, with two local minima, η_1 and η_2, whereas the second term controls the relative depth $\Delta F = F(\eta_2) - F(\eta_1)$. In Fig. 1.3, the global minimum is at η_1 for $\beta > 0$, and it is switched to η_2 when $\beta < 0$. Therefore, when β depends on a control parameter X that can be tuned, the variation of X can cause the crossing of the boundary between two local minima, leading to a first order phase transition.

1.2 Out-of-equilibrium phenomena in Mott systems

The fragility of strongly correlated materials to small and adiabatic changes of temperature and pressure extends also to external perturbations such as applied voltages or ultrashort light pulses. These perturbations (collectively denoted as X in Fig. 1.3) offer an additional way to control the phase and physical properties of the system [327, 15].

The interaction between matter and an external perturbation can create long-lived non-equilibrium states that could not be realized in thermal equilibrium,

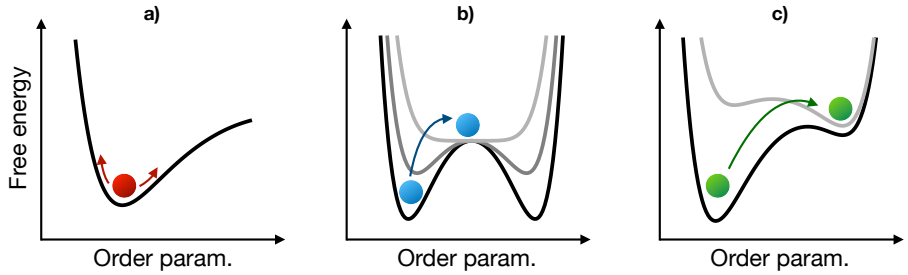

Figure 1.4: Sketch of non-thermal pathways initiated by an external perturbation. a) For weak perturbations, the free energy landscape of the system is unvaried; the excitation around the ground state allows to disentangle the dynamics of different degrees of freedom and to probe collective modes. b) An ultrafast excitation can transiently modify the free energy landscape and induce an out-of-equilibrium critical behavior. c) Strong excitations can induce a phase transition and drive the system into a non-thermal metastable state. Adapted from Ref. 59.

that is through adiabatic transformations of pressure or temperature. One of the approaches that over the last few decades has mostly been used and studied to realize out-of-equilibrium states is the employment of light pulses of ultrashort time duration (from few to several hundred femtoseconds). These pulses allow to generate non-equilibrium conditions on timescales faster than the typical relaxation times of the internal degrees of freedom, such as lattice vibrations and magnetic excitations, therefore initiating physical phenomena not observable at equilibrium [98, 327, 59]. The outcome of the interaction strongly depends on the frequency and the intensity of the applied perturbation, with the possibility of inducing a transition to a different phase in the strong excitation regime. Similarly to radiation fields, out-of-equilibrium phase transitions can be induced in Mott systems also upon application of THz fields [168, 327], pulsed voltages or static electric fields [333, 130, 61, 303].

In the following we outline possible different scenarios of out-of-equilibrium phenomena in strongly correlated materials.

1.2.1 Relaxation dynamics and excitation of collective modes

When the perturbation is weak, the free energy potential of the system is not altered by the excitation. In this case, the system is instantaneously brought to a non-equilibrium configuration not too far from the potential minimum occupied at equilibrium. It then relaxes back to the initial state following a dynamics that is governed by same thermodynamic parameters of the unperturbed system (see Fig. 1.4a) [98]. The recovery dynamics can, however, explore non-thermal pathways, that is the relaxation pathway is in general different from the one following the sudden change of thermodynamic

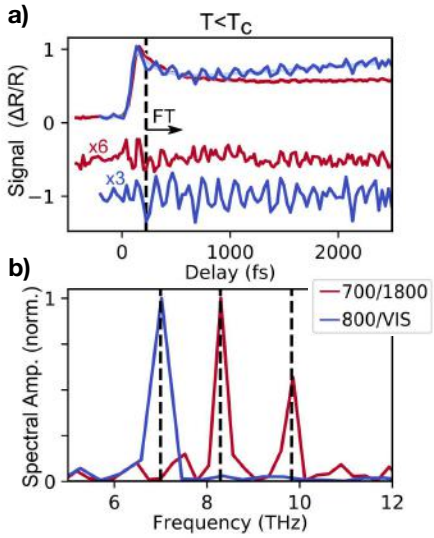

Figure 1.5: a) Time-resolved transient reflectivity measurement performed in the insulating phase of V_2O_3. The observed oscillations are due to the excitation of coherent phonons. b) Fourier transform of the fit-subtracted oscillations in a), agreeing with the frequencies of optical phonon modes of the material. Adapted from Ref. 131.

variables. This is a consequence of the fact that the initial non-equilibrium condition is usually represented by a non-thermal distribution of quasi-particles, that cannot be obtained by adiabatically changing the common thermodynamic variables, such as temperature and pressure [98]. Under these conditions, it may be possible to disentangle the interplay among intertwined degrees of freedom by investigating in time domain thermalization processes characterized by different timescales.

In addition, the recovery toward the equilibrium state can be sensitive to collective modes, such as lattice vibrations or charge/spin waves, that the impulsive excitation can couple to [98, 59]. This triggers a response that oscillates in time at a frequency corresponding to the frequency of the mode; the relaxation time of the induced oscillation is instead related to the dephasing time of the excited collective mode [98]. This time-domain technique has been employed to study a number of bosonic modes in strongly correlated materials [327, 59]. Some examples are amplitude modes of charge-density waves [116, 71], Josephson plasmons [156] and Higgs modes [253] in superconductors, and coherent phonon modes in vanadium oxides [181, 131]. Figure 1.5 reports an example of oscillations generated by the excitation of coherent phonons in V_2O_3, and detected by means of optical transient reflectivity experiment.

1.2.2 Critical behavior in vicinity of phase transitions

A stronger photoexcitation by means of an ultrashort light pulse can induce instantaneous changes in the free energy of the system, as sketched in Fig. 1.4b. In this case, if the initial equilibrium state of the system is an ordered phase characterized by a finite order parameter, the effect of the ultrafast excitation can be a sudden suppression of the relevant order parameter [59].

A typical manifestation of such order parameter suppression is the slowing down of the recovery dynamics, observed in proximity of the phase transition temperature T_c. This behavior is similar to what occurs at equilibrium, where the relaxation time of the order parameter fluctuations tends to infinity in proximity of the critical temperature because of the divergence of the fluctuations' spatial extend [59, 26]. The time evolution of the order parameter is, in fact, related to the derivative of the free energy according to the following kinetic equation [26, 98, 172]

$$\frac{d\eta}{dt} = -\gamma \frac{\partial F}{\partial \eta} \tag{1.2}$$

where γ is a kinetic coefficient. The flattening of the free energy landscape occurring as the critical temperature is approached, implies that the dynamics of the order parameters diverges in the limit $T \to T_c$ [98]. This critical behavior, that is the slowing-down of the out-of-equilibrium order parameter dynamics right below T_c, has been reported in several strongly correlated materials undergoing symmetry-breaking transitions. Some examples are charge-order in $La_{1/3}Sr_{2/3}FeO_3$ [335], spin- and orbital-order in RVO_3 (R = Y, Gd, La) [325, 172] and charge-density wave in $LaTe_3$ [337].

When ultrashort light pulses are employed, the suppression of the order parameter takes place on timescales that are shorter than those of the intrinsic fluctuations. This allows the investigation of the role played by topological defects in the establishment of the long-range ordered phases [59, 338]. Topological defect are typical of systems undergoing symmetry breaking phase transitions; their formation usually results from the simultaneous emergence of the ordered phase in separate regions of space [338]. An example of topological defect is sketched in Fig. 1.6a, showing a CDW discommensuration line induced and stabilized by superconductivity [300]. Ultrafast optical excitations allow to study these phenomena during non-adiabatic transitions. Such approach has been employed to study the influence of topological defects of long-range ordered phases on the out-of-equilibrium dynamics, for example, in CDW materials [298, 338, 47] and high temperature superconducting cuprates [201, 300]. For instance, a strong coupling between topological defects in the CDW order parameter and superconductivity was observed in $YBa_2Cu_3O_{6+x}$ (YBCO) by Wandel et al. (Ref. 300), that reported an enhancement of the CDW spatial coherence following the ultrafast optical quench of superconductivity (see Fig. 1.6b).

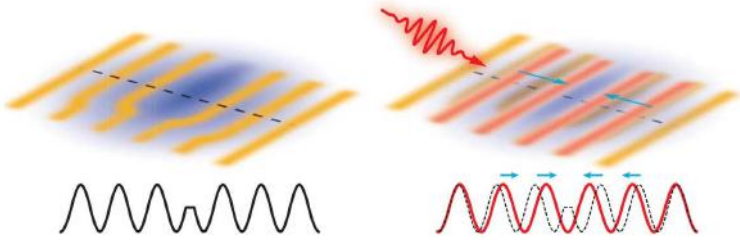

Figure 1.6: a) Example of a topological defect in copper oxide YBCO hosting competing CDW (yellow lines) and superconductivity (blue area). The cartoon reported here sketches a discommensuration line within the CDW domain. b) Ultrafast suppression of superconductivity by means of optical excitation was shown to result in an annihilation of the topological defect, and a consequent enhancement of the CDW phase coherence. Adapted from Ref. 300.

1.2.3 Out-of-equilibrium switching

High-intensity excitations can drive a system far from equilibrium, leading to novel non-equilibrium "phases" through non-thermal pathways. As sketched in Fig. 1.3 and 1.4c, light excitation and electric-fields are able to modify the free energy landscape and drive the system into a new local minimum of the free energy. The external perturbation thus induces a phase transition to a metastable state that is not accessible at equilibrium through adiabatic transformations [98].

Light- or electric-field-induced phase transitions have been reported, for example, in several Mott materials, where external stimuli can drive the collapse of the electronic band structure and the sudden release of a large number of free carriers [189, 267]. The insulator-to-metal transition can be induced by either light pulses or applied voltages, for instance, in vanadium oxides VO_2 and V_2O_3 [169, 321, 306, 61, 63], ruthenium oxides [170, 231, 209, 297] and manganese oxides [328, 126]. Another example is given by the layered charge density wave system 1T-TaS_2 where both in-plane bias voltages and light pulses can induce an abrupt drop in resistance (see Fig. 1.7) along with the possibility of switching between different charge density wave orders, namely incommensurate, nearly-commensurate and commensurate CDW [320, 118, 296, 261, 268, 94]. Optical excitation in 1T-TaS_2 can also drive the formation of hidden metallic states that do not exist at equilibrium, which can be erased by increasing the sample temperature or by thermal annealing controlled by a train of light pulses [261].

Other examples of optical manipulation achieved in this strong excitation regime include reversible phase switching between an antiferromagnetic insulator and ferromagnetic metal in manganites [80, 273, 328, 192], light-induced superconducting-like states [41] and enhanced CDWs [300].

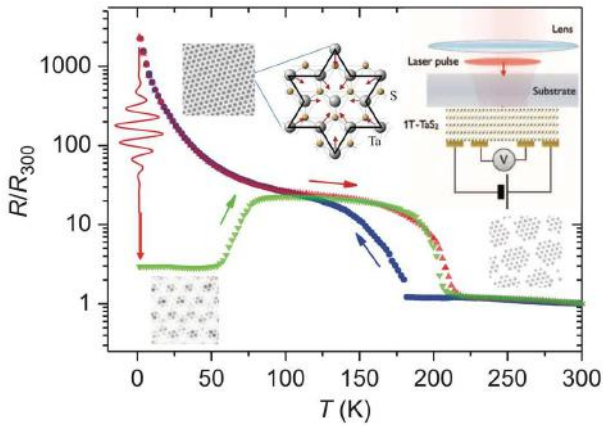

Figure 1.7: Example of insulator-metal switching induced by a light pulse. Blue and red markers show the resistance of a 1T-TaS_2 sample upon thermal cycling. An above threshold 35-fs optical pulse can switch the system from a high resistance state to a low resistance hidden state (green data points). The insets show sketches of the experimental setup and of the different CDW ordered phases. Adapted from Ref. 296.

1.3 Towards achieving control in quantum materials

Non-thermal metastable phases, insulator-metal transitions and fragility to external perturbations offer great opportunities for controllable and reversible manipulation of the electronic properties of a system, therefore holding remarkable potential for technological applications [281, 317]. In the following, we outline some of the main open challenges in the field.

1.3.1 Accessing quantum coherence

One of the key elements expected to open a new route toward the understanding and the control of correlated materials is the ability to access quantum coherence [266]. When laser pulses are employed, the initial excitation creates coherent states whose wavefunctions evolve in phase with the electric field. In the case of a two-level system, for example, the state prepared by a quantum-coherent excitation is a superposition of the ground state $|0\rangle$ and the excited state $|1\rangle$:

$$|\psi\rangle = a_0(t)|0\rangle + a_1(t)|1\rangle, \tag{1.3}$$

where we can write $a_i(t) = c_i(t)\exp(-i\omega_i t)$, with $i = 0, 1$ and $\omega_i = E_i/\hbar$ eigenfrequencies of the $i-$th state, and assume that $c_i(t)$ are slowly varying functions [93]. The concept of quantum coherence is best described by making use of the density matrix operator defined as

$$\rho = |\psi\rangle\langle\psi|, \tag{1.4}$$

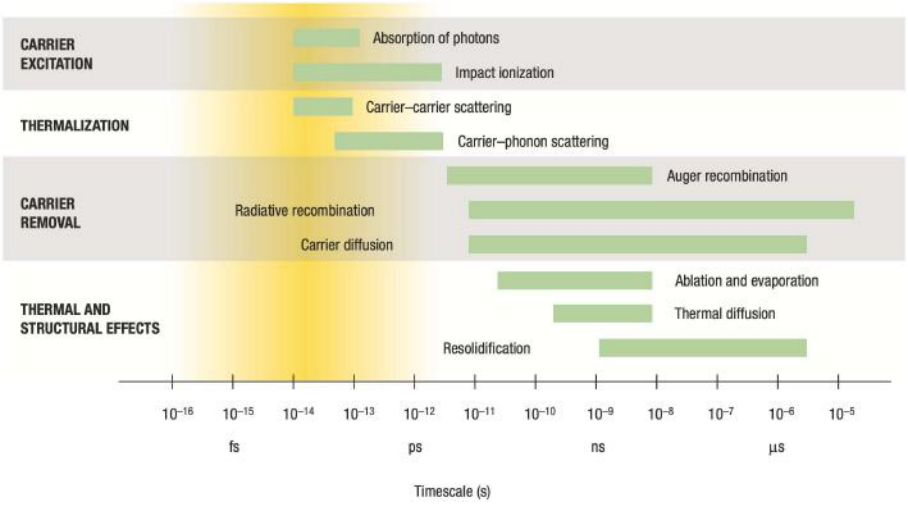

Figure 1.8: Typical timescales of various electron and lattice processes occurring in solid state systems after ultrashort laser excitation. Decoherence due to scattering events takes place within tens of femtoseconds. Adapted from Ref. 270.

which, for the two-level system considered here, reads [93]:

$$\rho = \begin{pmatrix} \rho_{00} & \rho_{01} \\ \rho_{10} & \rho_{11} \end{pmatrix} = \begin{pmatrix} |c_0(t)|^2 & c_0(t)c_1^*(t)e^{i\omega_{01}t} \\ c_0^*(t)c_1(t)e^{-i\omega_{01}t} & |c_1(t)|^2 \end{pmatrix} \tag{1.5}$$

with $\omega_{01} = (E_1 - E_0)/\hbar$. While the diagonal terms of ρ represent the time-dependent populations of the ground and excited states, the off-diagonal ones describe the coherence between $|0\rangle$ and $|1\rangle$. Importantly, the physical meaning of the density matrix elements extends also to the case of statistical ensembles, where the density matrix elements are given by the average over all the N components of the ensemble indexed by s, namely $\bar{\rho}_{ij} = 1/N \sum_s \rho_{ij}^{(s)}$ [93]. The interaction of the system with the incoherent fluctuations of the environment (charge, spin and lattice background) can result in dephasing processes that destroy quantum coherence, captured by the time decay of the off-diagonal terms of the density matrix. In solid-state systems, scattering causes rapid dephasing resulting in typical decoherence times of the order of tens of femtoseconds (see Fig. 1.8 for typical timescales of electron scattering processes) [93, 270].

The exploitation of quantum-coherent phenomena, originating from the propagation of many-body excitations without loss of quantum-coherence, is a long sought-after goal of condensed matter physics [15, 145]. For example, the coherent conversion of photons into charge excitations could enormously increase the performances of optoelectronic, spintronic and photovoltaic devices. This requires preserving the electronic coherence on timescales longer than the transfer time of the charges to external collectors (Fig. 1.9a) [93]. Coherence-enhanced transport was predicted to be achievable in devices composed of few

atomic layers of transition-metal-oxides, such as $LaVO_3/SrVO_3$ heterostructures [150].

Another tantalizing approach is the employment of coherent control protocols to manipulate the electronic properties of materials. By creating suitable coherent superposition of quantum states that evolve faster than the decoherence processes, coherent control approaches employ the phase of the electromagnetic field as the control parameter that determines the outcome of a chemical reaction in atoms and molecular systems [101] or of a phase transition is solid-state materials. The ability to quantum-coherently guide and control electronic excitations would tremendously impact the development of quantum-information processes and communication technologies [145]. So far, the implementation of coherent control approaches in solid-state systems has been hindered by the extremely fast decoherence of charge excitations (tens of fs). Optical control of the insulator-to-metal transition has recently been demonstrated in organic correlated crystals [186], atomic indium wires [122] and CDW material 1T-TaS_2 [180] where the coherence of a photoinduced collective vibrational mode was exploited. Purely electronic coherent control has been experimentally reported in V_2O_3 by means of resonant excitation of the $e_g^\pi \rightarrow a_{1g}$ interband transitions, which are manipulated on a timescale faster than the electronic decoherence time of the system (Fig. 1.9b) [84].

On the fundamental understanding level, accessing and measuring the decoherence time of electronic excitations would shed light on the mechanisms and hierarchy of interactions with the different degrees of freedom that lead to dephasing and, eventually, thermalization. The onset of either short-range or long-range ordered phases in strongly correlated materials, such as orbital order, magnetic order or superconductivity, is expected to significantly affect the decoherence dynamics. In this context, exploiting the variation of the coupling between electronic transitions and the bosonic bath in proximity of a phase transition could potentially represent a promising strategy to tune the decoherence time and tailor quantum-coherent effects [93].

The novel approaches mentioned above crucially depend on the knowledge of the decoherence timescales and the mechanisms driving the ultrafast dephasing. In solid-state systems, the direct measurement of the fundamental decoherence time of photoexcitations (i.e., addressing the lifetime of the ρ_{01} or ρ_{10} terms of the density matrix in Eq. 1.5) has so far been difficult: in the frequency domain, conventional optical spectroscopies are strongly affected by inhomogeneous broadening, which reflects the statistical distribution of impurities and electronic or structural inhomogeneities; in the time domain, the well established ultrafast pump-probe spectroscopy is capable of probing only the population dynamics of a transition, that is measuring the dynamics of the populations difference $\rho_{11} - \rho_{00}$, while remaining blind to the fundamental decoherence processes [93]. One of the most promising approaches that can overcome these limitations is 2D spectroscopy, an ultrafast optical approach based on the employment of multiple phase-coherent laser pulses. The working principle of this time-resolved

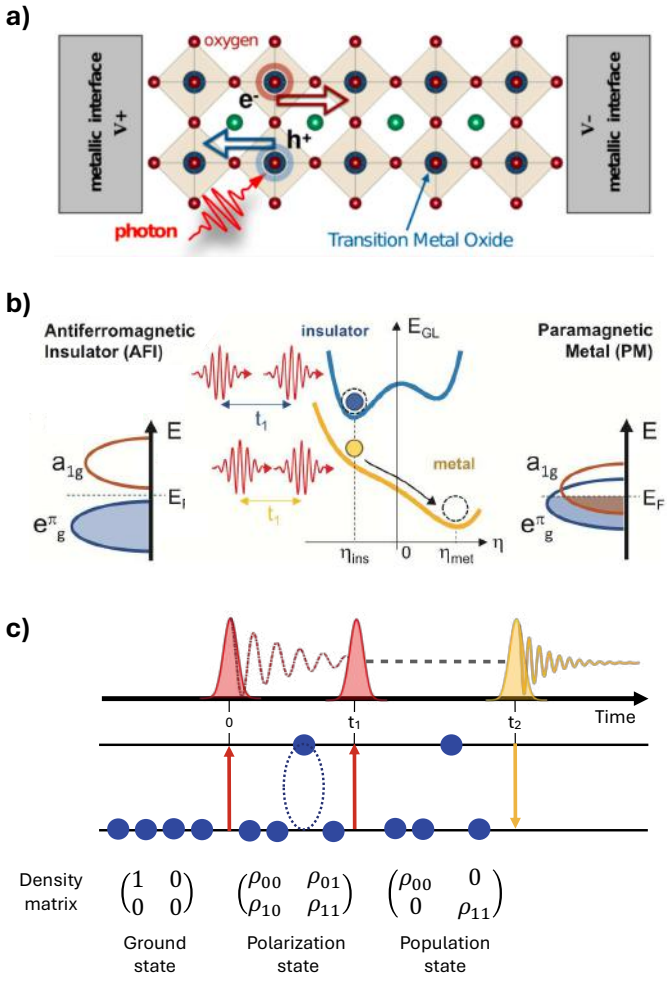

Figure 1.9: a) Cartoon of a transition-metal-oxide device where the generation and collection of the charges can occur along quantum coherent pathways. Adapted from Ref. 150. b) Sketch of an electronic-coherent-control protocol based on the employment of phase-coherent excitation pulses to tune the insulator/metal phase of vanadium oxide V_2O_3. Adapted from Ref. 84. c) 2D spectroscopy working principle. The system, initially at equilibrium (ground state $|0\rangle$) is excited by a first pulse that leaves the system in a coherent state (polarization state), described by nonzero off-diagonal terms (ρ_{01} and ρ_{10}) of the density matrix. A second phase-coherent pulse transforms the polarization state into a population state with zero off-diagonal terms, that depends on the coherence of the system at t_1. A third pulse at t_2 determines the emission of the signal.

technique, which will be discussed in detail in Chapter 2, is sketched in Fig. 1.9c. A first pulse creates a macroscopic polarization P that is related to the off-diagonal terms of the density matrix according to $P = \mu_{01}(\rho_{01} + \rho_{10})$, with μ_{01} being the transition dipole moment. The polarization oscillates in time with frequency ω_{01} and decays due to dephasing. At time t_1, a second pulse converts the macroscopic polarization into a population state, which is reminiscent of the phase of the polarization at t_1. Lastly, a third pulse at time t_2 converts back to a coherent polarized state that radiates the measured signal field. In this way, 2D spectroscopy is capable of directly accessing the off-diagonal terms of the density matrix (ρ_{01} in Eq. 1.5) and, therefore, disentangling the real polarization dephasing from the population decay and from inhomogeneous effects, while preserving simultaneous high temporal and spectral resolutions.

1.3.2 Inhomogeneites in real space

The phenomena emerging in strongly correlated materials are often characterized by the spontaneous appearance of spatially separated regions with distinct structural, magnetic, and electronic properties. This is the case, for example, of Mott transitions which display a first order nature, as already predicted by Mott [206] and confirmed in Hubbard-like models [39, 12, 307, 278]. In addition, the frequently observed involvement of the lattice degree of freedom in the IMT further enhances the discontinuous character of the transition. This first order character of the Mott transition implies the existence of a region of metal-insulator phase coexistence that is already present at equilibrium and could be substantially widened in out-of-equilibrium conditions, therefore offering great opportunities for potential applications.

The inherent inhomogeneity of the IMT was recently reported by spatially resolved X-rays diffraction, optical imaging and photoemission spectroscopy performed on paradigmatic Mott systems such as VO_2 [226, 228], V_2O_3 [176, 191] and $NdNiO_3$ (see Fig. 1.10) [188]. These experiments reported the co-existence of insulating and metallic domains across the temperature driven IMT and imaged the nucleation, growth and percolation of one of the two phases over the other. Photoemission electron microscopy (PEEM) of V_2O_3 also showed that the insulating phase itself displays a hidden nanotexture that strongly affects the IMT [238].

However, most out-of-equilibrium studies of the light-/electrically-induced IMT have so far employed time-resolved techniques or transport measurements that return spatially integrated information, therefore washing out the rich physics related to spatial inhomogeneities and phase coexistence. O'Callahan and coworkers [212] showed that the spatial inhomogeneities of VO_2 can also affect temporal dynamics, therefore calling for techniques that combine out-of-equilibrium studies with spatial resolution. Unveiling the out-of-equilibrium dynamics of Mott materials at the relevant spatial scale would therefore provide fundamental insights into the forces driving the phase transformation and into

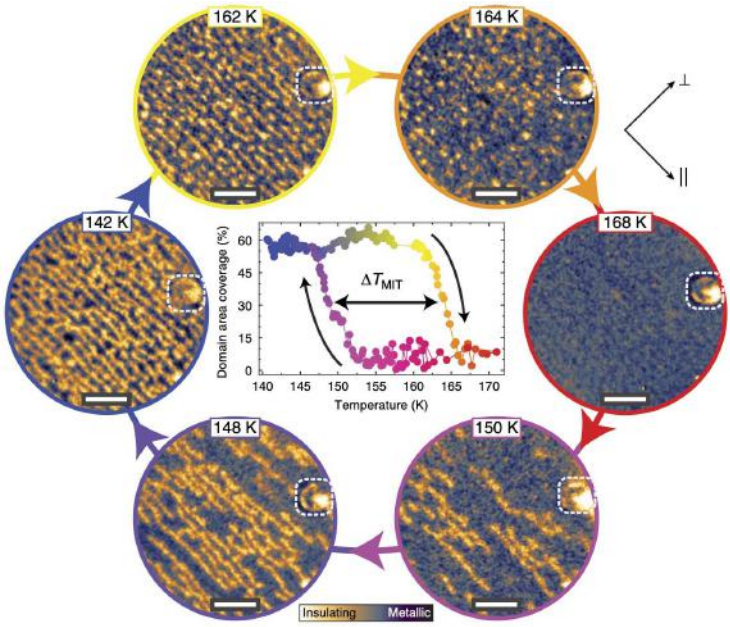

Figure 1.10: PEEM microscopy imaging of the nanotexture of $NdNiO_3$ across the temperature-driven IMT. Scale bar: 1 μm. Adapted from Ref. 188.

the competing mechanism between the structural phase transition and the electronic IMT. A deeper understanding of the nascent metallic nanodroplets would also greatly enhance the ability to control the ultrafast IMT and the electrical breakdown in nanometric resistive-switching devices [15, 281]. In fact, while most of the models describing electrical breakdown of Mott insulators are phenomenological descriptions based on resistor network models [262, 264, 2], the nature and the mechanisms driving the early-stage formation of the nanometric metallic seeds that eventually lead the percolative transition are still unknown.

1.4 Quantum simulation

An alternative approach that can be employed to investigate the many-body physics of correlated systems is the use *quantum simulators* [30, 6]. These refer to simpler and artificial platforms that contain the same physical ingredients as the relevant ones of real materials, but where the key parameters can be easily tuned and controlled. The development of the quantum simulation paradigm has been led by ultracold-atoms systems [21, 20, 50, 87]. Quantum particles can be trapped in artificial lattices by means of optical traps, i.e. periodic potentials generated by the interference pattern of overlapping laser beams. Such optical lattices can be employed to simulate the lattice potential where electrons move in a condensed-matter system. For example, interacting ultracold atoms on a

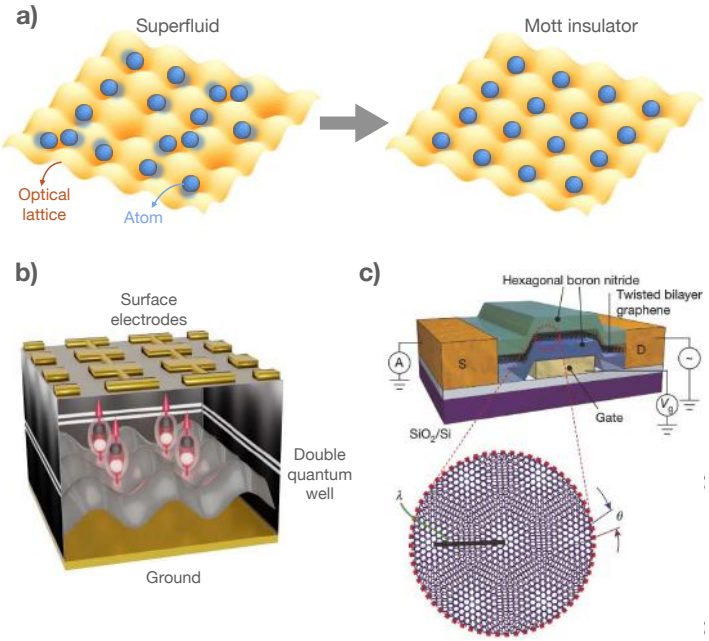

Figure 1.11: Examples of platforms employed for the quantum simulation of strongly correlated materials. a) The quantum phase transition from a superfluid to a Mott insulator phase can be realized with ultracold atoms trapped in an optical lattice. Adapted from Ref. 30. b) Dipolar excitons in a periodic potential, produced by an array of surface gate electrodes, allow to simulate the extended Bose–Hubbard Hamiltonian. Adapted from Ref. 153. c) Twisted bilayer graphene hosts Mott insulating and superconducting phases that can be controlled by tuning the temperature and the carrier concentration via proper gating. Adapted from Ref. 33.

lattice can implement the Hubbard model, which represents one of the most prominent models for correlated materials. By tuning the ratio between the tunneling and on-site interaction energies, which can be controlled for example by varying the depth of the optical lattice, it is possible to realize the quantum phase transition from a superfluid to a Mott insulator (see Fig. 1.11a) [20, 30]. In these ideal implementations, the phononic degree of freedom is lacking because of the absence of imperfections and thermal fluctuations of the optical lattice. Therefore, despite their tunability and flexibility, cold-atoms simulators are mostly suited to the investigation of fundamental physical phenomena, while their limitations in terms of temperatures and experimental complexity leave them far from direct applications.

More recently, quantum simulation has been extended to solid-state platforms [6, 30]. One example is given by the employment of nano-devices where

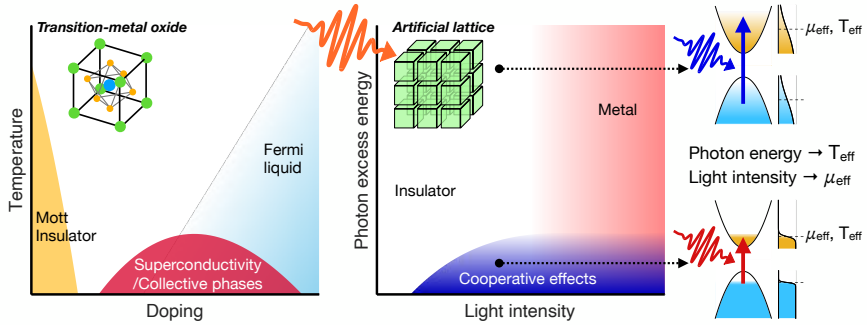

Figure 1.12: Sketch of the mapping between the phase diagram of a real correlated material (left panel) and that of an artificial platform employed for quantum simulation. Light pulses can be used as a tool to access and explore the phase diagram of the artificial platform. The effective chemical potential (μ_{eff}) and the effective temperature (T_{eff}) are controlled by tuning the intensity and photon energy of the excitation pulses, respectively.

semiconductor excitons are confined in two-dimensions and are subject to a periodic potential generated by nano-patterned metallic electrodes (see Fig. 1.11b) [154, 153]. Another platform extending the realm of quantum simulators to solid-state systems is represented by heterostructures of twisted bidimensional materials (see Fig. 1.11c) [140]. In these systems, a rich physics emerges from the realization of moiré patterns that act as an effective way to modify the band structure, with the twist angle providing a control knob to tune the system. In twisted bilayer graphene, for example, superconductivity [34, 173, 260, 318], correlated insulators [33, 173, 260] and the quantum anomalous Hall effect [251, 249] have been realized at the so-called "magic-angle".

So far, solid-state platforms for quantum simulations have mostly relied on electrical transport to probe the quantum properties of the systems and to tune the carrier density by application of a gate voltage [140, 34]. Another promising approach is to develop platforms based on optical spectroscopy measurements [140], where the carrier density and distribution is controlled by means of ultrashort light pulses. More specifically, in a semiconducting system, photoexcitation across the gap can create an excited carriers population whose density and effective chemical potential is controlled by the light intensity; on the other hand, the photon energy in excess with respect to the semiconducting gap is stored as internal energy of the hot electronic population in the conduction band. By tuning the intensity and photon energy of the excitation pulses, it is therefore possible to control the effective chemical potential of the photoinduced non-thermal population as well as its effective temperature, thus providing a way to map the phase diagram of the artificial platform, as sketched in Fig. 1.12.

1.5 Thesis outline

In this work, we explore out-of-equilibrium phenomena in Mott systems that exhibit long-range ordered phases coupled with symmetry-breaking phase transitions. We adopt two different approaches. In the first part of the thesis, we investigate vanadium oxide materials under out-of-equilibrium conditions induced by either laser pulse excitation or the application of a static electric field. In these paradigmatic Mott systems, we address the challenges of measuring decoherence dynamics across a phase transition and of performing spatially resolved experiments at the nanoscale. In the second part, we introduce superlattices composed of semiconducting lead halide perovskite nanocrystals as a potential novel quantum simulator. Using ultrafast optical spectroscopies, we study the physics of excitons in artificial lattices and explore the possibility of linking their dynamics to the formation of Mott insulating states and collective ordered phases.

More specifically, the thesis is structured as follows.

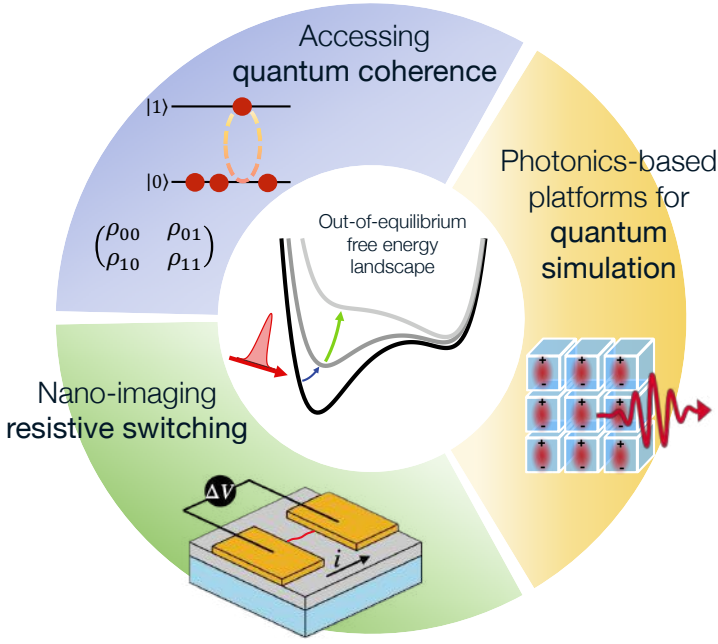

Figure 1.13: Overview of topics addressed in this thesis. They include the measurement of the decoherence time in a Mott insulator, the nanoscale spatially resolved investigation of resistive switching in a Mott insulator-metal system and the development of novel quantum simulation platforms based on halide perovskite artificial lattices.

Chapter 2 introduces the theoretical description and experimental implementation of the ultrafast optical techniques employed in this work, namely pump-probe spectroscopy and 2D coherent electronic spectroscopy (2DES). In particular, we focus on the possibility of measuring the decoherence time by extending pump-probe to 2DES. We also describe the experimental setups developed for the time-resolved experiments discussed in Chapters 3, 5 and 6.

In Chapter 3, we report an example of excitation by means of ultrashort laser pulses on the Mott insulator $LaVO_3$. We study the critical behavior of the Hubbard exciton ultrafast dynamics across the orbital and spin ordering transition. By means of 2DES we directly observe the shortening of the coherence time due to the pump-induced perturbation of the spin and orbital-ordered background.

Chapter 4 presents an example of phase switching upon application of a static electric field in vanadium oxide V_2O_3. In this system, application of an above threshold voltage across micro-patterned electrodes induces a resistive switching from a high resistance (insulator) to low resistance (metal) state. We employ PEEM microscopy, combined with simultaneous transport measurements, to image the resistive switching process at the nanoscale and investigate the role played by the topological defects of the intrinsic nanotexture of the symmetry broken insulating phase of V_2O_3 on the resistive switching.

The second part of the thesis is dedicated to the development of novel quantum simulation platforms able to reproduce the physics of long-range ordering in proximity of a Mott transition.

In Chapter 5, we first introduce the lead halide perovskite nanocube superlattices and analyze the theoretical framework that allows to exploit the exciton interactions in these systems to simulate the main features of correlated materials. We then investigate the suitability of $CsPbBr_3$ nanocube superlattices as a novel platform for quantum simulation. By means of resonant-pump broadband-probe spectroscopy we study the photoexcited system and explore the possibility of accessing different quantum phases that include an excitonic Mott insulating phase, a super-radiant collective state, and a metallic electron-hole liquid phase, by continuously tuning the light excitation intensity.

Lastly, Chapter 6 addresses the possibility of exploiting the tunability of lead halide perovskite nanocubes and extending the paradigm of quantum simulation also to hybrid organic-inorganic nanocube superlattices. The ultrafast dynamics of excitons in formamidinium lead iodide (FAPI) superlattices is here investigated by means of 2DES, which reveals that the coherent ultrafast dynamics is limited by the combination of the inherently short exciton decay time ($\simeq$ 40 fs) and the dephasing due to the coupling with selected optical phonon modes at higher temperatures. A significant change of the excitonic coherence time is also observed across the cubic to tetragonal structural transition.

CHAPTER 2

Methods: coherent multi-dimensional spectroscopies

In this chapter, we describe the ultrafast optical spectroscopy techniques employed in this thesis to study out-of-equilibrium dynamics on femtosecond and picosecond timescales. After introducing the theoretical framework of light-matter interaction in non-linear optical experiments, we consider the two experimental approaches used in this work, namely optical pump-probe and 2D coherent electronic spectroscopy. We discuss what are the measured quantities and the information that can be obtained, as well as their experimental implementation. We particularly focus on the lineshape analysis that enables the extraction of the intrinsic decoherence time of the excited resonance. Finally, we illustrate the experimental setups used for the experiments presented in Chapters 3, 5 and 6.

2.1 Introduction to time-resolved spectroscopies

Ultrafast spectroscopies are a fundamental and widely used approach to study out-of-equilibrium dynamics in correlated materials [327, 98, 59]. This field has flourished with the advent of pulsed lasers that, by delivering coherent light pulses with temporal duration down to few tens of femtoseconds, allow to generate non-equilibrium conditions on timescales faster than the energy exchange with the internal degrees of freedom of the system, therefore unveiling phenomena not observable by equilibrium spectroscopies [98]. The most commonly employed scheme is a two-pulse experiment, usually referred to

as *pump-probe*: a first ultrafast laser pulse (pump) perturbs the ground state of the system, while a second delayed pulse (probe) detects the temporal evolution of some observable of the system. Nowadays, time-resolved optical experiments can cover almost the entire electromagnetic spectrum, from THz to X-rays, using either conventional ultrafast laser sources or free electron lasers [179]. Additional capabilities can also come from time-resolved schemes based on photoemission or diffraction and inelastic scattering experiments [59]. In addition to the time-resolution, spectral resolution can be achieved by employment of probe pulses with a broad spectrum which allows to monitor the photoinduced changes in the optical/electronic properties in a wide spectral range. In the visible/near-infrared range, for example, broadband approaches provide the capability of disentangling the different physical mechanisms perturbing the equilibrium optical properties by using effective non-equilibrium models of the dielectric function [98]. Overall, ultrafast spectroscopies are able to investigate a surprisingly wide variety of phenomena while employing the same pump-probe experimental scheme. In strongly correlated systems, some examples include coherent oscillations of vibrational modes (e.g. phonons, magnons, CDWs, superconducting amplitude modes), interplay between charge-transfer excitations and the emergence of ordered phases, photoinduced phase transitions [327, 98, 59].

Further advances can be achieved by multi-pulse techniques that employ three or more pulses [98], often referred to as multi-dimensional spectroscopies (within this framework, pump-probe experiments are called one-dimensional (1D) spectroscopies because they scan only one time delay, namely the pump-probe delay). These advanced schemes allow to expand the amount of information accessible by time-resolved experiments. With 1D spectroscopy, for example, there is an intrinsic limitation in accessing the fundamental decoherence dynamics of an excited state since only the depopulation process is probed. As introduced in Chapter 1, two-dimensional (2D) coherent spectroscopy, a three-pulse experimental scheme employing two phase-coherent pump pulses, allows to overcome this limitation and investigate dephasing mechanisms [283].

2.2 Theoretical framework

2.2.1 Non-linear polarization in density matrix formalism

Optical phenomena originate from of the interaction between the electromagnetic field of the incoming radiation and the charged particles inside the material. The result of the interaction is the generation of a macroscopic optical polarization $P(t)$ that acts as a source for the emitted radiation field. As a consequence, the knowledge of the optical polarization generated by the impinging electromagnetic field is the key element in the interpretation of time- and frequency-domain spectroscopies.

In first approximation, the induced polarization scales linearly with the electric field. The linear expression, however, is no longer valid when working with large-amplitude fields. In this case, the nonlinear dependence of the response of the medium on the applied field amplitude must be taken into account by including higher-order terms in the field. Under the assumptions of instantaneous response and lossless and dispersionless medium, the polarization $P(t)$ can then be written as [23]

$$\begin{aligned} P(t) &= \epsilon_0[\chi^{(1)}E(t) + \chi^{(2)}E^2(t) + \chi^{(3)}E^3(t) + ...] \\ &\equiv P^{(1)}(t) + P^{(2)}(t) + P^{(3)}(t) + ... \\ &\equiv P^{(1)}(t) + P^{NL}(t), \end{aligned} \tag{2.1}$$

with ϵ_0 electric permittivity of vacuum, and $E(t)$ electric field of the incoming radiation. $P^{(N)}(t)$ is referred to as N-th order nonlinear polarization and $\chi^{(N)}$ are $(N+1)$-rank tensors, called N-th order nonlinear susceptibilities. The wave equation for light propagation in a dispersionless medium, obtained by combining Maxwell's equations, reads

$$\nabla^2 E - \frac{n^2}{c^2}\frac{\partial^2 E}{\partial t^2} = \frac{1}{\epsilon_0 c^2}\frac{\partial^2 P^{NL}}{\partial t^2}, \tag{2.2}$$

where c is the speed of light in vacuum and n is the index of refraction, with $n^2 = 1 + \chi^{(1)}$. Eq. 2.2 shows that, in presence of a nonlinear component of the polarization, the wave equation is inhomogeneous, with P^{NL} acting as a source term and driving the emission of electric fields, i.e. the nonlinear signals measured in optical measurements.

In order to describe the induced non-linear polarization, in the following we shall adopt the semi-classical description where the radiation field is treated classically whereas the material system is treated quantum mechanically, with its time evolution governed by the Hamiltonian $H(t) = H_0 + H_{int}(t)$ [207, 111, 112]. H_0 is the time-independent Hamiltonian of the unperturbed system; $H_{int}(t)$ describes the radiation-matter interaction and, within the dipole approximation (also known as long wavelength approximation), can be expressed as

$$H_{int}(t) = -\mu E(t), \tag{2.3}$$

with μ dipole moment operator and $E(t)$ the external electric field. In this framework, the macroscopic polarization is given by the expectation value of the dipole moment μ which, in the density matrix formalism, can be written as [207, 111, 112]

$$P(t) = \mathrm{Tr}\{\mu\rho(t)\} \equiv \langle\mu\rho(t)\rangle, \tag{2.4}$$

where $\rho(t)$ is the density matrix of the system (see Section 1.3.1 and Eq. 1.4) and $\langle\rangle$ indicates the trace operation. We further assume that the electromagnetic field is sufficiently low to allow a perturbative description where the response

can be expanded, order-by-order, in power series of the electric field. In this case, the density matrix is written as

$$\rho(t) \equiv \rho^{(0)}(t) + \rho^{(1)}(t) + \rho^{(2)}(t) + ... \tag{2.5}$$

where $\rho^{(0)}(t) = \rho(-\infty)$ is the density matrix at equilibrium and $\rho^{(N)}$ is the $N-$th order contribution in $E(t)$. Upon integration of the Liouville equation in the interaction picture [207, 112], we obtain

$$\rho^{(N)}(t) = \left(-\frac{i}{\hbar}\right)^N \int_{t_0}^{t} d\tau_N \int_{t_0}^{\tau_N} d\tau_{N-1} ... \int_{t_0}^{\tau_2} d\tau_1 E(\tau_N)E(\tau_{N-1})...E(\tau_1) \\ U_0(t,t_0)[\mu_I(\tau_N),[\mu_I(\tau_{N-1}),...[\mu_I(\tau_1,\rho(-\infty))]...]]U_0^\dagger(t,t_0), \tag{2.6}$$

where $U(t,t_0) = \exp\left(-i\frac{H_0}{\hbar}t\right)$ is the time evolution operator and $\mu_I(t) = U_0^\dagger(t,t_0)\mu U_0(t,t_0)$ is the dipole operator in the interaction picture. Eq. 2.6 describes the interaction of the system with N radiation fields arriving at times $\tau_1, ..., \tau_N$, as sketched in Figure 2.1. t_0 represents a time before the interaction and can be sent to $-\infty$.

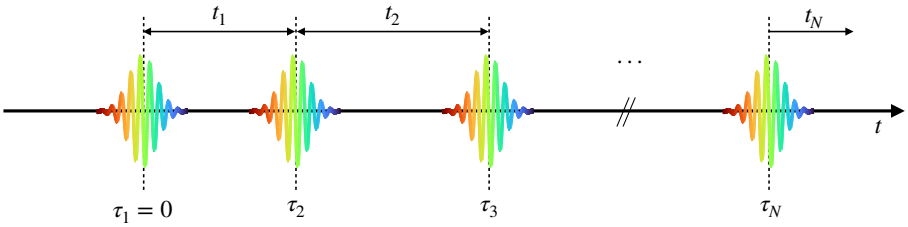

Figure 2.1: Sketch of the time variables for a systems interacting with N incoming radiation fields. τ_i indicate absolute times, t_i represent the time intervals between two successive interactions.

Finally, inserting Eq. 2.6 in Eq. 2.4, we obtain the N-th order polarization given by

$$P^{(N)}(t) = -\left(-\frac{i}{\hbar}\right)^N \int_{-\infty}^{t} d\tau_N \int_{-\infty}^{\tau_N} d\tau_{N-1} ... \int_{-\infty}^{\tau_2} d\tau_1 \\ E(\tau_N)E(\tau_{n-1})...E(\tau_1)\langle\mu(t)[\mu(_N),...[\mu(\tau_1),\rho(-\infty)]...]\rangle. \tag{2.7}$$

We can conveniently introduce a new set of time variables, defined as

$$\begin{aligned} &\tau_1 = 0, \\ &t_1 \equiv \tau_2 - \tau_1, \\ &t_2 \equiv \tau_3 - \tau_2, \\ &... \\ &t_N \equiv t - \tau_N, \end{aligned} \tag{2.8}$$

representing the delay intervals between successive interactions (see Fig. 2.1), and re-write Eq. 2.7 as

$$P^{(N)}(t) = \int_0^\infty dt_N \int_0^\infty dt_{N-1} ... \int_0^\infty dt_1$$
$$E(t-t_N)E(t-t_N-t_{N-1})...E(t-t_N-t_{N-1}-...-t_1)S^{(N)}(t_N,...t_1), \tag{2.9}$$

where

$$S^{(N)}(t_N,...t_1) =$$
$$-\left(-\frac{i}{\hbar}\right)^N \langle \mu(t_N+t_{N-1}+...+t_1)[\mu(t_{N-1}+...+t_1),...[\mu(0),\rho(-\infty)]...]\rangle \tag{2.10}$$

is the N-th order response function. Some important properties of the response function are listed below.

- $S^{(N)}(t_N,...t_1)$ is defined only for positive times t_N, i.e. $t_N \geq 0$. This reflects the principle of causality, which implies that the system emits a field only after the interaction with the incoming radiation field. This property can be guaranteed by including $\Theta(t_i)$ factors in $S^{(N)}$, with Θ being the Heaviside step function, which then allows to change the lower limits of integration in Eq. 2.9 from 0 to $-\infty$.
- The first $N-1$ interactions appear in Eq. 2.10 as part of commutators; they act either on the ket (on the left) or on the bra (on the right) of the density matrix $\rho(-\infty)$ generating a non equilibrium density matrix. The last interaction, occurring at t_N, is instead not part of a commutator and plays a different role, as it determines the emission of the light field from the off-diagonal elements of the non-equilibrium density matrix generated by the previous interactions.
- $S^{(N)}$ contains 2^N terms, only 2^{N-1} of which are independent since the other half is given by the respective complex conjugates.

$S^{(N)}(t_N,...t_1)$ represents the intrinsic material response and contains all the information of the properties of the system needed to calculate N-th order non-linear optical processes. The external electric field $E(\tau_i)$ in Eq. 2.9 determines the details of the experiment and the measured optical polarization, which distinguish the various spectroscopic techniques. The linear term $P^{(1)}$ is what is measured in linear optics. Second-order non-linear processes, such as sum frequency generation, are determined by $P^{(2)}$, which however vanishes in isotropic and centrosymmetric materials. $P^{(3)}$ represents the lowest order non-linear term that is non-zero in any system. The third order response is

responsible of a wide range of ultrafast spectroscopies commonly referred to as *four-wave-mixing* experiments. These include pump-probe and 2D spectroscopy, which is what we will focus on in the following paragraphs.

2.2.2 Third-order response function

According to Eq. 2.9, the third order polarization is the convolution of the electric fields of the incoming radiation and the response function:

$$P^{(3)}(t) = \int_0^\infty dt_3 \int_0^\infty dt_2 \int_0^\infty dt_1 \\ E(t-t_3)E(t-t_3-t_2)E(t-t_3-t_2-t_1)S^{(3)}(t_3,t_2,t_1). \tag{2.11}$$

Upon expansion of the commutators in Eq. 2.10, $S^{(3)}(t_3,t_2,t_1)$ reads [207, 111, 112]

$$S^{(3)} = \left(\frac{i}{\hbar}\right)^3 \Theta(t_1)\Theta(t_2)\Theta(t_3) \sum_{\alpha=1}^{4} [R_\alpha(t_3,t_2,t_1) - R_\alpha^*(t_3,t_2,t_1)], \tag{2.12}$$

where

$$\begin{aligned} R_1 =& \langle \mu(t_3+t_2+t_1)\mu(0)\rho(-\infty)\mu(t_1)\mu(t_2+t_1)\rangle, \\ R_2 =& \langle \mu(t_3+t_2+t_1)\mu(t_1)\rho(-\infty)\mu(0)\mu(t_2+t_1)\rangle, \\ R_3 =& \langle \mu(t_3+t_2+t_1)\mu(t_2+t_1)\rho(-\infty)\mu(0)\mu(t_1)\rangle, \\ R_4 =& \langle \mu(t_3+t_2+t_1)\mu(t_2+t_1)\mu(t_1)\mu(0)\rho(-\infty)\rangle \end{aligned} \tag{2.13}$$

and * indicates the complex conjugate. These different terms, obtained from the explicit expansion of $P^{(3)}$, each represent a different *quantum pathway*, that is a specific (time-ordered) sequence of interactions between the electric fields and the systems, leading to an emitted signal. They are often represented through *double-sided Feynman diagrams* (Fig. 2.2), where the vertical lines on the left and on the right represent the time evolution of, respectively, the ket and the bra of the density matrix, whereas the interactions with the transition dipole operator are indicated by arrows that act on the ket (arrow from the left) or on the bra (arrow from the right). The Feynman diagrams depicting the third-order interactions R_α, $\alpha = 1,2,3,4$, and their respective conjugates R_α^*, are displayed in Figure 2.2 for the most simple case of a two level system. For reasons that will be explained in Sec. 2.2.3, R_2 and R_3 are called *rephasing* signals, whereas R_1 and R_4 are referred to as *non-rephasing* signals.

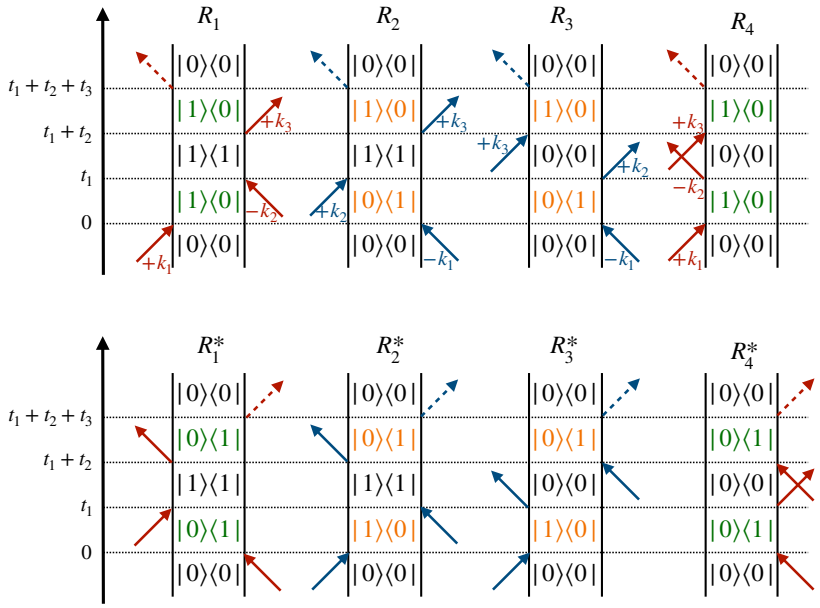

Figure 2.2: Double-sided Feynman diagrams of the third-order response. R_1, R_2, R_3 and R_4 (top panel) and their complex conjugates (bottom panel) indicate different quantum pathways, here explicated, as an example, for the case of a two-level system ($|0\rangle$ and $|1\rangle$). R_2 and R_3 are rephasing diagrams, R_1 and R_4 are non-rephasing.

Also the electric field $E(t)$ appearing in Eq. 2.11 contributes with multiple terms as it is given by the sum of three incoming radiation fields and can therefore be written as [111]:

$$E(t) = E_1(t)(e^{-i\omega_1 t}+e^{i\omega_1 t})+E_2(t)(e^{-i\omega_2 t}+e^{i\omega_2 t})+E_3(t)(e^{-i\omega_3 t}+e^{i\omega_3 t}), \quad (2.14)$$

where $E_\alpha(t)$, $\alpha = 1,2,3$ represent the envelopes of the electric fields. The overall number of terms in Eq. 2.11 can be significantly reduced by designing experiments that allow to discriminate between different terms and select only specific contributions. Below we list the strategies and approximation that can often be employed.

- Four-wave-mixing experiments are usually performed by employing ultrashort light pulses. If the pulse duration is shorter than any material timescale, the envelopes of the light pulses can be approximated to Dirac δ-functions; in this limit, Eq. 2.11 simplifies to $P^{(3)} = S^{(3)}(t, t_1, t_2)$. In addition, if the time separation between the pulses is long enough to avoid pulse overlap, the number of contributing terms is reduced because of the known time ordering (e.g. the first interaction $\mu(0)$ originates from the pulse $E_1(t)$, $\mu(t_1)$ from $E_2(t)$, etc.).

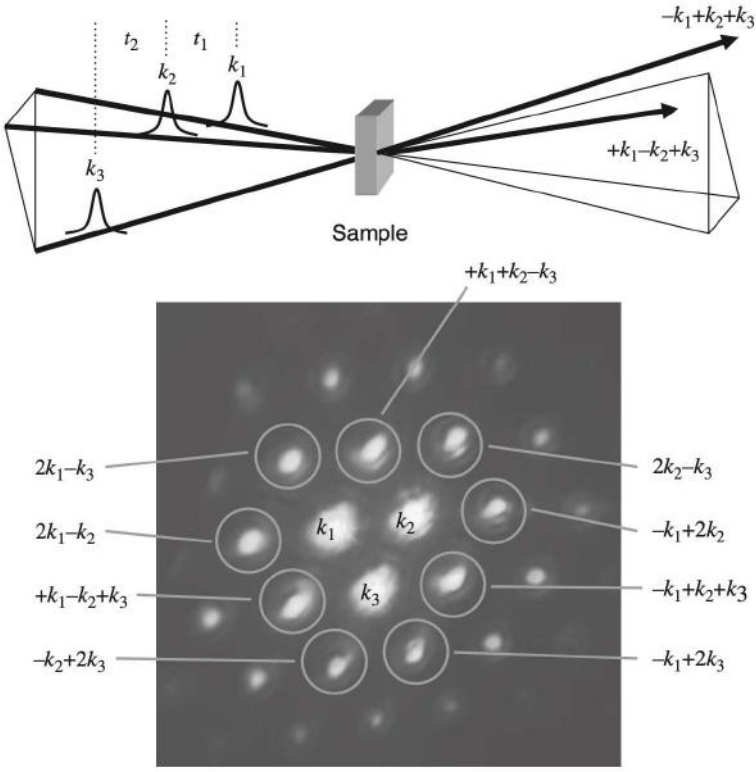

Figure 2.3: Sketch of a typical phase-matching geometry employed in four-wave mixing experiments. Three incoming beams propagating along $\boldsymbol{k_1}$, $\boldsymbol{k_2}$ and $\boldsymbol{k_3}$ excite the system (top panel). Various non-linear fields are emitted in different directions based on phase-matching conditions (bottom panel). In addition to the third-order responses (circles), also the weaker signals originating from the fifth-order responses are visible. Image from Ref. 112.

- If the envelope of the electric field is slowly varying in time (i.e. pulse duration long compared to the optical periods) and the carrier frequency ω_α is near resonance with the material transitions, we can apply the rotating wave approximation (RWA) where only one term between $e^{i\omega_\alpha t}$ and $e^{-i\omega_\alpha t}$, but not both, contributes to $P^{(3)}$.

- When the wavevectors of the electric fields are included, the product $E(t-t_3)E(t-t_3-t_2)E(t-t_3-t_2-t_1)$ carries a wavevector $\boldsymbol{k} = \pm\boldsymbol{k}_1 \pm \boldsymbol{k}_2 \pm \boldsymbol{k}_3$. Different quantum pathways emit the signal in different directions, as illustrated in Fig. 2.3, corresponding to different *phase-matching* conditions. The signals emitted in the directions $\boldsymbol{k} = \pm\boldsymbol{k}_1 \mp \boldsymbol{k}_2 + \boldsymbol{k}_3$ are the most commonly used; rephasing signals are collected along $\boldsymbol{k} = -\boldsymbol{k}_1 + \boldsymbol{k}_2 + \boldsymbol{k}_3$, non-rephasing ones along $\boldsymbol{k} = +\boldsymbol{k}_1 - \boldsymbol{k}_2 + \boldsymbol{k}_3$.

2.2.3 Response function for a two level system

In order to illustrate the meaning of the response functions introduced above (Eq. 2.10 and 2.12), we consider, as an example, the most simple case of a two level system identified by eigenstates $|0\rangle$ (ground state) and $|1\rangle$ (excited state) [111, 112]. In this case the density matrix can be written as

$$\begin{pmatrix} \rho_{00} & \rho_{01} \\ \rho_{10} & \rho_{11} \end{pmatrix}, \tag{2.15}$$

where diagonal elements ρ_{ii} represent the occupation probability of the i-th state (population), whereas off-diagonal elements ρ_{ij} indicate the probability of finding the system in a coherent superposition of the i-th and j-th states. In the case of no external perturbation, the Hamiltonian determining the time evolution of the system according to Liouville equation can be represented as

$$H_0 = \begin{pmatrix} E_0 & 0 \\ 0 & E_1 \end{pmatrix}, \tag{2.16}$$

where E_0 and E_1 are the energy levels of the ground state and excited state respectively. Upon integration of Liouville equation, we find that the diagonal elements of the density matrix are stationary in time:

$$\rho_{00}(t) = \rho_{00}(0), \tag{2.17}$$

$$\rho_{11}(t) = \rho_{11}(0), \tag{2.18}$$

whereas the off-diagonal element oscillate at the frequency of the energy splitting $\omega_{01} = (E_1 - E_0)/\hbar$:

$$\rho_{01}(t) = \rho_{01}(0)e^{+i\omega_{01}t}, \tag{2.19}$$

$$\rho_{10}(t) = \rho_{10}(0)e^{-i\omega_{01}t}. \tag{2.20}$$

Phenomenologically, we can include the process of dephasing, that is the loss of coherence between $|0\rangle$ and $|1\rangle$, by considering a decay time for the off-diagonal elements of the density matrix:

$$\rho_{01}(t) = \rho_{01}(0)e^{+i\omega_{01}t}e^{-\Gamma t}, \tag{2.21}$$

$$\rho_{10}(t) = \rho_{10}(0)e^{-i\omega_{01}t}e^{-\Gamma t}. \tag{2.22}$$

Similarly, the relaxation of the population of the exited state can be described as

$$\rho_{11}(t) = \rho_{11}(0)e^{-t/T_1}, \tag{2.23}$$

$$\rho_{00}(t) = 1 - \rho_{11}(t). \tag{2.24}$$

Since a population relaxation causes a decay also of the off-diagonal elements, the dephasing rate Γ and the depopulation time T_1 are related by

$$\Gamma = \frac{1}{T_2} = \frac{1}{2T_1} + \frac{1}{T_2^*}, \tag{2.25}$$

where T_2 is the homogeneous dephasing time, and T_2^* is the *pure dephasing time*, which is caused by interactions and fluctuations of the environment.

Let us now add the interaction of the system with an optical light field. In this case the total Hamiltonian is $H = H_0 - \mu E(t)$, where the transition dipole operator μ connects the two states $|0\rangle$ and $|1\rangle$ and can be represented by the matrix

$$\begin{pmatrix} 0 & \mu_{01} \\ \mu_{10} & 0 \end{pmatrix}. \tag{2.26}$$

In first approximation, we can consider $\mu_{01} = \mu_{10}$. As seen in Sec. 2.2.1, this interaction gives rise to a macroscopic polarization given by Eq. 2.4; for the case of the two level system we get

$$P = \langle \mu\rho(t) \rangle = \left\langle \begin{pmatrix} 0 & \mu_{01} \\ \mu_{10} & 0 \end{pmatrix} \begin{pmatrix} \rho_{00} & \rho_{01} \\ \rho_{10} & \rho_{11} \end{pmatrix} \right\rangle = \mu_{01}\rho_{10} + \mu_{10}\rho_{01}, \tag{2.27}$$

which shows that it is the off-diagonal terms of the density matrix that are responsible for the establishment of $P(t)$ and the emission of the light field.

In order to illustrate the effect of the interaction with one laser pulse, we depict the time evolution of the density matrix by calculating, step by step, the linear response function [111, 112]:

$$\begin{aligned} S^{(1)} &\propto \langle \mu(t_1)[\mu(0), \rho(-\infty)] \rangle \\ &= \langle \mu(t_1)\mu(0)\rho(-\infty) - \mu(t_1)\rho(-\infty)\mu(0) \rangle. \end{aligned} \tag{2.28}$$

- Before the interaction, the system is in the ground state

$$\rho(-\infty) = \begin{pmatrix} 1 & 0 \\ 0 & 0 \end{pmatrix}. \tag{2.29}$$

- At $t = 0$, an off-diagonal term in the density matrix is generated with probability proportional to μ_{01} due to the interaction with the dipole moment; for the first of the two terms in Eq. 2.28 we have

$$\mu(0)\rho(-\infty) = \begin{pmatrix} 0 & 0 \\ \mu_{01} & 0 \end{pmatrix}. \tag{2.30}$$

- During the time interval t_1, the system propagates according to the unperturbed Hamiltonian (see Eq. 2.22)

$$\begin{pmatrix} 0 & 0 \\ \mu_{01} e^{-i\omega_{01}t_1} e^{-\Gamma t_1} & 0 \end{pmatrix}. \tag{2.31}$$

- At $t = t_1$, the off-diagonal element emits a light field proportional to $P^{(1)}$:

$$\langle \mu(t_1)\mu(0)\rho(-\infty) \rangle = \left\langle \begin{pmatrix} \mu_{01}^2 e^{-i\omega_{01}t_1} e^{-\Gamma t_1} & 0 \\ 0 & 0 \end{pmatrix} \right\rangle = \mu_{01}^2 e^{-i\omega_{01}t_1} e^{-\Gamma t_1}. \tag{2.32}$$

The second term in Eq. 2.28, which was not explicitly calculated here, represents the complex conjugate part.

We can now use a similar approach to analyze the third order response $S^{(3)}$ resulting from the interaction with three laser pulses. As an example, we consider the term R_1 in Eq. 2.13:

$$\rho(-\infty) = \begin{pmatrix} 1 & 0 \\ 0 & 0 \end{pmatrix} \xrightarrow{\mu(0)\rho(-\infty)} \begin{pmatrix} 0 & 0 \\ \mu_{01} & 0 \end{pmatrix} \xrightarrow{t_1} \begin{pmatrix} 0 & 0 \\ \mu_{01} e^{-i\omega_{01} t_1} e^{-\Gamma t_1} & 0 \end{pmatrix}$$

$$\xrightarrow{\mu(0)\rho(-\infty)\mu(t_1)} \begin{pmatrix} 0 & 0 \\ 0 & \mu_{01}^2 e^{-i\omega_{01} t_1} e^{-\Gamma t_1} \end{pmatrix} \xrightarrow{t_2} \begin{pmatrix} 0 & 0 \\ 0 & \mu_{01}^2 e^{-i\omega_{01} t_1} e^{-\Gamma t_1} e^{-t_2/T_1} \end{pmatrix}$$

$$\xrightarrow{\mu(0)\rho(-\infty)\mu(t_1)\mu(t_1+t2)} \begin{pmatrix} 0 & 0 \\ \mu_{01}^3 e^{-i\omega_{01} t_1} e^{-\Gamma t_1} e^{-t_2/T_1} & 0 \end{pmatrix}$$

$$\xrightarrow{t_3} \begin{pmatrix} 0 & 0 \\ \mu_{01}^3 e^{-i\omega_{01}(t_1+t_3)} e^{-\Gamma(t_1+t_3)} e^{-t_2/T_1} & 0 \end{pmatrix}$$

$$\xrightarrow{\langle \mu(t_1+t2+t3)\mu(0)\rho(-\infty)\mu(t_1)\mu(t_1+t2)\rangle} \mu_{01}^4 e^{-i\omega_{01}(t_1+t_3)} e^{-\Gamma(t_1+t_3)} e^{-t_2/T_1}. \tag{2.33}$$

Overall, the step-by-step calculation above returns

$$R_1 = \mu_{01}^4 e^{-i\omega_{01}(t_3+t_1)} e^{-\Gamma(t_1+t_3)} e^{-t_2/T_1}. \tag{2.34}$$

The expression in Eq. 2.33 shows that the first pulse at $t = 0$ creates a coherent superposition of $|0\rangle$ and $|1\rangle$, as indicated by the non-zero off-diagonal term in the density matrix. The second pulse at t_1 transforms the coherence state into a population state, which at $t_1 + t_2$ is converted back to a coherence state that finally emits the signal field at $t_1 + t_2 + t_3$. These processes are also represented, in a more compact form, in Feynman diagrams (R_1 in Fig. 2.2).

The same procedure can be applied to all other quantum pathways; for R_2, for example, we get

$$R_2 = \mu_{01}^4 e^{-i\omega_{01}(t_3-t_1)} e^{-\Gamma(t_1+t_3)} e^{-t_2/T_1}. \tag{2.35}$$

The difference between R_1 and R_2 is that for R_1 the third pulse creates the same coherence generated by the first pulse (ρ_{10}), while it creates the complex conjugate in R_2 (ρ_{01}). The flip in sign of the oscillation between t_1 and t_3 in R_2 implies that the phase acquired during t_1 is reversed during t_3, resulting in a rephasing mechanism after the third pulse. For this reason, the diagrams R_2 and R_3 are called rephasing pathways, whereas R_1 and R_4 are non-rephasing pathways.

2.3 Third-order nonlinear spectroscopies

2.3.1 Detection of third-order signals

A number of non-linear spectroscopic techniques, referred to as *four-wave mixing*, are based on the measurement of the third order response introduced above. Among these, we focus here on pump-probe and 2D spectroscopy that will be extensively employed in the following chapters. In the most general scheme (see Fig. 2.4), there are three ultrashort light pulses impinging on the sample: E_1 and E_2 are the excitation pulses (pumps), E_3 is the probe pulse. The emitted signal field (E_{sig}) represents the fourth wave.

The measurement of the emitted signal $E_{sig} \propto P^{(3)}$ usually employs an *heterodyne detection* scheme (see Fig. 2.4), where E_{sig} is overlapped to an additional laser pulse called *local oscillator* (LO) having the same wavevector of the signal field, and is then sent to a square-low detector that measures [112]

$$\begin{aligned} \mathcal{S}(t_1,t_2,t_{LO}) &\propto \int_0^\infty \mid E_{LO}(t_3-t_{LO}) + E_{sig}(t_1,t_2,t_3) \mid^2 dt_3 \\ &\approx I_{LO} + 2\,\mathrm{Re}\left\{\int_0^\infty E_{LO}(t_3-t_{LO})\cdot E_{sig}(t_1,t_2,t_3)\right\} dt_3, \end{aligned} \tag{2.36}$$

where the square term E_{sig}^2 is neglected in the approximation of weak signal.

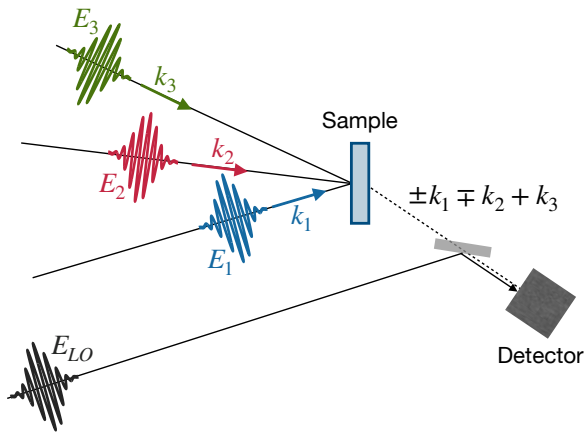

Figure 2.4: Sketch of the heterodyne detection scheme employed in four-wave-mixing experiments. Adapted from Ref. 112.

While I_{LO} represents the intensity of the laser pulse hitting the detector, the second term in Eq. 2.36 is an interference term that depends on both the local oscillator and the signal. Since the latter term contains the information we want to measure, it is usually isolated by subtracting the spectrum of the laser

pulse. In the semi-impulsive limit, where the envelopes of the laser pulses are approximated to δ-functions, Eq. 2.36 is further simplified by the removal of the convolution, and the measured signal results directly proportional to the third order response of the system. In phase-matching geometries where E_{sig} is emitted along $\boldsymbol{k}_3$, the probe pulse itself acts as the local oscillator and the signal is said to be *self-heterodyned*.

2.3.2 Pump-probe spectroscopy

Pump-probe spectroscopy represents one of the most widely used four-wave mixing experiments. As sketched in Fig. 2.5a, it employs only two light pulses. The pump generates an out-of-equilibrium state, whose time-evolution is detected by the time-delayed probe that measures the pump-induced changes in either the transmissivity or reflectivity of the sample.

Described as a third-order nonlinear process, there are two interactions with the field of the single incoming pump pulse. This corresponds to $t_1 = 0$ and $\boldsymbol{k}_1 = \boldsymbol{k}_2$. The signal is then emitted along the direction $\boldsymbol{k} = \boldsymbol{k}_3$, that is collinearly with the probe, and therefore measured in self-heterodyne configuration. By controlling the $t_2 \equiv \Delta t$ time delay (pump-probe time delay), population relaxation dynamics can be measured.

The detection of the signal is usually performed in frequency domain by employment of a spectrometer that implements the Fourier transform of the signal over t_3. In this way, by using a broadband probe, we obtain the typical pump-probe signal (see Fig. 2.5b) where the differential transmissivity or reflectivity is plotted as a function of probe frequency $\omega_3 \equiv \omega_{pr}$ and pump-probe time delay. Regarding the pump excitation, both narrowband or broadband spectra can be employed. The former configuration allows to select the response of phenomena resulting from a specific excitation frequency at the cost of limited temporal resolution. Conversely, simultaneous multifrequency excitation induced by ultrashort broadband pump pulses can result in several responses being overlapped in the pump-probe spectrum.

In the next section we will see how 2D spectroscopy allows to overcome this limitation and achieve simultaneous high temporal and spectral resolution.

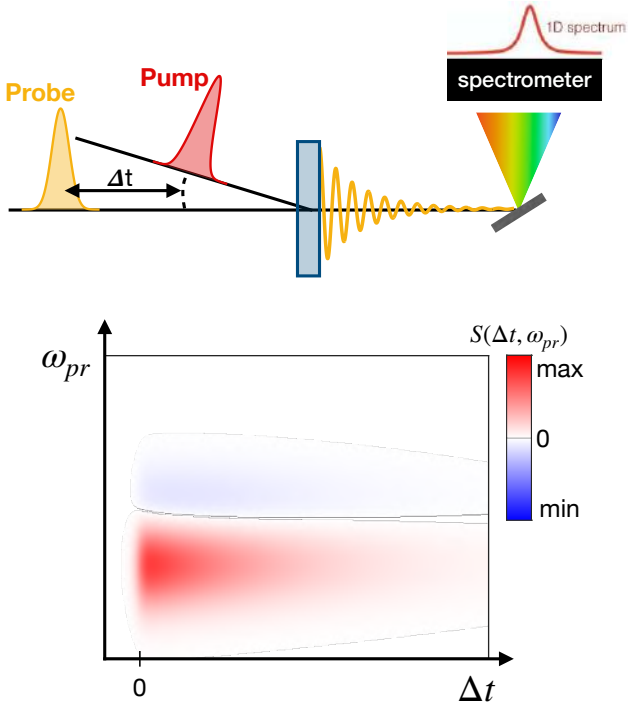

Figure 2.5: a) Sketch of a pump-probe experiment, where two light pulses are employed and their relative time delay Δt is controlled. b) Sketch of a pump-probe signal, measured as a function of pump-probe time delay and probe frequency.

2.3.3 2D spectroscopy

2D spectroscopy can be considered the most general four-wave mixing experiment where both the time intervals t_1 and t_2 are scanned and the wavevectors of all incoming beams, $\boldsymbol{k}_1$, $\boldsymbol{k}_2$ and $\boldsymbol{k}_3$, are controlled.
As the detected signal $\mathcal{S}(t_3, t_2, t_1)$ can be quite hard to interpret in time domain, it is often preferred to transform it to the frequency domain by performing 2D Fourier transforms with respect times t_1 and t_3, where the system is in a coherent state:

$$\mathcal{S}(\omega_3, t_2, \omega_1) = \int_0^\infty \int_0^\infty \mathcal{S}(t_3, t_2, t_1) e^{i\omega_1 t_1} e^{i\omega_3 t_3} dt_1 dt_3. \tag{2.37}$$

This leads to two-dimensional spectra where the new coordinates ω_1 and ω_3 represent the excitation frequency axis (usually plotted along the y-axis) and the detection frequency axis (usually along x-axis), respectively. Since during t_2 the system is in a population state, the signal is not Fourier transformed over t_2. Overall this results in a sequence of 2D spectra for each t_2 (see Figure 2.6b).

Experimentally, the spectral resolution along ω_3 is achieved by employment of a spectrometer, in analogy to the scheme used in broadband pump-probe, while spectral resolution along ω_1 is obtained from scanning the pump-pump time delay t_1 and Fourier transforming the oscillating signal. This requires the employment of laser pulses with broad spectrum which determines the excitation frequency window that is explored. Broadband pulses come with short time duration, resulting in 2D spectra measured with both high spectral and temporal resolutions [112, 54].

2D spectroscopy can be considered an extension of pump-probe; in the following section, we discuss how the introduction of the additional excitation frequency axis ω_1 allows to access more information about the system and its dynamics.

2.3.4 Information revealed by 2D spectroscopy

The 2D spectrum can be interpreted as a frequency-frequency correlation map capable of revealing couplings and interactions between different spectral features (see Fig. 2.7a). Resonances that are pumped and probed at the same energy appear in the 2D spectrum as peaks located on the diagonal; conversely, cross-correlations between different states can give rise to cross-peaks where, upon pumping one feature, a signal is revealed at the energy corresponding to another feature.

The positions of the features revealed by 2D spectroscopy provide great insight into the electronic structure of the system under investigation, with cross-peaks identifying states that are interacting [112, 54]. If, for example, multiple diagonal-peaks are observed but there are no cross-peaks, the system can be effectively modelled as a set of isolated two-level systems [283].
The intensities of the peaks in a 2D spectrum depend on amplitude of the dipole moments involved in the transition.
Lastly, the shape of the peaks depends on the interactions with the environment and on broadening mechanisms. When both homogeneous and inhomogeneous contributions are present, the measured peak is elongated along the diagonal of the 2D spectrum, as sketched in Fig. 2.7b. The diagonal width represents, in first approximation, the inhomogeneous linewidth and the anti-diagonal one the homogeneous linewidth, that is the intrinsic linewidth related to the dephasing time T_2. A more detailed and rigorous analysis of the 2D peaks lineshape is provided in Section 2.3.5 [112, 54, 283].

The capability of disentangling homogeneous and inhomogeneous broadening is peculiar of 2D spectroscopy and can not be achieved in linear or pump-probe spectroscopies. In fact, pump-probe lacks the spectral resolution along ω_1 so that the measured spectrum corresponds to the integral of the 2D spectrum along ω_1, if broadband pump pulses are employed, or to a horizontal slice of 2D spectrum in the case of narrowband excitation, thus preventing the resolution of the diagonal elongation of the peaks.

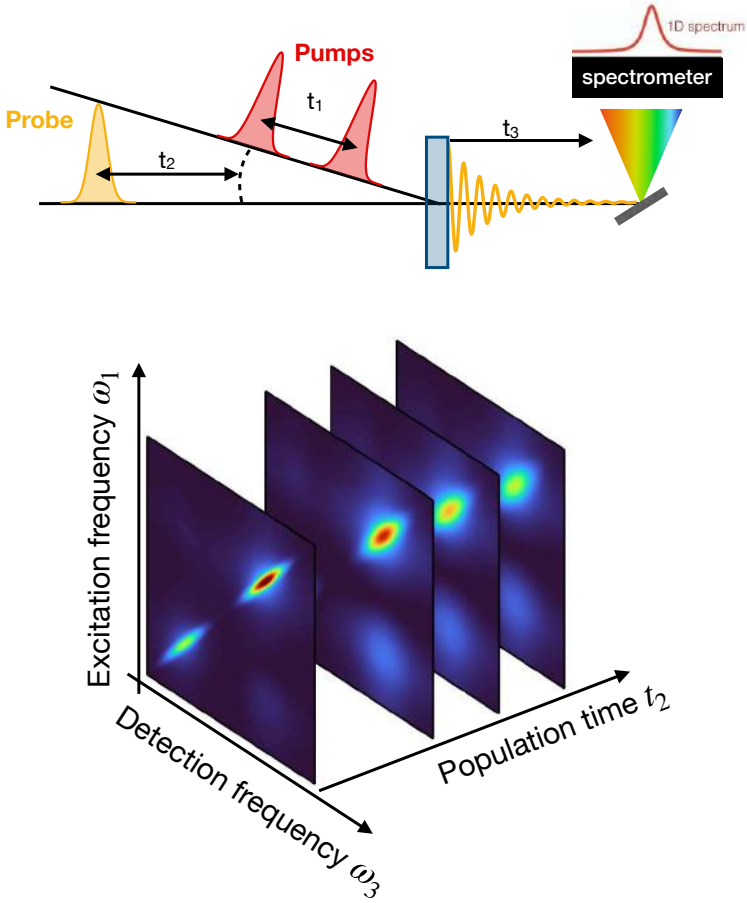

Figure 2.6: a) Example of a 2D spectroscopy scheme, where three light pulses are employed. At fixed t_2, a spectrometer measures the signal as a function of t_1. Fourier transform over t_1 returns the 2D spectrum. b) Sketch of 2D spectra showing the measured third order signal as a function of detection frequency (ω_3), excitation frequency (ω_1) and pump-probe time delay t_2.

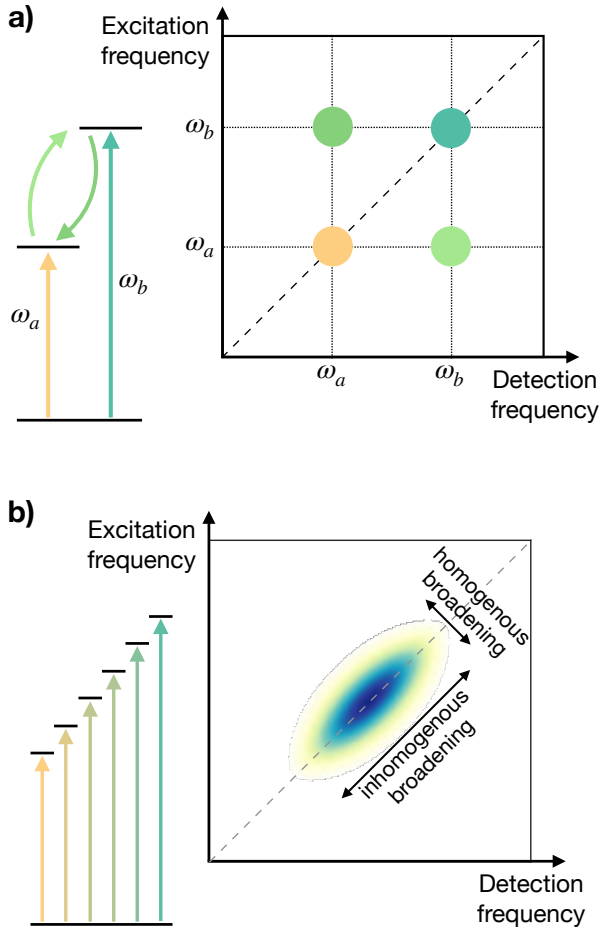

Figure 2.7: a) Schematic representation of a 2D spectrum for a multilevel system. It displays diagonal peaks originating from direct transitions at frequencies ω_a and ω_b, and cross-diagonal peaks representing couplings or interactions among states a and b. b) Sketch of an inhomogeneously broadened resonance resulting in a peak elongated along the diagonal of the 2D spectrum.

2.3.5 2D spectral lineshapes for a two-level system

In this section we consider the case of two-level system subject to both homogeneous and inhomogeneous broadening and compute the third-order signal measured in frequency domain in 2D spectroscopy. As mentioned above, in the semi-impulsive limit, the signal field is proportional to a suitable sum of response functions R_i in Eq. 2.13, which will depend of the specific experimental geometry. In order to account for inhomogeneous broadening, we include a Gaussian term in the response functions obtained in Eq. 2.34 and 2.35. At $t_2 = 0$, the signal emitted from the rephasing pulse sequence then reads

$$\begin{aligned} s^R(t_3, t_1) &\propto R_{2,3} \\ &= S^R_{0,0} e^{-[\Gamma(t_3+t_1)+i\omega_0(t_3-t_1)+\sigma^2(t_3-t_1)^2/2]}\Theta(t_3)\Theta(t_1), \end{aligned} \tag{2.38}$$

while for the non-rephasing pulse sequence we have

$$\begin{aligned} s^{NR}(t_3, t_1) &\propto R_{1,4} \\ &= S^{NR}_{0,0} e^{-[\Gamma(t_3+t_1)+i\omega_0(t_3+t_1)+\sigma^2(t_3+t_1)^2/2]}\Theta(t_3)\Theta(t_1), \end{aligned} \tag{2.39}$$

where ω_0 is the absorption peak central frequency, Γ is the dephasing rate, σ is the inhomogeneous width, $S^R_{0,0}$ and $S^{NR}_{0,0}$ are amplitude factors and $\Theta(t_i)$ is the Heaviside function [207, 240]. An example of the rephasing and non-rephasing signals in time domain, $s^R(t_3, t_1)$ and $s^{NR}(t_3, t_1)$, are plotted in Figures 2.8a and b, respectively, as a function of the coherence time t_1 and the detection time t_3.

The 2D spectrum in frequency domain is obtained from the Fourier transform over t_1 and t_3 (see Eq. 2.37). Fig. 2.8c and d show the real part of the signal so obtained for the rephasing and non-rephasing contributions, respectively.

As mentioned above, the analysis of the peak lineshape along the diagonal and anti-diagonal directions in the 2D frequency domain provides useful information about the homogeneous and inhomogeneous broadening in the system. In order to calculate the analytic expression for the diagonal and anti-diagonal lineshapes, we apply the projection-slice theorem of 2D Fourier transforms, following the procedure outlined in Ref. 255. According to the projection-slice theorem, a slice of 2D frequency domain spectrum at an angle θ with respect to the ω_3 axis can be obtained from Fourier transforming the 2D time domain signal projected onto a line at the same angle θ with respect to the t_3 axis.

We therefore decompose the time domain signal along the directions $t = t_3 - t_1$ ($\theta = -45°$, anti-diagonal direction) and $t' = t_3 + t_1$ ($\theta = +45°$, diagonal direction), which yield:

$$s^R(t, t') = S^R_{0,0} e^{-\Gamma t' - i\omega_0 t - \sigma^2 t^2/2}\Theta(t - t')\Theta(t + t'), \tag{2.40}$$

$$s^{NR}(t, t') = S^{NR}_{0,0} e^{-\Gamma t' - i\omega_0 t' - \sigma^2 t'^2/2}\Theta(t - t')\Theta(t + t'). \tag{2.41}$$

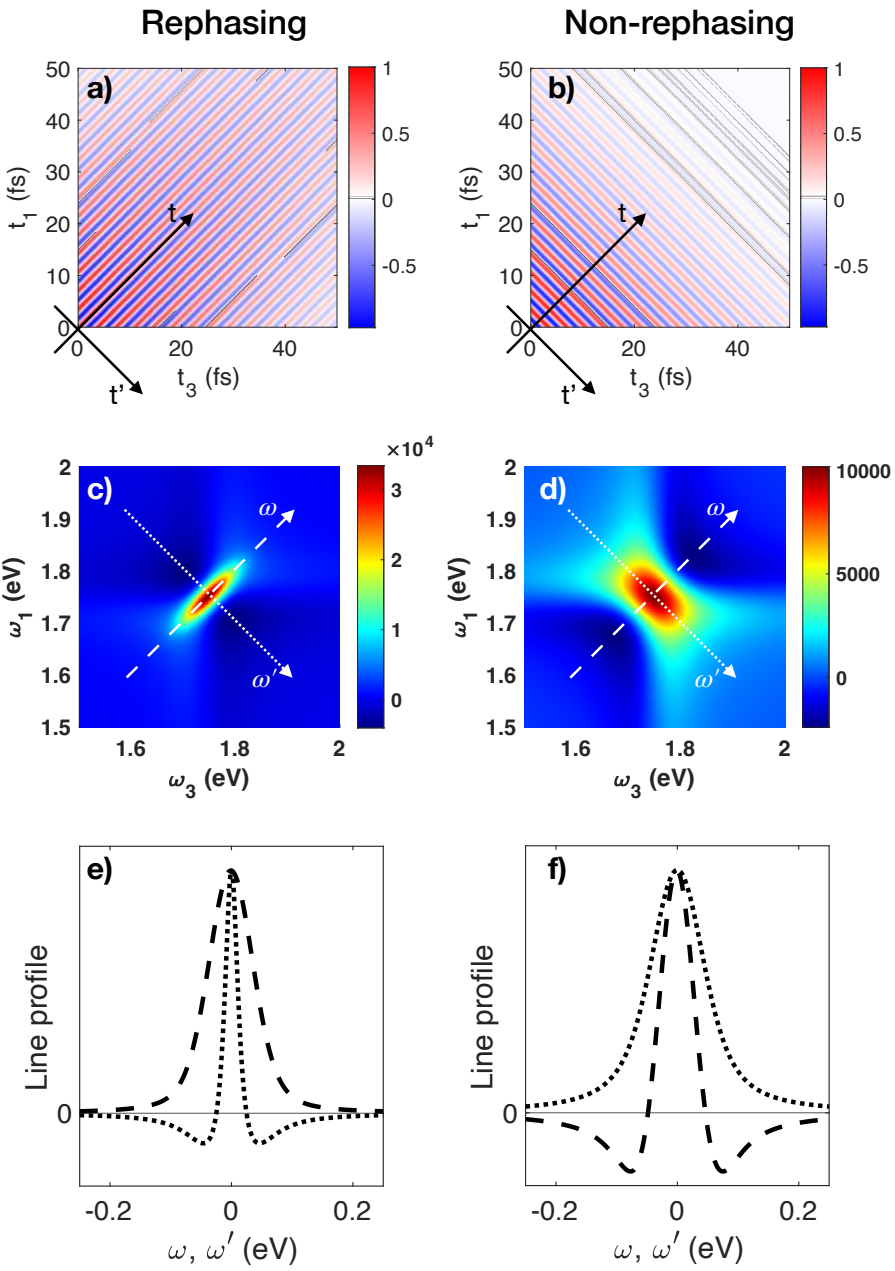

Figure 2.8: a,b) Plot of the third order signal $s(t_3, t_1)$ at $t_2 = 0$ for a two level system with Gaussian inhomogeneous broadening. The plotted signal is computed using Eq. 2.38 (panel a) and 2.39 (panel b) with $\omega_0 = 1.75$ eV, $\sigma = 0.03$ eV and $\Gamma = 0.014$ eV. c,d) 2D Fourier transform of the signals in panels a and b, respectively. e,f) Diagonal (dashed) and anti-diagonal (dotted) slices of the 2D spectra plotted in c and d.

The frequency axes along the anti-diagonal and diagonal directions of the 2D spectrum will be indicated as ω and ω', respectively. Since the oscillation at frequency ω_0 corresponds, in frequency domain, just to a shift along ω' and ω for the rephasing and non-rephasing signals respectively, we can equivalently consider the following shifted and normalized signals in time domain:

$$s^R_{\omega_0}(t,t') = s^R(t,t')\frac{e^{i\omega_0 t}}{S^R_{0,0}} = e^{-\Gamma t' - \sigma^2 t^2/2}\Theta(t-t')\Theta(t+t'), \tag{2.42}$$

$$s^{NR}_{\omega_0}(t,t') = s^{NR}(t,t')\frac{e^{i\omega_0 t'}}{S^{NR}_{0,0}} = e^{-\Gamma t' - \sigma^2 t'^2/2}\Theta(t-t')\Theta(t+t'), \tag{2.43}$$

which will return the resonance peak centered at the origin of the (ω,ω') frequency domain.

The projections onto the t and t' axis are obtain from the integration of the signal along the perpendicular direction:

$$s^{R,NR}_{proj}(t') = \int_{-\infty}^{\infty} s^{R,NR}_{\omega_0}(t,t')dt, \tag{2.44}$$

$$s^{R,NR}_{proj}(t) = \int_{-\infty}^{\infty} s^{R,NR}_{\omega_0}(t,t')dt', \tag{2.45}$$

By inserting Eq. 2.42 and 2.43 into Eq. 2.44 and 2.45 we obtain:

$$s^R_{proj}(t') = e^{-\Gamma t'}\int_{-t'}^{t'} e^{-\sigma^2 t^2/2}dt, \tag{2.46}$$

$$s^R_{proj}(t) = e^{-\sigma^2 t^2/2}\int_{-|t'|}^{\infty} e^{-\Gamma t'}dt', \tag{2.47}$$

$$s^{NR}_{proj}(t') = 2t' e^{-\Gamma t' - \sigma^2 t'^2/2}, \tag{2.48}$$

$$s^{NR}_{proj}(t) = \int_{-|t'|}^{\infty} e^{-\Gamma t' - \sigma^2 t'^2/2}dt'. \tag{2.49}$$

The final lineshapes are then obtained from the Fourier transforms of Eq. 2.46-2.49. For the rephasing signal we obtain:

$$\begin{aligned} S^R_{\omega_0}(\omega) &= \frac{1}{2\pi}\int_{-\infty}^{\infty} s^R_{proj}(t)e^{i\omega t}dt \\ &= \frac{1}{\sigma(\Gamma - i\omega)}\exp\left\{\left[\frac{(\Gamma - i\omega)^2}{2\sigma^2}\right]\right\}\mathrm{erfc}\left[\frac{\Gamma - i\omega}{\sqrt{2}\sigma}\right] \end{aligned} \tag{2.50}$$

for the anti-diagonal direction, and

$$\begin{aligned} S^R_{\omega_0}(\omega') &= \frac{1}{2\pi}\int_{-\infty}^{\infty} s^R_{proj}(t')e^{i\omega' t'}dt' \\ &= \sqrt{\frac{2}{\pi\sigma^2}}e^{-\omega'^2/2\sigma^2} * \frac{1}{\Gamma^2 + \omega'^2} \end{aligned} \tag{2.51}$$

for the diagonal direction. Here, erfc indicates the complementary error function and $*$ the convolution in frequency domain. Analogously, the anti-diagonal and diagonal lineshapes for the non-rephasing signal are:

$$\begin{aligned} S^{NR}_{\omega_0}(\omega) =& \frac{1}{2\pi}\int_{-\infty}^{\infty} s^{NR}_{proj}(t)e^{i\omega t}dt \\ =& -\frac{ie^{\Gamma^2/2\sigma^2}}{\sqrt{2}\sigma}\frac{1}{\omega}e^{-\omega^2/2\sigma^2} \\ & \left[e^{-i\omega\Gamma/\sigma^2}\,\mathrm{erfc}\left(\frac{\Gamma-i\omega}{\sqrt{2}\sigma}\right) - e^{i\omega\Gamma/\sigma^2}\,\mathrm{erfc}\left(\frac{\Gamma+i\omega}{\sqrt{2}\sigma}\right)\right] \end{aligned} \tag{2.52}$$

and

$$\begin{aligned} S^{NR}_{\omega_0}(\omega') &= \frac{1}{2\pi}\int_{-\infty}^{\infty} s^{NR}_{proj}(t')e^{i\omega' t'}\,dt' \\ &= \frac{1}{\sigma}e^{-\omega'^2/2\sigma^2} * \frac{1}{(\Gamma+i\omega')^2}. \end{aligned} \tag{2.53}$$

An example of the diagonal and anti-diagonal slices calculated using Eq. 2.50-2.53 for the rephasing and non-rephasing signals plotted in Fig. 2.8a-d are displayed in Fig. 2.8e and f.

The expressions above (Eq. 2.50-2.53) assume a simpler form in the limiting cases of strong inhomogeneous broadening ($\sigma \gg \Gamma$) and absence of inhomogeneous broadening (homogeneous limit, $\sigma \ll \Gamma$) [255]. Figure 2.9 displays the 2D spectra and the diagonal and anti-diagonal linecuts of the purely absorptive signal (sum of real parts of rephasing and non-rephasing) in these two limit cases. For pure homogeneous broadening ($\Gamma = 0$), diagonal and anti-diagonal slices are equal (Fig. 2.9 b and d). In the case of strong inhomogeneity, the lineshapes reduce to a Gaussian function of width σ along the diagonal direction and to a Lorentzian function of width Γ along the anti-diagonal direction (Fig. 2.9 a and c). When, however, σ and Γ are of the same order of magnitude, the inhomogeneous and homogeneous broadening are not completely decoupled along diagonal and anti-diagonal, respectively. In this case, a global lineshape analysis based on the Eq. 2.50-2.53 is needed to extract quantitative information [255].

2.4 Experimental implementation

Over the last few decades, a wide variety of experimental schemes have been developed for the implementation of time-resolved spectroscopies based on the third-order non-linear response. They differentiate for the specific experimental configuration and for the spectral coverage, which can range from THz to

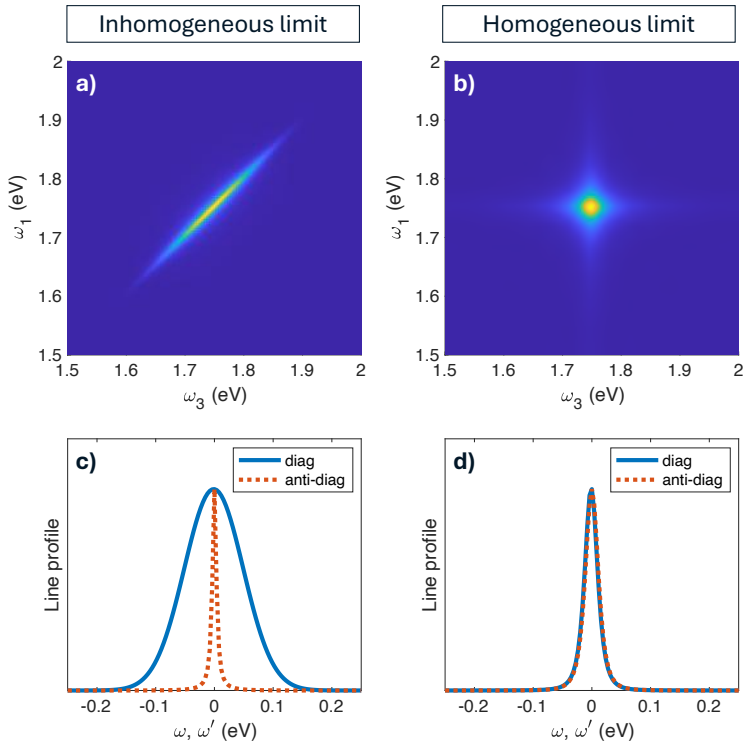

Figure 2.9: a,b) Purely absorptive 2D spectra for a two-level system in the limit cases of strong inhomogeneous broadening ($\sigma = 0.05$ eV, $\Gamma = 0.004$ eV) and no inhonomegeous broadening ($\sigma = 0$, $\Gamma = 0.02$ eV). c,d) Diagonal and anti-diagonal slices of the data plotted in a and b.

X-rays [98, 179]. In the following we focus on pump-probe and 2D spectroscopy experiments in the optical range (visible-near infrared range). 2D spectroscopy at optical frequencies is often referred to as 2D electronic spectroscopy (2DES).

As mentioned in Section 2.3.2, pump-probe experiments are based on the employment of two ultrashort light pulses and the ability to vary systematically the time delay t_2 between them. In order to do so, the optical path of one of the two beams is usually controlled by a mechanical delay line, consisting of a motorized stage whose position determines the optical path length. In terms of spectral content of the employed pulses, narrowband and tunable pump pulses are most frequently used in order to be able to resonantly and selectively excite different transitions. The probe pulse is instead preferred to be as broadband as possible to allow to simultaneously probe the response of different transitions. In the optical range this is usually achieved by white-light generation in transparent crystals (e.g. sapphire, YAG, CaF_2). Pump-probe signals are emitted in the same direction of the probe pulse and are typically very small

($10^{-5} - 10^{-2}$ relative variation in the probe intensity). Therefore, their detection requires the employment of modulation techniques where the pump pulse is periodically switched on and off by means of a mechanical chopper or acousto-optic/electro-optic modulator; the synchronous demodulation of the probe after the interaction with the sample then measures the pump-induced changes in either the transmitted or reflected probe. The measured time-dependent differential signal is $\Delta T(\omega_3, t_2)/T(\omega_3) = (T_{pump-on} - T_{pump-off})/T_{pump-off}$ or $\Delta R(\omega_3, t_2)/R(\omega_3) = (R_{pump-on} - R_{pump-off})/R_{pump-off}$, for transmission and reflection geometries, respectively [179]. When broadband probe pulses are used, detection systems capable of spectral resolution are needed. These usually employ spectrometers that spatially separate the different frequency components of the probe (ω_3) which are simultaneously detected by an optical multi-channel analyzer. Alternatively, time-domain Fourier transform detection is also possible. In this case, the broadband probe pulse is sent to a linear interferometer which generates an interferogram, measured by a single channel detector, whose Fourier transform returns the spectrum of the signal [223].

2D spectroscopy schemes need three separate laser pulses whose relative time delays must be carefully controlled. Different experimental geometries can be adopted [283, 54]. One of the most widely employed is the so-called BOXCARS configuration, a fully non-collinear geometry where each of the three pulses propagates in a different direction and have a unique wave-vector. The emitted signal is fully separated from the incoming beams, as determined by the phase-matching condition, and is heterodyne detected by means of a fourth laser pulse acting as the local oscillator. Partially non-collinear or collinear schemes are also possible; in these geometries two or more pulses have the same wave-vector. A commonly used partially non-collinear scheme is the pump-probe geometry, which is also employed in the present work, where the first two pulses propagate collinearly (pumps) and the third probe travels along a different direction (probe). In this case, the signal is emitted along the beam path of the probe, which therefore serves as the intrinsic reference for the self-heterodyne detection. In the partially collinear pump-probe geometry, the detected 2DES signal is the sum of both rephasing and non-rephasing contributions and is called *purely absorptive* signal.

One of the greatest challenges for the implementation of 2D spectroscopy in the optical range comes from the need of phase stability between the different pulses, required due to the interferometric detection of the signal. Phase stability is in particular mandatory during t_1 and during t_3 when the system is in a coherent state. The phase stability during t_3 is automatically verified in the partially collinear pump-probe geometry thanks to the self-heterodyne detection, whereas achieving phase coherence between the two pump pulses is not trivial. Indeed, at optical frequencies, inabilities of the opto-mechanical components and different beam optical paths cause fluctuations in the relative phase of the excitation pulses [283, 54]. Several methods that allow to achieve phase stability have been developed; these include, among other approaches, both active and passive stabilization methods. In the former case, phase fluctuations are compensated

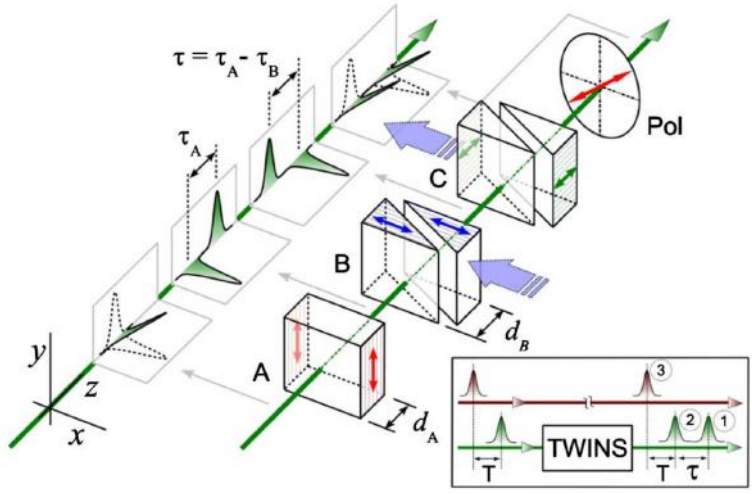

Figure 2.10: TWINS scheme. A pulse polarized at $45°$ with respect to the x and y axis propagates to a plate (A) of uniaxial birefringent material with optical axis aligned along y (red arrows) and is separated into two orthogonally polarized pulses with a relative delay $\tau_A = d_A(1/v_{ge} - 1/v_{go})$, with v_{ge} and v_{go} group velocities for ordinary and extra-ordinary polarizations and d_A thickness of the A plate. A pair of birefringent wedges (B) with the optical axis along x (blue arrows) are then used to introduce a relative delay τ with opposite sign with respect to A, controllable by moving one of the wedges and varying its beam insertion: $\tau = \tau_A - \tau_B = (d_A - d_B)(1/v_{ge} - 1/v_{go})$. A second pair of birefringent wedges (C) with optical axis along z (green arrows) is moved anti-symmetrically to the pair B so that the amount of material crossed by the beam is maintained constant. Lastly, a polarizer projects both replicas onto a single polarization at $45°$. Image from Ref. 28

for by nanoscale changes to mirror positions; passive stabilization approaches are instead based on the idea of using common optics for all beams [283]. The approach employed in this thesis is a passive method based on a common-path interferometer that exploits the Translating-Wedge-Based Identical Pulses eNcoding System (TWINS) scheme to generate the two phase locked pump pulses and control their relative delay t_1. The TWINS device, sketched in Fig. 2.10, uses a series of birefringent optics, so that a single pulse polarized at $45°$ relative to the optical axis is converted into two orthogonally polarized pulses separated by a fixed time delay, determined by the thickness of the birefringent material. By employing birefringent wedges and controlling their insertion in the beam path, it is possible to continuously vary the material thickness and, therefore, to introduce an arbitrary delay between the first and second pulses while maintaining excellent phase stability [28].

2.5 Experimental setup

2.5.1 Pump-probe setup

The optical setups used for pump-probe experiments presented in this thesis are sketched in Fig. 2.11 and 2.12. They are based on a Yb:KGW laser system (Pharos, Light Conversion) delivering 37.5 µJ, 250 fs pulses at 1030 nm wavelength and 400 kHz repetition rate. A pulse peaker allows to change the repetition rate of the emitted pulses while keeping unchanged the energy per pulse. A portion of the laser output (30 µJ) pumps an optical parametric amplifier (OPA; Orpheus-F, Light Conversion) generating narrowband pulses ($\sim 10-30$ nm bandwidth, depending on the central wavelength) of ~ 50 fs duration, tunable in the range between 650 and 900 nm.

In SetUp1 (Fig. 2.11) the signal of the Orpheus-F OPA is used as the excitation pulse in the experiment; the rest of the laser light (7.5 µJ) is employed to synthesize a supercontinuum probe pulse, obtained by means of White Light Generation (WLG) in a 6-mm-thick YAG crystal.
In SetUp2 (Fig. 2.12), the pump beam is obtained by frequency doubling 7.5 µJ of laser system at 1030 nm in a 1-mm-thick BBO crystal, returning 515 nm excitation wavelength. The supercontinuum pulse for the probe beam is produced by means of WLG in a 4-mm-thick sapphire crystal pumped by the signal of the Orpheus-F OPA tuned to 800 nm.

In both setups, the time delay between the arrival times of pump and probe pulses is controlled through a linearly motorized stage which delays the pump pulse in a time window covering ~ 300 ps. The two beams are then routed to the sample; the pump beam hits the sample at normal incidence while the incident angle of the probe is less than 10°. The pump beam is focused by a 400 mm focal length concave mirror to a $\sim$200 µm $\times$ 200 µm spot size; the spot size of the probe beam is ~ 2 times smaller than the pump spot in SetUp1 (focused by 200 mm focal length concave mirror) and 10 times smaller than the pump in SetUp2 (focused by an achromatic lens of 100 mm focal length). The excitation intensity can be continuously varied by rotating a half-waveplate positioned on the pump beam path and followed by a polarizer that transmits linearly polarized light. The probe beam is cross-polarized with respect to the pump polarization, in order to allow filtering of the signal background, which is mainly given by sample scattering of the pump beam. The signal can be acquired either in reflection or transmission geometry and its detection is performed by lock-in acquisition with a mechanical chopper working at 2.6 kHz modulating the pump beam. Spectral resolution over the probe energy axis is achieved by employment of a common-path birefringent interferometer (GEMINI by NIREOS) and Fourier transform of the generated interferogram [223]. The sample is mounted inside a closed-cycle helium cryostat that allows to perform the ultrafast optical spectroscopy experiments at temperatures between 15 K and 300 K.

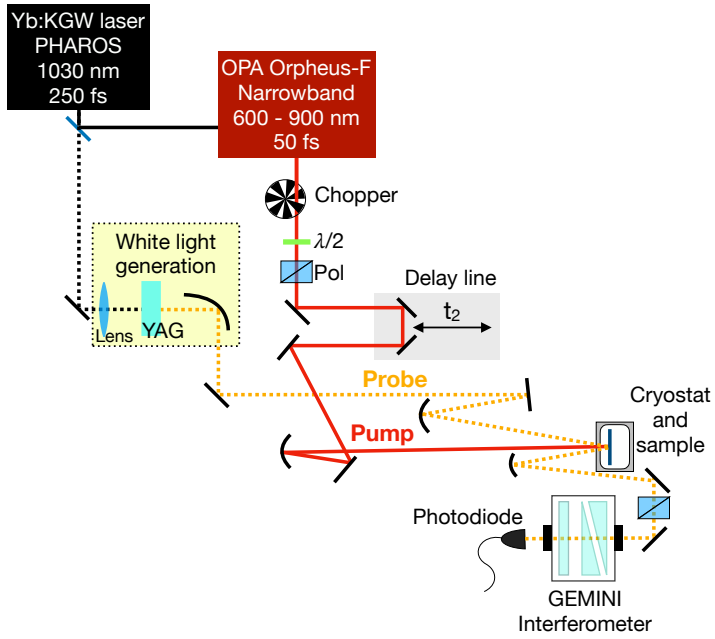

Figure 2.11: Sketch of SetUp1 employed for pump-probe experiments in Chapter 3.

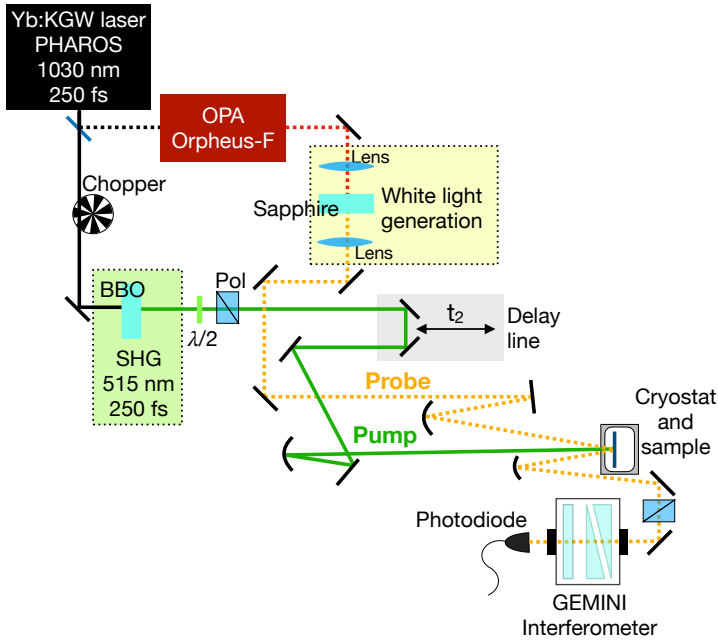

Figure 2.12: Sketch of SetUp2 employed for pump-probe experiments in Chapter 5.

2.5.2 2DES setup

Figure 2.13 reports a sketch of the scheme employed for 2DES. Both pump and probe pulses are generated by a home-built non-collinear optical parametric amplifier (NOPA), seeded by the same Yb:KGW laser mentioned in the previous section (see appendix A for details on the NOPA design and setup). The signal generated by the NOPA is a broadband pulse that can cover the spectral range between at 650 and 950 nm and has a time duration of 30 fs. Pump and probe beams are obtained from dividing the NOPA output by means of a 90:10 beam splitter. The pump beam then goes through a common-path birefringent interferometer (GEMINI 2D by NIREOS, implementing the TWINS scheme described in Sec. 2.4 and Fig. 2.10) that generates the pair of phase-coherent excitation pulses [28]. In order to compensate for the additional dispersion introduced in the pump pulses by the GEMINI 2D interferometer and other optical elements on the pump beam (beam splitter, half-waveplate and cryostat window), a pulse compressor is implemented on the pump beam path. Two-prism compressor was employed for 2D spectroscopy experiments presented in Chapter 6, chirped mirrors were used for the data discusses in Chapter 3. Similarly, another pulse compressor is employed for fine compensation of dispersing elements on the probe beam, namely a half-waveplate and the cryostat window. Pump and probe pulses, orthogonally polarized in order to minimize pump scattering, are then focused onto the sample by two concave mirrors, resulting in a partially collinear 2DES scheme (collinear pump pulses and non-collinear probe propagation). The focused spot size is $\sim$200 µm $\times$ 200 µm for the pump beam and $\sim$70 µm $\times$ 70 µm for the probe beam. The delay between the two pump pulses, t_1, is controlled by varying the insertion of the GEMINI 2D birefringent wedges on the beam path, whereas the pump-probe time delay t_2 is controlled through a linearly motorized stage. The detection system employed here is the same used in the pump-probe setups, consisting in GEMINI interferometer and lock-in acquisition. The data are acquired by fixing t_2 and scanning t_1 in a suitable range (e.g. between -55 fs and 110 fs); Fourier transform of the measured $\Delta R(\omega_3, t_1; t_2)/R(\omega_3)$ or $\Delta T(\omega_3, t_1; t_2)/T(\omega_3)$ over t_1 returns the 2D map as a function of ω_3 and ω_1.

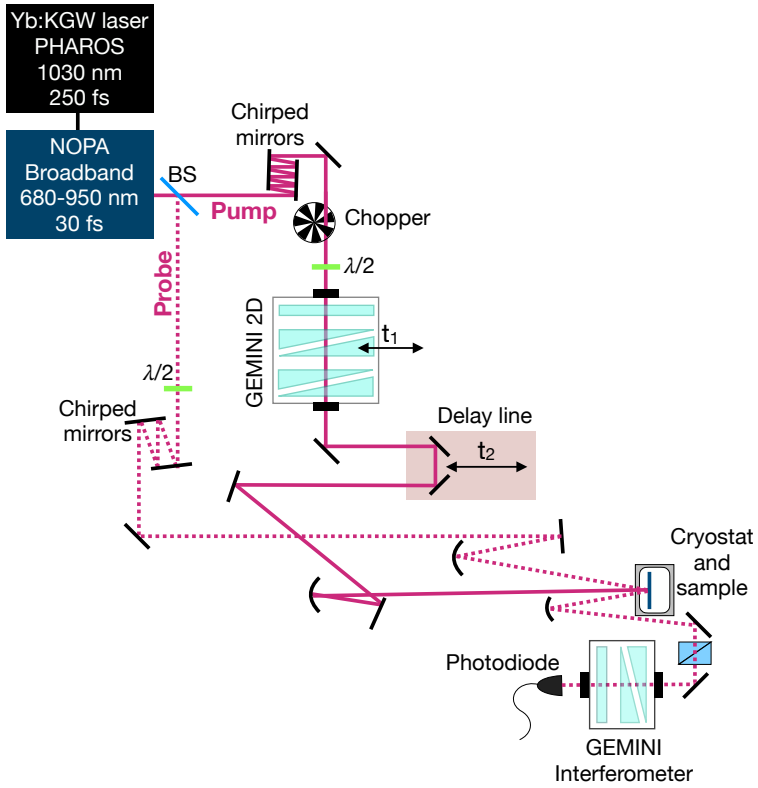

Figure 2.13: Sketch of the 2DES experimental setup.

Part I

Out-of-equilibrium phenomena in Mott systems

CHAPTER 3

Role of spin and orbital fluctuations on Hubbard exciton linewidth in Mott-Hubbard insulator $LaVO_3$

In this chapter, we explore the light-induced out-of-equilibrium physics of $LaVO_3$, a prototypical Mott insulator characterized by a complex phase diagram. Upon decreasing the temperature below 140 K, $LaVO_3$ undergoes a structural phase transition that is accompanied by the establishment of antiferromagnetic spin and orbital orders. Insight on the exotic properties of such strongly correlated system can be obtained from the investigation of charge excitations across the Mott-Hubbard gap. In $LaVO_3$ the lowest energy electronic excitation across the gap can result in the formation of a Hubbard exciton, a bound state between a doubly-occupied and an empty V-site. The stabilization and dynamics of this excitonic resonance are strongly affected by spin and orbital degrees of freedom and the emergence of long-range ordered phases, as revealed by the temperature-dependent equilibrium optical properties [202] and by the critical slowing-down of the dynamics in proximity of the symmetry-breaking phase transition [172]. Here, we study the Hubbard exciton in $LaVO_3$ by employing pump-probe spectroscopy and 2DES, which reveal pump-induced variations of both spectral weight and linewidth of the excitonic resonance. Direct observation of the broadening of the homogeneous linewidth component provides a signature of the decrease of the Hubbard exciton intrinsic lifetime time due to the perturbation of the spin and orbital ordered background.

3.1 Spin and orbital orders in vanadium oxide $LaVO_3$

Vanadium oxides RVO_3 (R = rare-earth or Y) are prototypical Mott insulators considered ideal systems where to investigate the interplay between electronic excitations and spin, orbital and lattice degrees of freedom [143, 76, 60, 141, 120, 203]. These compounds have a rich phase diagram characterized by structural, magnetic and orbital phase transitions, leading to exotic spin and orbital ordered phases [292, 291, 246]. Within this class of materials displaying interesting magnetic and electronic properties, in this chapter we focus in particular on lanthanum vanadate $LaVO_3$.

$LaVO_3$ has a perovskite-type structure that can be derived from the cubic perovskite through a $GdFeO_3$-type distortion, that is by rotating the VO_6 octahedra around the c-axis and tilting them in alternating directions around the b-axis, as shown in Fig. 3.1a [22, 60]. The crystal structure of $LaVO_3$ is orthorhombic (space group $Pnma$) at room temperature, and it transforms to monoclinic lattice (space group $P2_1/a$) through a first order phase transition taking place at the critical temperature $T_c = 140$ K [22]. Upon the orthorhombic-monoclinic transition, the c-axis undergoes a small rotation, with the angle α (see Fig. 3.1a) changing from 90° at $T > T_c$, to 90.125° at $T < T_c$ [22]. The low temperature structure is also characterized by an additional Jahn-Teller deformation of VO_6 octahedra that determines an elongation of the VO bond along the [110] and [1$\bar{1}$0] directions for adjacent vanadium sites, respectively [22, 60].

These structural variations affect the electronic structure of the material. The orthorhombic crystal field splits the vanadium $3d$ orbitals into t_{2g} and e_g orbitals as sketched in Fig. 3.1b. In the valence shell there are two electrons that occupy the t_{2g} orbitals, with fairly equal occupation of d_{xy}, d_{yz} and d_{zx} in the high temperature phase [60, 172]. The structural phase transition occurring at 140 K lifts the degeneracy of the t_{2g} orbitals and modifies the orbital occupation, which develops a *G-type orbital order*: d_{xy} is occupied at all V-sites, whereas d_{xz} and d_{zy} orbitals of the V-sites are alternatively occupied along all crystallographic axes (see sketch in Fig. 3.1c) [141, 142, 121, 60, 246, 143, 202].

At T_c, the systems undergoes also a magnetic phase transition from paramagnetic (at high temperature) to antiferromagnetic (at $T < T_c$). The low temperature phase shows *C-type spin ordering*, meaning that there is a ferromagnetic stacking (along the c-axis) of antiferromagnetic planes (see sketch in Fig. 3.1c) [142, 121, 246, 143, 202].

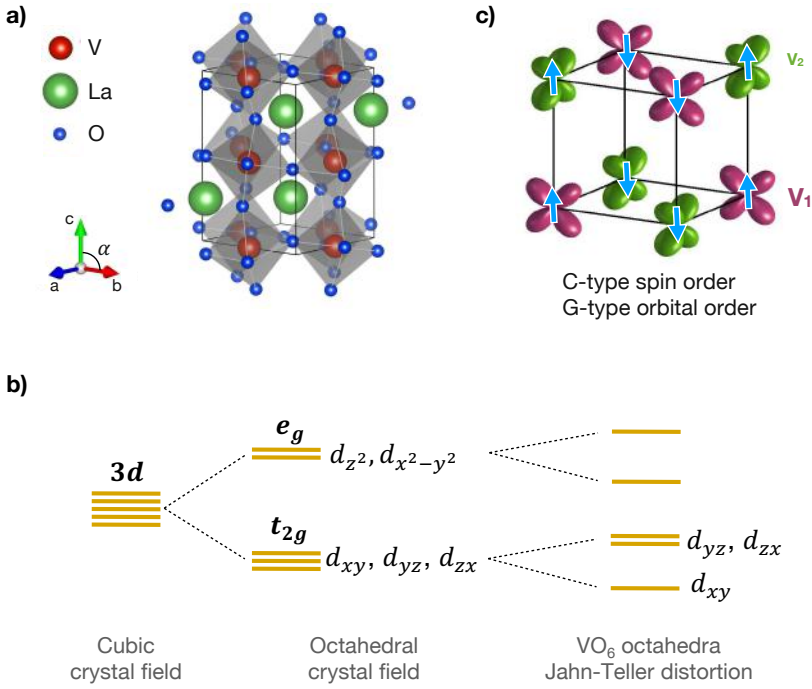

Figure 3.1: a) High temperature crystal structure of $LaVO_3$ [22]. At T_c the materials transitions from orthorhombic to monoclinic lattice, where α becomes $\alpha = 90.125°$. b) V-3d orbital splitting in $LaVO_3$; two valence electrons occupy the t_{2g} orbitals. c) Spin and orbital ordered configuration in $LaVO_3$, establishing below 140 K.

3.2 Hubbard exciton in $LaVO_3$

In the Mott insulator $LaVO_3$, the electronic excitations across the Mott-Hubbard gap are strongly influenced by the spin and orbital degrees of freedom and their phase transitions. The lowest-energy electronic excitation across the Mott-Hubbard gap is the transition of a d_{yz} or d_{zx} electron on a V-site to an adjacent vanadium site along the c-axis (see sketch in Fig. 3.2a), which takes place via the hopping of the electron through the π-bonding with the O-2p_y or 2p_x state [202].

This transition gives rise to a resonance in the optical properties of $LaVO_3$ in the photon energy range around 2 eV [202]. The optical conductivity measured with light polarized parallel to the c-axis is reported in Fig. 3.1b and show two peaks at 1.8 eV and 2.4 eV. Both peaks are ascribed to the $d_{yz,zx} - d_{yz,zx}$ transition: the higher energy peak is associated to a single-particle excitation consisting of a double occupancy and an empty site (holon) that are well-separated; the lower energy one corresponds, instead, to a bound state between a holon and a

double occupation, which is known as a *Hubbard exciton* (HE) [235, 202, 172].

As opposed to conventional semiconductors where exciton formation is governed by a lowering of the Coulomb energy, the stabilization of Hubbard excitons in antiferromagnetic Mott-Hubbard systems is driven by the gain in kinetic energy [53, 311, 235]. In an antiferro-magnetic/orbital ordered phases, in fact, hopping of a bound empty-site/double-occupancy pair is favored because it preserves the spin/orbital order, as compared to the hopping of a single holon or double-occupancy that instead locally disrupts the order and leaves a trace of disordered sites behind (see sketch in Fig. 3.2c) [172]. Therefore, the bound state is the energetically most favorable state, stabilized by the spin/orbital ordered environment [53, 311]. Indeed, the HE peak in the optical conductivity is enhanced in the low temperature phase of $LaVO_3$, suggesting a significant involvement of the spin and orbital orders in the formation of the HE.

3.3 Out-of-equilibrium dynamics in $LaVO_3$

Optical measurements near the HE peak can provide significant insight about this excitonic resonance and the coupled spin and orbitals degrees of freedom. Ultrafast optical pump-probe has in particular been employed to investigate the low-energy transitions across the Mott-Hubbard gap and the out-of-equilibrium behavior of the Hubbard exciton in Mott insulators RVO_3 [211, 284, 172].

For $LaVO_3$, the typical transient reflectivity dynamics is shown in Fig. 3.3, reporting pump-probe data measured for 1.77 eV probe photon energy. In agreement with previous experimental reports [172], the time-resolved trace displays three main components: a nearly instantaneous electronic response, decaying within 500 fs, an intermediate component raising on $\sim$ 20 ps timescale and a slow recovery taking place over hundreds of picoseconds. The fast component is typically assigned to photocarrier injection by intersite vanadium $d-d$ excitations, which relax over $\sim$ 500 fs via electron-electron and electron-phonon scattering [172]. The slower part of the dynamics is instead related to the Hubbard exciton; specifically, this signal has so far been ascribed to spectral weight transfer away from the HE after pump excitation and back to it during the recovery dynamics.

As shown in Fig. 3.3, these components and, hence, the overall dynamics strongly depend on temperature; in particular, the intermediate component is significantly enhanced when the system is close to the critical temperature T_c, while it disappears both at room temperature (dark red line in Fig. 3.3, left panel) and at low temperatures (dark blue line in Fig. 3.3, right panel). Lovinger et al. (Ref. 172) also showed that the intermediate component displays a critical slowing-down behavior in proximity of the phase transition (see Sec. 1.2.2 in Chapter 1), with diverging timescale as $T \to T_c$. It has been suggested that the HE spectral weight changes detected in pump-probe experiments are determined by spin and orbital fluctuations that disrupt the HE binding and

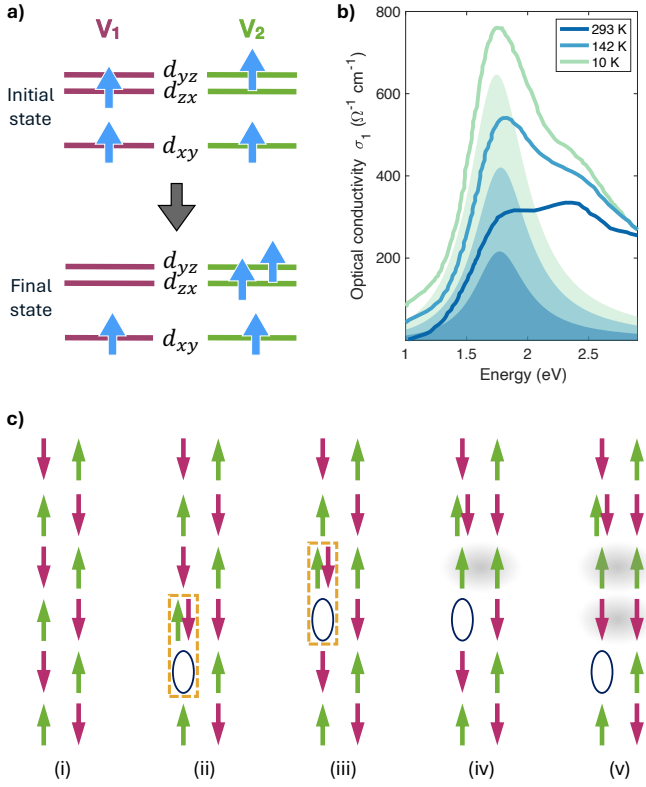

Figure 3.2: a) Initial and final electronic configurations of the t_{2g} orbitals on adjacent V-sites (V_1 and V_2) along the c-axis in the case of the optical transition across the Mott-Hubbard gap. b) Equilibrium optical conductivity of $LaVO_3$ for light polarization parallel to the c-axis (electric field $E \parallel c$) at three different temperatures across T_c. Adapted from Ref. 202. The lowest energy peak, highlighted by filled areas, is associated with the Hubbard exciton resonance. c) Schematic representation of the hopping of a double occupancy generated by electronic excitation across the Mott-Hubbard gap in a spin or orbital ordered phase (i). Electron hopping between adjacent V-sites along the c-axis (i→ii) creates a holon and a double occupancy that can bound and form a HE. Hopping of the HE as a bound pair (ii→iii) preserves the spin/orbital order. Hopping of the single double-occupancy (iii→iv) or single holon (iv→v) generates a trace of disordered spin/orbitals. In $LaVO_3$, motion along the c-axis results in orbital disorder, whereas motion along the a- or b-axes produces both spin and orbital disorder.

become larger in proximity of T_c or due to pump-induced spin/orbital disorder [172]. At low temperatures, the HE pump-probe signal is instead suppressed because spin and orbital degrees of freedom freeze, strong order is established and spin/orbital fluctuations are reduced [172].

The transient reflectivity signal also strongly depends on the excitation fluence. Figure 3.3b, which shows the pump-probe signal at 70 K as a function of pump fluence, reveals that increasing the excitation intensity has an effect similar to increasing the sample temperature toward T_c: it introduces a slow component that builds up over a timescale of tens of picoseconds. This suggests that high excitation fluence enhances the disruption of the ordered background, with larger intensities required to perturb the spin and orbital order as the temperature is further lowered below T_c.

In this chapter, we deepen the investigation of the HE dynamics on the picosecond timescale by extending single-color pump-probe to time-resolved spectroscopy. We perform broadband pump-probe and 2D coherent electronic spectroscopy on a $LaVO_3$ thin film, which allow us to add spectral resolution in the HE energy range and probe not only spectral weight changes, by also lineshape dynamics.

3.4 Pump-probe experiment

Broadband pump-probe was performed in reflection geometry by employing SetUp1 described in Sec. 2.5.1. The pump wavelength is tuned to 1.4 eV; the probe spectral range goes from 1.3 to 2 eV, therefore covering the HE spectral region. The employed sample is a 30 nm thick $LaVO_3$ thin film grown on LSAT ($(LaAlO_3)_{0.3}(Sr_2TaAlO_6)_{0.7}$) substrate by Molecular Beam Epitaxy (MBE) [326, 25].

Fig. 3.4a and c display transient reflectivity $\Delta R/R$ colormaps measured at two different temperatures below T_c, namely 110 K and 40 K respectively. Consistently with single-color pump-probe (see Fig. 3.3 and Sec. 3.3) and previous experimental reports [172], we observe an ultrafast electronic response (< 1 ps) followed by a slower dynamics surviving for hundreds of picoseconds. The long-lived signal displays the expected temperature-dependent behavior characterized by a slow component, building-up over a few tens of picoseconds, that emerges in proximity of T_c and is instead suppressed at lower temperature (see white solid lines in Fig. 3.4a and c). The employment of a supercontinuum probe reveals that this slow and negative signal in $\Delta R/R$ is a broad response peaked around the HE energy. The spectral response at selected pump-probe delays t_2, namely 30 and 250 ps, obtained from vertical line cuts of Fig. 3.4a and c, is plotted in Fig. 3.4b and d for the two temperatures, respectively.

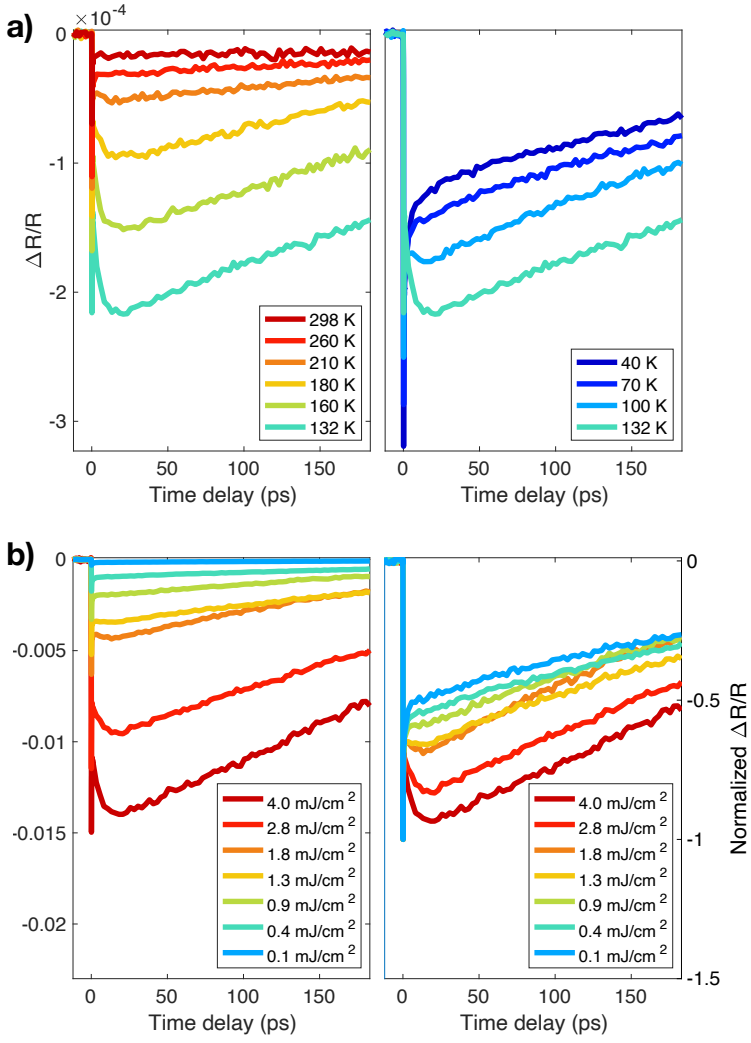

Figure 3.3: a) Optical transient reflectivity of a $LaVO_3$ thin film sample at different temperatures, above (left panel) and below (right panel) T_c. The measurements have been performed with 1.65 eV pump, 1.77 eV probe photon energy, and 0.1 mJ/cm^2 excitation fluence. b) Fluence dependence of the transient reflectivity signal, measured at 70 K, 1.65 eV pump, 1.77 eV probe photon energy. For comparison purposes, the right panel displays the same fluence-dependent pump-probe traces of the left panel, normalized to the fast peak.

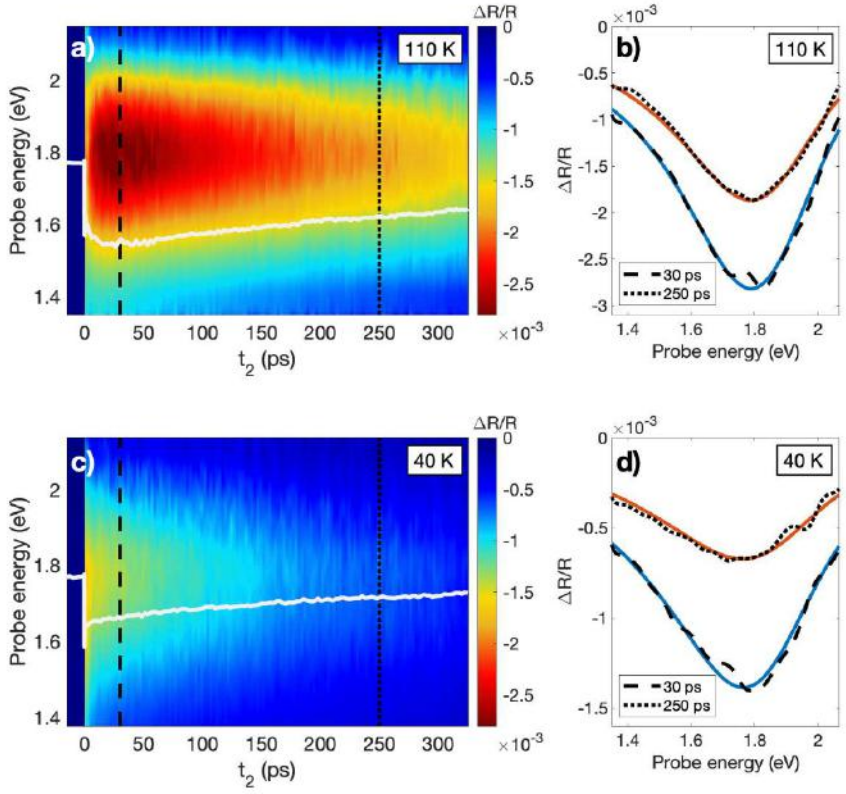

Figure 3.4: Broadband pump-probe measurements performed with 1.4 eV pump and supercontinuum probe in reflection geometry. The transient reflectivity spectra are plotted as a function of pump-probe time delay (horizontal axis) and probe wavelength (vertical axis), for sample temperatures of 110 K and 40 K in panels a) and c), respectively. The pump incident fluence is 1 mJ/cm^2. The white lines plotted on top show the time evolution of the signal at 1.77 eV and display the same behavior described in Fig. 3.3. Panels b) and d) report the transient reflectivity spectra at two selected delays, highlighted in a) and c) by black dashed (30 ps) and dotted (250 ps) lines. Red and blue solid lines are transient reflectivity fits performed as described in Sec. 3.4.

In order to relate the pump-probe signal to changes in the optical properties of the sample, we analyze the broadband transient reflectivity data by fitting the vertical slices of the pump-probe map to a differential reflectivity $(R^{outeq} - R^{eq})/R^{eq}$. The differential fit is performed, for all time delays $t_2 \geq 500$ fs, as described below.

We start from a parametrization of the equilibrium optical properties of $LaVO_3$ - which are reported in Ref. 202 and plotted in Fig. 3.2b - based on a multi-peak Drude-Lorentz model. The dielectric function ε as a function of frequency ω is given by

$$\varepsilon(\omega) = \varepsilon_\infty + \sum_j \frac{\omega_{p,j}^2}{\omega_{0,j}^2 - \omega^2 - i\Gamma_j\omega}. \tag{3.1}$$

where ε_∞ is the value of the dielectric constant at high frequency, $\omega_{p,j}$ is the plasma frequency, $\omega_{0,j}$ is the central frequency of the optical transition and Γ_j is the linewidth of the j-th oscillator. The real part of the optical conductivity σ_1 is then related to ε according to

$$\sigma_1 = \frac{\omega\varepsilon_2}{4\pi} \tag{3.2}$$

with ε_2 indicating the imaginary part of Eq. 3.1. Eq. 3.2 with three Drude-Lorentz oscillators ($j = 1, 2, 3$) is used to fit the optical conductivity data in Fig. 3.2b. The lowest energy oscillator, which is highlighted by the filled area in Fig. 3.2b, is related to Hubbard exciton. It is centered at $\omega_{0,HE}$=1.82 eV and has a spectral weight ($\propto \omega_{p,HE}^2$) that increases as the temperature is lowered below T_c, from $\omega_{p,HE} = 0.9$ eV at room temperature to 1.6 eV at cryogenic temperature. Since this parametrization is based on literature data measured on bulk $LaVO_3$ rather than thin film, and the differential fit does not strongly depend on the specific value used for the equilibrium HE plasma frequency (as we are looking at the variation in the optical properties), we consider the same equilibrium parameters to fit both measurements at 40 K and 110 K. The parameters of the equilibrium dielectric function of low-temperature $LaVO_3$, employed in the differential fitting of the pump-probe data, are reported in Table 3.1.

	$\omega_{0,j}$ (eV)	$\omega_{p,j}$ (eV)	Γ_j (eV)
$j = 1$ (HE)	1.82	1.31	0.56
$j = 2$	2.40	1.68	1.21
$j = 3$	4.61	2.16	0.70

Table 3.1: Parameters of the $LaVO_3$ low-temperature equilibrium dielectric function (Eq. 3.1 with $\varepsilon_\infty = 3$) employed in the differential fit of the pump-probe data.

The pump-probe signal can then be described by pump-induced changes in optical properties of the sample, captured through the variation of some of the parameters modeling ε in Eq. 3.1, as compared to equilibrium. We specifically find that, in order to fit the transient reflectivity data of Fig. 3.4, two parameters related to the HE need to be modified in the out-of-equilibrium configuration, namely the plasma frequency $\omega_{p,HE}$ and the width Γ_{HE}. The transient reflectivity data $\Delta R/R$ at fixed t_2 are therefore fitted (see red and blue lines in Fig. 3.4b and d) according to the following equation:

$$\frac{R(\omega_{p,HE}^{outeq}, \Gamma_{HE}^{outeq}) - R(\omega_{p,HE}^{eq}, \Gamma_{HE}^{eq})}{R(\omega_{p,HE}^{eq}, \Gamma_{HE}^{eq})} \tag{3.3}$$

where the reflectivity R is obtained by means of transfer matrix formalism for a $LaVO_3$ 30 nm film (whose dielectric function is given by Eq. 3.1 with parameters in Table 3.1) on LSAT substrate. *outeq* and *eq* superscripts indicate the plasma frequency or exciton width parameters in out-of-equilibrium and equilibrium conditions, respectively.

The output of the fitting procedure reveals that the ultrafast reflectivity variation is not simply related to exciton spectral weight transfer; the ultrafast photo-excitation has, in fact, two concurrent effects on the HE resonance:

(i) a decrease of excitonic spectral weight;

(ii) a broadening of the HE peak linewidth Γ_{HE}.

Fig. 3.5a and b display the output fit parameters, plotted as a function of pump-probe time delay. In panel a, the orange and light blue circles show the dynamics of the plasma frequency $\omega_{p,HE}$ of the HE Drude-Lorentz oscillator extracted for $T = 110$ K and 40 K, respectively. The ultrafast reduction in $\omega_{p,HE}$, following the impulsive pump excitation, is recovered over a timescale of hundreds of picoseconds. The variation in the HE spectral weight can be regarded as a direct representation of the number of photoinduced electronic excitations, n_{exc}, generated by pump excitations across the Mott-Hubbard gap. Such electronic population returns to the equilibrium state through an exponential decay (Fig. 3.5a), so it can overall be described as

$$n_{exc}(t) = n_{exc,0}\Theta(t)e^{-t/\tau_{exc}} \tag{3.4}$$

where $\Theta(t)$ is the Heaviside function and τ_{exc} is the characteristic relaxation time. An exponential fit of $\omega_{p,HE} - \omega_{p,HE}^{eq}$ returns $\tau_{exc} = 350$ ps at 40 K and 650 ps at 110 K.
On the other hand, the linewidth of the HE peak displays a significantly different dynamics (see Fig. 3.5b). The broadening of Γ_{HE} is delayed in time, reaching a maximum after ∼20 ps at 40 K and after ∼40 ps at 110 K, and then relaxing back to the equilibrium value on a timescale similar to the one for $\omega_{p,HE}$.

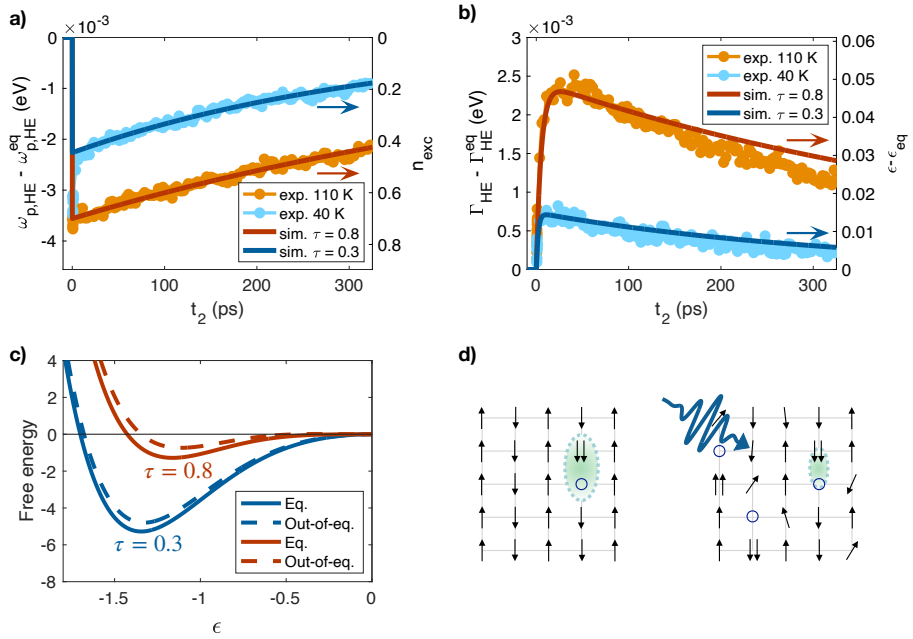

Figure 3.5: a,b) Time evolution of the spectra fit parameters: panels a) and b) display the variation of Hubbard exciton's plasma frequency $\omega_{p,HE}$ and width Γ_{HE}, respectively, as compared with the equilibrium values (left $y-$axis). Light blue and orange dots are relative to the measurements performed at 40 K and 110 K, respectively. Their time dependence is compared to the dynamics of the number of excitations n_{exc} and the order parameter ϵ in a system showing a coupling between a first-order phase transition and n_{exc}. The simulations plotted here (red and blue lines, right $y-$axis) result from numerical integration of Eq. 3.7 with $g = 0.6$, $\alpha = 5$, $\gamma = 0.01\ ps^{-1}$. c) Free energy functional at equilibrium (solid lines) and right after excitation of n_{exc} (dashed lines) computed according to Eq. 3.5 and 3.6, respectively, using the same parameters of the simulations in panels a and b. d) Cartoon of the Hubbard exciton in the spin and orbital ordered background. Disruption of the ordered background due to pump excitation leads to a reduction of the intrinsic lifetime.

3.5 Gingzburg-Landau description

In order to assess the origin of HE behavior in time domain and address the coupling between the light excitation and the long-range order in $LaVO_3$, we model our system in the framework of Gingzburg-Landau's theory. Spin ordering in $LaVO_3$ can be described as either a second-order or a weakly first-order phase transition [142, 121], while the structural one is a first-order transition [22, 202]. We therefore consider a phase transition that is overall first-order and write the

free energy as

$$F(\epsilon) = \alpha(\tau - 1)\epsilon^2 + \epsilon^2(\epsilon^2 - 1)^2, \tag{3.5}$$

with ϵ order parameter, α a numerical constant and $\tau = T/T_c$ normalized temperature. The first-order nature of the process is guaranteed by the negative coefficient of the fourth-order term ϵ^4. This description is similar to the approach employed by Lovinger et. al. in Ref. 172, where the free-energy for a first-order phase transition is written in terms of second-, fourth- and sixth-order powers of the order parameter. In Ref. 172, since only single-color pump-probe experiments are analyzed, preventing disentanglement of spectral weight transfers from broadening mechanisms, the authors simply identify the order parameter with the transient reflectivity signal, and study the temperature dependence of the order parameter exponential relaxation dynamics to rationalize the divergence of the exciton timescale in proximity of T_c. Here, we can refine this model by taking into account that the order parameter ϵ, describing the spin and orbital ordered background, is not directly coupled to the light, but it is rather coupled to the electronic excitations across the Mott-Hubbard gap, that is to n_{exc}. We therefore address the contribution of n_{exc} to the free energy of the system by including an additional coupling term $g\epsilon^2 n_{exc}$. Then, the free energy overall reads

$$F(\epsilon, n_{exc}) = \alpha(\tau - 1)\epsilon^2 + \epsilon^2(\epsilon^2 - 1)^2 + g\epsilon^2 n_{exc} \tag{3.6}$$

with n_{exc} given by Eq. 3.4 and g coupling constant between the number of photoinduced electronic excitations and the order parameter. Fig. 3.6a shows a sketch of the free energy curve at equilibrium (dark blue solid line, Eq. 3.5) and its instantaneous variation (light blue solid line, Eq. 3.6) due to coupling with the electronic excitations generated by the light pulse excitation. This light-induced change of the free energy functional results in a perturbation of the order parameter ϵ because, upon excitation of n_{exc}, the free energy minimum shifts to a different value of ϵ. The dynamics of the order parameters ϵ is then determined by the kinetic equation [98]:

$$\frac{d\epsilon}{dt} = -\gamma \frac{\partial F}{\partial \epsilon}, \tag{3.7}$$

with γ kinetic constant. No source term appears in the kinetic equation because of no direct coupling between the light and the order parameter of the system, which includes structural, orbital and magnetic degrees of freedom. The coupling g to the electronic excitation is what determines the perturbation of ϵ after pulse excitation. In Fig. 3.6b (bottom panel), we show an example of order parameter dynamics, obtained upon integrating Eq. 3.7, plotted for several normalized temperatures τ. For a fixed excitation n_{exc} (plotted in Fig. 3.6b, top panel), the variation in the order parameter displays a larger amplitude and slower build-up dynamics when the temperature increases, as a result of the free energy flattening around the minimum as the critical temperature is approached.

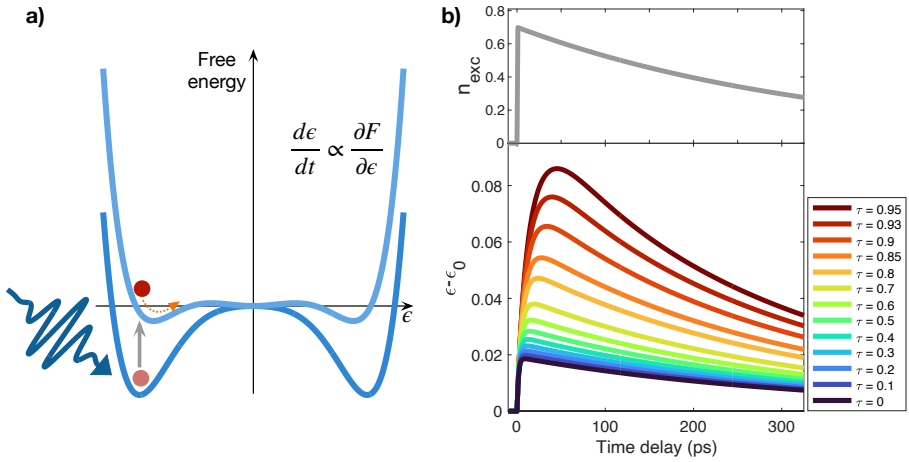

Figure 3.6: a) Sketch of a first-order phase transition free energy, as a function of the order parameter ϵ, and its pump induced perturbation. The photoexcited electronic population couples to the order parameter, whose dynamics is governed by the out-of-equilibrium free energy potential. b) The top panel reports an example of dynamics of n_{exc} (Eq. 3.4) that, by coupling to the orbital/spin order and perturbing the free energy (Eq. 3.6), initiates the order parameter dynamics, plotted in the bottom panel for several normalized temperatures τ. The parameters used in the time evolution simulation plotted here are: $\alpha = 5$, $g = 0.6$, $n_{exc} = 0.7$, $\gamma = 0.01\ ps^{-1}$.

Going back to the data (Fig. 3.5), we now compare the dynamics of the HE linewidth, extracted from pump-probe measurements, with the numerical solutions of the kinetic equation (Eq. 3.7). In doing so, we make the two following assumptions, which will be justified in Sec. 3.6 and 3.7, respectively:

(a) the variation in HE linewidth measured in pump-probe spectroscopy corresponds to a variation in intrinsic lifetime;

(b) the Hubbard exciton intrinsic lifetime can be considered as representative of the order parameter of the phase transition.

The Γ_{HE} dynamics is compared to the time evolution of ϵ in Fig. 3.5: red and blue solid lines (right axis) are obtained starting from Eq. 3.6-3.7 using a possible set of parameters, chosen as described in the following, that allow to match the experimental trend. The normalized temperature is set to $\tau = 0.3$ and 0.8 for blue and red plots, respectively, according to the experimental temperature at which the experiment is performed. The time-dependent term $n_{exc}(t)$ is given by the red and blue solid lines in Fig. 3.5a (right axis), having amplitude that matches the experimental trends of $\omega_{p,HE} - \omega_{p,HE}^{eq}$ for the two temperatures (we chose $n_{exc,0} = 0.45$ and 0.7 for $T = 40$ K and 110 K,

respectively). The value of the parameters γ, α and g is then set in order to match the experimental trends of Γ_{HE}. The parameters α and g appearing in the free energy profile determine the amplitude of $\epsilon - \epsilon_{eq}$, which depends linearly also on $n_{exc,0}$; when $n_{exc,0}$ is fixed as discussed above, setting $\alpha = 5$ and $g = 0.6$ allows to match, simultaneously for both measured temperatures, the amplitude of the order parameter dynamics and the linewidth variation. Lastly, γ determines the build-up time of the dynamics of $\epsilon - \epsilon_{eq}$ variation, with a time constant that depends, on top of γ, on the normalized temperature τ and on the free energy coefficient α. With τ being fixed to the experimental values and $\alpha = 5$, we find that the value $\gamma = 0.01$ ps^{-1} allows to reproduce the experimental dynamics at both temperatures. For the parameters chosen as described above, the free energy F at equilibrium (Eq. 3.5) and right after excitation (Eq. 3.6) are plotted in Fig. 3.5c. In this way, the time dependence of the order parameter ϵ, extracted from the kinetic equation, reproduces all the main features observed in the experimental dynamics of the linewidth Γ_{HE}, as listed below.

(i) The response is delayed due to a finite build-up time of few tens of ps, determined by γ; the subsequent relaxation decay is governed by τ_{exc}.

(ii) The perturbation of the order parameter is enhanced when the temperature of the system is closer to T_c, as observed from $\epsilon - \epsilon_{eq}$ being a factor 3.3 larger at 110 K compared to 40 K, despite $n_{exc,0}$ being only a factor 1.5 larger at the higher temperature.

(iii) For a fixed value of γ, the dynamics slows down as the temperature approaches T_c, as observed from the longer build-up time that characterizes both $\Gamma_{HE} - \Gamma_{HE}^{eq}$ and $\epsilon - \epsilon_{eq}$ at 110 K compared to 40 K.

The agreement between the free energy model and the experimental results suggests that the variations in width parameter Γ_{HE} are ascribable to a coupling between the light-induced electron excitations and the order parameter. The emerging scenario is that ultrafast excitation of charges across the Mott-Hubbard gap causes a local perturbation of the order parameter, corresponding to an increases of spin/orbital fluctuations, as sketched in Fig. 3.5d, and a broadening of the Hubbard exciton linewidth.

The linewidth variations obtained from pump-probe data, however, are not directly related to the exciton lifetime because the pump-probe spectral response can be dominated by inhomogeneous broadening. As opposed to 1D spectroscopy, 2DES can instead directly access the exciton intrinsic lifetime. We therefore employ 2DES, discusses in the next section, with the aim of providing further insight on the HE scattering rate and intrinsic lifetime.

3.6 2D spectroscopy experiment

We perform 2DES on $LaVO_3$ thin film by employing degenerate and cross-polarized pump and probe pulses in the 1.45-1.9 eV spectral range, thus allowing to investigate the response of the Hubbard exciton. The experiment is performed in partially collinear scheme (collinear pump pulses and non-collinear probe) and reflection geometry, as detailed in Section 2.5.2 and sketched in Fig. 2.13. The sample is cooled down to $T \lesssim T_c$, where the pump-probe transient reflectivity displays the maximum signal in the slow build-up component, and the 2D spectrum is then collected at selected t_2 delays. To partially mitigate the influence of the spectral shape of the light source on the 2D map [32], we normalize the 2DES signal over both the light spectrum along both pump and probe energy axes. Fig. 3.7a reports the 2D spectrum measured for $T = 140$ K and $t_2 = 40$ ps, and reveals a broad transient reflectivity response around 1.8 eV.

In order to study the dynamics of the homogeneous linewidth of the excitonic resonance, as discussed in Sec. 2.3.4, we extract an anti-diagonal profile of the 2D spectrum. The line-cut is taken, for each measured t_2 delay, along the black dashed line displayed in Fig. 3.7a. In Fig. 3.7b the resulting signal is plotted along the anti-diagonal energy axis for a short time delay ($t_2 = 100$ fs) and at a later delay ($t_2 = 40$ ps). Normalization of the two anti-diagonal profiles for comparison purposes clearly shows a broader peak on tens of picosecond timescale as compared to the linewidth at ultrashort times. The full width at half maximum Γ_{hom} is extracted for the five t_2 delays where 2D spectroscopy is performed, which are highlighted by the colored dots plotted along the pump-probe dynamics in Fig. 3.7c, top panel. Since the width of the excitonic resonance is comparable to the pulse bandwidth, the extraction of absolute values for the homogeneous linewidth is difficult and subject to possible artifacts originating from the spectral shape of the pulse [32]. We therefore focus only on relative variations of the spectral response as a function of time delay t_2. The bottom panel in Fig. 3.7c reports the relative anti-diagonal width variation, compared to the linewidth $\Gamma_{hom,0}$ at $t_2 = 100$ fs, as a function of time delay, revealing a 20% broadening building up on a tens of picosecond timescale.

Similarly to pump-probe spectroscopy, 2DES shows a broadening of the exciton linewidth, whose dynamics is also compatible to the time evolution of Γ_{HE} found in Sec. 3.4. 2D spectroscopy gives additional insight revealing that this broadening affects the homogeneous component of the linewidth and, therefore, indicates a decrease of the Hubbard exciton intrinsic lifetime due to disruption of the ordered background caused by the pump excitation. Quantitatively, the value of $\Delta\Gamma_{hom}/\Gamma_{hom,0}$ obtained from 2D spectroscopy is larger compared to what measured in pump-probe because, in the former case the linewidth variation is observed only along the anti-diagonal direction, whereas the latter approach measures the signal integrated along the pump energy axis and projected onto the probe energy axis, thus resulting in a smaller measured broadening.

The observation that the time-resolved signal measured in ultrafast spectroscopy

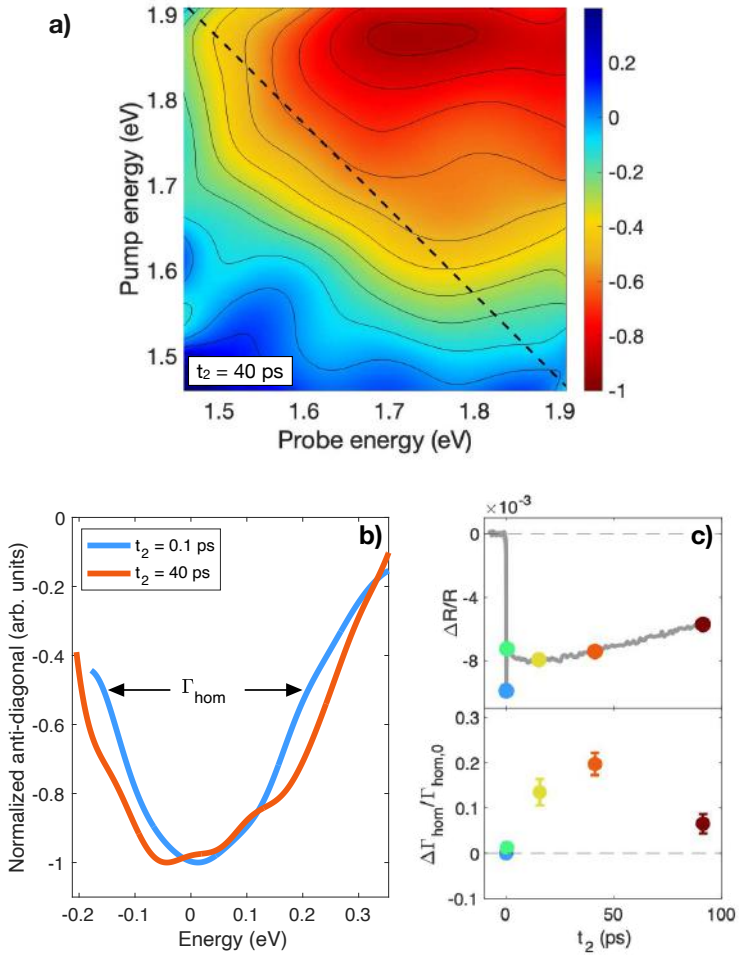

Figure 3.7: a) 2D spectroscopy measurement performed at $T = 140$ K, $t_2 = 40$ ps and excitation fluence 1.4 mJ/cm^2. The 2D spectrum (arb. units) is normalized over both the probe and pump spectra. b) Anti-diagonal profiles of 2D spectra; they are obtained from line-cut along the direction indicated by the black dashed line in a) and are integrated over 25 meV width. The blue and red lines refer to two different time delays t_2 and are normalized for comparison purposes. c) Top panel: Pump-probe dynamics (grey line) measured in the same experimental configuration of a) with broadband (1.45-1.9 eV) and degenerate pump and probe beams at $T = 140$ K and 1.4 mJ/cm^2 excitation fluence. The colored dots indicate the t_2 delays where 2D spectra are collected. Bottom panel: relative variation of the anti-diagonal FWHM extracted from 2D spectra as a function of t_2. The value obtained at the shortest time delay $t_2 = 100$ fs is used as reference $\Gamma_{hom,0}$.

originates from a perturbation of the intrinsic exciton lifetime justifies the assumption (a) made in Sec. 3.5. In the next section we address assumption (b) and discuss the ascription of the exciton linewidth to the order parameter.

3.7 Dynamical mean field theory

In order to connect the experimental results to a microscopic description of the electronic properties of the material and investigate the effect of the establishment of long-range orders below the critical temperature, we compare our experimental data to the results of Dynamical Mean-Field Theory (DMFT), which as been performed by Massimo Capone (International School for Advanced Studies (SISSA)). DMFT is an accurate many-body method which includes non-perturbatively correlation effects and allows for calculations of experimentally accessible spectra [95].

DMFT calculations are performed for a three-orbital model based on density-functional theory bandstructure. The bandstructure has been computed using Quantum Espresso [99] and maximally localized Wannier orbirals have been derived using Wannier90 [259]. Only the three low-lying orbitals of vanadium are included, as they are those that mainly contribute to the relevant bands. The interactions are then included in the popular Hubbard-Kanamori form

$$H_{int} = U \sum_{i,a} n_{ia\uparrow} n_{ia\downarrow} + (U - 3J) \sum_{i,a<b,\,\sigma} n_{ia\sigma} n_{ib\sigma} + (U - 2J) \sum_{i,a\neq b} n_{ia\uparrow} n_{ib\downarrow} \tag{3.8}$$

where i, $a, b = 1, 2, 3$, σ are respectively site, orbital and spin indices. The (screened) interaction parameters appearing in Eq. 3.8 are set to $U = 5$ eV and $J = 0.68$ eV following previous literature [217, 204, 331]. DMFT calculations are performed using a finite-temperature exact diagonalization (ED) solver [35, 7] with three levels in the bath allowing for spontaneous symmetry breaking both in the orbital and magnetic sections. In agreement with Ref. [331], the low-temperature solution has both orbital ordering and Néel magnetic ordering. Within the accuracy of the calculation, magnetic ordering appears to take place at slightly larger temperatures, even if the ED solution is expected to lose some accuracy around the transition point because of truncation effects. The theoretical transition temperatures ($T_{c,DMFT} = 0.025$ eV) are nonetheless significantly larger than the experimental ones due to the mean-field nature of the approximation.

In order to compare with the time-resolved experiments, DMFT results are used to compute the scattering rate as the imaginary part of the self energy Σ (lifetime $\tau_{th} = \hbar / \mathrm{Im}(\Sigma)$) [98]. Specifically, as an estimate of the lifetime τ_{th}, an average of the electronic self-energy in a window of 0.2 eV around the

Fermi level on the real-frequency axis is extracted from the calculation. This averaging is necessary to smooth out the discrete features inherent to the exact diagonalization solution. The results of this calculation are plotted in Fig. 3.8a as a function of temperature (the plotted values are normalized to the value of $\mathrm{Im}(\Sigma)$ at 0 K). The results show that the scattering rate grows with temperature, as expected, with a rather clear change occurring at the transition temperature. In particular, when the long-range order is included, a significant reduction of $\mathrm{Im}(\Sigma)$, compared to the disordered (paramagnetic) phase, is observed at fixed temperature upon transitioning to the ordered phase (see gray arrow in Fig. 3.8a). This behavior indicates that the carriers lifetime strongly depend on the presence of the long-range order, establishing below the critical temperature.

For comparison, we report also the results of a much simpler calculation where a single-band Hubbard model is considered (see Fig. 3.8b). In this case, the only ordering allowed at half filling is antiferromagnetism. The calculation is performed choosing an arbitrary value of $U = 2.9D$ ($D = 6t$, t being the hopping) which leads to the same ordering temperature if the hopping is taken as 0.25 eV. We clearly observe a similar trend with respect to the calculations for $LaVO_3$.

Upon suppression of the long range order, a larger increase in scattering rate, of the order of 20%, is observed for the realistic three-band model as compared to the single-band Hubbard model. This 20% value is close to the variation of homogeneous linewidth detected by means of 2DES (Sec. 3.6), therefore suggesting that, on top of the antiferromagnetic ordering, the ordering in the orbital degree of freedom also plays a crucial role.

The DMFT results presented here show that the scattering rate and, correspondingly, the lifetime are strongly affected by the establishment of long range order, and therefore represent a suitable order parameter, justifying assumption (b) (Sec. 3.6). In order to show that the order parameter can indeed be identified with the scattering rate, we compare in Fig. 3.9 the temperature-dependence of the scattering rate (Fig. 3.9a), obtained from DMFT, to that of the order parameter of the free energy in Eq. 3.5 (Fig. 3.9b). Specifically, Fig. 3.9a displays the variation $\Delta\,\mathrm{Im}(\Sigma)$ between the ordered and disordered phases (difference between blue and red data points in Fig. 3.8a), whereas in Fig. 3.9b we report $\epsilon_{eq}(T) - \epsilon_{eq}(T_c)$ (normalized to the value of ϵ_{eq} at 0 K), where ϵ_{eq} indicates the minimum of F, as plotted in the inset. We observe that both curves display a similar decreasing behavior as the temperature is increased, until reaching zero at $T \geq T_c$.

DMFT results therefore confirm that the suppression of long-range order results in a decrease of intrinsic lifetime, as observed experimentally for the Hubbard exciton upon pump-perturbation of the spin and orbital ordered background. This validates the ascription of the pump-probe and 2DES signals to an increase in the scattering rate that is due to the coupling with the spin and orbital long-range orders. We lastly note that the signal enhancement in proximity of T_c observed in ultrafast spectroscopy is not directly related to the temperature

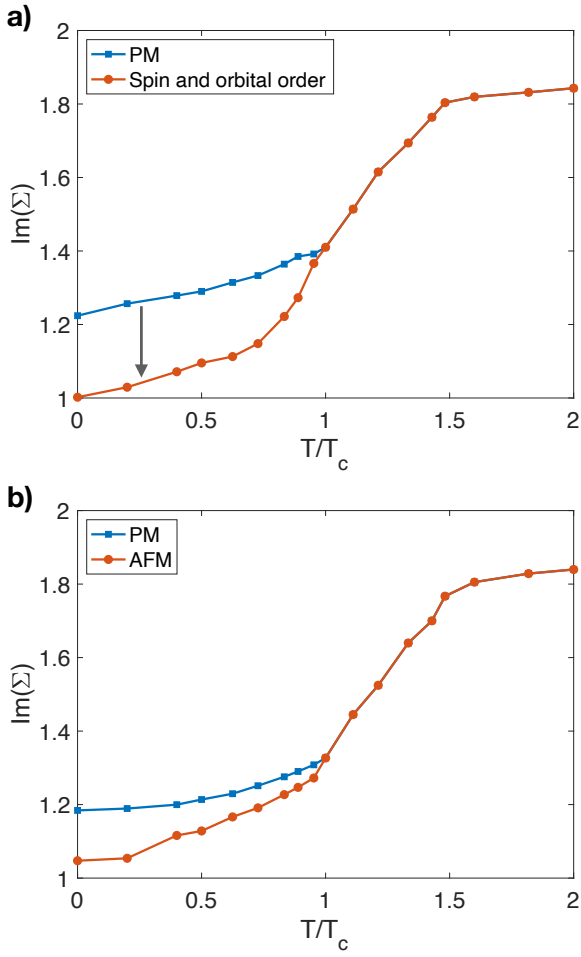

Figure 3.8: Scattering rate, calculated as the imaginary part of the self energy Σ by means of DMFT, for the cases of a realistic three-band model of $LaVO_3$ (panel a) and single-band Hubbard model (panel b). The establishment of spin and orbital order in panel a and of antiferromagnetic (AFM) order in panel b (red data points), results in a decrease of the scattering rate, highlighted by the gray arrow, as compared to the disordered (paramagnetic, PM) phase (blue data points). The plotted values for $\mathrm{Im}(\Sigma)$ are normalized to the value at $T = 0$ K.

dependence of variation in scattering rate due to removal of the long-range order; rather, it is the coupling with the light-induced electronic excitations that becomes more efficient in proximity of T_c and leads to a larger variation in the order parameter upon perturbation, in agreement with the curve in Fig. 3.9b being steeper right below T_c.

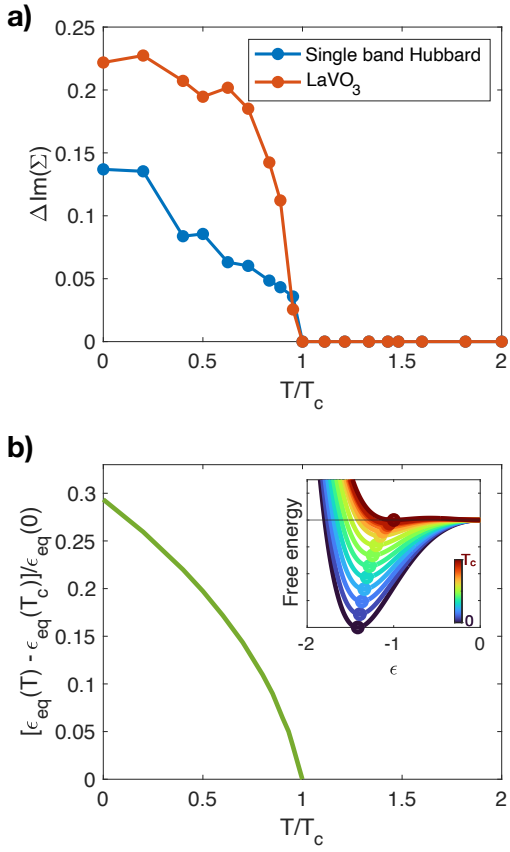

Figure 3.9: a) Variation of the scattering rate, obtained by DFMT calculation (Fig. 3.8a), between the ordered and disordered phase as a function of temperature. b) Temperature-dependence of order parameter estimated as the position ϵ_{eq} of the minimum of the free energy in Eq. 3.5, plotted in the inset.

3.8 Discussion and conclusions

In this chapter we analyzed pump-probe and 2DES data on $LaVO_3$ thin film. Employment of a broadband probe in 1D spectroscopy revealed a broadening in the Hubbard exciton linewidth upon pump excitation. 2DES further showed that, due to the pump excitation, there actually is an increase in the homogeneous component of the linewidth, Γ_{hom}, which can be related to the order parameter of the spin and orbital degrees of freedom of the system, as shown by DMFT calculation for a three-band model of $LaVO_3$.

When light pulses are used to perturb the system, the photoinduced electronic excitations couple to the order parameter and result in a disruption of the

spin/orbital ordered background. This coupling and the resulting dynamics of the order parameter are captured within Ginzburg–Landau theory, which explains the signal enhancement observed in proximity of T_c and the critical slowing down of the order parameter dynamics upon approaching the transition temperature.

Overall, our results represent a direct observation of the decoherence time of an electronic excitation being strongly affected by the coupling with long-range orders. Whereas this was here observed specifically on $LaVO_3$, the change in scattering rate upon crossing a symmetry breaking phase transition is likely a general mechanism that extends to many other strongly correlated materials displaying ordered phases (e.g. magnetic or charge order). The possibility of controlling the thermal bath fluctuations in the proximity of a phase transition could then provide a novel approach to tune the ultrafast electronic decoherence in solid state materials.

CHAPTER 4

Resistive switching initiated by topological defects in Mott insulator V_2O_3

Parts of this chapter have been adapted from the following manuscripts:

Mott resistive switching initiated by topological defects, A. Milloch, I. Figueruelo-Campanero, W.-F. Hsu, S. Mor, S. Mellaerts, F. Maccherozzi, L. I. Veiga, S. S. Dhesi, M. Spera, J. W. Seo, J.-P. Locquet, M. Fabrizio, M. Menghini, C. Giannetti, *Nature Communications*, 2024, 15:9411, doi: 10.1038/s41467-024-53726-z

Mott materials: unsuccessful metals with a bright future, A. Milloch, M. Fabrizio, C. Giannetti, *npj Spintronics*, 2024, 2:49, doi: 10.1038/s44306-024-00047-y

In this chapter we investigate the prototypical Mott insulator V_2O_3 where an out-of-equilibrium state is induced by the application of a static electric field. V_2O_3 is a paradigmatic Mott material, which undergoes a first-order metal-to-insulator phase transition together with a lattice transformation that breaks the threefold rotational symmetry of the rhombohedral metallic phase. In V_2O_3, the insulator-metal transition can be induced by an above threshold current or voltage that triggers the sudden change of its electrical properties and results in volatile resistive switching. Despite the relevance of this process for ultrafast electronics, resistive memories and neuromorphic computing, the

nature of the local stochastic fluctuations that drive the formation of metallic regions within the insulating state has remained hidden.
Here, we use operando X-ray nano-imaging to capture the origin of resistive switching in a V_2O_3-based device under working conditions. We reveal a new class of volatile electronic switching triggered by nanoscale topological defects appearing in the shear-strain based order parameter that describes the insulating phase. These results suggest that the manipulation of lattice topological defects via strain engineering can represent a new route to control the electronic switching dynamics.

The chapter is organized as follows. First, we introduce the electronic and structural properties of V_2O_3 and provide a brief overview of resistive switching in Mott materials. Next, we describe the nanoscale spatial self-organization of the Mott insulating phase. We then discuss the performed experiment, which combines resistive switching with PhotoElectron Emission Microscopy (PEEM). Finally, we analyze the results using a Ginzburg-Landau theoretical framework to describe the nanotexture and associated topological defects, while a two-resistor model is employed to capture the evolution of the metallic filaments formed during resistive switching.

4.1 V_2O_3: electronic and structural properties

Phase diagram. V_2O_3 is a prototypical Mott insulator with a rich phase diagram displayed in Figure 4.1a [128, 113]. In the undoped compound, V_2O_3 undergoes an electronic, magnetic and structural phase transition with a pronounced first order character at the critical temperature $T_{IMT} \simeq 170$ K: at atmospheric pressure, the high temperature phase is metallic, paramagnetic and rombohedral, whereas at low temperature the system becomes insulating, antiferromagnetic and monoclinic. The phase diagram also includes an insulating paramagnetic phase entered through an isostructural transition upon doping with Cr, whereas Ti doping favors the metallic phase by quenching the insulator-metal transition [195, 194, 193, 152].

Crystal structure. The high temperature paramagnetic phase has curundum structure with symmetry space group $R\bar{3}c$ (n° 167). The non-primitive unit cell is displayed in Fig. 4.1b. Vanadium atoms form a honeycomb structure in the ab plane with ABC stacking along the c-axis, so that each atom has only one vanadium nearest neighbor along c forming pairs (V_1-V_2 in Fig 4.1d), referred to as dimers. Each vanadium is surrounded by an oxygen octahedron, subject to weak trigonal distortion. At low temperature the crystal structure becomes monoclinic (symmetry space group $I2/s$, n° 15) with an increased length of two edges of the hexagons (distance V_1-V_3 in Fig. 4.1d), which results in a 1.4% increase of the unit cell volume. The structural transition is also characterized by a tilting of the hexagons with respect to the ab plane, which increases the dimer V_1-V_2 length (see Fig. 4.1e) [195, 194, 193, 64, 239].

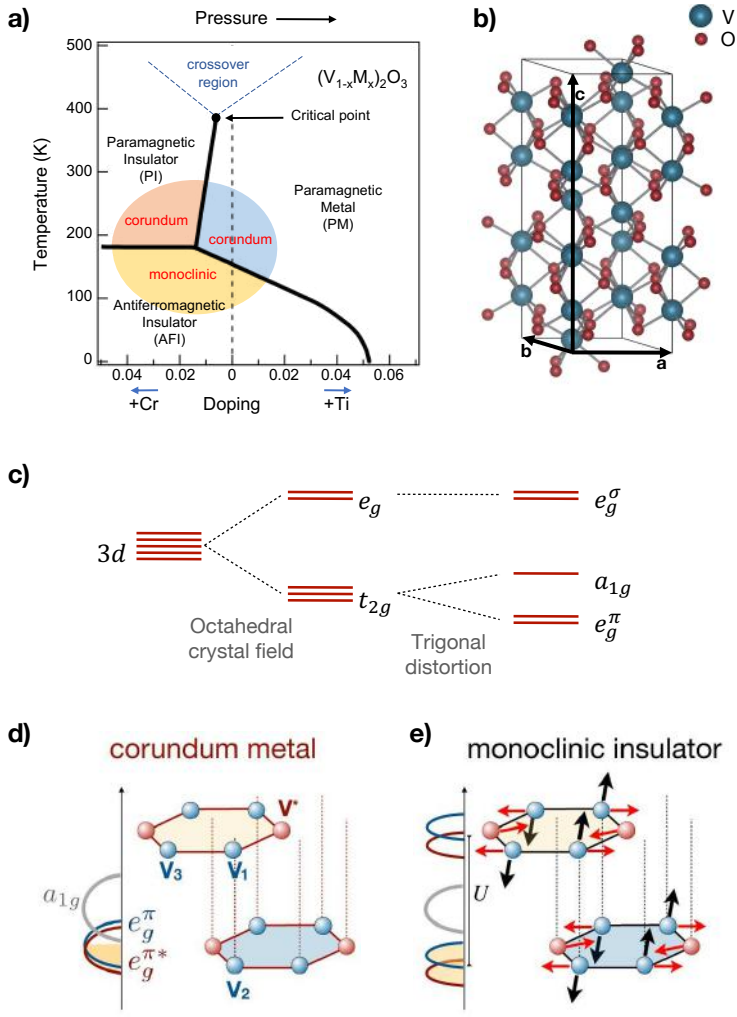

Figure 4.1: a) Phase diagram of V_2O_3 as a function of temperature and Cr/Ti doping. The effect of pressure, favoring the metallic phase, is similar to that of Ti-doping. Adapted from Ref. 113. b) Non-primitive hexagonal unit cell of the high-temperature corundum phase of V_2O_3. The atom positions are taken from Ref. 239. c) Splitting of the V-$3d$ levels due to the octahedral crystal field and the trigonal distortion. d) Sketch of the stacked honeycomb planes in the high-temperature rombohederal phases. The equivalence, in the hexagonal symmetry, of the V-sites colored in blue and red in the figure implies the degeneracy of e_g^π orbitals. Adapted from Ref. 238. e) Sketch of the stacked honeycomb planes in the low-temperature monoclinic phases, where the distortion of the hexagons lifts the e_g^π degeneracy. The tilting of the hexagons, associated to the out-of-plane movement of the vanadium atoms (black arrows), controls the $a_{1g} - e_g^\pi$ energy distance. Adapted from Ref. 238.

Electronic structure. In V_2O_3 there are two electrons in the valence shell occupying the V-3d levels. As sketched in Figure 4.1c, the V-3d orbitals are split into a lower t_{2g} band and an upper e_g band by the octahedral crystal field. The trigonal distortion further splits the t_{2g} orbitals into an upper a_{1g} singlet and a lower e_g^π doublet [40]. The former is aligned along the c-axis, while the latter are mainly oriented in the ab plane. The average occupation of the a_{1g} orbital is $n_{a_{1g}} \simeq 0.25$ ($n_{e_g^\pi} \simeq 0.75$) in the metallic phase, while it decreases to $n_{a_{1g}} \simeq 0.17$ in the insulating phase [214], where the e_g^π degeneracy is lifted and the system behaves as a half-filled two-band Mott insulator with an effective charge gap of 0.5 eV (see density of states sketches in Fig. 4.1d and e) [227]. The jump in the a_{1g} orbital occupation occurring at T_{IMT} suggests that $n_{a_{1g}}$ can be exploited as a control parameter to modify the free energy of the system (X in Fig. 1.3, as seen in Chapter 1) and induce the phase transition. Orbital excitation in the visible range, for example, can be exploited to manipulate $n_{a_{1g}}$ nonthermally [84].

4.2 Current-induced insulator-metal transition in Mott materials

V_2O_3, similarly to many other Mott materials displaying insulator-to-metal transition, is fragile to the application of an electric field, which can drive the collapse of the electronic band structure and the sudden release of a large number of free carriers [189, 267]. At the macroscopic level, this phenomenon manifests in the resistive switching process, i.e., a sharp increase of the current flow when the applied voltage exceeds a threshold value [309, 135, 262, 62, 109, 209, 91, 92, 130].

In Mott insulators such as V_2O_3, the electric-field induced IMT is a volatile phenomenon that leads to a transient non-equilibrium metal phase; it is not accompanied by a full structural and electronic reorganization (contrary to a non-volatile resistive switching), but just by a local collapse of the Mott gap along a conducting path [333, 130, 61, 303]. The strong non-linearity of this process triggered many efforts to develop neuromorphic building blocks for the hardware implementation of neural networks [197] or for ultrafast volatile and non-volatile memories or processors [304, 127, 234].

The mechanism underlying the resistive switching is subject of a longstanding debate. For materials undergoing a temperature-driven IMT (see for example resistivity vs temperature plot in Figure 4.2a), Joule heating was shown to play a key role in triggering the transition under the application of a bias voltage [257, 336, 162, 63]. At the same time, it was also argued that a purely thermal mechanism is not always sufficient to account for resistive switching, and electronic non-thermal mechanisms of electric-field-induced IMT were also reported [100, 262, 263, 294, 67, 135]. Recently, a large effort has been devoted to achieving *operando* characterization of micro and nano-devices. Pioneering microscopy experiments are opening the possibility of imaging the

Mott switching process at the micro- and nano-scale in real devices. Optical microscopy, scanning electron microscopy (SEM) and scanning microwave microscopy (SMM) experiments, performed during the application of the electric field, allowed capturing the formation of metallic filaments short-circuiting the device in vanadium oxides VO_2 [243, 137, 257, 178], V_2O_3 (Figure 4.2) [106, 155], nickelates $SmNiO_3$ and $NdNiO_3$ [174]. The metallic filament is observed to widen as the current flowing in the device is increased (see optical microscopy images in Fig. 4.2c) and disappear once the electric field is removed and the insulating state of the system is recovered. The size of the metallic filaments depends also on the sample temperature, with filaments being wider as the critical temperature for the IMT is approached [174]. The lattice structure of the non-equilibrium state has been investigated in VO_2 thin films and single crystals by means of nanoscale X-rays and electron diffraction, which revealed signals of a structural transition into the rutile high-temperature phase [257, 86, 46]. One of the key parameters influencing resistive switching and filament formation is the resistivity drop across the thermally-driven IMT, which was shown to influence the nucleation dynamics, the filament widening rate and the stochasticity of the firing process [63, 174]. Intrinsic defects also play a crucial role, pinning and controlling the formation of conductive filaments [135, 63]. This suggests the possibility of controlling the resistive switching by artificially creating defects in the material. By creating permanent defects using focused-ion-beam irradiation, it was demonstrated that it is possible to change the resistive switching mechanism from a thermal to a non-thermal field-induced IMT [135], as well as to localize the filament formation [96].

The state-of-the-art macroscopic models for resistive switching [158] are based on resistor networks that consider interconnected nodes transforming from the insulating to metallic state in the presence of an electric field. Above a certain threshold, a percolative, avalanche transition takes place, thus leading to the formation of conductive filaments and the consequent sudden drop in resistivity [262, 264]. The full control and exploitation of this process is currently prevented by a limited knowledge of the early-stage firing dynamics. Microscopically, still little is known about the nature of the nanoscale regions that trigger the avalanche process. Also the relation between the electronic and structural properties of the switched regions and those of the pristine insulating template is a matter of debate. The pioneering microscopy experiments mentioned above captured the real-time formation of macroscopic metallic channels [61, 155, 63, 13, 174], but lacked the resolution and sensitivity to address the microscopic origin of the switching process.
In this chapter, we combine a X-ray microscopy with nanoscale resolution (PEEM) with resistive switching. This allows us to investigate the role of the intrinsic nanotexture of the low temperature phase of V_2O_3 of the electric-field induced IMT.

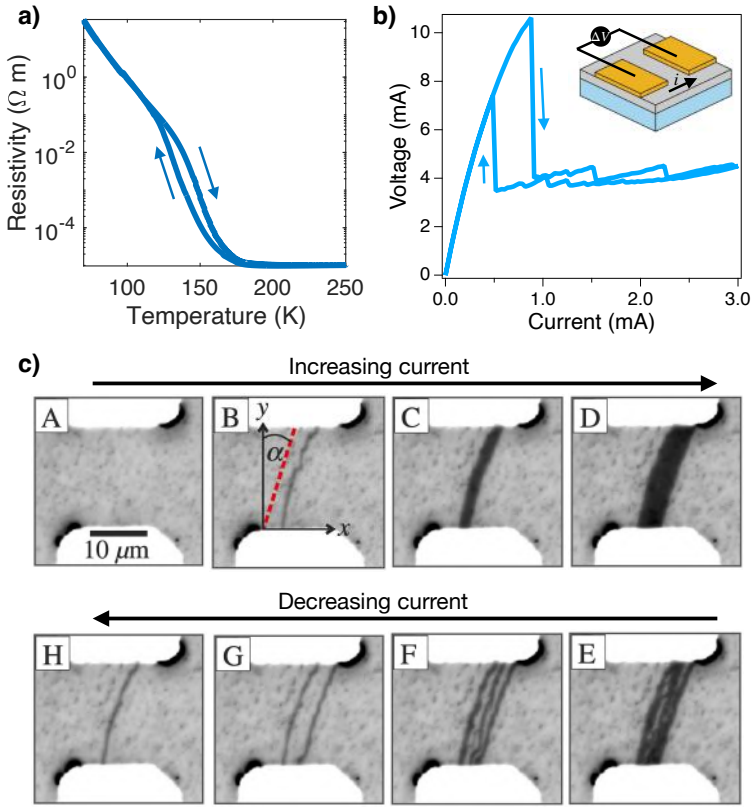

Figure 4.2: a) Resistivity hysteresis of a 20 nm V_2O_3 film. b) Typical current-voltage curve of a V_2O_3 device, sketched in the inset, where resistive switching occurs at 0.9 mA upon driving of a current across a 2 μm gap. c) Wide-field optical microscopy photomicrographs of a V_2O_3 device acquired simultaneously to a current sweep. A narrow metallic filament (dark line) connecting the electrodes appears above the threshold current for the switching (panel B) and widens for increasing currents (panels B-C). When the current is decreased, the metallic channel splits into multiple filaments (panels E-H) until disappearing when the current is removed and the device returns to an insulating state. Adapted from Ref. 155.

4.3 Domain nanotexture in V_2O_3

On the nanometer scale, V_2O_3 exhibits inherent spatial inhomogeneities - resulting from the first-order character of the Mott transition - whose role in the formation of metallic channels upon resistive switching remains an open question.
In the insulator-metal coexistence region, the spatial nanotexture originates from the nucleation and growth of domains of one phase (formerly metastable), eventually prevailing over the other phase (formerly stable) [191]. In addition, due to the symmetry breaking at T_{IMT} that lowers the crystal structure symmetry, the low temperature insulating phase is itself nanotextured because of the existence of monoclinic twins [238, 236].

Within a macroscopic description of the structural and electronic transitions in V_2O_3, based on Landau–Ginzburg theory, the C_3 symmetry breaking rhombohedral-to-monoclinic transition can be be described [236] by a vector order parameter:

$$\overrightarrow{\epsilon} = (\epsilon_{31}, \epsilon_{23}) = \epsilon \left(\cos\phi_n, \sin\phi_n\right) \tag{4.1}$$

associated to the shear strain components ϵ_{31} and ϵ_{23} that are linked to the tilting of the dimers and characterize the monoclinic distortion. Below T_{IMT}, the amplitude of the order parameter, ϵ, becomes non-zero, while the phase can assume three different values:

$$\phi_n = (2n-1)\frac{\pi}{3} \tag{4.2}$$

corresponding to the distortion along the three equivalent hexagonal axes of the rhombohedral phase, indicated in the following by the versors $\hat{\epsilon}_n$, n=1,2,3 (see Fig. 4.3 a and b).

The stabilization of the monoclinic nanotexture is driven by the elastic strain associated with the lattice distortion and is constrained by Saint-Venant compatibility condition [236], which ensures the continuity of the medium during the rombohedral-to-monoclinic deformation via the curl-free condition:

$$\overrightarrow{\nabla} \times \overrightarrow{\epsilon}(\mathbf{r}) = 0. \tag{4.3}$$

As shown in the sketch in Fig. 4.3c, the conservation of the parallel component of $\overrightarrow{\epsilon}(\mathbf{r})$ across an interface between two different domains has two important implications:

i) the interface between two different monoclinic domains is oriented along $\hat{\epsilon}_n$ of the third domain;

ii) the interface between a monoclinic and a rhombohedral metallic domain is oriented perpendicularly to $\hat{\epsilon}_n$ of the monoclinic domain.

The Saint-Venant condition corresponds to a fixed phase jump $\delta\phi$=$2\pi/3$ of $\overrightarrow{\epsilon}(\mathbf{r})$ across any interface between two monoclinic domains. If we consider, for

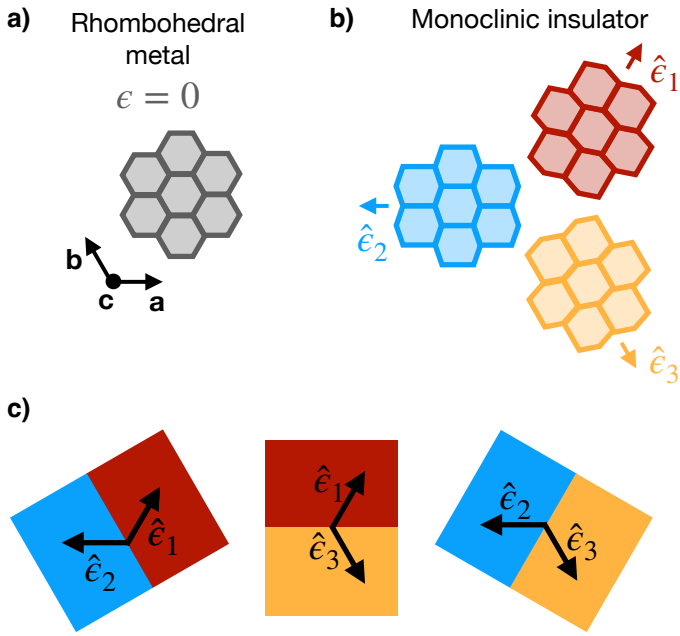

Figure 4.3: a) sketch of the hexagonal symmetry of V_2O_3 is the high-temperature rombohedral structure where the amplitude of the order parameter ϵ is zero. b) Sketch of the structural deformation from romnohedreic to monoclinic, which can occur along three equivalent directions that identify the possible directions of $\overrightarrow{\epsilon}$ in the low temperature phase. c) Sketch of the three allowed directions for the boundary between monoclinic domains with different order parameter $\overrightarrow{\epsilon}$. The curl-free condition of Eq. 4.3 imposes the conservation of parallel component the order parameter across the interface.

example, a domain with order parameter along $\hat{\epsilon}_2$ (blue in Figure 4.8b), its interface is oriented along $\hat{\epsilon}_1$, i.e. at $\pi/3$ angle, when it neighbours an $\hat{\epsilon}_3$ domain (yellow), whereas it is oriented along $\hat{\epsilon}_3$, i.e. at $2\pi/3$ angle, when it neighbours an $\hat{\epsilon}_1$ domain (red). Figure 4.3c summarizes the only three interfaces that are allowed by Eq. 4.3.

Direct observation of the domain nanotexture of the low temperature monoclinic phase has been achieved by means of PhotoEmission Electron Microscopy (PEEM, see Fig. 4.4a). PEEM in a microscopy technique that, through a set of electrostatic and electromagnetic lenses, images the spatial distribution of secondary electrons that are photo-emitted upon absorption of X-ray radiation, usually tuned to a strong absorption edge of the material [205]. X-ray magnetic dichroism is often exploited to produce contrast images, obtained by acquiring PEEM images with two different polarizations (linear vertical/horizontal or circular right/left) and by then taking their difference, normalized to the sum of the two images [205]. This is usually employed, for example, to study magnetic

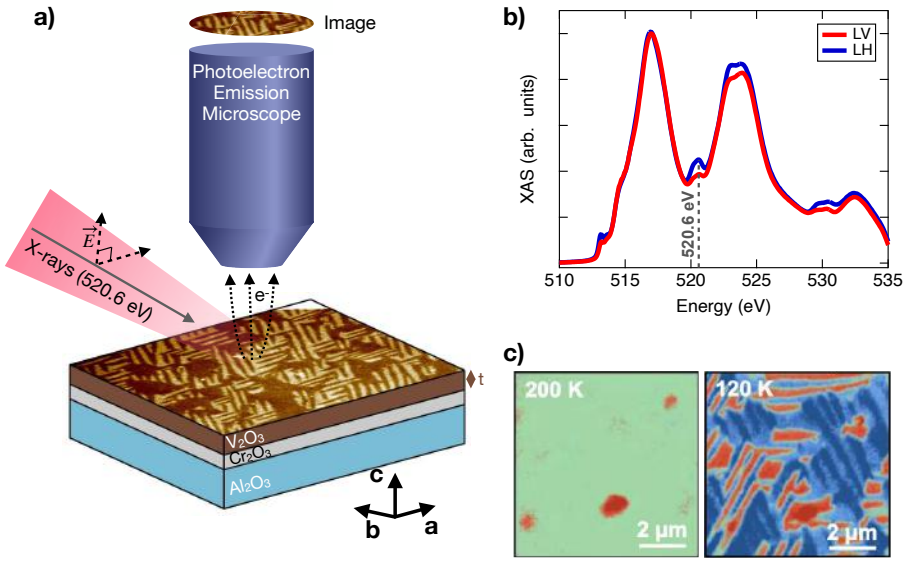

Figure 4.4: a) PEEM experimental setup. X-ray radiation, with tunable energy resonant with the vanadium $L_{2,3}$ edge, impinges on the sample surface and the emitted electrons are collected and imaged through electrostatic and magnetic lenses. b) X-ray absorption spectra at the vanadium L-edge with the electric vector perpendicular to the sample surface normal (linear vertical polarization, LV, red curve) and at 16° to $\hat{n}$ (linear horizontal polarization, LH, blue curve). PEEM imaging was performed by exploiting the X-ray linear dichroism (XLD) at photon energy of 520.6 eV, indicated by the dashed line. c) PEEM images of V_2O_3 at $T > T_{IMT}$ (left panel) and at $T < T_{IMT}$ (left panel), revealing the nanotexture of the low-temperature phase. Adapted from Ref. 238.

surfaces and image ferromagnetic or anti-ferromagnetic domains with a spatial resolution down to 15 nm [205].

In the case of V_2O_3, the $L_{2,3}$ ($2p \rightarrow 3d$) vanadium edge (513-530 eV, see Fig. 4.4b) displays X-ray Linear Dichroism (XLD) that can be exploited to image the domain nanotexture of the monoclinic phase [214, 238, 236]. Fig. 4.4c shows XLD-PEEM images of a V_2O_3 sample with c-axis perpendicular to the sample surface, recorded with the light electric field vector, $\vec{E}$, perpendicular and 16° to the surface normal at 520.6 eV photon energy. Because of the directionality of the V-3d orbitals that changes among the three equivalent monoclinic twins, the XLD signal depends on the direction along which the monoclinic distortion takes place compared to the X-ray linear polarization direction, that is on the angle between the in-plane component of $\vec{E}$ and the position dependent order parameter, $\vec{\epsilon}(\mathbf{r})$ [236] (see Fig. 4.3b and 4.4a). Therefore, XLD-PEEM of low-temperature V_2O_3 provides a map - with ∼30 nm spatial resolution - of the three different monoclinic domains. As shown in Figure 4.4c, the low temperature nanotextured phase appears as a patchwork of the three equivalent

monoclinic twins oriented along the three hexagonal axes of the high-temperature rhombohedral phase, in agreement with the domain boundary constraints of Figure 4.3c. When the temperature is increased, metallic domains nucleate at the interfaces between monoclinic twins until the percolative phase transition takes place and leads to the homogeneous rhombohedral phase (Fig. 4.4c, right panel) [238].

4.4 Combined PEEM-resistive switching experiment

In order to investigate the role of the domain nanotexture on the IMT induced by a static electric field, we here combine resistive swtiching with PEEM microscopy. Resistive switching is induced by applying an electric field across a patterned micro-gap at temperatures close to T_{IMT} [106, 61, 63]. The resistive switching device investigated here is formed by a 20 nm V_2O_3 film coated with gold electrodes. V_2O_3 is grown by oxygen-assisted Molecular Beam Epitaxy on a (0001)-Al_2O_3 substrate with a 40 nm Cr_2O_3 buffer layer to reduce any interfacial residual strain [68]. The resulting V_2O_3 film has the *c*-axis oriented parallel to the surface normal, with $T_{IMT} = 145$ K (the resistivity-temperature hysteresis curve for the sample under investigation is plotted in Figure 4.2a). Two gold electrodes allow the application of an electric bias across the gap of width $w = 2$ µm and length $l = 30$ µm. The gap region between the electrodes is imaged using PEEM.

Figure 4.5a shows an XLD-PEEM image obtained in the monoclinic insulating phase at $T = 120$ K. The V_2O_3 nanotexture exhibits features typical of the monoclinic insulating phase [238, 236]. Monoclinic domains with different ϕ_n give rise to different XLD contrast, which can be identified as different color intensities within the XLD-PEEM image. The minimization of the total strain leads to the formation of stripe-like domains, with symmetry-constrained directions [236], as discussed in Sec. 4.3. Each monoclinic insulating domain extends over a few micrometers, thus connecting the two electrodes, and it is characterized by a width $w_{dom} \sim$200 nm.

The XLD-PEEM imaging is then repeated while driving a current, I, through the device and measuring the voltage drop, V, across the gold contacts. Figures 4.5b-j show the XLD-PEEM images acquired at increasing values of I, following the upward branch of the hysteresis cycle. The presence of an in-plane electric field across the electrodes introduces a weak image blurring that becomes significant for $V \geq$ 6-8 V. Despite this, the nanodomains are well resolved during the resistive switching process, which first manifests itself at the voltage drop observed between 0.8 mA and 1.1 mA (Fig. 4.5c and d respectively). As the current is further increased, the melting of the monoclinic nanotexture in the region delimited by white dashed lines (Fig. 4.5e-j) progresses with a widening channel with a homogenous intensity. The XLD contrast measured in the region between the white dashed lines corresponds to the signal of the

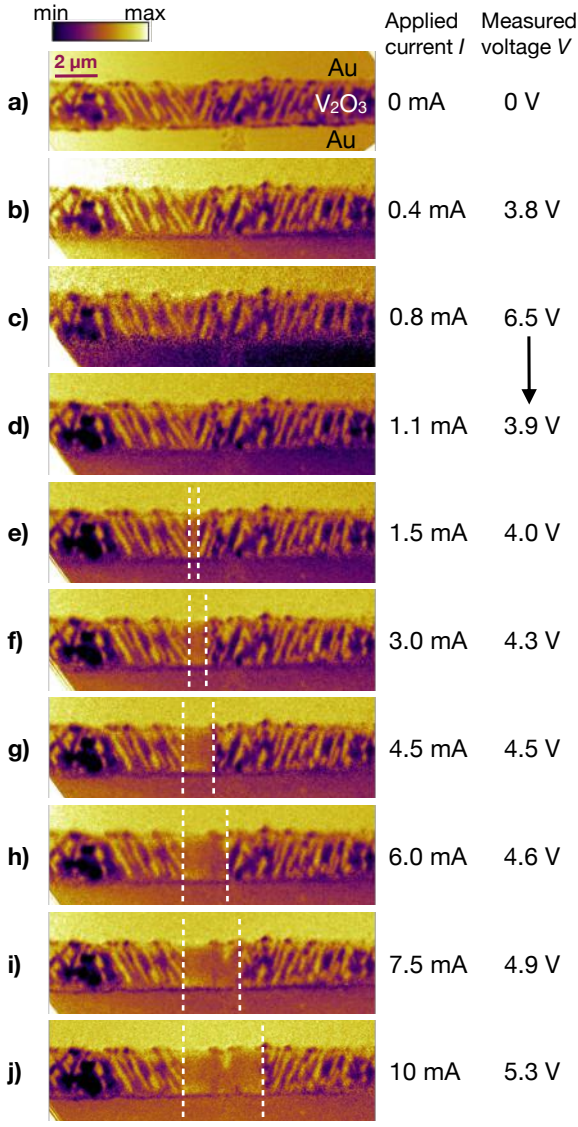

Figure 4.5: XLD-PEEM images before (a) and during (b-j) the application of an electric current at $T = 120$ K. The homogeneous regions at the top and bottom of each image are the gold electrodes. The area in between is the exposed V_2O_3 antiferromagnetic monoclinic phase, exhibiting a striped domain nanotexture. For currents larger than 1.5 mA, the striped domains disappear in the region delimited by the white dashed lines, demonstrating the appearance of a rhombohedral metallic filament, which widens as the current is increased.

high-temperature rhombohedral phase. This is also confirmed from the angle dependence of the XLD signal [236]. As shown in Fig. 4.6, images collected with two different X-rays polarization angles, with respect to the in-plane V_2O_3 axes, show no intensity variation upon sample rotation in the metallic channel, as opposed to the monoclinic domains on the sides of the image, where the XLD signal depends on the angle between the light polarization and $\overrightarrow{\epsilon}(\mathbf{r})$. The constant XLD contrast region in the middle of the gap therefore appears due to the formation of a metallic channel with rhombohedral lattice structure (ϵ=0). XLD-PEEM images obtained under the same conditions, but with a larger field of view in order to capture the whole gap of the device are displayed in Fig. 4.7, which reports an independent set of PEEM measurements compared to the data shown in Fig. 4.5, performed after thermal cycling to 250 K. The metallic channel consistently forms in the same location within the gap with no additional metallic paths observed. Furthermore, when the applied current is removed, the metallic channel disappears and the monoclinic domains reappear with the same pre-switching configuration, indicating a volatile process.

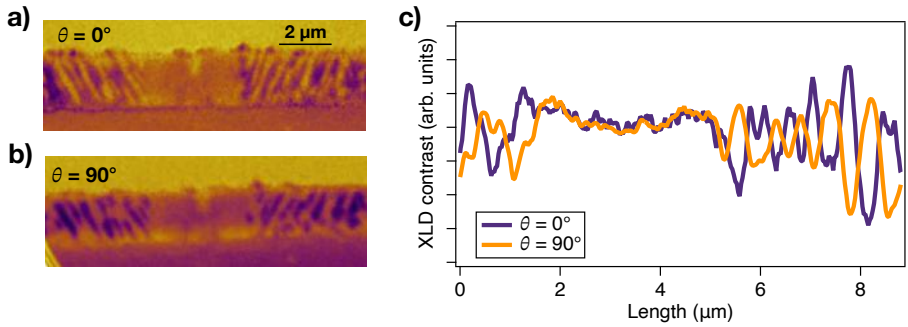

Figure 4.6: a, b) XLD-PEEM images collected for two orthogonal directions of the X-ray polarization with respect to the crystalline axes of the V_2O_3 film. Upon rotation of the sample by 90° about the $\hat{n}$, the XLD signal is unchanged in the untextured metallic region in the middle of the image while the contrast reverses sign in the insulating region. c) Line profile of the XLD-PEEM images in a) and b).

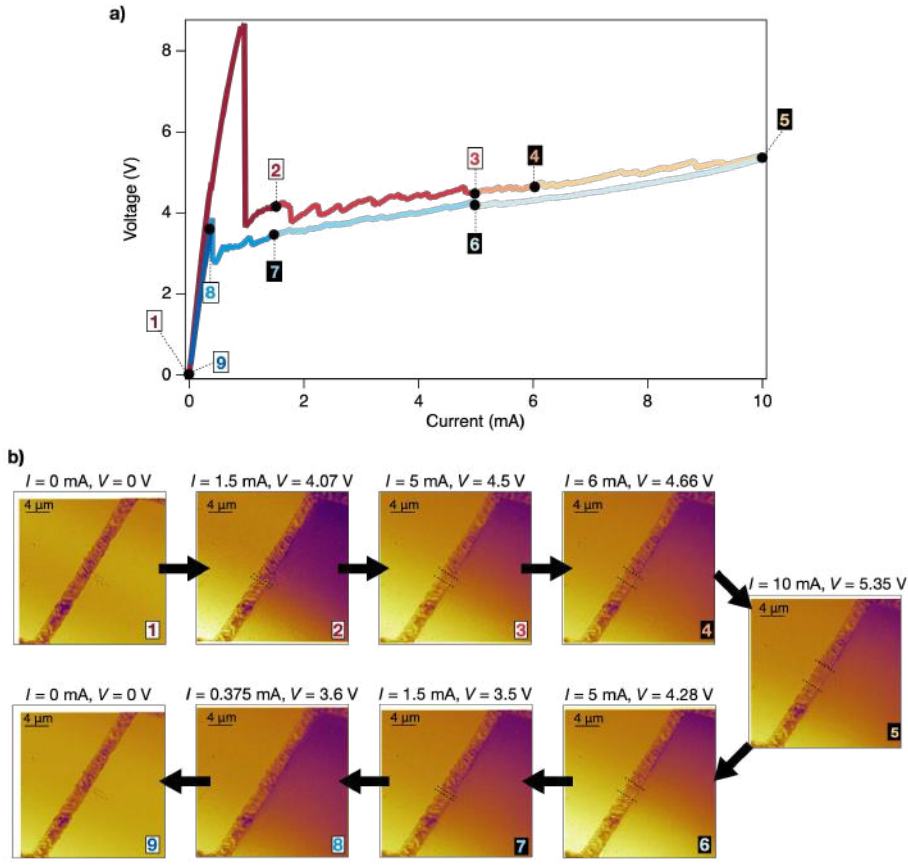

Figure 4.7: a) $I - V$ curve obtained from a current sweep from 0 to 10 mA (red lines) and back from 10 to 0 mA (blue lines). The colored numbers in the plot indicate the point in the $I - V$ curve where XLD-PEEM imaging is performed while keeping constant the current I running through the device. b) XLD-PEEM images collected on the device gap while an electric current is applied. The 25 µm field of view employed here allows to image the full device length. The corundum filament formed after resistive switching is detected for currents $I > 1.5$ mA and is highlighted by black dashed lines. When the current is decreased, the corundum filament disappears at $I = 0.375$ mA (panel 8), i.e. just outside of the hysteretic region of the $I - V$ curve.

4.5 Role of domain topology on resistive switching

We note that the location where the metallic channel forms corresponds to an area characterized by a peculiar topology of the lattice nanotexture where the monoclinic domains form a V-shape. In fact, the formation of the metallic channel is pinned at the crossing point of domains of same ϕ_n with directions that differ by $\pi/3$. Fig. 4.8a shows a detail of the switching region, using a colorscale that highlights the three different domains with a monoclinic distortion along $\hat{\epsilon}_1$ (red, $\phi_1{=}\pi/3$), $\hat{\epsilon}_2$ (blue, $\phi_2{=}\pi$) and $\hat{\epsilon}_3$ (yellow, $\phi_3{=}5\pi/3$). The V-shaped arrangement is realized by two $\hat{\epsilon}_2$ domains with boundaries oriented along $\hat{\epsilon}_1$ and $\hat{\epsilon}_3$ and intersect forming a $\pi/3$ angle.

We note that the curl-free condition (Eq. 4.3), that is satisfied throughout the nanotextured domain structure, is actually violated at the V-shaped vertex structure. If we consider a circuit Γ_1 (see Fig. 4.8b) across the boundary between two striped domains, the total phase shift is given by $\delta\phi = +2\pi/3 - 2\pi/3 = 0$ thus adhering to the curl-free condition in Eq. 4.3. In contrast, the topology of the V-shaped structure is such that, if we move around the internal apex (Γ_2), the total phase-shift is constrained to $\delta\phi = +2\pi/3 + 2\pi/3 = 4\pi/3$, thus breaking the curl-free condition. The consequence is that the vertex of the V-shaped domains acts as a topological defect. These topological defects are inherently characterized by the strong frustration of the local value of the order parameter $\overrightarrow{\epsilon}(\mathbf{r})$ and fluctuations on spatial and temporal scales that cannot be captured by the present experiment. We further note that the formation of the topological defect is a direct and unavoidable consequence of the quasi-1D confined geometry of the system. Whereas the component of the order parameter parallel to the electrodes ($\epsilon_{||}$, see Fig. 4.8b) can be compensated outside the gap, the perpendicular component ($\epsilon_{\perp}$) has to be minimized to avoid the accumulation of excessive strain energy within the gap region. Thus, considering the directions of $\overrightarrow{\epsilon}(\mathbf{r})$ at the boundaries between different monoclinic domains (see Fig. 4.8b), the formation of V-shaped domains is a unique configuration that fulfils the requirement $\epsilon_{\perp}{=}0$.

The suppression of the symmetry-breaking order parameter, $\overrightarrow{\epsilon}(\mathbf{r})$, at topological defects has far-reaching implications related to the nature of the resistive switching process. The electronic IMT can be described by a scalar order parameter $\eta(\mathbf{r})$ (related to the V-V dimer length) [236], which depends on the position $\mathbf{r}$ and is such that $\eta = -1$ in the metallic state and $\eta = +1$ in the insulating state. The coupling between the electronic and structural transitions can be described by the energy functional [236]:

$$F[\epsilon, \eta] \propto \int d\mathbf{r} \left\{ \left(\eta^2(\mathbf{r}) - 1\right)^2 - g\big(\epsilon^2(\mathbf{r}) - \epsilon_t^2(V)\big)\,\eta(\mathbf{r}) \right\}, \tag{4.4}$$

where g is the coupling between the electronic order parameter and the strain and $\epsilon_t(V)$ is a threshold parameter that controls the first-order IMT and can depend on the applied voltage V. When $\epsilon^2(\mathbf{r}) > \epsilon_t^2(V)$, the insulating phase with

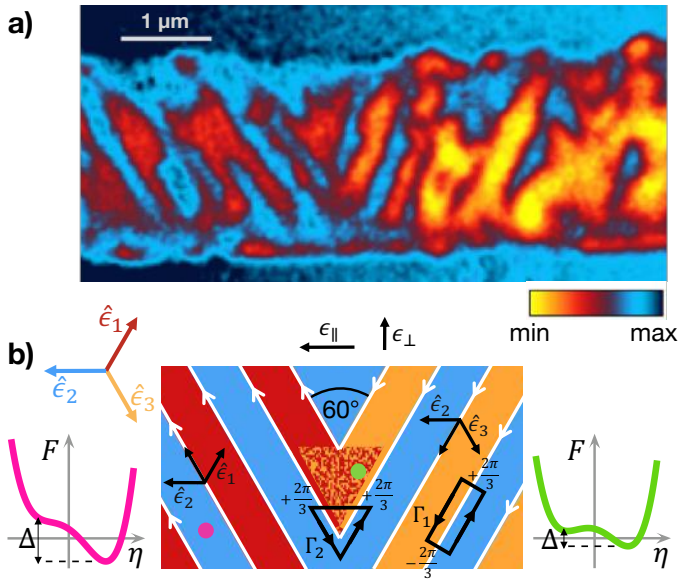

Figure 4.8: a) Detail of the XLD-PEEM image shown in Fig. 4.5 in the region where the metallic filament is formed upon the application of a current above the threshold I_{th}. b) Schematic of the monoclinic domains crossing at $60°$ and forming a topological defect. Blue, red and yellow areas identify the three possible monoclinic domains corresponding to the three equivalent order parameter directions $\hat{\epsilon}_n$. The order parameter at the boundaries between different domains is oriented along $\hat{\epsilon}_1 + \hat{\epsilon}_2$ $(2\pi/3)$ for the red-blue interface and along $\hat{\epsilon}_2 + \hat{\epsilon}_3$ $(4\pi/3)$ for the blue-yellow interface. The mixed red-yellow triangular region indicates the local suppression of the strain at the topological defect. The energy functionals shown on the left and right, illustrate how a topological defect (green plot, solid line) decreases the insulator-metal energy difference, Δ.

$\eta = +1$ is locally favoured, whereas for strain smaller than the threshold value, i.e. $\epsilon^2(\mathbf{r}) < \epsilon_t^2(V)$, the metallic solution is stabilized. $\epsilon_t^2(V)$ thus represents the threshold above which the insulating monoclinic state ($\eta = +1$, $\epsilon \neq 0$) becomes stable. The description of the electric-field induced transition is based on the observation [189] that the electric field directly couples to the electronic bandstructure of a Mott insulator, making the metallic phase more stable. The transition can thus be described assuming that $\epsilon_t^2(V)$ increases with increasing V. The energy difference between the insulating and metallic phase can be expressed as $\Delta(\mathbf{r}, V) = F[-1] - F[+1] \simeq g\left[\epsilon^2(\mathbf{r}) - \epsilon_t^2(V)\right]$. If we start from the insulating phase with $\epsilon^2(\mathbf{r}) > \epsilon_t^2(V = 0)$, the IMT takes place when V is increased up to the point that $\Delta(\mathbf{r}, V)$=0. A topological defect, which locally suppresses $\epsilon^2(\mathbf{r})$, thus acts as a seed with a lower threshold compared to the rest of the system.

4.6 Resistive switching mechanism and metallic filament expansion

Intriguingly, we also note from Eq. 4.4 that the IMT can take place at a non-zero value of $\epsilon^2(\mathbf{r})$, which allows the formation of a non-thermal metallic state ($\eta = -1$) with a finite monoclinic distortion ($\epsilon^2(\mathbf{r}) \lesssim \epsilon_t^2(V)$), as already observed in non-equilibrium optical experiments [236, 237]. The nature of the early-stage switching process can be inferred by a direct comparison between the electrical state of the device and the melting of the monoclinic domains. The $I-V$ curve of the device, as measured *in-situ* during the PEEM imaging, is plotted in Fig. 4.9a. XLD-PEEM images were recorded at specific values of I. The $I-V$ plot shows that the first resistive switching event occurs at the threshold current $I_{th} = 1.05$ mA. In Figure 4.9b we report a linecut of the XLD-PEEM image acquired at specific values of I; the image profile is taken along a line crossing the monoclinic domains in the middle of the device gap (see white solid line in Fig. 4.9, top panel). For large currents running through the device, the line profile in Fig. 4.9b displays a flat region, which indicates the melting of the monoclinic nanodomains due to the formation of the rhombohedral metallic channel. As highlighted by the grey area in Fig. 4.9b, the width d of the metallic filament increases with the current, from $d = 0.23 \pm 0.05$ µm at $I = 1.5$ mA to $d = 3.7 \pm 0.2$ µm at $I = 10$ mA.

Modelling the device as a circuit with two parallel resistors allows an estimation of d of the rhombohedral filament corresponding to the observed voltage drop (Fig. 4.10a). The metallic channel is described as a wire with resistance $R_M = \rho_M w/dt$, where ρ_M is the V_2O_3 resistivity of the high-temperature phase, w is the separation between the two electrodes, d is the width of the metallic filament formed after resistive switching and t is the vanadium oxide film thickness. The region of the device gap that remains in the monoclinic phase is assumed to have resistivity $\rho_I = R_I(l-d)t/w$, with R_I resistance measured from a two-point measurement at $T = 120$ K. The metallic filament width is estimated considering the instantaneous equivalent resistance R_{eq} - obtained from the $I-V$ curve in Fig. 4.9a and taking into account the estimated contact resistance of 200 Ω - and $\rho_M = 0.001$ Ω cm, which is the value for the high-temperature resistivity of V_2O_3 thin films (see Fig. 4.2a). The values obtained from the two resistors model are plotted in Figure 4.10a (green solid line) as a function of current I. The shaded area represents the range of the values estimated for d when ρ_M, t and l are varied by 10% to account for experimental uncertainty. For $I > I_{th}$, this simple model accounts for the filament width measured experimentally (red markers in Fig. 4.10a). In the proximity of the resistive switching, however, there is worse agreement between the values of d estimated from the model and the experimentally determined values. In particular, as highlighted in the plot in the inset, at I_{th} the two resistors model predicts the formation of a 200 ± 50 nm wide filament, which, despite being well above the experimental resolution of XLD-PEEM imaging, is not detected experimentally. Figure 4.10c-e display a detail of the XLD-PEEM

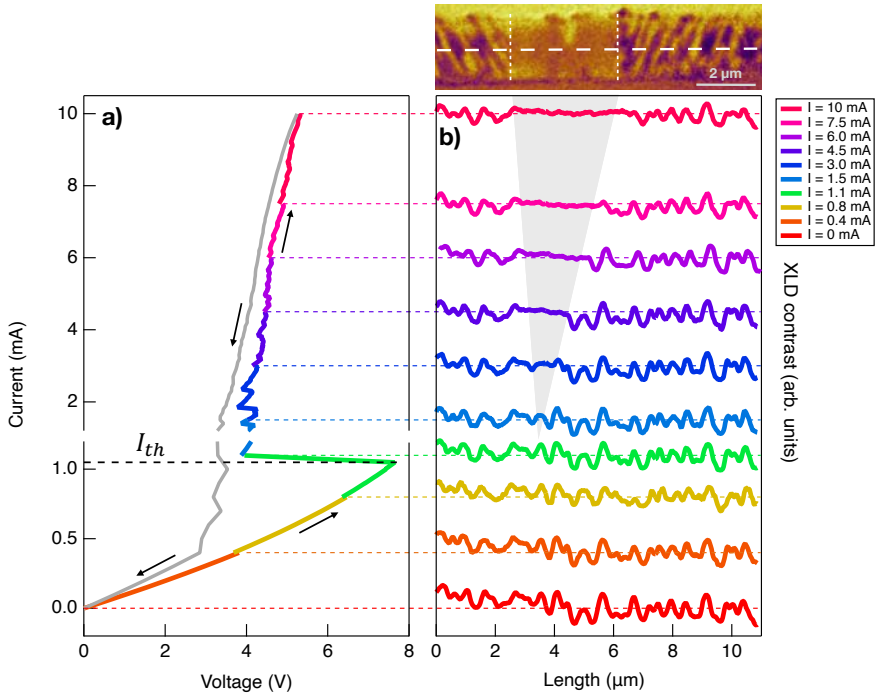

Figure 4.9: a) $I - V$ curve measured during the XLD-PEEM imaging. The sudden drop in the voltage measured at I_{th}=1.05 mA indicates the first resistive switch. b) Line profiles of the XLD-PEEM images in Fig. 4.5. The grey shaded area indicates the progressive widening of the metallic rhombohedral filament. The direction of the line profiles is shown by the white dashed line in the XLD-PEEM image on top, where we report a detail of Fig. 4.5j.

images in the region of the filament formation. In the first image acquired at $I > I_{th}$ (Fig. 4.10 d), namely at $I = 1.1$ mA which corresponds to the point in the $I - V$ curve at the base of the voltage drop, the nanodomains arrangement appears unchanged as compared to the configuration observed before switching (Fig. 4.10c). This is better highlighted from the comparison of the XLD-PEEM line profiles reported in fig. 4.10b. The XLD signal modulations obtained at $I = 0.4$ mA and $I = 1.1$ mA overlap very well, as opposed to the curves for $I \geq$1.5 mA that deviate from the before-switching ones in the 3.5 µm region where the metallic filament is formed.

To explain the discrepancy at I_{th}, one might suspect that a rhombohedral metallic filament forms below the surface of the V_2O_3 film, where it is not detected by PEEM which has a surface sensitivity limited to the first few nanometers. In fact, two arguments act against this possibility. i) The presence of the Cr_2O_3 buffer layer reduces the substrate-film lattice mismatch from 4.2% to 0.1%, thus almost entirely removing the residual epitaxial strain in

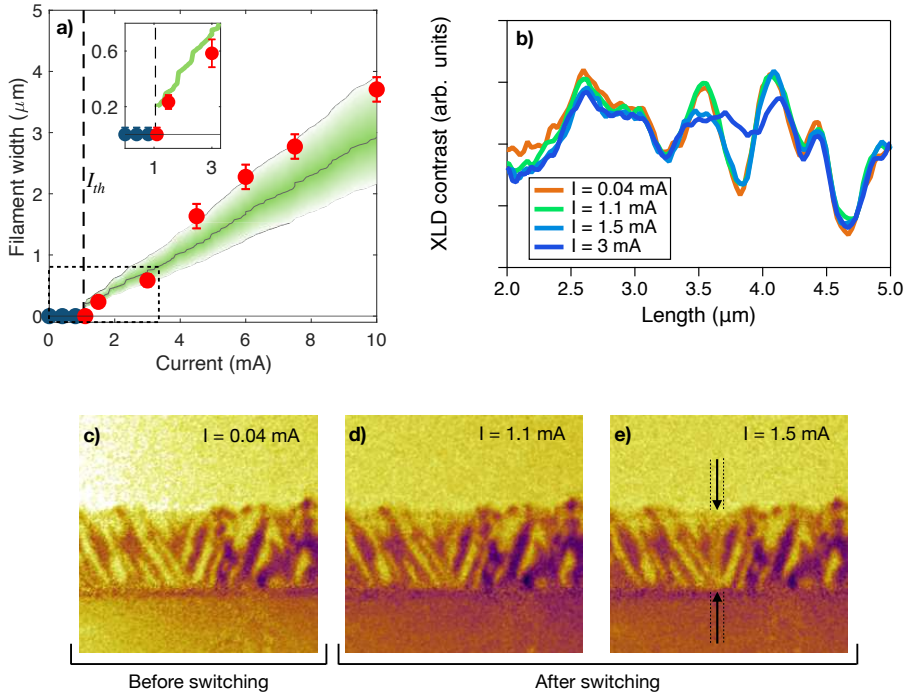

Figure 4.10: Details of the filament formation across the resistive switching threshold current, I_{th}. c) Width, d, of the metallic filament as a function of current. The blue/red markers represent the values of d obtained from the XLD-PEEM images below/above I_{th}. The green solid line shows an estimate of d, derived from a parallel resistors model predicting a sudden jump of d to 200 μm at I_{th}. The inset represents a zoom-in of the area highlighted by the black dashed rectangle. b) Line profiles of the XLD-PEEM images where the metallic filament forming at position ∼3.5 μm is detected by the flattening of XLD contrast. No variation is observed right after resistive switching, but only starting from $I = 1.5$ mA. c-e) XLD-PEEM images collected with applied currents lower (c) and higher (d-e) than 1.05 mA where resistive switching happens. No 200 nm wide metallic filament is observed immediately after the voltage drop (d).

the film [68], which is known to suppress the monoclinic phase and favour interfacial metallicity [68, 222]. In contrast to highly-strained films, in which the metal to insulator resistivity jump is strongly suppressed [222], the films in the present study display the 5-order of magnitude resistivity change typical of the unstrained metal-to-insulator transition. ii) The curl-free conditions force the interface between monoclinic and rhombohedral metallic regions to be oriented perpendicularly to the order parameter of the monoclinic domain. The formation of a sub-surface metallic layer would lead to a sharp ($\ll$ 20 nm) monoclinic-rhombohedral interface parallel to $\overrightarrow{\epsilon}$, thus leading to a dramatic increase of the strain energy of the system.

Our results are compatible with a complex scenario in which the topology-driven resistive switching likely occurs via the sudden transformation of a single 200 nm wide insulating monoclinic area into a metallic channel with a non-thermal monoclinic lattice structure. At a second stage, the Joule heating leads to a local temperature increase and, consequently, to the thermally driven monoclinic-to-rhombohedral structural transition and the formation of a rhombohedral metallic channel perpendicular to both the metallic electrodes and the $\hat{\epsilon}_2$ order parameter direction, as observed in Fig. 4.5.

4.7 Conclusions

The X-ray-based nanoimaging of a Mott device under operating conditions allowed us to simultaneously capture the formation of nanoscale conductive paths and the topology of the underlying symmetry-broken nanotexture. The present results expand our knowledge of the resistive switching process in Mott materials by demonstrating the leading role of inherent topological defects in initiating the avalanche process. The methodologies used in this work imply that nanoscale strain engineering approaches could unlock a gate to manipulating topological defects and controlling the electronic switching dynamics in real devices, such as Mott-transition-based RRAM [245, 302], Mott memristor [221, 320, 151] and artificial neurons [277, 330]. Fine tuning of crystal growth by adjustment of the substrate parameters [119, 124], manipulation of the geometry and orientation of metallic over-layers and use of nano-patterning approaches [196] represent possible viable routes to introduce topological defects in a controlled way via strain manipulation. The concept of topology-driven resistive switching will be key to assessing the possible non-thermal nature of the early stage electronic phase [236] as well as the microscopic origin of memory and non-volatile effects recently observed in Mott devices [62]. We note that the relation between topological defects and electronic phase transitions established here is a general concept, potentially extendable to other systems that undergo first-order phase transitions accompanied by a symmetry breaking, as described by the energy functional in Eq. 4.4. Relevant examples embrace transition-metal oxides [128, 281], such as vanadates, nickelates and manganites, and layered materials, such as $1T$-TaS_2 [296, 118, 160, 94], in which the IMT is accompanied

by charge-, lattice- and orbital-ordered states with reduced symmetry. Further platforms include cuprate superconductors [138] and kagome metals [10] in which light- or magnetic-induced discontinuous electronic transitions coexist with charge-order. Topological defects in the order parameter therefore provide a framework for understanding non-equilibrium electronic phase transitions, allowing all-optical control of hidden states of matter in a broad class of quantum materials [261, 328, 94, 300, 47, 297] .

Part II

Novel platforms for quantum simulation

CHAPTER 5

$CsPbBr_3$ artificial solids as a new platform to simulate collective phenomena in doped Mott insulators

This chapter has been adapted from the publication:

Halide Perovskite Artificial Solids as a New Platform to Simulate Collective Phenomena in Doped Mott Insulators, A. Milloch, U. Filippi, P. Franceschini, M. Galvani, S. Mor, S. Pagliara, G. Ferrini, F. Banfi, M. Capone, D. Baranov, L. Manna, and C. Giannetti, *Nano Letters*, 2023, 23, 10617 - 10624, doi: 10.1021/acs.nanolett.3c03715

The development of quantum simulators, artificial platforms where the predictions of many-body theories of strongly correlated materials materials can be tested in a controllable and tunable way, is one of the main challenges of condensed matter physics. The paradigm of quantum simulations [6, 52] has been pioneered by the development of ultracold-atom systems [21, 20, 50, 87] and extended to solid state via nano- and hetero-structured [6, 17, 30, 153] devices and, more recently, twisted bidimensional materials [33, 34, 38, 140]. An additional promising path consists in coupling a quantum material with the photons of a cavity [299, 114], which opens the possibility to optically drive and control the emergence of collective phenomena and long-range coherence. Intense efforts are currently dedicated to the development of photonics-based platforms aimed at replicating the many-body physics of quantum correlated materials. External optical control of the microscopic parameters entering the

relevant Hamiltonian, such as doping, hopping, and interaction strength, is key to tackle open problems relevant for solid state physics.

In this chapter we introduce macroscopic lattices constituted by lead halide perovskite nanocubes as a possible new photonics-based platform where to simulate the physics of strongly correlated systems. We first discuss the two phenomena suggesting lead halide perovskite nanocube superlattices as a potential quantum simulator, namely superradiance and the excitonic Mott transition, and introduce the theoretical framework that can be exploited to map the physics of strongly correlated materials onto the excitonic dynamics in halide perovskites. We then present broadband pump-probe measurements that demonstrate the suitability of lead halide perovskite artificial lattices as a novel photonics-based platform for quantum simulation. We show the possibility of spanning different quantum phases - namely, the excitonic Mott insulating phase, the superradiant collective state, and the metallic electron-hole liquid phase - on the same artificial solid system by continuously tuning the light excitation intensity. The results indicate the suitability of this system for mapping the physics of strongly correlated materials, specifically of Mott insulators where cooperative effects such as superconductivity and charge ordering processes are observed for temperature and doping regimes close to the IMT.

5.1 Halide perovskite nanocube superlattices for quantum simulation

Lead halide perovskites (chemical structure $APbX_3$) are semiconducting materials that are attracting considerable attention thanks to their many appealing electronic properties - such as strong excitonic resonances, tunable band gap, strong absorption and emission features in the visible range, high photoluminescence quantum yield - that make them promising materials for optoelectronic applications [90, 104, 115]. In these compounds, the anion X can be Cl^-, Br^- or I^-, whereas the cation A can be either inorganic (e.g. Cs^+) or organic (methylammonium $CH_3NH_3^+$, MA, or $HC(NH_2)_2^+$ formamidinium, FA). Tunability of the optical properties can be achieved not only by chemical composition, but also by quantum confinement that is possible through the synthesis of nanometric cubes (NCs) with edge size L comparable to the exciton Bohr radius [250, 65, 225]. The synthesis of halide perovskite nanocubes [250] has recently encountered significant advance that have enabled unprecedented control of the emission properties [117, 136, 229], making lead halide perovskites ideal materials for a wide variety of applications ranging from optoelectronics to photovoltaics [265, 229]. These quantum dots can further self-organize into highly ordered three-dimensional superlattices (see sketch in Fig. 5.1a), thus creating large-scale artificial solids - with the nanocube acting as the fundamental unit cell - whose properties, such as superlattice parameter Λ, hopping, exciton energies and symmetry of the unit cell, can be tuned by chemical means [27, 49].

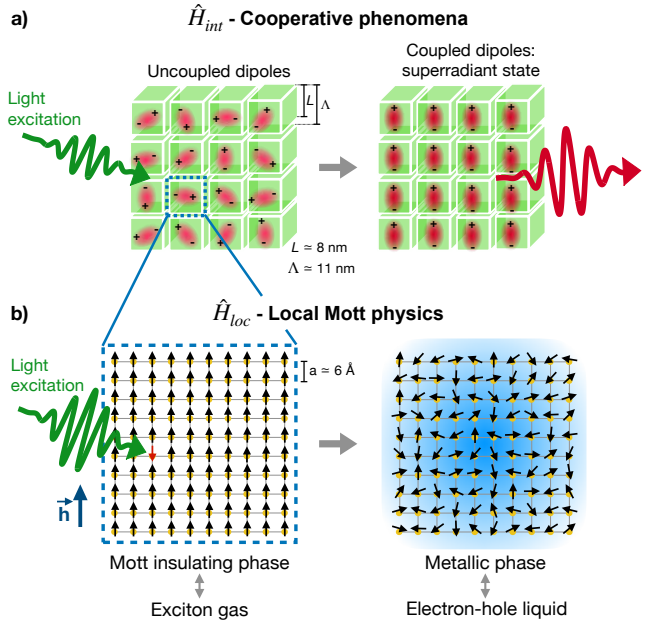

Figure 5.1: Cartoon describing how perovskite quantum dot artificial solids can be harnessed to simulate cooperative phases in the vicinity of the Mott insulator-to-metal transition. a) Cooperative effects - such as superradiance - emerge from long-range interactions $\hat{H}_{int}$ when coupled via an external light field. b) Local interactions $\hat{H}_{loc}$ govern the photo-induced transition from an exciton gas and an electron-hole liquid in a semiconductor, realizing a Mott transition that can be fully mapped onto a repulsive Hubbard model in a magnetic field h.

Each individual nanocube can host quantum confined excitons [225, 248], whose density can be controlled by tuning the light excitation.

The use of this platform to simulate the many-body problems that characterize quantum correlated materials, such as transition metal oxides, is based on the possibility of simultaneously controlling short-range correlations, which determine the Mott insulating ground state, and long-range interactions, which are responsible for the emergence of collective phases such as superconductivity or charge-density waves. To this purpose, we introduce the total Hamiltonian:

$$\hat{H}_{tot} = \hat{H}_{loc} + \hat{H}_{int} \tag{5.1}$$

where $\hat{H}_{loc}$ describes the local interactions within each single nanocube and is defined on the perovskite cubic lattice with periodicity a, whereas $\hat{H}_{int}$ describes the inter-unit cell interactions and is defined on the superlattice with periodicity $\Lambda > a$.

In the following sections (Sec. 5.1.1 and 5.1.2), we discuss how the local excitonic physics within each nanocube, captured by $\hat{H}_{loc}$, allows to artificially

implement the Hubbard model, while the long-range interactions among excitons in different nanocubes, described by $\hat{H}_{int}$, drive the emergence of collective phase-coherent states. So far, the emergence of long-range orders from incoherent fluctuations controlled by $\hat{H}_{int}$ and the Mott transition described by $\hat{H}_{loc}$ have been addressed separately in different materials. The lack of a single platform combining the two physics has been the main obstacle for the development of artificial simulators for real materials. By simultaneously realizing $\hat{H}_{int}$ and $\hat{H}_{loc}$, halide perovskite superlattices fill this gap, therefore offering a new, low-cost and high-temperature alternative to state-of-the-art quantum simulators based on cold-atoms trapped into optical lattices [132, 105, 108, 11, 78, 77, 256, 184].

5.1.1 Long-range interactions: $\hat{H}_{int}$

The first element to realize $\hat{H}_{tot}$ is given by the transverse electromagnetic field that drives the long-range interaction among excitons in different quantum dots, which can be expressed by [190, 187]:

$$\hat{H}_{int} \propto (a + a^{\dagger}) \sum_{\boldsymbol{K}_{\Lambda}} g_{\boldsymbol{K}_{\Lambda}} [d^{\dagger}_{\boldsymbol{K}_{\Lambda} c} d_{\boldsymbol{K}_{\Lambda} v} + d^{\dagger}_{\boldsymbol{K}_{\Lambda} v} d_{\boldsymbol{K}_{\Lambda} c}] \tag{5.2}$$

where $g_{\boldsymbol{K}_{\Lambda}}$ is the dipole transition element; $\boldsymbol{K}_{\Lambda}$ is a wavevector in the first Brillouin zone of the superlattice with periodicity Λ; $d^{\dagger}_{\boldsymbol{K}_{\Lambda} v}$ and $d^{\dagger}_{\boldsymbol{K}_{\Lambda} c}$ ($d_{\boldsymbol{K}_{\boldsymbol{\Lambda}} v}$ and $d_{\boldsymbol{K}_{\Lambda} c}$) are the creation (annihilation) operators for an electron with momentum $\boldsymbol{K}_{\Lambda}$ in the valence and conduction band, respectively. The terms a and $a^{\dagger}$ denote the bosonic creation and annihilation operators for the photon field. The $\hat{H}_{int}$ term is responsible for a rich family of collective phenomena, broadly indicated as superradiant [56]. As sketched in the cartoon in Figure 5.1a, superradiance occurs when the electromagnetic-field-driven interaction leads to the phase-coherence of N quantum emitters. A typical manifestation is the collective emission of radiation (superfluorescence), which is both enhanced and faster than the emission from individual nanocubes, with the radiative rate scaling as N^2 for large N [56, 66]. Groundbreaking photoluminescence (PL) experiments recently reported evidence of superfluorescence effects in halide perovskites [232, 81, 216, 148, 49, 332, 18]. Figure 5.2 reports the main manifestations of this collective phenomenon:

(i) the superlinear dependence of the emission amplitude with respect to the intensity of the exciting external field (see Fig. 5.2a) [232, 81, 148, 49];

(ii) the emergence of a narrow red-shifted peak in the PL spectrum (see Fig. 5.2b), which is assigned to the cooperative emission from a sub-population of nanocubes within a single superlattice [232, 81, 148, 49, 216].

These cooperative effects are suppressed at high temperature in nanocube superlattices due to thermal noise that undermines quantum coherence [187, 216].

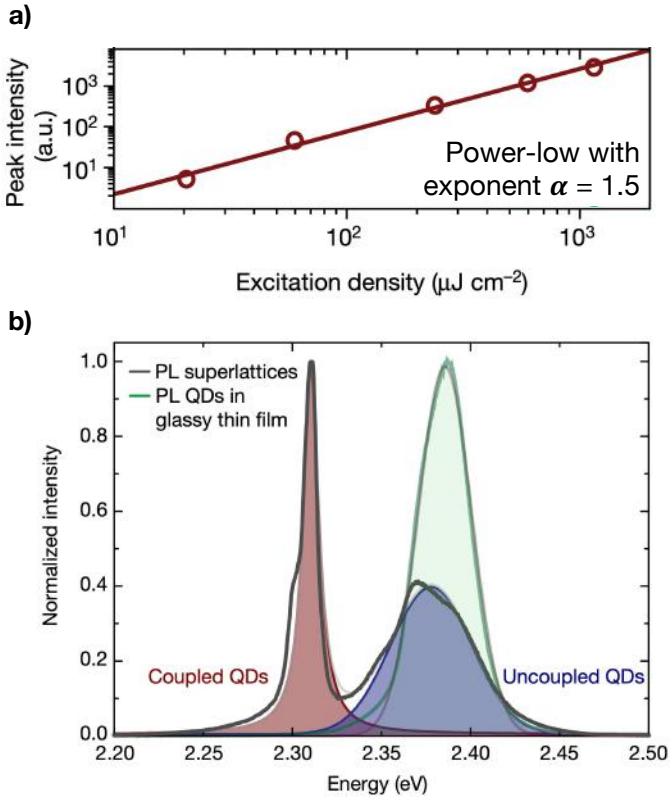

Figure 5.2: First experimental evidences of superfluoresces in lead halide perosvkite superlattices reported in Ref. 232. a) Superlinear behavior of the excitation-intensity-dependent PL emission assigned to superfluorescence in $CsPbBr_3$ nanocube superlattices. b) Photoluminescence spectrum of a $CsPbBr_3$ nanocube assemblies measured at 6 K. The high energy peak observed in both glassy nanocube films (green area) and superlattices (blue area) is assigned to the emission from uncoupled nanocubes. Nanocube supelattices display also an additional narrow and red-shifted peak (red area) originating from the cooperative emission. Adapted from Ref. 232.

The emergence of collective states driven by $\hat{H}_{int}$ mimics the onset of long-range phases, such as superconductivity and charge-density waves, that ubiquitously pervade the phase diagram of doped Mott insulators [128, 138, 281, 139], therefore representing a key element for the employment of lead halide perivskite superlattices as quantum simulators.

5.1.2 Short-range interactions: $\hat{H}_{loc}$

The second element necessary to reproduce the physics of correlated materials is described by $\hat{H}_{loc}$. It is well known that short-range electronic interactions can give rise to a transition from an exciton gas (EG) to a liquid of weakly interacting electrons and holes (EHL), achieved when a very large number of excitons is photo-injected in bulk and low-dimensional semiconductors [213, 48, 16, 247, 323].

This transition is believed to almost perfectly realize the insulator-to-metal Mott transition, i.e. a transition driven by the weakening of the electronic interactions without any symmetry breaking. It has been demonstrated [29, 107] that the Hamiltonian describing the EG→EHL transition in photoexcited semiconductors has a one-to-one correspondence with the repulsive Hubbard model ($\hat{H}_U$) in a magnetic field, in which the electron spins play the role of the electron-hole excitations. This mapping can be directly argued starting from the Hamiltonian describing an ensemble of symmetric spinless holes (created by $h^\dagger_{\mathbf{k}}$) and electrons (created by $e^\dagger_{\mathbf{k}}$) at momentum $\mathbf{k}$, with energy $\epsilon_{\mathbf{k}}$ and subject to a short-range electron-hole Coulomb attraction $-U$:

$$\hat{H}_{loc} = \sum_{\mathbf{k}} \epsilon_{\mathbf{k}} (h^\dagger_{\mathbf{k}} h_{\mathbf{k}} + e^\dagger_{\mathbf{k}} e_{\mathbf{k}}) - U \sum_i n_{ei} n_{hi} - \mu \sum_i (n_{ei} + n_{hi}) \qquad (5.3)$$

where the short-range Coulomb attraction -U is considered as momentum independent, $n_{e(h)i}$ represents the density of electrons(holes) at site i and μ is the chemical potential, which fixes the number of excited electron-hole pairs n_{eh}=$\langle n_{ei} \rangle$=$\langle n_{hi} \rangle$.

By applying the transformations $e_i \rightarrow c_{i\downarrow}$ and $h_i \rightarrow (-1)^i c^\dagger_{i\uparrow}$, the Hamiltonian in Eq. 5.3 can be mapped into the Hamiltonian [107]:

$$\hat{H}_{loc} = \hat{H}_U - h \sum_i (n_{i\uparrow} - n_{i\downarrow}) \qquad (5.4)$$

where $\hat{H}_U$ is a repulsive Hubbard model:

$$\hat{H}_U = -t \sum_{\langle ij \rangle \sigma} (c^\dagger_{i\sigma} c_{j\sigma} + c^\dagger_{j\sigma} c_{i\sigma}) + U \sum_i n_{i\uparrow} n_{i\downarrow} \qquad (5.5)$$

t being the hopping parameter, $n_{i\sigma}$ is the occupation number at site i of electrons with spin $\uparrow$ and $\downarrow$; $c^\dagger_{i\sigma}$ and $c_{i\sigma}$ are creation and annihilation operators for an electron of spin σ at site i. In this case, n_{eh} is mapped into the number of flipped spins with respect to the ferromagnetic background, i.e. n_{eh}=$\sum_i \langle n_{i\downarrow} \rangle / N$ (N being the total number of particles). The exciton density is therefore controlled by the Lagrange multiplier h, which acts as an auxiliary magnetic field inducing the effective magnetization m=1-2n_{eh}. As sketched in Fig. 5.1b, for large h, the auxiliary repulsive model is fully polarized (m=1), which corresponds to the absence of excitons in the original model (Eq. 5.3). The sudden reduction of h,

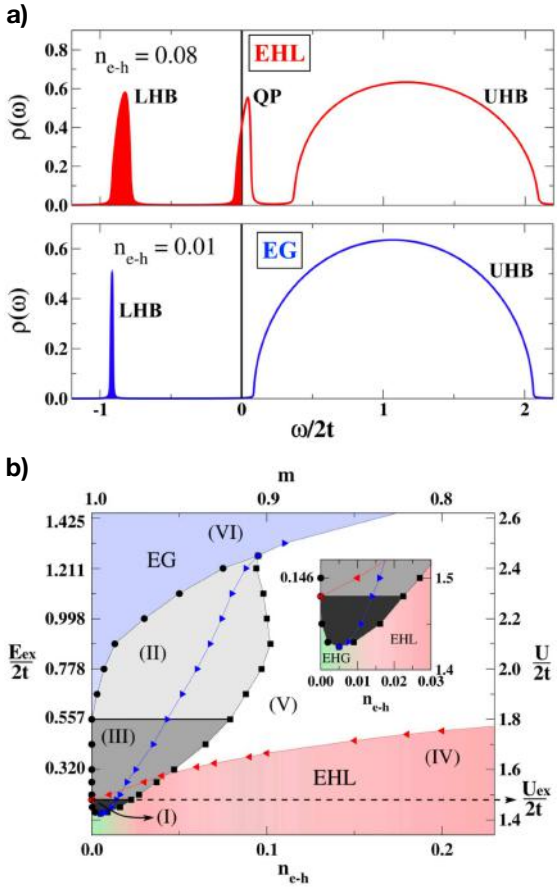

Figure 5.3: a) Density of states for the Hamiltonian $\hat{H}_{loc}$ with $U/2t = 2.2$. For $n_{\rm eh} = 0.01$ the system is in an insulating state (EG), wheres at $n_{\rm eh} = 0.08$ the appearance of a quasiparticle peak at the chemical potential indicates the transition to a metallic behavior (EHL). In the corresponding photoexcited semiconductor problem, the LHB corresponds to the exciton and the UHB to the conduction band, which are separated by the exciton binding energy E_{ex}. b) Phase diagram of $\hat{H}_{loc}$ as a function of of $n_{\rm eh}$ and E_{ex}, or, equivalently, of magnetization m and U. The system is in the exciton gas phase (EG) in region VI (blue area) and in the electron-hole-liquid phase (EHL) in region IV (red area). The white and gray areas represent intermediate phases characterized by EG-EHL phase separation. Adapted from Ref. 107.

which injects a finite numbers of spin excitations (m <1), mimics the sudden photoinjection of excitons (n_{eh} >0).

Figure 5.3a shows the density of states for a systems described by Eq. 5.4, or equivalently by Eq. 5.3, for $U/2t$=2.2 and two different values of n_{eh}. For low exciton densities (bottom panel), two Hubbard bands are visible, corresponding to the exciton state (lower Hubbard band, LHB, in the language of the Hubbard model) and to the electron conduction band (upper Hubbard band, UHB). As n_{eh} is increased, a metallic phase, characterized by a quasiparticle peak emerging at the chemical potential (top panel), is established. The phase diagram is shown in Fig. 5.3b as a function of n_{eh} and the exciton binding energy E_{ex}, corresponding to, respectively, the magnetization m and the interaction U in the Hubbard description. It includes exciton gas phase (at low n_{eh} and large U, blue area), electron-hole-liquid phase (red area) and EHL-EG phase separation regions (gray and white areas). It also shows that the region of the phase diagram in which U is of the order of the bandwidth $4t$ is characterized by the boundary between Mott insulating and metallic phases, therefore representing the most relevant region of the phase diagram for real transition metal oxides. In the effective description of Eq. 5.4, the Hubbard Hamiltonian $\hat{H}_U$ is in fact identical to that capturing the insulator-to-metal Mott transition in transition metal oxides [95, 128] and the insulating ground state of cuprate parent compounds [159].

5.2 Time-resolved optical spectroscopy of CsPbBr$_3$ nanocube superlattices

The physics generated by the Hamiltonian $\hat{H}_{tot}$ introduced in the previous section is here investigated by broadband transient reflectivity measurements (1D pump-probe spectroscopy). We performed experiments on artificial lattices constituted by CsPbBr$_3$ nanocubes with edge size $L = 8$ nm (Bohr exciton diameter ∼7 nm [225]), arranged in cubic superlattices of periodicity $\Lambda = L + l = 11$ nm, where l is the thickness of the ligand layer in between two neighboring NCs. The size of each superlattice is of the order of a few micrometers (1-10 µm). Ultrashort light pulses are used to impulsively inject optical excitons, whose density is controlled by the light intensity. The broadband probe (2.1-2.5 eV photon energy) measures the femto/picosecond time evolution of the optical properties following the impulsive excitation. In particular, we employ a resonant pumping scheme in which the pump photon energy (≃2.41 eV) is tuned to the exciton energy, thus limiting the direct generation of free carriers in the conduction band. The details of the setup employed for the present experiment are reported in Section 2.5.1 (SetUp2).

Figures 5.4a and b display the typical data collected from pump-probe experiments on two types of CsPbBr$_3$ samples: disordered NCs and NC superlattices (SLs), respectively. Samples preparation and characterization

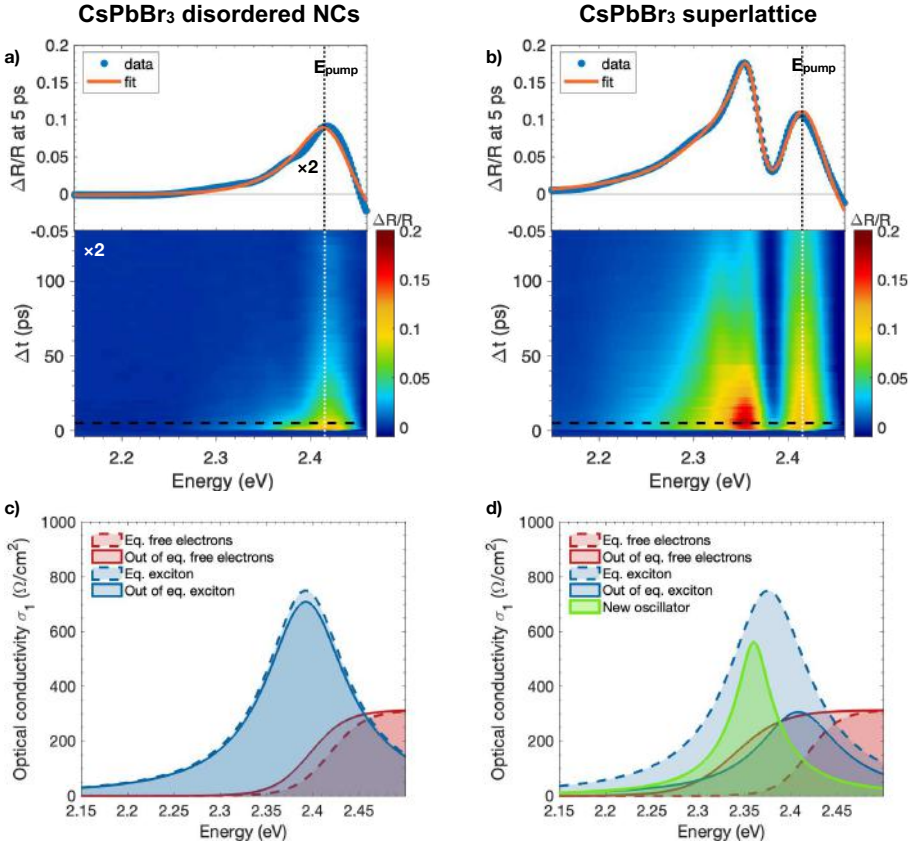

Figure 5.4: Ultrafast transient reflectivity of $CsPbBr_3$ disordered NCs sample (left panels) and NC superlattice sample (right panels), measured at 17 K, 230 μJ/cm^2 excitation fluence and pump photon energy resonant with the excitonic line, i.e. $E_{pump} = 2.41$ eV. The bottom a) and b) panels report the two-dimensional pump-probe maps displaying the $\Delta R/R$ signal (see color scale on the right) as a function of the delay (Δt) and probe photon energy. The top a) and b) panels report the $\Delta R/R$ signal (blue dots) as a function of the probe photon energy at fixed delay time, Δt=5 ps (horizontal dashed line in the color maps). The orange solid lines represent the differential fit to the data. c) and d): optical conductivity (σ_1) at equilibrium (dashed lines) and out of equilibrium at Δt=5 ps (solid lines) obtained from experimental absorbance and fit of $\Delta R/R$ spectra. The colors represent the different contributions to the total optical conductivity: i) main excitonic line (blue); ii) across gap optical transitions (red) and the photo-induced peak emerging at low temperature in ordered NC superlattices (green).

are presented in Appendix B.1. The samples are cooled down to 17 K and are excited by 230 µJ/cm^2 fluence pulses. The bottom panels show the reflectivity variation $\Delta R/R$ induced by the pump pulse, as a function of pump-probe time delay (Δt) and probe photon energy. The top panels report a horizontal cut of the data, representing the spectrally resolved reflectivity variation of the system 5 ps after the pump excitation. For the disordered sample (see Fig. 5.4a), the signal is characterized by a positive reflectivity variation of the order of 5% centered at 2.41 eV. The same experiment performed on NC superlattices (see Fig. 5.4b) displays a larger signal amplitude, with a similar spectral response around 2.41 eV and, additionally, a more structured spectral response extending down to $\simeq$2.20 eV probe energy.
The origin of these structures in the $\Delta R/R$ signal is assessed by performing a differential fit, which consists in modifying the parameters of the model describing the equilibrium optical properties that are responsible for the observed reflectivity variation. The starting point is the equilibrium optical conductivity that is obtained from a Kramers-Krönig constrained model matching the experimental absorbance of the samples and the temperature dependent trends reported in literature (see model of the equilibrium optical properties in Sec. C.1, Appendix C). In the 2-2.5 eV energy range, the model is dominated by the conduction band edge absorption (red dashed line in Fig. 5.4c) and the exciton peak (blue dashed line), modelled through a Drude-Lorentz oscillator. The outcome of the differential fitting procedure is depicted in Figures 5.4c and d, where the solid lines represent the out of equilibrium components of the optical conductivity σ_1 necessary to fit the experimental $\Delta R/R$ signal (see orange solid lines in the top panels of Fig. 5.4a,b). In order not to weigh down the text, the fitting procedure is detailed in Appendix C, where all output parameters are reported and the robustness of the fitting procedure is discussed; here we summarize its output and analyze the results.

In order to reproduce the measured spectral response of $CsPbBr_3$, for both samples it is necessary to assume:

(i) a decrease of the excitonic spectral weight and a concomitant blueshift of the exciton energy;

(ii) an increase of in-gap free-electron states accounted for by a red-shift of the semiconducting band gap.

In addition to the (i) and (ii) contributions observed in both samples, the low-energy feature observed in the 2.2-2.4 eV energy range solely for NC superlattices (see Fig. 5.4b) requires an additional narrow structure (iii) that we model through a new oscillator (green line in Fig. 5.4d) appearing in the out of equilibrium optical conductivity.

In the next sections we will discuss separately the different contributions to the out-of-equilibrium reflectivity. Specifically, in Sec. 5.3 we will show that the new spectral feature (iii) scales superlinearly with the excitation intensity,

and disappears at ≃200 K and in disordered samples, thus emerging as the signature of a cooperative superradiant dynamics driven by the coupling with the electromagnetic field as described by $\hat{H}_{int}$. In Sec. 5.4 we will demonstrate that the photo-induced increase of the spectral weight of in-gap free electrons states (ii) indicates the transition from an insulating excitonic Mott phase to an electron-hole liquid phase, thus realizing the excitonic Mott transition described by $\hat{H}_{loc}$. In Sec. 5.5 we will combine the different time and fluence-dependent results to trace a trajectory in the phase diagram of $\hat{H}_{tot}$=$\hat{H}_{int}$ + $\hat{H}_{loc}$ and demonstrate that the parameters spanned by time-resolved experiments are relevant for strongly correlated materials.

5.3 $\hat{H}_{int}$ and cooperative superradiant effects

As introduced in Sec. 5.1.1, the dipole-dipole long-range interactions among excitons occupying different NC, as described by $\hat{H}_{int}$, can lead, under proper density conditions, to the formation of a collective superradiant state. This state is generally characterized by a novel red-shifted emission line that scales superlinearly with the excitation fluence [232, 81, 148, 49]. In the following we will report evidence of superradiance in the time-resolved optical spectra obtained by broadband transient reflectivity.

Figure 5.5 reports the details of the photo-induced changes in the excitonic resonance observed for NC superlattices at 5 ps delay time. The grey and black lines represent the exciton contribution to the equilibrium and out of equilibrium optical conductivity, respectively, as obtained from the fit described above (Sec. 5.2) and in Appendix C. After the interaction with the excitation light pulse, we observe a ≃60% spectral weight decrease of the excitonic peak, whose out of equilibrium optical conductivity is shown by the blue filled area in Fig. 5.5, along with the appearance of a new resonance, represented by the green area and highlighted by the black arrow. The linewidth of the new peak is ≃ 40 meV, to be compared to 100 meV width of the main excitonic line. This second component is centered at 2.36 eV, corresponding to a red-shift δ with respect to the instantaneous position of the main excitonic resonance. By comparing results obtained on 9 different NC superlattice samples with the same nominal characteristics, we obtain a value of δ that varies between 40 and 80 meV. The estimated δ allows us to exclude multi-excitons effects, which would cause smaller (10-30 meV) red-shifts in similar systems, [233, 88, 8, 276] and would appear also in disordered NCs. Sample to sample variability manifests also in the fine structure of the $\Delta R/R$ signal for $\hbar\omega < 2.37$ eV. As discussed in Appendix C, in some samples two distinguished structures (e.g. see data in Fig. 5.4b at long Δt) are visible particularly for long delays. The presence of these multiple fine structures, which share the same origin and characteristics, is related to local inhomogeneity in the NCs and superlattice sizes. Samples of various aging have been measured and always show a similar response, with variability smaller than that observed from different points on the same sample.

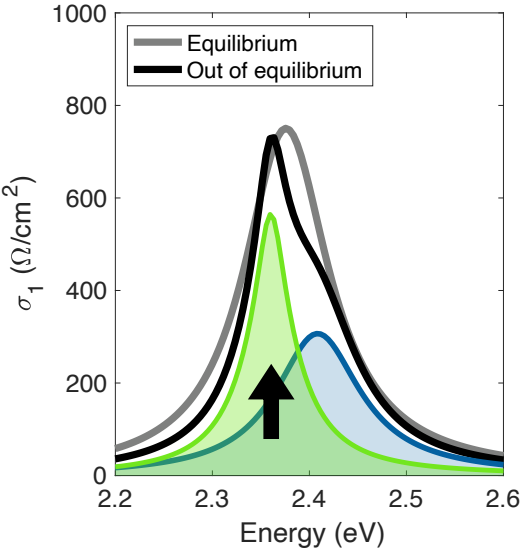

Figure 5.5: Equilibrium (gray line) and out of equilibrium (black line) excitonic resonance in CsPbBr$_3$ superlattices obtained from differential fit of pump-probe signal at 5 ps delay time. After pump excitation two components are distinguished: the main perovskite exciton (blue area), which undergoes a pronounced decrease of spectral weight, and the additional oscillator (green area) associated to cooperative photo-induced effects.

The narrow additional peak emerging in the transient reflectivity properties is visible for both high excitation fluence (230 µJ/cm^2, Figure 5.4b,d) and low pump intensity (see Fig. C.5, in Appendix C, corresponding to 30 µJ/cm^2 pump fluence) and features characteristics very similar to the superfluorescence recently observed in perovskite superlattices by means of low-temperature photoluminescence [232, 81]. In order to unambiguously address the cooperative origin of this emergent spectral feature, we performed a detailed fluence dependence study. In Figure 5.6 we plot the $\Delta R/R$ signal at a fixed time delay (50 ps) as a function of the excitation intensity and integrated over selected spectral regions of interest, which are highlighted by the filled areas in the inset. The top x-axis in Figure 5.6 reports the excitation intensity expressed as the mean number of excitons in each NC, $\langle N \rangle$ (estimated as described in Section C.3). The signal amplitude tends to saturate when $\langle N \rangle \gg 1$, in accordance with what is reported in literature for similar systems [8, 102, 144]. This behavior can be well described, as reported in Ref. 144, by an empirical function of the form $a\langle N \rangle^\alpha / (b + \langle N \rangle^\alpha)$, which accounts for both a low-fluence power-law increase and the high-fluence saturation. If we consider the integrated signal for $\hbar\omega > 2.37$ eV, i.e. far from the photoinduced additional peak, we obtain $\alpha = (0.91 \pm 0.07)$, which corresponds to a linear behaviour at low fluence. In contrast, the spectral region corresponding to the additional photo-induced peak ($\hbar\omega < 2.37$ eV) features a

clearly superlinear fluence dependence, corresponding to $\alpha = (1.43 \pm 0.05)$, in agreement with what expected for superradiant phenomena [232, 18, 49, 148]. It is useful to compare the present results with those obtained on disordered NCs, in which collective superradiant phenomena should be quenched [185, 184, 256] due to disorder-driven dephasing. As reported in Fig. 5.6 (green dots and lines), the fluence-dependence of the signal is always linear, independent of the energy region considered. We note that the fluence dependent signals shown in Fig. 5.6 collapse to the same curve above a fluence of approximately 150-200 $\mu J/cm^2$. This threshold value, which we will indicate as F^t in the following, indicates that the observed cooperative effect is sustained only for moderate densities of excitons, as it will be discussed in more detail in the next sections.

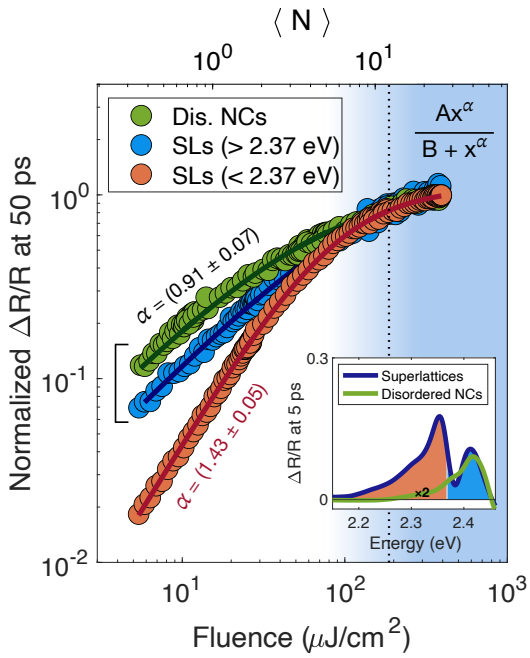

Figure 5.6: Normalized amplitude of $\Delta R/R$ signal at 50 ps delay time as function of excitation intensity, represented by pump fluence on the bottom axis and mean number of excitons per NC, $\langle N \rangle$, on the top axis. For NC superlattice samples (SLs in legend), the data are collected by integrating the signal in the spectral region below and above 2.37 eV, as highlighted by the coloured areas in the inset (orange and blue respectively). In the top right corner we display the fitting function, where x represents both fluence and $\langle N \rangle$. The dotted vertical line represents the excitation density threshold for the Mott transition, as determined from the temporal dynamics discussed in Sec. 5.4.

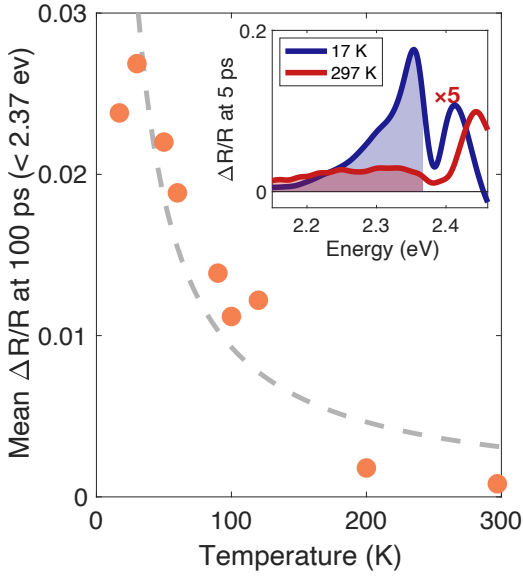

Figure 5.7: Temperature dependence of $\Delta R/R$ at 100 ps delay time, integrated in the spectral region highlighted in the inset ($\hbar\omega < 2.37$ eV). Dashed gray line: guide to the eye showing the typical T^{-1} dependence of coherence phenomena.

The cooperative origin of the photo-induced structure at 2.36 eV observed on the ordered NC superlattices is further corroborated by the temperature dependence data reported in Fig. 5.7. The top-right panel shows the transient reflectivity spectra 5 ps after pump excitation at 17 K (blue) and 300 K (red), the latter being multiplied by a normalization factor for comparison purposes. At room temperature, the reflectivity variation corresponding to the spectral feature at 2.36 eV is considerably reduced. In the main graph we report the $\Delta R/R$ signal at 100 ps, integrated in the 2.15-2.37 eV energy region as a function of temperature T. The suppression of the photo-induced peak at temperatures as high as 200 K is compatible with the thermally driven loss of coherence of superradiant emitters [187]. The comparison to a T^{-1} guide to the eye (gray dashed line in Fig. 5.7) indicates a fair agreement with the scaling behavior of the superradiance enhancement factor, that reduces to 1 in the high temperature limit according to a T^{-1} power law [187].

Lastly, we note that, in the same spectral range (2.30-2.37 eV), intense fluorescence induced by the pump beam is observed under the form of stray light emitted by NC superlattices and arriving at the detector. This fluorescence is suppressed by ∼70% in the disordered NCs, thus further demonstrating that the superlattice is the key element for achieving the collective superradiant regime described by the inter-unit cell hamiltonian $\hat{H}_{int}$.

5.4 $\hat{H}_{loc}$ and the excitonic Mott transition

As argued in Sec. 5.1.2, the local interactions among excitons living in the same NC can be described by the Hamiltonian $\hat{H}_{loc}$=$\hat{H}_U - h\sum_i(n_{i\uparrow} - n_{i\downarrow})$, where $\hat{H}_U$ is the popular repulsive Hubbard model. As discussed in Ref. 107, the parameters controlling the ground state of $\hat{H}_{loc}$ are the repulsive Coulomb interaction U and the effective magnetization m=1-2$n_{\rm eh}$. For large values of U and m, the magnetized Hubbard model is characterized by insulating solutions constituted by localized spins that are frozen by the electronic repulsion. When either m or U decrease, the system undergoes a transition towards a metallic state in which the spins are delocalized and can hop throughout the lattice. Interestingly, in a large parameter phase space the transition is of first order nature and it is therefore characterized by real space coexistence of insulating and metallic solutions with different spin densities [107]. In terms of the excitonic problem, the insulating phase of the magnetized Hubbard models maps the existence of well defined localized excitonic states (lower Hubbard band), separated from the upper Hubband band by an energy amount E_b (see Fig. 5.8a), which depends on the value of U [107]. When the excitonic density $n_{\rm eh}$ overcomes a critical value of the order of 1-10%, the emergence of metallic states, corresponding to a liquid of delocalized electrons and holes, manifests itself in the appearance of new in-gap states at the expenses of the excitonic states (see Fig. 5.8a).

The excitonic Mott transition from EG to EHL can be therefore detected by measuring the photo-induced increase of free electron states with energy between the excitonic resonance and the gap edge. This physics can be experimentally accessed in the saturation region (see Fig. 5.6) at excitation intensities of the order of $\sim$200 μJ/cm^2. As shown in Sec. 5.2, in this regime the transient optical response of NC superlattices is dominated by a decrease of the excitonic spectral weight, and the corresponding increase of in-gap free electrons states, as indicated by the effective red-shift of the semiconducting gap (see Figs. 5.4d and 5.8b). Interestingly, this kind of response, surviving on a $\sim$ 100 ps timescale, is remarkably different from what usually reported for above-resonance excitation experiments in similar materials, where the large number of free carriers injected in the conduction band leads to a very fast band-gap renormalization followed by a band filling effect after $\sim$ 1 ps [8, 83, 224]. The transient increase of in-gap states at the expenses of the intensity of the exciton peak demonstrates that, at high fluence, the NC superlattices no longer support well defined excitons but rather delocalized electron-hole excitations.

To assess the nature of this high-excitation regime, we calculated from the differential model (see Appendix C) the total spectral weight:

$$SW_{tot} = \int_0^{+\infty} \sigma_{1,tot}(\omega) d\omega \tag{5.6}$$

which is, by definition, a conserved quantity depending on the total number

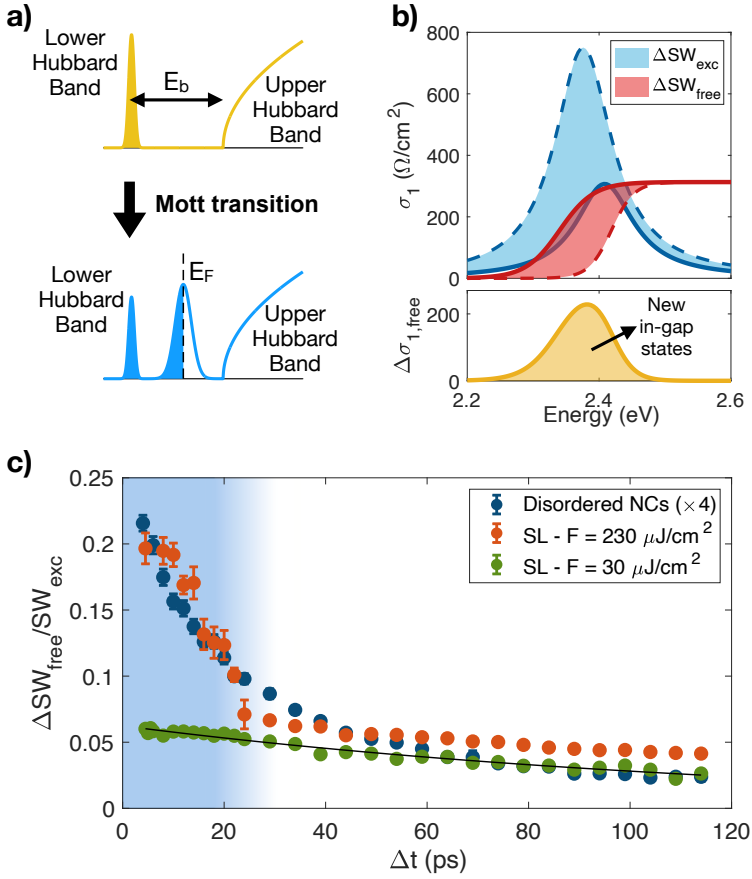

Figure 5.8: a) Sketch of the Mott transition from an insulator to a metal where new metallic states appear at the Fermi level. b) Top panel: plot of the equilibrium (dashed lines) and out of equilibrium (solid lines) optical conductivity obtained from fitting the experimental data at $\Delta t = 5$ ps. The blue filled area represents the excitonic spectral weight decrease, which is counterbalanced by the appearance of new states below the conduction band minimum, described by a red-shift of the band edge (red filled area). Bottom panel: difference between out of equilibrium and equilibrium $\sigma_{1,free}$, which represents the contribution from the conduction band states to the optical conductivity. c) Time evolution of the spectral weight transfer from the exciton state to free carrier states, estimated as $\Delta SW_{free}/SW_{exc}$. The black line denotes an exponentially decaying function fitted to the data. The blue area highlights the region where an excess of ΔSW_{free} is observed for large excitation fluence.

of electrons in the system [308]. In particular, we obtained from the data the different contributions:

$$SW_{tot} = SW_{2.36eV} + SW_{exc} + SW_{free} \tag{5.7}$$

where $SW_{2.36eV}$ is the spectral weight of the photo-induced cooperative peak at 2.36 eV, SW_{exc} is the spectral weight of the excitonic peak already present in the equilibrium optical conductivity, and SW_{free} is the spectral weight associated to the direct across-gap transitions. The analysis indicates that the photo-induced decrease of the excitonic spectral weight ($\Delta SW_{exc} \simeq$ -74 ΩeV/cm^2 at Δt = 5 ps) is perfectly compensated by both the new peak at 2.36 eV ($\Delta SW_{2.36eV} \simeq 49$ ΩeV/cm^2) and by an increase of in-gap free electron states ($\Delta SW_{free} \simeq 25$ ΩeV/cm^2). Normalization to the total spectral weight of the excitonic peak returns $\Delta SW_{free}/SW_{exc} \simeq 0.2$, indicating that approximately 20% of the initial exciton SW is transferred into in-gap free electrons states. We note that, in the saturation regime, the number of excitons for each single nanocube is of the order of $\langle N \rangle$=20 (see Fig. 5.6), which corresponds to a photodoping $n_{\rm eh}$ ∼1% (see Sec. C.3). This value cannot account for the observed spectral weight change, unless we assume a transformation of the electronic band structure of the system. The spectral weight transfer from excitonic states to free-electron ones can be therefore considered as the direct manifestation of the excitonic Mott transition [107], as captured by $\hat{H}_{loc}$.

The time-resolved dynamics contains important information about the temporal evolution of the newly created metallic states and the recovery of the initial excitonic gas. Since during the relaxation $n_{\rm eh}$ decreases due to the slow recombination across the semiconducting gap, at some time the system will undergo the transition from the photo-induced EHL state back to the EG insulating phase. In Fig. 5.8c we plot the fraction of the excitonic spectral weight that is transferred to free carrier states as a function of pump-probe time delay Δt. At low fluence (∼30 µJ/cm^2, green markers in Fig. 5.8c), the spectral weight of the photoinduced metallic states is very limited and exponentially decays with a timescale of 130 ps (black solid line in Fig. 5.8c). This slow relaxation is in agreement with what expected for the recombination of electron and holes across the gap and with the fluorescence timescale [232, 69]. At large fluences (∼230 µJ/cm^2, red markers in Fig. 5.8c), we observe additional spectral weight variation which exceeds that present in the low-fluence data. This additional ΔSW_{free} component rapidly relaxes with a timescale of ∼20 ps, thus allowing us to estimate the critical number of excitations necessary for re-establishing the insulating EG phase. Assuming that $n_{\rm eh}$ spontaneously decays with the timescale of 130 ps, the change in slope of the $\Delta SW_{free}/SW_{exc}$ dynamics at ∼20 ps corresponds to a threshold value $n^t_{\rm eh}$=0.5%. If we calculate the pump fluence necessary to inject this density of photoexcitations, we obtain a threshold fluence $F^t \simeq$190 µJ/cm^2, which is compatible with the fluence at which cooperative effects saturate (see Sec. 5.3). A similar conclusion is obtained by analyzing the data on disordered NCs, which display a similar change in slope of the $\Delta SW_{free}/SW_{exc}$ dynamics (see Fig. 5.8c). We note that,

although the dynamics in disordered NC is qualitatively very similar to what observed in ordered samples at high fluence, the measured signal is significantly smaller. This observation suggests that, although the Mott transition takes place in both ordered and disordered NCs, finite size effects [301], which go beyond the scope of this work, emerge when NC are arranged in a disconnected and random network (disordered NCs) thus suppressing coherent hopping and inter-cube delocalization [19].

5.5 The phase diagram

Establishing halide perovskites artificial solids as quantum simulators is crucially based on the possibility of controlling the Hamiltonians $\hat{H}_{loc}$ and $\hat{H}_{int}$ and spanning a phase-space region that is relevant for describing real correlated materials [95, 146]. Considering relevant examples, such as vanadium [128], manganese [244], and copper oxides [138, 55] or fullerides [36, 37], the fundamental ground state properties are reproduced by the Hubbard model $\hat{H}_U$, formally identical to that introduced in Eq. 5.5. In these materials, the effective Coulomb repulsion U is of the order of the bandwidth $4t$ (with t being proportional to the hopping parameter, following the notation of Ref. 107), thus leading to a Mott insulating ground state [128]. When additional free carriers are introduced by chemical doping [159], these doped Mott insulators progressively develop spatially inhomogeneous correlated metallic states or undergo insulator-to-metal phase transitions [128]. In many interesting cases, the doped Mott insulating state close to the condition $U \simeq 4t$ witnesses the emergence of low-temperature long-range collective states [159] such as unconventional superconductivity and spin- or charge-density waves. Independently of the specific microscopic mechanism (e.g. electron-phonon or electron-spin interactions) at play in different materials, the formation of collective macroscopic states is mediated by long-range interactions, similar to those contained in $\hat{H}_{int}$, that favour the phase-locking of fundamental incoherent local fluctuations.

In this section we discuss how the fluence and time-dependent experiments presented in the previous sections allow to access an important region of the zero-temperature phase diagram of $\hat{H}_{loc}$+$\hat{H}_{int}$ [107]. As discussed in Ref. 107, the parameters controlling the electronic phases of photoexcited halide perovskites are the excitation density n_{eh}, which is mapped into the magnetization m through $\hat{H}_{loc}$, and the binding energy E_b, which is mapped into the Coulomb repulsion U. For small excitation densities (n_{eh} <1%) and moderately large Coulomb repulsion ($U > 3.8t$), the phase diagram is characterized by the boundary between an excitonic insulating gas and a mixed state with phase separation between EG and EHL, as shown in Fig. 5.3b and 5.9 [107]. The resonant excitation of the excitonic line directly modifies n_{eh} without creating an additional effective electron-hole population which would require a finite temperature description. At the same time, as anticipated in Sec. 5.2, the

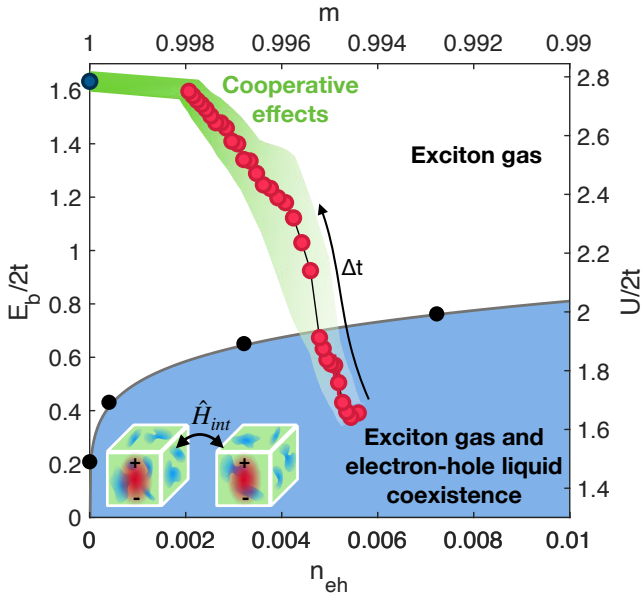

Figure 5.9: Phase diagram showing the electron gas (EG) and electron-hole liquid (EHL) regions. The electron-hole density n_{eh} and the exciton binding energy E_b correspond to the magnetization m and the on-site interaction U in the equivalent Hubbard model. The black points are taken from Ref. 107. The red dots are the experimental data points representing the trajectory the system follows while relaxing to the equilibrium EG phase from the photo-induced EHL phase. The plotted values are the binding energy values extracted from the time-resolved fit of the pump-probe data on NC superlattices at 230 μJ/cm^2 fluence, as a function of the estimated electron-hole density at the corresponding Δt. The green shaded area represents the phase-space region compatible with the outputs of the time-resolved experiment when the error bars associated to n_{eh} and E_b are considered.

excitonic energy undergoes a transient blueshift, δE_b (see Fig. 5.4 and related discussion), that is maximum at short delays (~ 5 ps) and progressively decreases as the system relaxes and returns to the initial state. The observed blue shift is likely related to a dynamical weakening of the exciton binding energy as a consequence of the increased screening after the light excitation. The determined time-dependent values of n_{eh} and δE_b define a trajectory in the phase diagram, in which the energy scales are expressed as a function of the unknown effective hopping t. The determination of n_{eh}^t=0.5% as the density threshold for the instability of the EG (see Sec. 5.4), allows us to anchor the time-dependent trajectory and fix the range of the $U/2t$ values spanned by the time-resolved experiment. Fig. 5.9 shows the experimental phase-space trajectory plotted on the theoretical phase diagram, taken from Ref. 107, for the high-fluence experiment. At very short delays, the NC superlattices are driven into a non-equilibrium state corresponding to $U/2t \approx$1.6 and n_{eh}=0.6%,

which is characterized by phase separation between insulating EG and metallic EHL regions. In this regime, cooperative phenomena start to be quenched (see Fig. 5.6) due to the progressive growth of metallic domains. During the relaxation dynamics, the system undergoes a dynamical transition back to the EG insulating phase before the initial parameters ($U/2t \approx 2.8$ and $n_{\mathrm{eh}}=0$) are recovered on longer timescales.

When combined together, our results demonstrate the possibility to explore the region of the magnetized Hubbard model $\hat{H}_{loc}$ that is the most relevant to describe many-body effects in correlated materials (U=3.2-5.6t). Importantly, perovskite NC superlattices also host long-range collective states (superradiance) driven by $\hat{H}_{int}$ (see Sec. 5.3) in the proximity of the insulator-to-metal transition controlled by $\hat{H}_{loc}$, i.e. for values of U ranging from $\approx 4t$ to $\approx 5.6t$ (see Fig. 5.9). Although in the present case we access the insulator-to-metal transition in $\hat{H}_{loc}$ only in the presence of a magnetic field h, the observed phenomenology is a very general property of correlated materials, such as iron-based superconductors, superconducting copper oxides and fullerides, which develop superconductivity and other long-range collective phases, e.g. charge density waves, nematicity, antiferromagnetism, spin density waves, when the Mott insulating state is lightly doped [138, 139].

5.6 Conclusions and outlook

We have here demonstrated that halide perovskite NC artificial solids represent a unique platform to investigate the emergence of long-range cooperative phases in systems displaying a Mott insulator-to-metal transition. As compared to cold-atoms based or solid-state platforms, halide perovskite NC superlattices allow to continuously tune the excitonic density and span collective phenomena and Mott insulating phases in a region of the phase diagram that is directly relevant for correlated quantum materials. The possibility to simulate the physics of interacting systems in which local correlations and long range orders interact on similar time (5-100 ps) and spatial ($\Lambda \simeq 10a$) scales has direct impact on a general class of solid-state problems. The most relevant case is the physics of copper oxides that host unconventional superconductivity and other exotic orders when the insulating Mott state is properly doped [138, 139]. Controlling the interplay between short-range Coulomb interactions and macroscopic collective states [218] is key to understand how phase-coherence on length scales larger than the lattice spacing may emerge out of incoherent fluctuations of pre-formed Cooper pairs or of the charge distribution and give rise to the superconducting condensate and charge density waves. The full tunability of Λ, of the exciton energy and density, allows to artificially reproduce the equilibrium phase diagram of cuprates or other quantum materials and implement models that describe the formation of long-range collective phases through the interaction term $\hat{H}_{int}$.

We also foresee that time-resolved experiments will provide tools to unlock the

gate to a wider region of the phase diagram and a richer physics. First, the light control of the $\hat{H}_{int}$ term offers a new platform to investigate the transient formation of non-equilibrium phases, such as photo-induced superconducting-like states in cuprates [41] and fullerides [42] or charge-density waves with enhanced coherence [300] in copper oxides. The new platform based on halide perovskite superlattices allows to investigate the ground state properties of repulsive Hubbard models in magnetic field, relevant for the physics of both fullerides [36] and cuprates [159], when long-range coherence induced by the transverse electronic magnetic field is externally forced. Second, the excitonic Mott transition described by $\hat{H}_{loc}$ is a Mott transition to an ensemble of isolated excitons localized in real space without any phase coherence and it can be dubbed as an incoherent excitonic Mott transition [29]. Another interesting case is given by the coherent excitonic Mott transition [219] that takes place between a coherent extended excitonic state, which is the counterpart of the excitonic Bose-Einstein condensate, and the metallic EHL. The time-resolution of pump-probe experiments, which is of the order of the excitonic decoherence, allows to investigate how the initially photo-excited excitonic state, which is intrinsically coherent and exhibits a macroscopic polarization, evolves into an incoherent gas of localized excitons as consequence of the decohernce led by electron-electron and elctron-phonon interactions. The description of the direct transition from a coherent excitonic condensate to an incoherent excitonic Mott gas is a difficult challenge that requires to consider both localized interactions and long-range screening phenomena [219]. Third, future non-resonant experiments will allow to directly create a non-equilibrium electron-hole population at a very high effective temperature, thus providing a platform to simulate the magnetized Hubbard model at finite temperatures and with controllable disorder and lattice size.

CHAPTER 6

The fate of optical excitons in $FAPbI_3$ nanocube superlattices

This chapter has been adapted from the following manuscript:

The fate of optical excitons in $FAPbI_3$ nanocube superlattices, A. Milloch, U. Filippi, P. Franceschini, S. Mor, S. Pagliara, G. Ferrini, F. V. A. Camargo, G. Cerullo, D. Baranov, L. Manna and C. Giannetti, *ACS Photonics*, 2024, 11, 9, 3511–3520, doi: 10.1021/acsphotonics.4c00105

Quantum simulation based on lead halide perovskite superlattices can greatly benefit from the huge tunability of these systems. One of the key control parameters that can be employed to modify the optical and electronic properties of these systems, in addition to the size and shape of nanocubes and superlattices, is the chemical composition. The inorganic cation (e.g. Cs^+ for the system investigated in Chapter 5) can be replaced also by organic ions which reduce the band gap and extend the optical absorption to the near infrared range. Understanding the nature of the photoexcitation and ultrafast charge dynamics pathways in these systems is key for the implementation of quantum simulation protocols, as well as for their potential applications as tunable light emitters, photon harvesting materials and light-amplification systems.

In this chapter, we apply two-dimensional coherent electronic spectroscopy (2DES) to track in real time the formation of near-infrared optical excitons and

their ultrafast relaxation in nanocube superlattices of hybrid organic-inorganic perovskite $CH(NH_2)_2PbI_3$. We report evidence of early-stage excitons which rapidly decay and form novel bound states compatible with bi-excitons, both at room temperature and at cryogenic temperatures. 2DES data unveil that the coherent ultrafast dynamics is limited by the combination of the inherent short exciton decay time ($\simeq$ 40 fs) and the dephasing due to the coupling with selective optical phonon modes at higher temperatures. The analysis of the temperature dependence of the excitonic intrinsic linewidth, as extracted by the anti-diagonal components of the 2D spectra, unveils a dramatic change of the excitonic coherence time across the cubic to tetragonal structural transition. On the picosecond timescale, we observe the progressive formation of long lived trap-states, ascribable to self-trapping of excitons or defect-trapping [258]. Overall these results provide a snapshot of the ultrafast exciton dynamics in FAPI nanocubes deposited on a solid substrate, which is key for future modelling and control of possible collective properties emerging in complex structures.

6.1 Probing FAPI optical excitons by 2DES

The synthesis of lead halide perovskite nanocube superlattices (Figure 6.1a) [134, 285, 14] paves the way to the development of novel photonics platforms based on cooperative superradiant effects [232, 332, 148, 216] such as light-emitting devices based on superfluorescence [232, 332, 148, 216] and quantum simulators of solid state problems [198]. Since the collective superradiant phenomena in nanocube superlattices are driven by the long-range electromagnetic interactions among excitons in different nanocubes [56, 187, 97], these developments are crucially affected by the exciton dynamics following light excitation of the individual nanocubes [19]. Light emission in lead halide perovskites can also be affected by strong coupling of excitons with the lattice, which results in broad spectra originating from self-trapped exciton (STE) states [258, 164]. Capturing the exciton formation and subsequent relaxation is therefore essential for improving and tailoring the emission and absorption properties of halide perovskites superlattices.

Among lead halide perovskites, hybrid organic-inorganic compounds represent an important case because their excitonic energy extends down to the near infrared (1.5 eV), thus significantly broadening the potential exploitation of these synthetic materials [182, 44, 250, 74]. Formamidinium lead iodide $FAPbI_3$ (FAPI) is especially promising because of its smaller band gap and increased chemical and thermal stability as compared to the archetypal compound MAPI [161, 275, 75]. In hybrid organic-inorganic halide perovskites, however, the presence of collective superradiance effects, analogous to those reported in fully inorganic superlattices, remains unclear; the possibility of extending superradiant phenomena to hybrid organic-inorganic perovskite superlattices requires an understanding of the ultrafast exciton dynamics of these systems. The photophysics of these materials is in fact characterized by a complex

interplay of free carrier excitations, bound excitons, multi-excitons and trapped states which generally give rise to multiple optical resonances in the visible/near-infrared range. These resonances overlap in energy and cannot be disentangled by linear or pump-probe spectroscopy. In Figure 6.1b, for example, we report a typical absorption spectrum of FAPI superlattices which shows multiple features compatible with the existence of multiple excitonic-like resonances in the 1.6-1.8 eV range (see Appendix B.2.2 for details of the analysis and fitting of the linear). Due to the overlap of different structures, however, a linear fit can hardly offer a decisive answer regarding the nature of the absorption. Therefore, the nature of the photocarrier generation and recombination processes in hybrid halide perovskite superlattices is still a matter of debate [313, 220, 272, 165]. Since addressing the early-stage dynamics of these processes is of central importance for controlling and enhancing macroscopic coherent effects, advanced optical techniques that go beyond linear spectroscopies and combine high temporal and spectral resolution should be employed [271, 332].

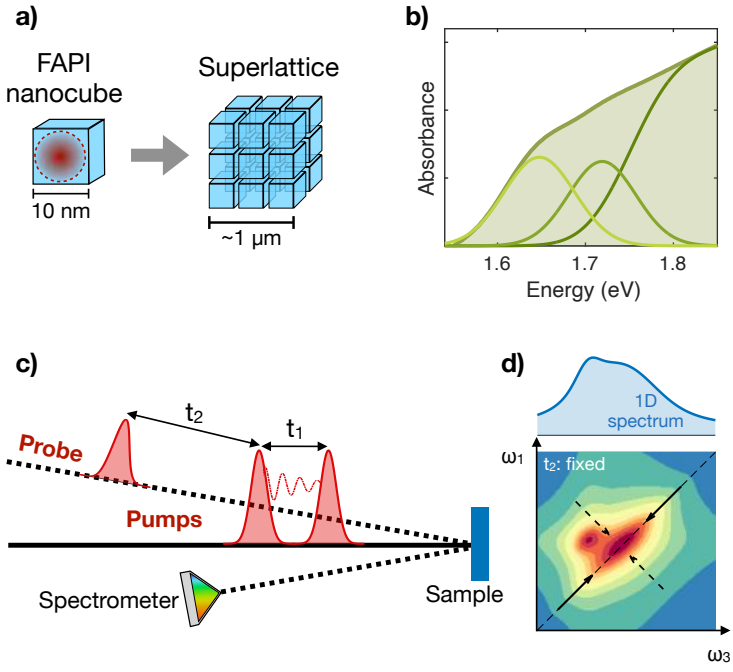

Figure 6.1: a) Cartoon of FAPI nanocubes, hosting quantum confined excitons, and FAPI superlattices. b) Absorption spectrum (green area) of the FAPI superlattices sample measured in this work. The green solid lines represent a free carriers edge and two peaks, as obtained from Elliott analysis of the room temperature absorbance (see Appendix B.2.2). c) Scheme of 2DES experiment. d) Sketch of a typical 2D spectrum (vertical axis: excitation, horizontal axis: detection) where, as opposed to 1D experiments (top panel), homogeneous and inhomogeneous linewidths and correlations between spectral features can be resolved.

Here, we employ 2DES (see Fig. 6.1c) to study the exciton photophysics in FAPI superlattices and unveil the hierarchy of the photoexcitation and relaxation processes. As discussed in Chapter 2, 2DES allows to disentangle the intrinsic decoherence dynamics of optical excitations, which manifest as a broadening along the anti-diagonal direction (see Fig. 6.1d), from disorder-induced inhomogeneous broadening along the diagonal of the ω_1-ω_3 map. By monitoring the temporal evolution of different peaks in the map, it is also possible to infer a cause-effect relation between different spectral features. This capability is key for monitoring the real-time transformation of the initial photoexcited carriers into the long-lived states responsible for the slow fluorescence emission.

2DES experiments are performed with the setup detailed in Chapter 2 (Section 2.5.2). The samples investigated here (see Figure 6.1a) are assembled from a colloidal dispersion of uniform ∼10 nm nanocubes. The studied samples comprise ∼ 0.3 - 1 µm superlattices of close-packed nanocubes deposited on a silicon substrate (see Appendix B.2 for sample preparation and characterization). In order to perform temperature-dependent investigations, the samples are mounted inside a closed-cycle helium cryostat that allows performing ultrafast optical spectroscopy experiments at temperatures between 20 K and 300 K. For the measurements presented in this chapter, the laser repetition rate was set to 40 kHz. A different repetition rate, selected by means of a pulse picker that allows keeping unvaried the energy per pulse, was employed for fluence-dependent studies where the repetition rate was increased up to 200 kHz as the excitation intensity was decreased, in order to maintain the average power at the sample constant throughout the fluence scan. The pump fluence F can be continuously varied between 0 and 230 µJ/cm^2 (as measured at $t_1 = 0$) by rotating a half-waveplate positioned on the pump beam path before the GEMINI 2D, whose polarizers select the 45° polarized component of the light.

In Figure 6.2 we report the 2D spectra measured on FAPI superlattices at $T = 200$ K as a function of the excitation ($\hbar\omega_1$, vertical axis) and detection ($\hbar\omega_3$, horizontal axis) photon energies and for different t_2 delays. The 2DES spectra are collected in the reflection geometry, which guarantees a better signal-to-noise ratio compared to the transmission configuration (see Sec. D.4 in Appendix D).

They display two distinct spectral features:

(i) a component located along the diagonal of the spectrum around 1.72 eV (Fig. 6.2a);

(ii) a broad structure centred off-diagonal, at $\hbar\omega_1 \simeq 1.72$ eV pump photon energy and $\hbar\omega_3 \simeq 1.61$ eV probe photon energy (Fig. 6.2b and 6.2c).

These features can be ascribed to transient photobleaching and stimulated emission signal (see also the positive transmissivity variation reported in Sec. D.4). As observed from 2D spectra at different t_2 time delays, these two spectral

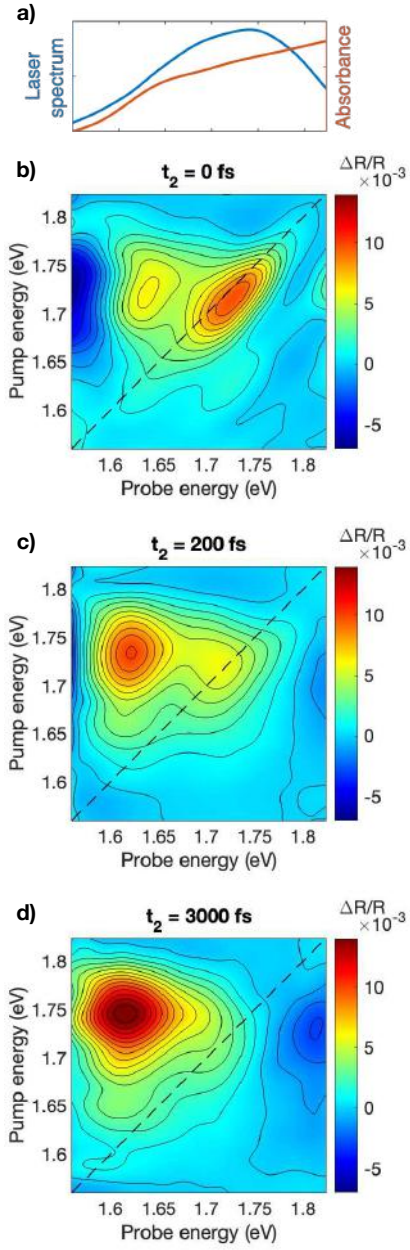

Figure 6.2: a) FAPI sample absorption spectrum (red) and the laser pulse spectrum (blue). b-d) 2D spectra of FAPI superlattice measured at 200 K with 175 μJ/cm^2 excitation fluence for three different t_2 delays: b) $t_2 = 0$ fs, c) 200 fs, and d) 3 ps.

features are characterized by different dynamics, with feature (i) decaying on a sub-picosecond timescale and feature (ii) building up on a longer timescale. The well-defined and well-localized diagonal structure reveals the existence in FAPI superlattices of a short-lived bound exciton at 1.72 eV, whereas the delayed off-diagonal feature suggests the formation of long-lived trap-states. In the following, we analyse in detail the characteristics of these two components.

6.2 Exciton and bi-exciton resonances

We first examine the short time delay ($t_2 = 0$ fs) 2D spectra. The elongation along the diagonal of the 2D spectrum allows estimating the inhomogeneous Full-Width-Half-Maximum (FWHM) that results $\simeq 83 \pm 4$ meV when projected along the probe axis. This value is compatible with the width of the resonance at 1.72 eV in the steady state absorbance (see Appendix B.2.2). The large inhomogeneous broadening originates from the size and shape dispersion of FAPI nanocubes and superlattices. The intrinsic homogeneous linewidth can instead be obtained from slicing the 2D spectrum measured at $t_2 = 0$ fs along the anti-diagonal direction crossing the exciton peak (see dotted lines in Figures 6.3a and 6.3c). The resulting anti-diagonal cuts are plotted in Fig. 6.3b and 6.3d for experiments conducted at two different temperatures; the horizontal axis represents the energy axis along the anti-diagonal direction, with positive values referring to the region above the diagonal in the 2D spectra (i.e. the region corresponding to pump photon energy larger than probe energy). The anti-diagonal profiles so obtained show a clear asymmetry that reveals the existence of two structures, one centred on the 2D spectrum diagonal (peak A) and one located above the diagonal (peak B). We stress that the signal acquired in a conventional pump-probe experiment, which corresponds to integrating along the $\hbar\omega_1$ axis (see Fig. 6.1c), would be dominated by the large inhomogeneous broadening of the exciton, thus preventing the possibility of inferring information about the decoherence and the emergence of secondary structures.

A multi-peak fitting, described in detail in Appendix D (Sec. D.1), is performed in order to extract the peaks amplitudes I_i, linewidths Γ_i and positions $x_{0,i}$, where i=A,B (see Sec. D.1 for the detailed list of values). In order to assess the origin of these two components, we perform fluence-dependent and time-resolved (t_2 dependence) 2DES at $T = 200$ K. In Figure 6.3e, we report the peak amplitudes (integrated areas along the anti-diagonal line-cut) as a function of the incident light fluence F. The power law $I_i{=}cF^{n_i}$ is fit to the data to determine possible non-linearities, c being a free coefficient. We observe that the peak amplitudes clearly display two different behaviours: I_A scales sub-linearly with the fluence ($n_\mathrm{A} = 0.59 \pm 0.09$) whereas I_B follows a superlinear power law ($n_\mathrm{B} = 1.19 \pm 0.06$), before saturating at large excitation intensity. From the t_2 scan between 0 and 450 fs (Figure 6.3f), we observe a fast decay of $I_\mathrm{A}(t_2)$, counterbalanced by an increase of $I_\mathrm{B}(t_2)$. This behaviour indicates that spectral weight transfers from peak A to B within tens of femtoseconds. To quantitatively

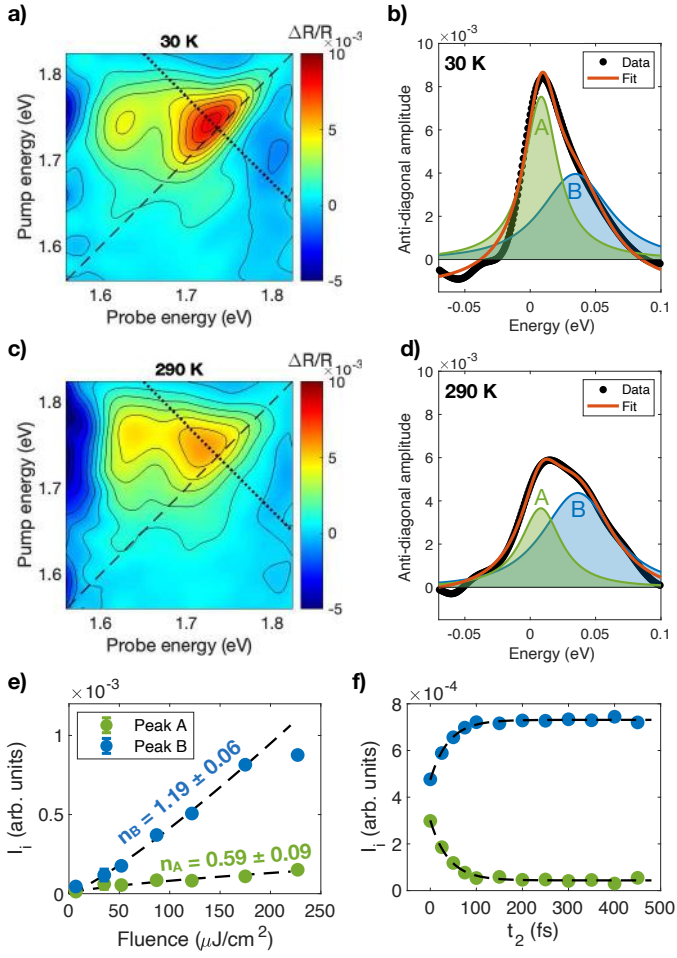

Figure 6.3: a) 2D spectrum of FAPI superlattices measured at 30 K and $t_2 = 0$ fs, with 175 µJ/cm^2 excitation fluence. b) Anti-diagonal profile of 2D spectrum in a) taken along the dotted line in a). The black dots are the experimental data points, the red line is the profile fit, the green and blue filled areas are peaks A and B associated with, respectively, exciton and bi-exciton resonances. c) and d) display 2D spectrum and anti-diagonal profile analogous to a) and b) but collected at a higher sample temperature (290 K). e) Fluence dependence of the integrated amplitude I_i of peaks A and B, extracted from fitting the 2D spectra anti-diagonal profiles at 200 K and $t_2 = 0$ fs. The black dashed lines represent the power-law fit to the data. f) Dynamics of the exciton (peak A) and bi-exciton (peak B) peak amplitudes I_i at 200K for 175 µJ/cm^2 excitation fluence.

analyze the I_i dynamics, we fit the data using the following exponential laws: $I_{\mathrm{A}}(t_2) = I_{\mathrm{A0}} \exp(-t_2/\tau_{\mathrm{A}}) + I_{\mathrm{A}\infty}$ and $I_{\mathrm{B}}(t_2) = I_{\mathrm{B0}} + K[1 - \exp(-t_2/\tau_{\mathrm{B}})]$. The best fit to the data returns $\tau_{\mathrm{A}} = \tau_{\mathrm{B}} = 39 \pm 6$ fs and $K \simeq I_{\mathrm{A0}}$ thus indicating the same time constant for the two processes and the conservation of the total spectral weight ($I_{\mathrm{A}}(t_2)$+$I_{\mathrm{B}}(t_2)$=*constant* for any delay t_2). The constant $I_{\mathrm{A}\infty}$ in $I_{\mathrm{A}}(t_2)$ accounts for a slow exciton decay occurring over a timescale that is longer than the t_2 range scanned here. Investigation of the dynamics of peak B on timescales longer than 500 fs is hindered by the appearance of the strong and broad off-diagonal structure. These results indicate that peak B corresponds to a new bound state that is formed following the photoinjection of excitons. One possible scenario is that peak B arises from the formation of bi-excitons that can live on a longer timescale [8]. Occupation of the bi-exciton state, i.e. a bound state originating from the interaction between two excitons and resulting in a lower energy state, gives rise to a transient signal at a probe photon energy smaller than the excitation energy, which corresponds to an off-diagonal signal at a distance from the diagonal equal to the exciton-exciton binding energy. The energy separation between peak A and B, i.e. $x_{0,\mathrm{A}}$-$x_{0,\mathrm{B}}$, therefore provides the exciton-exciton interaction strength, δE_{bi-exc}. The estimated value, $\delta E_{bi-exc} = 29 \pm 4$ meV, is compatible with the bi-exciton binding energy reported in the literature for similar systems [51, 125, 254].

In order to further support this picture, the fluence dependence in Fig. 6.3e and the dynamics in Fig. 6.3f are compared with numerical solutions of exciton and bi-exciton rate equations. The dynamics of bi-exciton formation is modelled through the following rate equations [314, 322]

$$\frac{dN_x}{dt} = I(t) - \gamma_x N_x + 2\gamma_{xx} N_{xx} - 2\beta N_x^2 \tag{6.1}$$

$$\frac{dN_{xx}}{dt} = -\gamma_{xx} N_{xx} + \beta N_x^2 \tag{6.2}$$

where N_x and N_{xx} represent the number of excitons and bi-excitons respectively and γ_x and γ_{xx} are the decay rate constants for exciton and bi-exciton respectively. $I(t) = I_0 \exp\left[-4\log(2)\left(\frac{t}{FWHM_t}\right)^2\right]$ is the source term that accounts for the ultra-short pump pulse generating excitons and it is described by a gaussian function of full width at half maximum $FWHM_t = 30$ fs and centred at $t = 0$. The β parameter describes the rate of bi-exciton formation, which originates from the interaction between two excitons. Numerical solutions of equations 6.1 and 6.2 with $\gamma_x = 0.01$ fs^{-1}, $\gamma_{xx} = 0.0001$ fs^{-1} and $\beta = 0.002$ fs^{-1} return the dynamics displayed in Figure 6.4a and b. We observe that excitons are instantaneously excited and quickly decay with a relaxation rate dominated by γ_x. The population of bi-exciton states occurs on a delayed timescale thanks to the coupling term βN_x^2 that accounts for exciton-exciton interaction leading to the formation of a two-body bound state.

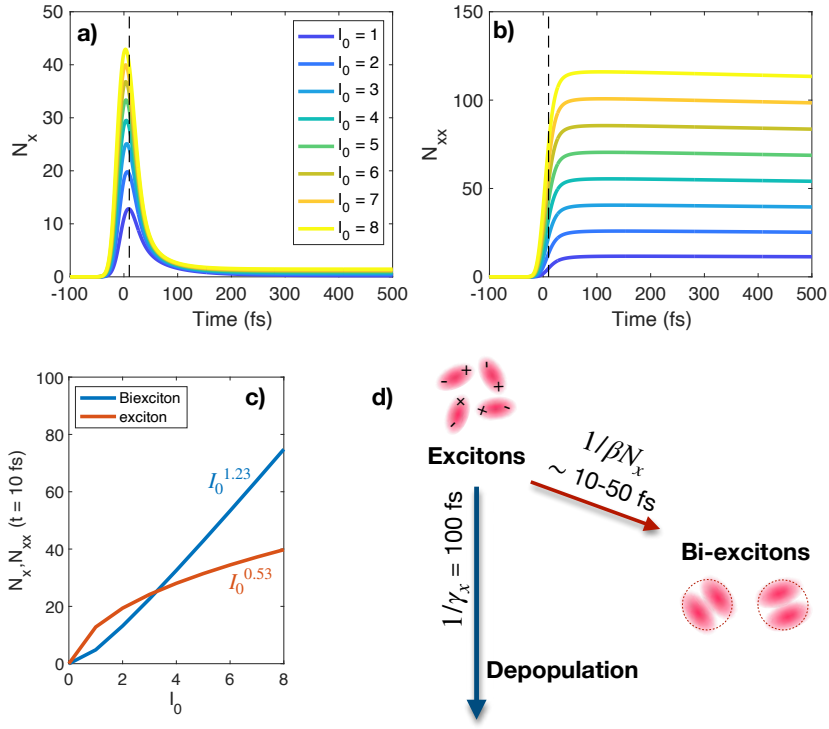

Figure 6.4: a) and b) display the numerical solution of the two coupled differential equations 6.1 and 6.2 for different values of the source term intensity I_0. c) Number of excitons and bi-excitons at $t = 10$ (dashed lines in a) and b)) as a function of excitation amplitude. d) Sketch of the relaxation channels for excitons, which can decay at a γ_x rate or bind into bi-excitons at a rate βN_x, N_x being the instantaneous number of excitons.

The simulation of the dynamics obtained from eq. 6.1 and 6.2 is repeated for increasing amplitude I_0 of the source term $I(t)$ with the aim of investigating the fluence-dependent behaviour. In order to compare with the experiment, we look at the number of excitons (red curve in Fig. 6.4c) and bi-excitons (blue curve in Fig. 6.4c) at a fixed time delay t^* after pump excitation as a function of the amplitude I_0 of the Gaussian source term. We chose $t^* = 10$ fs which is close to the time of maximum N_x and corresponds to the t_2 delay where fluence-dependent 2DES are performed. Regardless of the choice of parameters γ_x, γ_{xx} and β, we reveal an intensity-dependent trend that is always super-linear for the number of bi-excitons ($N_{xx} = c_{xx} {I_0}^{n_{xx}}$, $n_{xx} > 1$) and sub-linear trend for the excitons ($N_x = c_x {I_0}^{n_x}$, $n_x < 1$). The sublinearity of N_x at short time delays arises from the reduction in the number of excitons N_x due to their binding into bi-excitons, as described by the term $-2\beta N_x^2$ in Eq. 6.1. This process can occur already during the excitation pulse duration (30 fs) if the

bi-exciton formation characteristic time, $1/\beta N_x$, is comparable to $FWHM_t$. Consequently, since Eq. 6.2 includes a quadratic term in N_x (rather than in the excitation intensity $I(t)$), the resulting bi-exciton intensity dependence follows a super-linear power law with exponent $n_{xx} > 1$, instead of $n_{xx} = 2$ as might be expected. We find that there is a range of parameters γ_x, γ_{xx} and β whose power low scaling exponent is comparable to the experimental values ($n_{\mathrm{A}} = 0.59 \pm 0.9$ for peak A associated to the exciton, $n_{\mathrm{B}} = 1.19 \pm 0.06$ for peak B associated to the bi-exciton). For example, the experimental trend is compatible with $\gamma_x = 0.01$ fs^{-1}, $\gamma_{xx} = 0.0001$ fs^{-1}and $\beta = 0.002$ fs^{-1}, which give $n_x = 0.53$ and $n_{xx} = 1.23$ as shown in Figure 6.4c. In this case, the dynamics of exciton decay and bi-exciton build-up are governed by the large exciton decay rate γ_x that dominates over βN_x, resulting in characteristic decay and build-up times that are almost fluence-independent within the time resolution given by $FWHM_t$. We note that the dipole strength that determines the signal intensity of peak A and peak B measured in 2D spectroscopy will, in general, be different for the exciton and bi-exciton; this results in an exciton/bi-exciton intensity ratio (I_A/I_B) that can differ from the simulated N_x/N_{xx}.

The rate equation model therefore shows that both the experimental t_2-dynamics and the power-law exponents of peak A and peak B are compatible with the behaviour expected for exciton decay and bi-exciton formation originating from exciton-exciton interaction. More specifically, the rate equations model that reproduces the experimental trends, provides an out-of-equilibrium scenario where photo-injected excitons are subject to multiple decay channels, as sketched in Figure 6.4d. The excitonic population decays at a rate γ_x, which effectively includes all the direct depopulation channels, including relaxation to the ground state, formation of trap states and any mechanism that changes the exciton density; at the same time, exciton-exciton interaction leads to the formation of the bi-exciton bound states, which takes place at a rate βN_x. The parameters that better match the experimental findings suggest that direct excitonic decay takes place on a timescale of the order of $\gamma_x^{-1} = 100$ fs, whereas the bi-exciton formation rate, which depends on the product βN_x (N_x being the instantaneous number of excitons) strongly depends on the time considered. In the early stage dynamics (10-50 fs), the bi-excitonic production characteristic time ranges from $1/\beta N_x = 10$ to 70 fs. This indicates that the generation of bi-excitonic bound states occurs already within the 30 fs duration of both the pump and probe pulses. The formation of bi-excitons necessarily corresponds to fifth-order or higher nonlinear signals, since the generation of each exciton requires two field-matter interactions. In order to represent such a process, we describe the system with a density matrix that can describe two independent exciton states, $|eg\rangle\langle eg|$ and $|ge\rangle\langle ge|$ (the labels e and g indicate exciton and ground state, respectively), which account for the third order response, as well as two interacting exciton states, $|ee\rangle\langle ee|$, which account for the fifth-order response [70, 149]. The interacting excitons can then form the bi-exciton state, which is represented by $|bg\rangle\langle bg|$ (the label b refers to bi-exciton) and lead to a red-shifted signal due to the bi-exciton binding energy. Figure 6.5 shows a possible rephasing Feynman

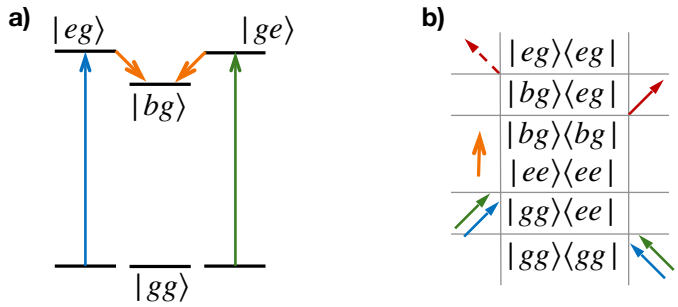

Figure 6.5: Representation of the energy levels scheme (a) and fifth-order rephasing double-sided Feynman diagrams (b) for the bi-exciton formation process.

diagram representing this process that is phase-matched in the direction of the probe pulses. The pathway displayed in Fig. 6.5 corresponds to a stimulated emission signal, in agreement with 2DES experiments in transmission geometry (see Section D.4), which, despite being noisier, show a transient increase of transmission in the energy region corresponding to peaks A and B.

6.3 Exciton decoherence

The homogeneous linewidth Γ_i of exciton and bi-exciton is estimated by lineshape analysis at short time delay t_2. As shown in Chapter 2 (Section 2.3.5), in the case of an intermediate degree of inhomogeneity the excitation resonance under investigation may have an anti-diagonal width that depends not only on the homogeneous broadening but also on inhomogeneous broadening effects [255]. Therefore, an accurate estimate of the homogeneous contribution calls for a simultaneous fit of diagonal and anti-diagonal slices of the 2D profile [255, 240] using as fitting functions the lineshapes that are obtained in Section 2.3.5 starting from the solutions of the optical Bloch equations for a two-level systems with Gaussian inhomogeneous broadening [255]. We consider the sum rephasing and non-rephasing signals (Eq. 2.50-2.53) to obtain the purely absorptive lineshape for the anti-diagonal and diagonal directions. As discussed in Sec. 2.3.5, the simultaneous fit of diagonal and anti-diagonal profiles then allows to estimate the inhomogeneous broadening parameter σ and the homogeneous linewidth Γ. In the present case, the presence of overlapping contributions hinders the performance of the global fitting, required by the approach presented above, for peak A and peak B separately. We therefore assume that the inhomogeneous broadening is the same for both features (peak A and peak B), i.e. $\sigma_A = \sigma_B$. Diagonal and anti-diagonal profiles are then fitted simultaneously: the diagonal one is fitted with $S_{A,\omega_0}(\omega')$, describing the linshape of feature A along the diagonal direction; for the anti-diagonal direction, where two peaks are needed to fit the data, the linecuts are fitted with $I_A S_{A,\omega_0}(\omega) + I_B S_{B,\omega_0}(\omega)$, with the

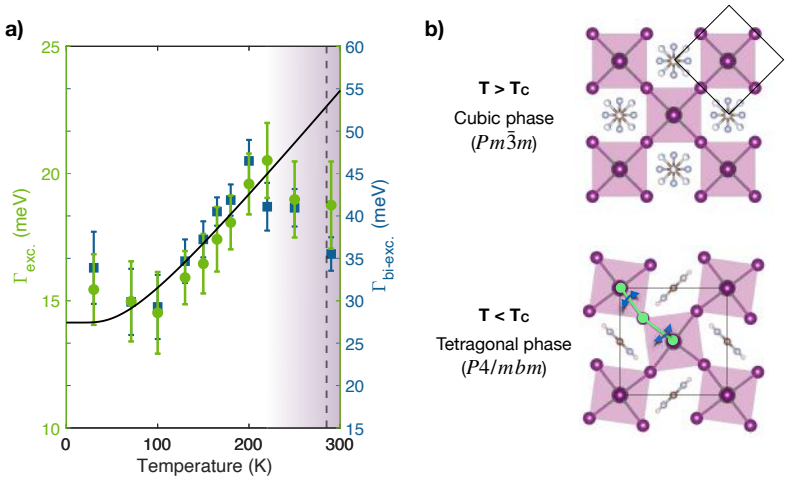

Figure 6.6: a) Temperature dependence of the exciton (green circles, left axis) and bi-exciton (blue squares, right axis) homogeneous linewidths extracted from simultaneous fitting of diagonal and anti-diagonal profiles at short time delay t_2. The black solid line represents the linewidth broadening originating from interaction with an optical phonon mode at $E_{OP} = 17$ meV. The purple shaded area represents the temperature range where FAPI nanocubes have cubic lattice structure and where the deviation from the expected temperature-dependent trend is observed. b) Top panel: FAPI crystal structure in the high-temperature cubic phase, with the organic cation subject to orientational disorder. Bottom panel: low-temperature tetragonal phase of FAPI perovskite. The black squares highlight the unit cell. The green lines and blue arrows indicate the I-Pb-I bending mode that softens in the proximity of the second-order tetragonal-to-cubic phase transition.

subscript I_i amplitude parameters and $i = A, B$. The complete list of values obtained from the fitting procedure are reported in Section D.1. This approach allows us to disentangle, from the measured 2D spectra, the homogeneous linewidth contribution for both exciton and bi-exciton resonances.
In the following, we will adopt the notation $\Gamma_{\mathrm{A}} = \Gamma_{exc}$ and $\Gamma_{\mathrm{B}} = \Gamma_{bi-exc}$ to directly link to the physical origin of the two structures. The extracted values are plotted in Figure 6.6a as a function of sample temperature T. At cryogenic temperature, we estimate $\Gamma_{exc} = 15 \pm 2$ meV (obtained from the average value of the three measurements at $T \leq 100$ K), which corresponds to a pure decoherence time $\tau_{dech} = 44 \pm 5$ fs, where $\tau_{dech}{=}\hbar/\Gamma_{exc}$. This value is of the same order of the $\tau_{\mathrm{A}} \simeq 40$ fs depopulation time, thus suggesting that the leading mechanism determining the homogenous linewidth is the decay into bi-excitons. The coherent propagation of the excitons is thus limited, even at cryogenic temperatures, by their ultra-short lifetime, preventing the development of delocalized states and superradiant coherent states similar to those observed in inorganic halide perovskite superlattices [232, 187, 198]. For

the bi-excitonic state, we obtain $\Gamma_{bi-exc.} = 31 \pm 4$ meV between $T = 30$ K and $T = 100$ K, corresponding to $\tau_{dech} = 21 \pm 3$ fs. In this case, the decoherence timescale is much shorter than the bi-exciton depopulation time, thus indicating the formation of a strongly incoherent gas of interacting bi-excitons, surviving for hundreds of femtoseconds.

The temperature dependence of both $\Gamma_{exc.}$ and $\Gamma_{bi-exc.}$ is reported in Fig. 6.6a (green circles and blue squares, respectively). We observe a similar temperature-dependent linewidth broadening, which suggests that at higher temperatures the decoherence process is accelerated by the coupling to the thermal bath, consisting of optical phonons. The temperature-dependent increase of $\Gamma_{exc}(T)$ is compared to the thermal broadening (black solid line in Fig. 6.6a) expected for coupling to longitudinal optical phonons, which is described by the function $\Gamma_{exc}(T) = \Gamma_{exc,0} + \Gamma_{OP}/[\exp(E_{OP}/k_BT) - 1]$, where $\Gamma_{exc,0}$ is the intrinsic linewidth at low-temperature, Γ_{OP} is the exciton-optical phonon coupling coefficient and E_{OP} is the optical phonon energy [157]. According to literature reports, FAPI displays optical phonon modes at energy E_{OP} between 15 meV and 19 meV [89, 79, 75, 51, 324], which have been ascribed to vibrations of the organic cation with respect to the inorganic cage [230, 79]. These libration modes of the organic cation have also been reported to affect the photoluminescence intensity and the lifetime of photoexcited states in MAPI perovskite [215]. Interaction with such vibrational modes fully accounts for the homogeneous broadening measured in the present work for $T < 250$ K. In this temperature range, fitting of $\Gamma_{exc}(T)$ returns $\Gamma_{exc,0} = 14 \pm 1$ meV and $\Gamma_{OP} = 8 \pm 2$ meV when E_{OP} is fixed to values between 15 meV to 19 meV. The temperature-dependent trend suggests that at low temperatures the exciton coherence is mainly limited by the bi-exciton formation, while at higher temperatures the scattering with thermally activated optical phonons also contributes to faster decoherence. Interestingly, a clear deviation from the trend expected for scattering with thermally activated phonons is observed for temperatures higher than $T^* \simeq 250$ K, where the measured homogeneous linewidth is smaller than what is expected due to thermal broadening in this temperature range. T^* is very close to the critical temperature for the symmetry-breaking structural phase transition undergone by FAPI. The transition from the high-temperature cubic phase (space group $Pm\bar{3}m$) to the low-T tetragonal phase (space group $P4/mbm$) occurs at $T_c^{bulk} \simeq 285$ K in the bulk material [73, 305], and at smaller temperature in perovskite nanocubes [167]. For 10 nm nanocubes we can expect a $\sim 15\%$ decrease in T_c, that corresponds to ~ 240 K. Therefore, the anomalous behaviour in $\Gamma_{exc}(T)$ emerging at 250 K suggests a suppression of the exciton-phonon interaction in the high-temperature structural cubic phase. More specifically, we note that the second-order structural phase transition from tetragonal to cubic at T_c is accompanied by a symmetry increase, as shown in Fig. 6.6b. The reduction of the unit cell in the high-T cubic phase implies the reduction of the number of optical phonon modes from 36 to 18 [177], thus limiting the phononic channels at $E_{OP} \simeq 17$ meV available for the excitonic decoherence.

6.4 Long-lived trap states

2DES further snaps the subsequent formation of the long-lived states that are responsible for the slower emission of light under the form of fluorescence (see photoluminescence spectrum in Appendix B.2.2). For this aim, we analyze the off-diagonal structure that appears in the 2D spectra shown in Fig. 6.2 after a few picoseconds at $\hbar\omega_1 \simeq 1.72$ eV and $\hbar\omega_3 \simeq 1.61$ eV coordinates. This off-diagonal feature can not be associated with multi-exciton states such as bi-excitons because of the large energy separation from the diagonal structure (100 meV) and the absence of super-linear fluence dependence (see 2DES data reported in section D.3 at the end of this chapter). Interpretation of the two spectral features (diagonal and off-diagonal) as originating from a charge transfer between two co-existing crystal structure phases, as previously done in Ref. 220 for MAPI thin films, is incompatible with XRD data showing tetragonal lattice at low-T and purely cubic crystal structure at room temperature (see Appendix B.2). Significant information on the nature of this low-energy response can be obtained from its dynamics compared to the excitonic one. Fig. 6.7a displays the dynamics of the two different spectral features obtained by integrating the 2D spectra over two different selected regions of interest, one centered on top of the diagonal and the other centered on the off-diagonal structures (see inset of Figure 6.7a). The off-diagonal structure shows a $\sim$ 300 fs build-up time, which coincides with the decay of the diagonal signal, as evidenced by the exponential fit reported in Fig. 6.7a. This finding demonstrates that the off-diagonal structure is a long-lived state that forms after the relaxation of the initial excitonic population. This long-lived state is in turn responsible for the slower light emission, which takes place several tens of picoseconds after the initial photoexcitation [220, 232]. We note that the dynamics reported in Figure 6.3f are compatible with what is reported in Fig. 6.7a because in the former case, the amplitude is obtained from integration over the whole anti-diagonal spectral range, whereas in the latter the integration was performed on a fixed squared area where the diagonal peak broadening caused by the rise of the bi-exciton component is not taken into account. This transfer of occupied states from free excitons to lower energy states is typical of trap states that get populated following the mechanism sketched in Figure 6.7b [310, 258, 103]. Such trap states can originate when the coupling between charge carriers and a local structural distortion of the lattice decreases the energy of the system.

One possible origin of trap states is related to the presence of static intrinsic defects, such as local lattice perturbations, structural disorder and vacancies [103, 175]. Another possibility is that the off-diagonal structure is associated to the formation of metastable STE, i.e. localized excitons dressed by a phonon mode, most likely involving the I-Pb-I bending. Indeed, we note that the build-up time (300 fs) of the off-diagonal structure is very close to half of the period of the optical modes at $\simeq$ 7 meV, which involve the halide-lead-halide bending (see Fig. 6.6b) [230] that has been shown to be closely coupled with photoexcited excitons [319]. In general, STE formation is facilitated in solid

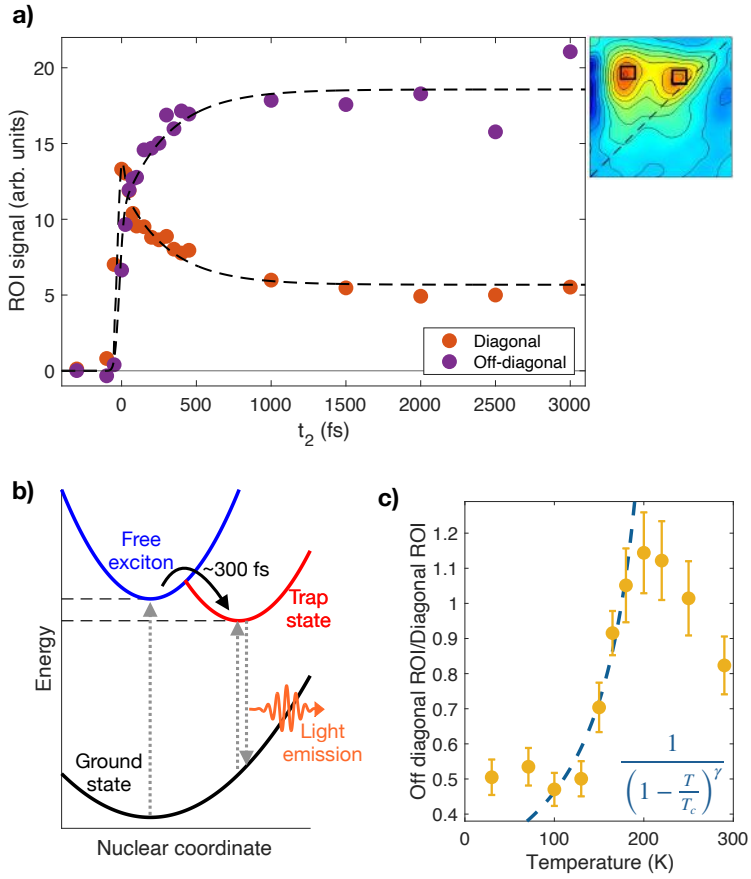

Figure 6.7: a) t_2 dynamics of the 2DES signal measured at 200 K and integrated over the two regions of interest depicted in the top left inset, which select the diagonal (orange) and off-diagonal (purple) structures. b) Sketch of the energy level structure and population dynamics of trap states originating from defects or self-trapped excitons. c) Temperature dependence of the off-diagonal spectral feature at $t_2 = 0$ fs as compared to the diagonal excitonic resonance. The yellow markers report the ratio between the signal intensities obtained from the integration of the 2D spectra over the areas indicated in the inset of Fig. 5a. The blue dashed line indicates the divergence of a second-order phase transition order parameter scaling as $(1 - T/T_c)^{-\gamma}$; here $\gamma = 1$ and $T_c = 240$ K.

systems displaying soft lattice, strong exciton-phonon coupling, large lattice constants and reduced electronic dimensionality [274]. These properties are often found in halide perovskites - which typically display strong electron-phonon interactions and soft lattice [312] - and in FAPI superlattices in particular, where the formamidinium cation represents a large cation molecule as compared to MAPI or all-metal halide perovskites [275], and where the nanocube synthesis reduces the dimensionality of the system to quasi 0D due to exciton quantum confinement. STE usually results in broad emission peaks [274], consistently with what is observed from room temperature photo-luminescence on the FAPI superlattices investigated in this work (see Appendix B.2.2). The formation of STE is also suggested by the temperature dependence of the off-diagonal structure, as reported in Fig. 6.7c for fixed time delay $t_2 = 0$. Starting from cryogenic temperature we clearly observe a significant increase of the intensity of the off-diagonal peak as the temperature is increased, with tendency to diverge when the critical temperature of the tetragonal to cubic transition is approached. The experimental data are fitted with the function $(1\text{-}T/T_c)^\gamma$ in order to determine the critical exponent. The data are compatible with $\gamma = 1$, which is the mean-field critical exponent of compressibility across a second-order phase transtion. This result suggests that the softening of the lattice and, more specifically, of the $\simeq 7$ meV phonons responsible for the I-Pb-I bending, which softens across the tetragonal-to-cubic transition, strongly favours the formation of STE with a binding energy as large as $\simeq 100$ meV. We also note that the 2D spectra contain a weak diagonal signal at $\hbar\omega_1 = \hbar\omega_3 \simeq 1.61$ eV (see Fig. D.1 in Appendix D) which displays a temperature-dependent behaviour similar to the off-diagonal component, thus indicating the possibility of direct excitation of this phonon-mediated transition, which consists in the simultaneous absorption of a photon and the local lattice distortion related to the STE. The lower intensity of the diagonal component as compared to the off-diagonal peak could be related to the scaling of the signal intensity with the dipole strength. Since the diagonal signal scales with the fourth power of the dipole strength, while the off-diagonal cross peak scales with the second power, small dipole strength of the trap state compared to the main excitonic line can result in the suppression of diagonal features in the 2DES spectra, despite the off-diagonal peak being clearly visible [282, 31]. The spectrum of the laser excitation (see Fig. 6.2a) can also play a role in scaling down the intensity of the measured signal at small photon energies ($\hbar\omega_1 \sim 1.61$ eV) [282, 32], thus further suppressing diagonal features.

6.5 Conclusions

In conclusion, our 2DES study has unveiled the complex hierarchy of the photophysics in FAPI superlattices. The initial excitons very rapidly ($\simeq 40$ fs) decay forming an incoherent gas of bi-excitons. Within hundreds of femtoseconds the optical excitations form trap states that originate from defects or lattice distortions causing self-trapping of excitons. The large binding energy and the

spatial localization protect these new and long-lived states that are responsible for the subsequent fluorescent emission [210, 334]. We note that a direct comparison with disordered FAPI nanocrystals cannot be performed due to the strong signal suppression in disordered films (see Section D.5). The way the ordered arrangement of the nanocubes enhances the signal calls for further investigation that goes beyond the scope of the present work. Nevertheless, the present results suggest that the short excitonic decoherence time prevents the onset of collective superradiant emission, in contrast with observations in inorganic superlattices [232, 332, 148, 216, 198]. At the same time, the strong coupling with the optical phonons, combined with the lattice softening across a continuous structural phase transition, offers a new tool to manipulate the excitonic/bi-excitonic coherent dynamics, as well as the down-conversion into trap-states, which ultimately controls the collective and coherent emission properties.

CHAPTER 7

Conclusions and outlook

This thesis explores out-of-equilibrium physics in strongly correlated materials, aiming to deepen the understanding of fundamental mechanisms that could be leveraged to fully control electronic and magnetic properties, as well as phase transitions, in quantum materials. Both ultrashort laser pulses and static electric fields were employed to generate out-of-equilibrium phases, that were then probed by means of either time- or space-resolved experimental techniques for the two types of excitation, respectively. Specifically, the ultrafast charge or exciton dynamics were detected by employment of pump-probe spectroscopy and 2D coherent electronic spectroscopy. The implementation of 2DES in particular aimed at accessing the fundamental dephasing processes that cause the ultrafast loss of electronic quantum coherence. For current-induced phase transitions, we adopted a X-ray based imaging technique, PEEM, to obtain nanoscale images and investigate the role of the topological defects of the underlying nanotexture - naturally emerging in systems displaying first-order phase transitions or symmetry breaking phenomena - on the phase switching and its potential control.

Out-of-equilibrium phenomena in Mott systems

In the first part of the thesis we considered two paradigmatic Mott insulators, vanadium oxides $LaVO_3$ and V_2O_3, perturbed by light pulses and a static electric field, respectively.

In $LaVO_3$, we explored the charge excitations across the Mott-Hubbard gap, which can provide great insight on the exotic properties of strongly correlated materials, among which the intertwining of multiple degrees of freedom and the establishment of long range ordered phases. $LaVO_3$ optical transitions in the visible and near-infrared range are in fact strongly dependent on the establishment of spin and orbital ordered phases: Hubbard excitons, bound states between a doubly occupied and an adjacent empty V-site, are stabilized by the ordered configuration of the V-3*d* electrons' orbital occupation and spin. Pump probe and 2DES experiments, presented in Chapter 3, revealed that the disruption of the ordered background due to ultrafast pump excitation results not only in a decrease of the spectral weight of the excitonic resonance, but also in a broadening of its linewidth. 2DES more specifically showed that it is the homogeneous linewidth, directly related to the intrinsic lifetime and decoherence time of the exciton, that is shorten over a tens of picosecond timescale after ultrafast excitation. This processes, rationalized within Gingzburg-Landau's theory, is likely due to the coupling of the electronic excitations across the Mott-Hubbard gap, enhancing spin and orbital fluctuations, to the order parameter of system. These results represent a proof of concept of the decoherence time being strongly affected by the onset of ordered states, which likely extends to many other systems undergoing first order phase transitions coupled to the establishment of long-range orders. Some examples include, for instance, charge order and antiferromagnetic correlations in copper oxides (e.g. $Nd_{2-x}Ce_xCuO_4$) [58, 85], and charge density wave (e.g. 1T-TaS_2) [160]. The variation of the fluctuations of the thermal bath, along with their interaction with electronic excitations, in proximity of a phase transition, could provide a novel mechanism to tune the decoherence dynamics in solids.

The case of out-of-equilibrium phase generated by static electric field was investigated in V_2O_3, where the application of an above threshold current or voltage can induce a volatile switching from high resistance to low resistance. This current-induced insulator-metal transition was explored in Chapter 4 by means of PEEM, which allowed us to image the nanotexture of low-temperature V_2O_3 - forming because of the breaking of the C_3 symmetry upon the structural phase transition - simultaneously to the application of the switching current. This experiment allowed us to directly observe the formation and widening of a rhombohedral metallic channel after the switching event, and to link it to the spatial arrangement of the monoclinic domains (twins). We in fact observed that the formation of the metallic channel is pinned by the existence of a topological defect in the domain nanotexture. Such topological defect corresponds to the breaking of the curl-free condition for the order parameter (which is related to the film shear strain), that guarantees the continuity of the rhombohedral-to-monoclinic deformation. This results in a local suppression of the order parameter, and a consequent lowering of the threshold needed for resistive switching, therefore triggering the insulator-metal transition to occur at the location of the topological defect. The observation of topological defects playing a role in electronic phase transitions is actually a general concept that could

be relevant to the many other systems displaying first-order phase transitions accompanied by a symmetry breaking. In CDW and charge-ordered systems, for example, topological defects strongly affect the dynamics of photo-induced transitions [298, 338, 47]; our results further indicate that topological defects of the order parameter can play a role also in initiating the induced transition and affecting the switching-threshold. Other systems where this physics could be relevant include transition-metal (V/Ni/Mn) oxides, where ordered phases in the charge, spin and orbital degrees of freedom emerge upon the IMT and result in a lowering of the systems symmetry [128, 281], kagome metals, where symmetry breaking occurs due to the emergence of a nematic phase [10], and copper oxides, which are characterized by the coexistence of multiple competing orders [138]. Our results also suggest novel viable routes to control resistive switching, for example by means of stain engineering to introduce topological defects in a deterministic way. We foresee various approaches that can be explored to achieve strain control. One possibility is to exploit the influence of the substrate on the film strain and its insulator-metal phase transition, as shown in V_2O_3 films tuned by fine variations in the substrate doping to change the film-substrate lattice mismatch [119, 124]. Localized control of the strain and related topological defects could instead be obtained by exploiting the strain applied by metallic overlayers, similarly to the gold electrodes employed in the experiment presented here, whose geometry and orientation with respect to the film crystallographic axis can affect the emergence of topological defects. Another promising approach is represented by nanopatterning to control antiferromagnetic domains [196] and, thus, to locate topological defects in a controlled way.
We further observed that the current-induced resistive switching is compatible with a non-thermal resistive switching mechanism at the threshold current, followed by the thermal expansion of the metallic filament due to Joule heating. Despite further work is necessary to finally address the exact nature of the topology-driven switching at the very early stages, the non-thermal scenario suggested here would open the possibility of exploiting topological properties to achieve an all-electronic Mott switching that is reversible and intrinsically much faster than the thermal process involving the lattice transformation.

Novel platforms for quantum simulation

In the second part of the thesis we focused on the possibility of simulating, on an artificial platform, the emergence of collective phenomena and the occurrence of the Mott transition, which are the two phenomena ubiquitously observed in doped Mott insulators. We specifically focused on cubic superlattices composed of lead halide perovskite nanocubes, which we propose as a suitable novel platform for quantum simulation.

As discussed in Chapter 5, the exciton dynamics in $CsPbBr_3$ nanocube superlattices, excited by a resonant pump, revealed the suitability of the platform for quantum simulation applications. Upon controlling the excitation intensity,

different quantum phases relevant for Mott materials were accessed, within one single platform: superradiant phase, exciton gas and electron-hole liquid. The emergence of superradiance, a long range collective phase, allows to mimic the physics of long range orders, such us superconductivity and charge density waves, in strongly correlated materials. The transition from exciton gas to electron-hole liquid, also known as the excitonic Mott transition, allows to map the insulator-metal Mott transition as described within the Hubbard model. Combined together, the long- and short-range interactions governing the excitons can be exploited to map the physics of many quantum materials, as they give access to the most relevant region of the phase diagram, where collective phases appear in proximity of the insulator-metal Mott transition. $CsPbBr_3$ superlattices therefore represent a low cost and much simpler alternative to state-of-the-art quantum simulators based on ultracold-atoms.
As future steps toward establishing quantum simulation schemes based on this novel system, we foresee several advancements, both in ultrafast optics and material development, that are well within reach. For example, as opposed to the resonant pump used here, different excitation protocols could be easily used in order to excite the exciton off-resonance and investigate finite-temperature phase diagrams. Time-resolved optical microscopy will allow to perform experiments on individual superlattices. By exploiting the flexibility in the chemical composition and super-lattice geometry, it will be possible, for example, to: tune the excitonic energy (from infrared to visible) and make it resonant with external cavities; change the lattice geometry, e.g. from cubic to perovskite [49]; create binary compounds in which the unit cell is characterized by a basis [49], thus adding additional internal degrees of freedom that can simulate multi-orbital physics; control the size, shape and dimensionality (from 3D to 2D) of the superlattice [129, 288, 166, 329], in order to investigate the role of dimensionality and superlattice symmetry in the emergence of long-range orders.

In order to move towards this direction, we considered in Chapter 6 the hybrid organic-inorganic compound FAPI, which can also be synthesized into nanocube superlattices. Here, we addressed the early-stage dynamics of excitons, which crucially determines the possibility of establishing collective superradiance effects. Indeed, ultrafast spectroscopy revealed that excitons in FAPI nanocube superlattices are extremely short-lived as they rapidly (within ~ 40 fs) form bi-excitons, and subsequently (within 1 ps) relax into a lower energy trap state. 2DES additionally gave access to the exciton and bi-exciton decoherence times. The short excitonic decoherence time ($\sim 30 - 40$ fs) is likely what prevents the onset of collective superradiance. In addition, the significant variation in the temperature-dependent behavior of decoherence time detected across the cubic to tetragonal structural transition, occurring because of the changes in the optical phonon modes causing exciton dephasing, suggests a possible new way to control and enhance the ultrafast coherent dynamics of photocarrier generation in hybrid halide perovskite synthetic solids.

Appendices

APPENDIX A

Non-collinear optical parametric amplifier: design and experimental implementation

In 2DES, the bandwidth of the pump and probe pulses determines the frequency window that can be accessed, therefore broadband pulses should be employed. Another crucial parameter is the time duration of these pulses, which affects the temporal resolution of the experiments and selects the timescale, and hence the processes, that can be accessed and probed. To investigate decoherence dynamics in solid-state systems, light pulses with duration of a few tens of femtoseconds or shorter, and a correspondingly large bandwidth,[1] are required.

Ultrashort light sources, such as Ti:sapphire or Yb:doped lasers, typically have narrow gain bandwidths, resulting in the emission of hundreds of femtoseconds long pulses at fixed wavelength. To overcome these limitations, optical parametric amplifiers (OPAs) can be used, providing tunability in both the radiation wavelength and pulse duration of the generated pulses [183].

In this appendix, we summarize the working principle of OPAs and describe the design of the home-made non-collinear OPA (NOPA) set up for the 2DES experiments presented in this thesis.

[1] Pulse time duration and spectral bandwidth are related via the time-bandwidth product: $\tau\Delta\omega \geq 2\pi c_B$, with $\Delta\omega$ spectral bandwidth and τ pulse duration defined as FWHM, where the equality holds for transform limited pulses. c_B is a constant of the order of 1, whose exact value depends of the shape of the pulse (e.g. $c_B = 0.441$ for Gaussian pulses).

A.1 Parametric amplification

Optical parametric amplification is a second-order nonlinear optical effect occurring when, in a suitable nonlinear crystal, energy is transferred from a high intensity beam (*pump*) at frequency ω_3 to a lower intensity beam (*signal*) at the lower frequency ω_1. Because of energy conservation, a third beam (*idler*) at frequency ω_2, determined by

$$\hbar\omega_3 = \hbar\omega_2 + \hbar\omega_1, \tag{A.1}$$

must be generated. Eq. A.1 implies that the signal and idler frequencies are smaller than the pump one ($\omega_1, \omega_2 < \omega_3$). The signal frequency ω_1 can vary from 0 to ω_3 as ω_2 varies, correspondingly, from ω_3 to 0, so that Eq. A.1 is always fulfilled. Once ω_3 is fixed, the variability in signal (and consequently idler) frequencies allows to achieve continuous wavelength tunability. Alternatively, it is possible to work in a specific geometry where the amplification process is efficient in a broads spectral range, resulting in the possibility of synthesizing pulses whose transform limited time duration is significantly shorter than the pump pulse duration [183].

A.1.1 Parametric amplification of monochromatic waves

We here provide a short theoretical treatment of the process of parametric amplification [183]. We start by considering three monochromatic waves propagating along the z direction in a non-centrosymmetric medium and we analyze their nonlinear interaction. In this case, the total electric field can be written as

$$E(z,t) = \frac{1}{2}\left[A_1(z)e^{i(\omega_1 t - k_1 z)} + A_2(z)e^{i(\omega_2 t - k_2 z)} + A_3(z)e^{i(\omega_3 t - k_3 z)}\right] + c.c. \tag{A.2}$$

The second-order nonlinear polarization (see Section 2.2.1) is given by

$$P_{NL}(z,t) = \epsilon_0 \chi^{(2)} E^2(z,t) = 2\epsilon_0 d_{\text{eff}} E^2(z,t), \tag{A.3}$$

where ϵ_0 is the electric permittivity of vacuum, $\chi^{(2)}$ is the second-order nonlinear susceptibility and d_{eff} is the so-called effective nonlinear optical coefficient which depends on the specific $\chi^{(2)}$ components involved in the interaction. $P_{NL}(z,t)$ contains components at the different combinations of two frequencies among ω_1, ω_2 and ω_3; in particular, we here assume that only the interactions verifying Eq. A.1 are efficient are therefore consider only the terms at frequencies $\omega_1 + \omega_2 (= \omega_3)$, $\omega_3 - \omega_2 (= \omega_1)$ and $\omega_3 - \omega_1 (= \omega_2)$. $P_{NL}(z,t)$ therefore reads:

$$\begin{aligned} P_{NL}(z,t) =& \epsilon_0 d_{\text{eff}} A_2^*(z) A_3(z) e^{i(\omega_1 t-(k_3-k_2)z)} \\ &+\epsilon_0 d_{\text{eff}} A_1^*(z) A_3(z) e^{i(\omega_2 t-(k_3-k_1)z)} \\ &+\epsilon_0 d_{\text{eff}} A_1(z) A_2(z) e^{i(\omega_1 t-(k_1+k_2)z)} + c.c. \end{aligned} \tag{A.4}$$

By inserting Eq. A.4 into the wave equation (Eq. 2.2 in Chapter 2) and applying the slowly varying envelope approximation (i.e. $\left|\frac{\partial^2 A}{\partial z^2}\right| \ll 2k \left|\frac{\partial A}{\partial z}\right|$), the following set of coupled wave equations are obtained:

$$\begin{aligned} \frac{\partial A_1}{\partial z} &= -i\frac{d_{\text{eff}}\omega_1}{c_0 n_1} A_2^* A_3 e^{-i\Delta k z} \\ \frac{\partial A_2}{\partial z} &= -i\frac{d_{\text{eff}}\omega_2}{c_0 n_2} A_1^* A_3 e^{-i\Delta k z} \\ \frac{\partial A_3}{\partial z} &= -i\frac{d_{\text{eff}}\omega_3}{c_0 n_3} A_1 A_2 e^{+i\Delta k z} \end{aligned} \quad , \tag{A.5}$$

where $\Delta k = k_3 - k_2 - k_1$ is the *wavevector mismatch* and n_i is the refractive index of the medium at frequency ω_i. Depending on the boundary initial conditions ($A_i(z=0)$), the following second-order nonlinear processes can occur:

- sum frequency generation (SFG): $A_1(0)$ at frequency ω_1 and $A_2(0)$ at frequency ω_2 are the two input fields; their interaction generates the field A_3 at $\omega_3 = \omega_1 + \omega_2$;
- difference frequency generation (DFG): $A_3(0)$ at frequency ω_3 and $A_1(0)$ at frequency ω_1 are the two input fields of similar intensity, producing A_2 at $\omega_2 = \omega_3 - \omega_1$;
- optical parametric amplification (OPA): analogously to DFG, $A_3(0)$ and $A_1(0)$ are the two input fields; here, however, the input field A_1, called seed, is much weaker than A_3, which is called pump. The result of the interaction is the amplification of A_1 (signal) and the generation of A_2 (idler).

Assuming $A_3 \approx$ *constant* (no pump depletion) and $A_2(0) = 0$ (no initial idler), from Eq. A.5 we can find the following differential equation for the amplitude of the signal field [183]:

$$\frac{\partial^2 A_1}{\partial z^2} = -i\Delta k \frac{\partial A_1}{\partial z} + \Gamma^2 A_1, \tag{A.6}$$

where

$$\Gamma^2 = \frac{2d_{eff}^2 \omega_1 \omega_2}{c_0^3 \varepsilon_0 n_1 n_2 n_3} I_3. \tag{A.7}$$

By integrating the equations above, we can obtain the intensities of signal and idler beams (I_1 and I_2, respectively) as a function of the interaction length L, which are given by:

$$\begin{cases} I_1(L) = I_{10}\left[1 + \left(\frac{\Gamma}{g}\sinh gL\right)^2\right] \\ I_2(L) = I_{10}\frac{\omega_2}{\omega_1}\left(\frac{\Gamma}{g}\sinh gL\right)^2 \end{cases}, \tag{A.8}$$

where I_{10} is the initial intensity of the signal field at frequency ω_1 and $g = \sqrt{\Gamma^2 - \frac{\Delta k^2}{4}}$ is called *small-signal gain*. The *parametric gain* G is then defined as:

$$G(L) = \frac{I_1(L)}{I_{10}} = \left[1 + \left(\frac{\Gamma}{g}\sinh gL\right)^2\right]. \tag{A.9}$$

Equation A.9 shows that the amplification gain is crucially influenced by the following parameters:

- wavevector mismatch Δk: g, and hence G, decrease significantly as soon as Δk deviates from $\Delta k = 0$, which is called phase-matching condition;
- crystal non-linearity: the amplification is lager when d_{eff} is higher;
- pump intensity I_3: $G \sim e^{\sqrt{I_3}}$;
- crystal length L: $G \sim e^L$.

Despite we are mostly interested in the signal beam, it is important to notice that the idler beam plays a crucial role in the process of parametric amplification. This is because, since there is symmetry between the fields A_1 and A_2 (see Eq. A.5), the idler can also undergo parametric amplification, which simultaneously generates photons at the signal frequency. This positive feedback mechanism gives rise to the exponential gain over the interaction length and, if missing because of spatial or temporal walk-off between idler and pump, causes a significant gain reduction.

A.1.2 Broadband parametric amplification

When dealing with ultrashort pulses rather than monochromatic waves, additional care must be taken in order to achieve efficient amplification [183]. In the following, we discuss the key points that must be taken into account. A full theoretical description of this case, not presented here, can be based on the monochromatic parametric amplification described in the previous section, considering that short pulses can be considered a superposition of monochromatic waves.

Pulse-splitting length

Pulses with different carrier frequency propagate with different group velocity; this mismatch introduces a temporal walk-off that reduces the temporal overlap

of the interacting pulses. The relative group delay acquired by two pulses simultaneously entering a medium is $\left(\frac{1}{v_{gi}} - \frac{1}{v_{gj}}\right) z \equiv \delta_{ij} z$, where v_{gi} is the group velocity of the i-th beam and δ_{ij} is called *group-velocity-mismatch* (GVM). The propagation length after which, in absence of gain, the signal or the idler beam temporally separates from the pump pulse is called *pulse-splitting length* and it is given by [183]:

$$l_{j3} = \left| \frac{\tau}{\delta_{j3}} \right| = \left| \frac{\tau}{\frac{1}{v_{gj}} - \frac{1}{v_{g3}}} \right|, \tag{A.10}$$

where τ is the pump pulse duration. The pulse splitting length depends on pulse duration, crystal properties and propagation direction. Two different scenarios exist:

- if $\delta_{13}\delta_{23} > 0$, the amplification is limited by the pulse-splitting length because both signal and idler walk away from the pump in the same direction; saturation in reached after the smaller between l_{13} and l_{23} [183].
- if $\delta_{13}\delta_{23} < 0$, signal and idler pulses are temporally localized under the pump pulse because they walk away in opposite directions with respect to the pump; the parametric process can occur for propagation lengths longer than l_{i3} and the gain saturates at pump depletion [183].

Broadband phase-matching

As for the monochromatic case, phase-matching is crucial for an efficient amplification of ultrashort pulses. In this case, one wishes to have a constant gain over a large bandwidth, which requires the phase mismatch to be as small as possible over the whole bandwidth.
The wavevector mismatch Δk can be evaluated by first order expansion around $\bar{\omega}_1, \bar{\omega}_2, \bar{\omega}_3$, which represent the set of signal, idler and pump frequencies, respectively, that perfectly satisfy phase matching. In the collinear case (pump and seed beams propagating collinearly) and for a fixed pump frequency $\bar{\omega}_3$, the phase mismatch when the signal frequency changes to $\bar{\omega}_1 + \Delta\omega$ is given by [183]

$$\Delta k \simeq \left(\frac{1}{v_{g1}} - \frac{1}{v_{g2}} \right) \Delta\omega = \delta_{12} \Delta\omega. \tag{A.11}$$

The parametric gain bandwidth can then be approximately estimated by inserting Eq. A.11 into Eq. A.9. In the non-collinear case, the same Taylor expansion procedure can be applied, with the additional care of accounting for the vectorial nature of the phase-matching condition; this leads to the following phase-matching condition [183]:

$$v_{g1} = v_{g2} \cos\Omega, \tag{A.12}$$

where Ω is the angle between signal and idler propagation directions. Equation A.12 states that broadband amplification can occur when the projection of

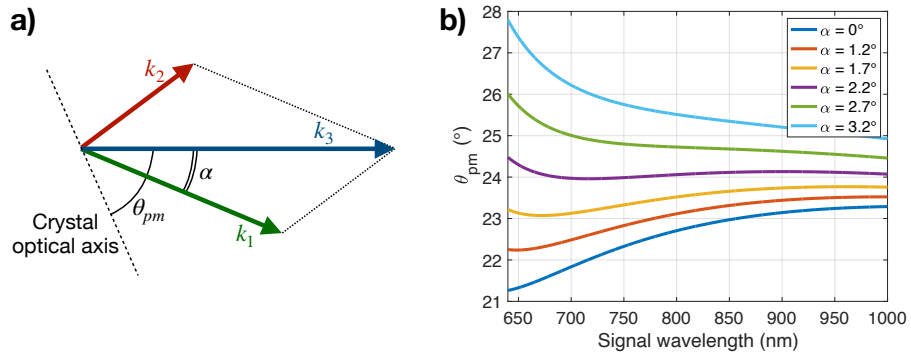

Figure A.1: a) Non-collinear phase-matching configuration obtained by tuning the angle of the optical axis of the non-linear crystal. Due to birefringence, the refractive index, and hence the wavevector, of the light with extraordinary polarization depend on the beam propagation direction with respect to the crystal optical axis. b) Phase-matching angle θ_{pm} as a function of signal wavelength λ_1 for different pump-seed angles α. The curves plotted here are calculated for the case of BBO crystal, type-I interaction with ordinary polarization for signal and idler beams, and extraordinary polarization for the pump beam (*ooe* configuration), and pump wavelength $\lambda_3 = 515$ nm.

the idler's group velocity along the signal propagation direction equals the group velocity of the signal; this is simply a generalization of the collinear case condition (where, according to Eq. A.11, $v_{g1} = v_{g2}$ provides the broadest phase-matching). Note also that Eq. A.12 can be satisfied only if $v_{g1} < v_{g2}$, i.e. if $\delta_{12} > 0$.

One approach commonly employed to achieve the phase matching condition is to exploit the birefringence of the non-linear crystal. In this case, it is possible to find a specific value of the angle between the pump beam propagation direction and the crystal optical axis (see Fig. A.1a), θ_{pm}, for which the phase matching condition is fulfilled. Efficient signal amplification can then be obtained by a suitable choice of the beams' polarization and propagation directions, and orientation of the crystal optical axis. Figure A.1b displays an example of the phase matching angle θ_{pm} for parametric amplification in a Type-I β-barium borate (β-BaB_2O_4 or, in short, BBO) pumped at 515 nm as a function of signal wavelength and for different angles α between the pump and the seed propagation directions. The plot shows that a non-collinear geometry can be advantageous for broadband amplification because it is possible to find a *magic angle*, around 2.2° for the case reported in Fig. A.1b, which allows amplification over the broadest bandwidth, as indicated by the θ_{pm} curve being flat over a broad range of wavelengths [183].

A.2 Setup layout

Many different OPA designs can be employed according to the the laser source and the desired properties of the amplified pulse (frequency range, time duration and energy per pulse). In general, however, all OPAs consist of three main parts:

- Seed pulse generation: supercontinuum generation is used to generate a broadband pulse to initiate the parametric amplification;
- Parametric amplification: the seed is overlapped to a suitable pump pulse in a nonlinear crystal where the amplification takes place, producing the signal beam;
- Pulse compression: the spectral phase accumulated by the amplified pulse is compensated in order to compress the signal to its transform limited duration.

The setup of our NOPA is displayed in Figure A.2 and it will be described in detail in the following sections.

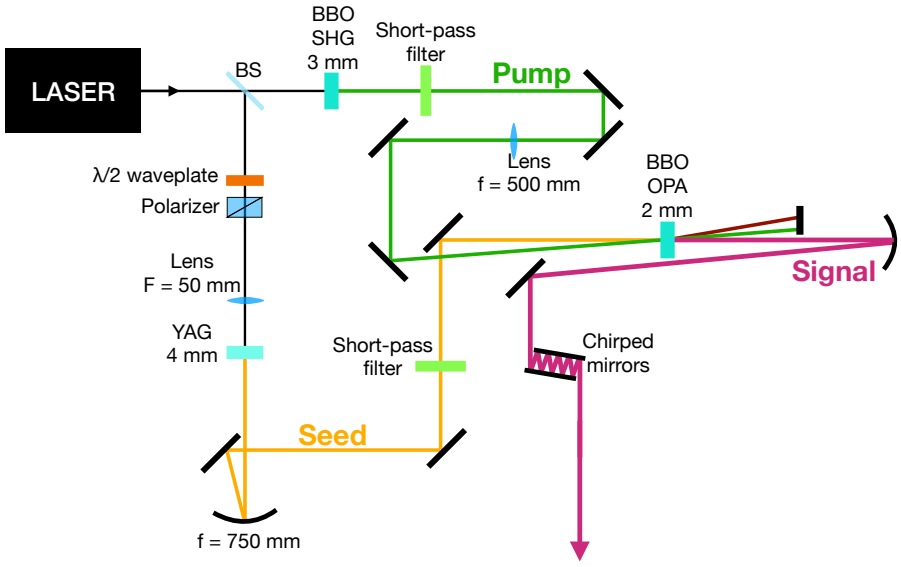

Figure A.2: Sketch of the optical setup employed for non-collinear parametric amplification.

A.2.1 Pump and seed pulses

Laser system. The laser system we are working with is a diode-pumped Yb:KGW laser (Pharos by Light Conversion), emitting ultrashort pulses at

1030 nm with 250 fs time duration. The laser emits 37.5 µJ pulses at 400 kHz repetition rate, resulting in 15 W average power. A pulse picker allows to change the repetition rate without varying the energy per pulse. 80% of the emitted radiation, i.e. 30 µJ/pulse, selected through a beam splitter, is routed into the NOPA setup. The light emerging from the laser has linear horizontal polarization, which is then rotated to vertical by a half-wave plate before entering the NOPA breadboard. The beam spot size is reduced through a telescope composed of a 500 mm focal length lens and a 150 mm focal length lens separated by 35 cm beam path.

Beam splitting. A pellicle beam splitter (Thorlabs CM1-BP5) is employed to split the beam into two parts, a low intensity one used for seed generation and a high intensity one for the NOPA pump. For vertical polarization and 1030 nm wavelength, $\approx 12\%$ of the light is reflected by the beam splitter, resulting in a 3.6 µJ pulse that can be employed for seed generation, and a 24 µJ/pulse beam to be used in the pump beamline.

Seed generation. The seed pulse is generated by white light generation (WLG), a phenomenon involving a number of non-linear processes that lead to wide spectral broadening [4]. In our setup, this is obtained by focusing a ≈ 1 µJ pulse on a 4 mm thick YAG (yttrium aluminum garnet) crystal by means of a 5 cm focal length lens. The optimal conditions for filamentation in the YAG crystal are achieved by fine tuning of the input pulse energy (by means of a half-wave plate and a polarizer selecting vertical polarization), the numerical aperture of the incoming beam (by means of an iris) and the beam focus position inside the YAG crystal [24, 293]. The resulting seed spectrum is plotted in Figure A.3; the spectral range extends up to 950 nm because the longer wavelengths are cut by a short-pass filter, required in order to remove the 1030 nm fundamental component that would otherwise undergo amplification.
The diverging beam that emerges from the WLG crystal needs to be re-focalized at the nonlinear crystal used for parametric amplification. In order to do so, we employ a $f = 75$ mm spherical mirror (f being the focal length) placed at a distance $d > f$ from the YAG crystal. In this way, we don't need an additional lens to focus the seed, therefore limiting the number of transmission optics on the optical path of the seed beam, which helps with keeping the seed pulse duration as small as possible.

Pump pulse. As a pump pulse for the parametric amplification, we employ a 515 nm beam obtained by second harmonic generation (SHG) of the laser fundamental wavelength in a 3 mm thick BBO. Similarly to the seed generation, the removal of the laser fundamental is of great importance also for the pump path. This is performed by a short-pass filter that absorbs the component at 1030 nm (Thorlabs FESH650).

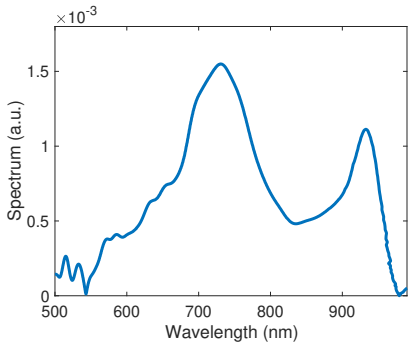

Figure A.3: Spectrum of the seed pulse obtained by WLG in a YAG crystal.

The choice of the pump wavelength is determined by the frequency range of interest for the signal pulse. In our case, we are interested in synthesizing pulses in the photon energy range between 1.2 eV and 1.9 eV. 515 nm is then an appropriate pump wavelength since it allows to amplify the components with photon energy smaller than 2.4 eV (see Eq. A.1). The lower bound of the amplifiable spectral range is, instead, manly determined by the transparency of the crystal (see Sec. A.2.2). We also need to keep in mind that the pump wavelength influences also the OPA gain: higher frequency means higher gain (according to Eq. A.9) but also larger GVM (i.e. shorter interaction length).

The energy per pulse of the pump beam is a key parameter since it strongly affects the pulse energy of the amplified beam. In our setup, the SHG process has $\sim 55\%$ efficiency resulting in 13.5 µJ pump pulses. A 500 mm focal lens shrinks the beam size to 160 µm FWHM diameter at the amplification spot; the pump fluence is then $\approx 67\text{mJ/cm}^2$ and the peak intensity is estimated ≈ 200 GW cm^{-2} assuming 250 fs pulse duration.

The pump pulse time duration does not directly affect the time duration of the amplified pulse. However, employment of a pump pulse with time duration longer or comparable to the seed one in preferable since this guarantees temporal overlap. Employment of transmission optics on the pump path (3 mm BBO, short-pass filter and lens) is, therefore, not expected to lower the OPA efficiency, but it rather contributes to stretch the pump pulse simplifying temporal overlap [183].

Spot size. Figure A.4 displays the pump and seed spots at the point of spatial overlap where the OPA interaction occurs. Since the seed is focused by a spherical mirror working not at perfect normal incidence, an iris is used to select the central section of the beam and improve its spot quality. From the images displayed in Fig. A.4, we estimate the spot diameter by performing a Gaussian

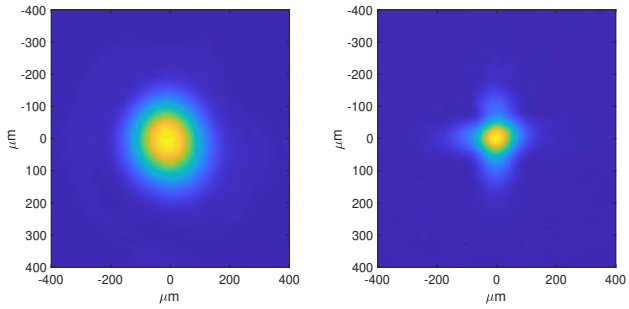

(a) Pump (b) Seed

Figure A.4: Imaging of pump and seed beams at spatial overlap.

fit on horizontal and vertical line profiles. This returns:

$$\begin{aligned} d_{PUMP,hor} &= 156\ \mu\text{m}, \quad d_{PUMP,ver} = 163\ \mu\text{m} \\ d_{SEED,hor} &= 104\ \mu\text{m}, \quad d_{SEED,ver} = 100\ \mu\text{m} \end{aligned} \tag{A.13}$$

These values fulfill the criterion of pump spot size larger than the seed spot size, which is the preferable configuration since it ensures homogeneous amplification [183].

A.2.2 Parametric amplification

OPA interaction crystal. The amplification process occurs in a type-I BBO crystal. This material is a suitable nonlinear medium for our laser system and desired NOPA properties because of the features listed below.

- Transparency range: 400 nm - 3 µm; in order to achieve amplification, both the signal and the idler wavelengths need to be within the transparency range of the crystal.
- Sufficiently high nonlinear coefficient: $d_{\text{eff}} = 2.15$ pm/V for type-I interaction in a crystal cut at an angle $\theta = 23.4°$.
- $\delta_{12} > 0$ in the range of interest, namely between 600 nm and 1000 nm, as needed in order to allow broadband phase amplification (see Eq. A.12).

Since, in this spectral range, we are in the case $\delta_{13}\delta_{23} > 0$, the crystal length needs to be chosen taking into account the pulse spitting length between the pulses. Assuming a pump time duration of 250 fs, from Eq. A.10 we estimate $l_{13}, l_{23} \sim 2$ mm for signal wavelengths in the range of interest (600-1000 nm). In non-collinear geometry, there is also a geometrical lateral walk-off between pump and seed beams. Since the pump spot size is ≈ 160 µm, the crystal length after which spatial overlap is lost is of the order of ~ 2 mm for $\alpha \sim 2°$, α being the angle between the pump and the seed propagation directions.

Another aspect to keep into consideration is that, in a birefringent medium, for the pulse with extraordinary polarization (the pump beam in our case), there is a walk-off between the beam propagation direction and its Poynting vector (birefringent walk-off) [183]. For BBO and $\theta = 23.4°$, the birefringent walk-off angle is $\rho = 3.3°$ at the pump wavelength 515 nm. Such effect can be mitigated by the fact that ρ is similar to the pump-signal internal angle, so that the birefringent walk-off and non-collinear walk-off can compensate each other.

Taking into account all of the above, we chose to employ a 2 mm thick BBO crystal for parametric amplification.

Pump-seed time delay. In order to find and tune the temporal overlap between pump and seed pulses, we employ a mechanical delay line that allows to vary the optical path of the pump beam. This not only facilitates NOPA alignment and optimization but also provides an additional degree of freedom that can be employed to tune the amplification frequency range by achieving temporal overlap between the pump pulse and a specific wavelength region of the chirped seed pulse.

A.2.3 Properties of the amplified pulse

The setup described above allows us to perform optical parametric amplification for synthesizing the desired light pulses. Here, we briefly summarize the properties of the NOPA output pules.

Pulse energy. Upon suitable optimization of the alignment (BBO orientation, pump-seed time delay and spatial overlap), the energy per pulse of the amplified signal can reach values to 1.25 µJ per pulse.
As discussed in Chapter 2, the output signal of the NOPA is employed for 2DES and it serves as both the pump and the probe pulses. Considering that the pump beam intensity is strongly attenuated by the large amount of optics encountered along the pump optical path before hitting the sample, such large energy per pulse is needed in order to guarantee sufficiently high intensity of the pump excitation at the sample position. For pump spot size of the order of 200 µm × 200 µm at the sample, fluences up to 400 µJ/cm^2 can easily be reached.

Spectrum. Figure A.5a displays three possible spectra of the amplified pulse. Tunability of the spectral range of parametric amplification can be achieved by rotating the BBO crystal and by optimizing the pump-seed temporal overlap. The spectral range between 650 and 950 nm can be covered, with the broadest bandwidth that can sustain a transform limited pulse duration of 10 fs. Tuning

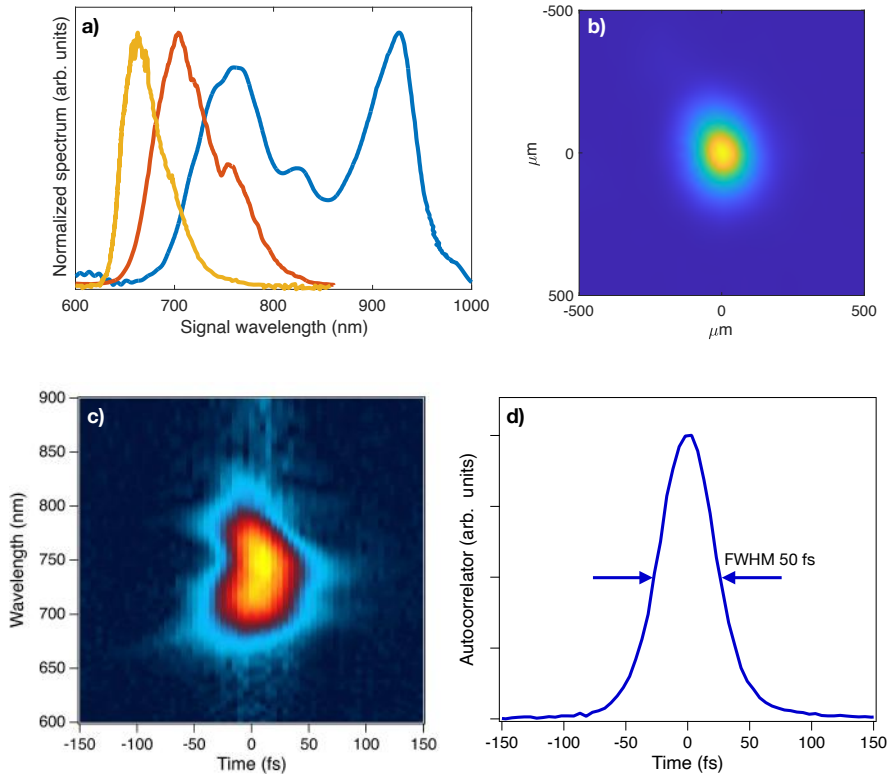

Figure A.5: a) Spectra of the amplified pulse emitted by the NOPA, which can be tuned in the 650-950 nm range. b) Image of the amplified signal beam spot collected by a CMOS camera. c) PG-FROG trace of the NOPA signal compressed by a pair of chirped mirrors. d) Autocorrelator of the NOPA signal pulse, indicating a 35 fs time duration.

the signal amplification towards shorter wavelengths (towards 600 nm) is possible but this strongly reduces the amplified bandwidth.

Signal spot size. The NOPA signal is collected and collimated by means of a 20 cm-focal length spherical mirror, which routes the beam into the last section of the amplifier, that is the pulse compressor. In order to evaluate the spatial quality of the amplified beam, we analyze the shape and size of the beam spot upon focalization, as needed in order to perform ultrafast spectroscopy experiments. We employ a 40 cm-focal length spherical mirror to focus the beam onto a CMOS camera (Thorlabs DCC1545M); the collected image, displayed in Figure A.5b, shows a homogeneous and quite symmetrical beam. The spot size is estimated by fitting a horizontal and a vertical profile with a Gaussian

function; the resulting FWHM of the two profiles are:

$$d_{SIG,hor} = 172 \text{ µm}, \quad d_{SIG,ver} = 213 \text{ µm}. \tag{A.14}$$

Time duration. The last section of the NOPA setup consists in a pulse compressor, which is required whenever generating sub-50 fs pulses since compensation for the positive chirp introduced by material dispersion (YAG crystal, amplification BBO crystal, filters) is needed. In order to do so, we employ a pair of chirped mirrors (Layertec), which are layered reflective optics that introduce a negative group delay dispersion (GDD) at each reflection. In our setup, we employ a pair of chirped mirrors introducing GDD = - 50 fs^2 at each reflection. Since the dispersion introduced by the chirped mirrors can by varied only discretely, fine tuning by means of propagation within a material of variable thickness is required. As further pulse compression of, separately, pump and probe beams, is required at a later stage in the 2DES steup (see Section 2.5.2), we here only employ a pair of chirped mirrors where the signal beam is reflected 14 times (7 reflections on each mirror), which results in the best pulse compression achievable in our NOPA.

In order to estimate the time duration of the amplified pulses, we performed polarization-gating frequency-resolved-optical gating (PG-FROG) [290]. The measured PG-FROG trace is plotted in Fig. A.5c for an amplified signal covering the spectral range between 680 and 800 nm. Figure A.5d displays the corresponding autocorrelation signal (equivalent to PG-FROG signal integrated along the wavelength axis), which shows a 50 fs FWHM, corresponding to ∼35 fs pulse duration of the NOPA signal.

APPENDIX B

Lead halide perosvkite superlattices: sample characterization

This chapter has been adapted from the following manuscripts:

Halide Perovskite Artificial Solids as a New Platform to Simulate Collective Phenomena in Doped Mott Insulators, A. Milloch, U. Filippi, P. Franceschini, M. Galvani, S. Mor, S. Pagliara, G. Ferrini, F. Banfi, M. Capone, D. Baranov, L. Manna, and C. Giannetti, *Nano Letters*, 2023, 23, 10617 - 10624, doi: 10.1021/acs.nanolett.3c03715

The fate of optical excitons in $FAPbI_3$ nanocube superlattices, A. Milloch, U. Filippi, P. Franceschini, S. Mor, S. Pagliara, G. Ferrini, F. V. A. Camargo, G. Cerullo, D. Baranov, L. Manna and C. Giannetti, *ACS Photonics*, 2024, 11, 9, 3511–3520, doi: 10.1021/acsphotonics.4c00105

Lead halide perovskite superlattices are cubic arrays of perovskite nanocrystals. Their synthesis and characterization was performed by the Nanochemistry group of the Italian Institute of Technology (IIT, Genova). In this appendix we summarize the main steps and results in the sample preparation and characterization. All details of nanocrystal synthesis and superlattice preparation, as well as sample aging, can be found in Ref. 198 and in Ref. 199 for the $CsPbBr_3$ and FAPI samples, respectively.

B.1 $CsPbBr_3$ nanocube superlattices

B.1.1 Samples

The fabrication of superlattices (SLs) is accomplished by drop-casting a toluene dispersion of nanocubes of mean lateral size ~ 8 nm onto a silicon substrate and letting the solvent evaporate overnight. During this process, the nanocubes spontaneously assemble into superlattices with sizes of 1-10 µm.

Disordered nanocubes films are fabricated starting from the same synthetic batches of superlattice films, and using fast solvent evaporation and mechanical scrambling (e.g. spreading or crushing). The disordered nature of nanocubes films prepared in such a way was characterized by X-ray diffraction, as discussed below (Sec. B.1.2). The lack of preferred orientation and superlattice diffraction signatures in diffraction patterns [289, 286] was taken as an evidence of random orientations of nanocubes in the sample.

B.1.2 Characterization of SL and disordered films

X-ray diffraction.

X-ray diffraction (XRD) patterns collected from disordered NCs film and superlattice sample are shown in Figure B.1.
For disordered NCs, the XRD pattern shows the Bragg reflections ascribed to the orthorhombic structure of $CsPbBr_3$ [171] and all the peaks expected from a film of randomly oriented NCs [289]. Conversely, for the SL sample, we observe the presence of two strong peaks at $2\theta \sim 15°$ and $2\theta \sim 30.5°$. As described in detail in previous works [289, 286], this XRD pattern originates from a close-packing of the cubes in the plane parallel to the substrate, which leads to the enhanced Bragg reflections from (110), $(1\bar{1}0)$ and (002) ($2\theta \sim 15°$) and (220), $(2\bar{2}0)$ and (004) ($2\theta \sim 30.5°$) planes of the orthorombic unit cell of $CsPbBr_3$. The precise periodicity between NCs inside SLs produces a phase modulation on the diffracted X-rays, causing additional interference which produces the fine structure for the $2\theta \sim 15°$ peak, observable in Figure B.1b (black solid line).

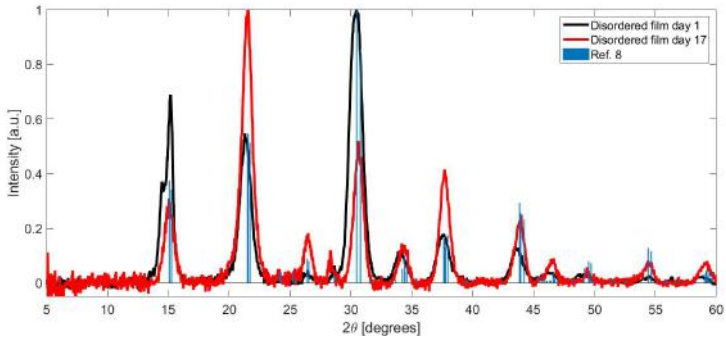

(a)

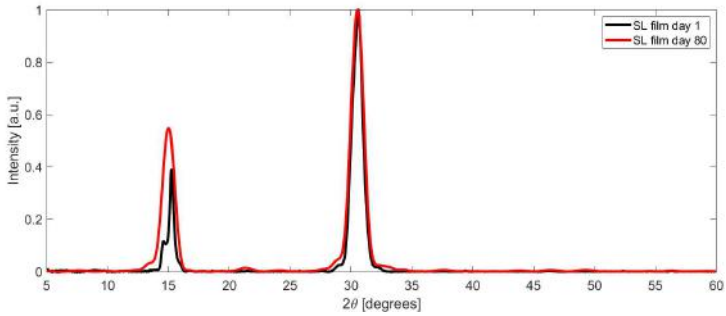

(b)

Figure B.1: XRD patterns of disordered NCs film (a) and superlattice film (b). The blue lines in (a) represent the Bragg peaks positions reported in literature (Ref. 171) for CsPbBr$_3$.

Photoluminescence and absorbance

The samples were optically characterized by absorbance and photoluminescence (PL) spectra. The equilibrium PL and absorption spectra of NCs dispersed in toluene and of NC deposited on a glass substrate are displayed in Figure B.2a and b for disordered NC and superlattices respectively. In both cases, we observe a PL red-shift (ΔPL_{NC} = 2.414 eV - 2.382 eV = 32 meV for the disordered NCs sample and ΔPL_{SL} = 2.414 eV - 2.386 eV = 28 meV for the SLs sample) and a PL peak broadening (ΔFWHM_{NC} = 142 meV − 86 meV = 55 meV for disordered NCs and ΔFWHM_{SL} = 116 meV - 86 meV = 30 meV for SLs) for the deposited films compared to NCs in toluene dispersion, consistently with previous observations [14, 147, 208, 295, 285].

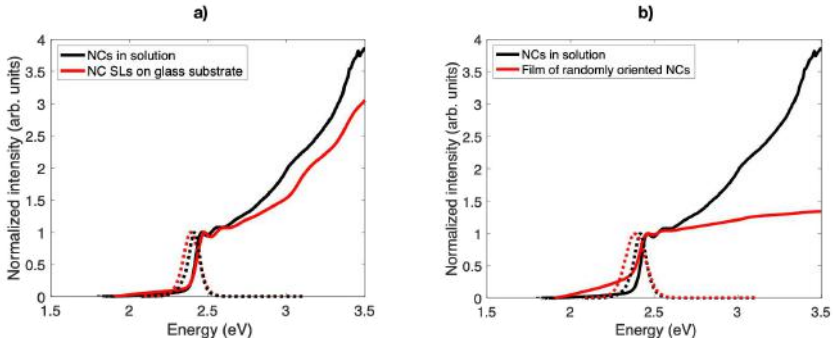

Figure B.2: a) Room temperature PL (dashed line) and absorption (solid line) spectra of NCs dispersed in toluene (black) and of disordered NCs on a glass substrate (red). b) Room temperature PL (dashed line) and absorption (solid line) spectra of NCs dispersed in toluene and of NC SLs deposited on a glass substrate.

Optical microscopy.

Optical microscope images of the NCs films are displayed in Figure B.3. For the disordered NCs film (Fig. B.3a), the image shows a roughly homogeneous spatial distribution of $CsPbBr_3$ NCs; no well-defined micron-sized rectangular structure, that typically corresponds to SLs, is observable in the sample, suggesting that mechanical scrambling produces largely disordered NC film. In the SL sample (Fig. B.3b), the NCs are assembled into aggregates of rectangular shape and size between 1 and 10 µm, each corresponding to a NC superlattice.

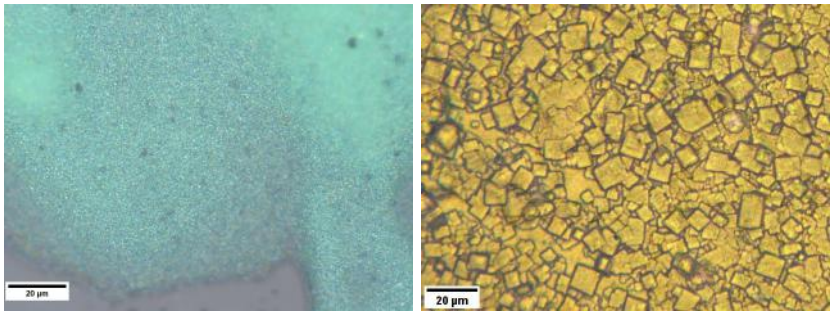

(a) (b)

Figure B.3: Optical microscopy images of disordered NCs film (a) and superlattice film (b).

B.2 FAPI$_3$ nanocube superlattices

B.2.1 Samples

$FAPbI_3$ (or FAPI) nanocubes (NCs) are synthesized following the procedure reported in Ref. 3. $FAPbI_3$ nanocube superlattices are then obtained by drop casting the solution of NCs dissolved in toluene on a 1 cm × 1 cm Si substrate; slow solvent evaporation results in the self-assembling of the FAPI nanocubes into ordered arrays, namely the superlattices. In order to obtain the disordered sample, the same nanocube synthesis was employed. The crude solution is then centrifuged in order to extract the precipitate, which is spread on a 1 cm × 1 cm Si substrate with a plastic scoop.

B.2.2 Sample characterization

X-ray diffraction

The XRD pattern of a film of FAPI NC superlattices is shown in Figure B.4 (top panel) and compared to the XRD pattern of a film of randomly oriented nanocubes (bottom panel).

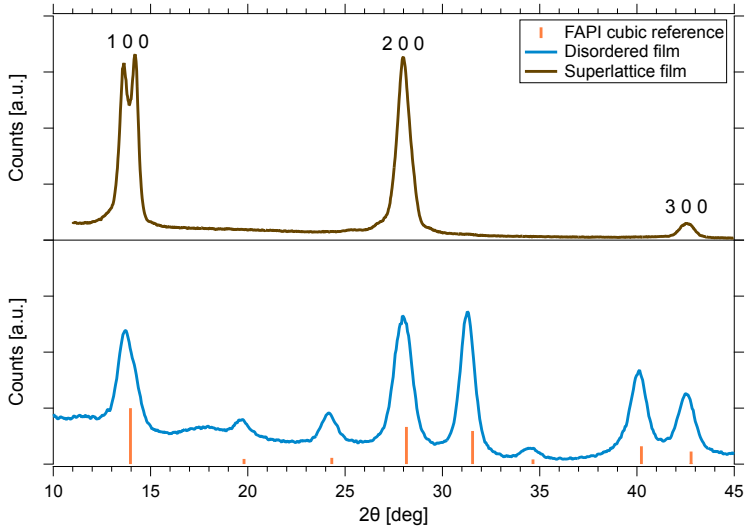

Figure B.4: XRD pattern of a nanocrystal superlattice film (brown solid line, top panel) and of a disordered film composed of randomly oriented nanocubes (blue solid line, bottom panel). The reference for the cubic structure (orange lines) is taken from Ref. 73.

The first peculiar feature that characterizes the XRD pattern of superlattices in Figure B.4 is the enhancement of some reflections with respect to others which belong to the same cubic phase of FAPI. This is a consequence of preferential orientation which comes from the fact that nanocrystals assemble with the (100) planes parallel to the substrate. Conversely, XRD pattern of the disordered sample displays all the peaks of the perovskite cubic structure. The second feature that marks the presence of superlattices is the splitting of the first Bragg reflection ($2\theta = 13.87°$): as explained in detail in previous works (Refs. 286 and 287), it originates from an additional interference which comes from the exact periodicity of NCs inside SLs and results in the fine structure observable in Figure B.4.

In order to confirm the continuous phase transition from the room temperature cubic α-phase ($Pm\bar{3}m$) to the low temperature tetragonal β-phase ($P4/mbm$) expected for the FAPI NCs (occurring around 285 K in the bulk counterpart [73, 305]), low-temperature XRD measurements in vacuum atmosphere were performed. In order to appreciate all the Bragg reflections belonging to the different crystal phases the measurement was performed on the film of randomly oriented nanocrystals. The resulting XRD patterns are shown in Figure B.5: it is possible to notice that, upon cooling, there is a shifting of the peaks towards higher angles, consistent with a shrinking of the lattice parameters expected with the decreasing of temperature, and the appearing of three new peaks, highlighted by transparent light blue columns, at $2\theta = 22.2°$, $26.3°$and $36.2°$, which belong to the low temperature tetragonal β-phase [73], and confirm the transition from the high symmetry cubic phase to the lower symmetry tetragonal phase.

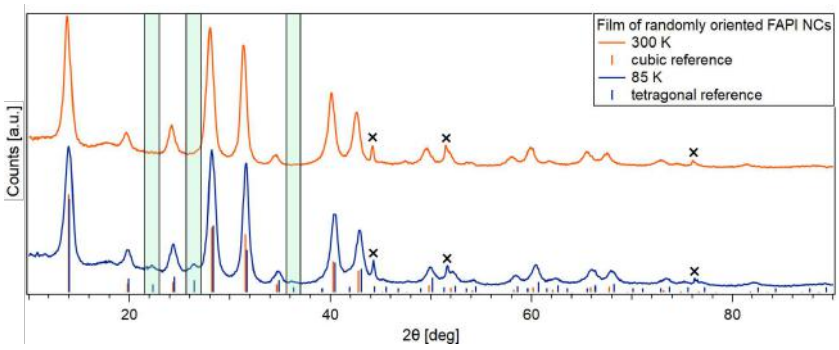

Figure B.5: XRD patterns at 300 K and at 85 K of a film of randomly oriented FAPI NCs (Ref. 73). The transparent light blue columns emphasize the new peaks arising with the phase transition. The "×" symbol indicates the impurity peaks belonging to the $FeNi_3$ sample holder (ICSD number 188242).

Optical microscopy

Figure B.6 reports optical microscope images of both the superlattice (right panel) and the disordered (left panel) samples. For the disordered NCs film, the image shows a roughly homogeneous spatial distribution of deposited material, suggesting that mechanical scrambling produces largely disordered NC film. Conversely, optical microscopy images of the superlattice sample (right panel), display ~ 1 µm aggregates each corresponding to a superlattice of FAPI nanocubes.

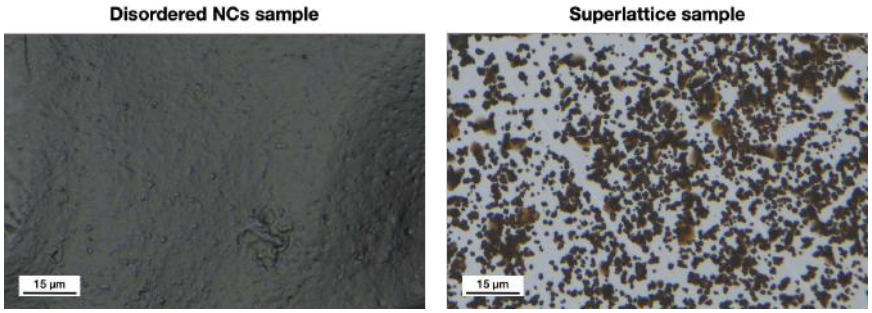

Figure B.6: Optical microscopy images of a film of randomly oriented nanocubes (left panel) and of a nanocube superlattices sample (right panel).

Transmission electron microscopy

FAPI nanocrystals and nanocrystal superlattices were characterized by means of transmission electron microscopy (TEM). By extracting the size distribution of the FAPI nanocrystals from 10 TEM images (similar to the one shown in Figure B.7a), we estimate a nanocube edge length of 9.7 ± 2.3 nm (for a total number of measured NCs ≈ 10000).

Photoluminescence and absorbance

Figure B.8 displays the equilibrium PL spectrum, measured under 350 nm excitation, and the absorbance spectrum of NCs dispersed in toluene and of NC superlattices deposited on a glass. We observe a red-shift of the PL of NCs assembled into superlattices, compared to NCs in toluene dispersion (max $PL_{superlattice}$−max $PL_{solution} = 1605$ meV -1635 meV $= -30$ meV) together with a PL broadening (FWHM$_{superlattice}$− FWHM$_{solution} = 122$ meV -102 meV $= 20$ meV).

In order to better characterize the equilibrium optical properties of the superlattice sample employed for 2D spectroscopy, we fit a multi-peak model to the PL and absorbance spectra (Figure B.9). The photoluminescence spectrum

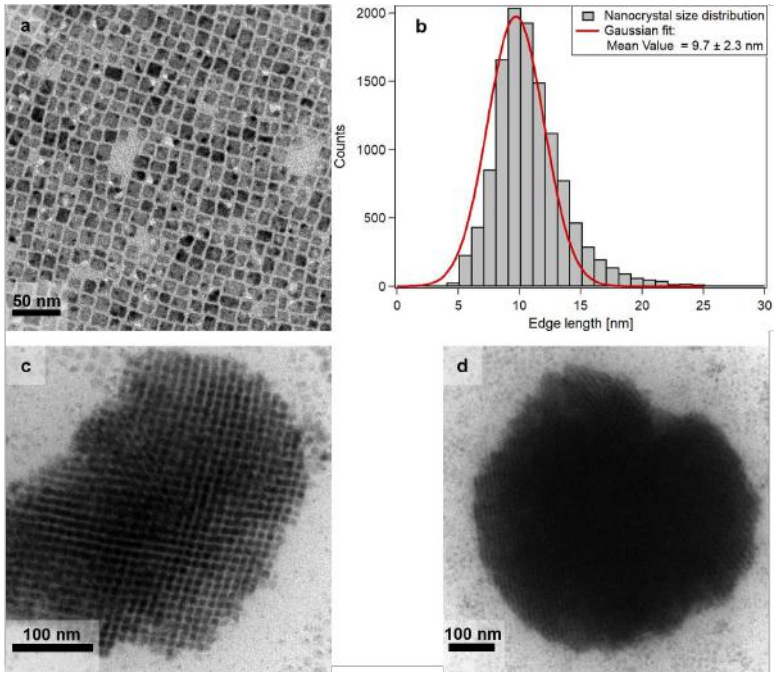

Figure B.7: a) TEM picture of FAPI NCs. b) NC size distribution calculated with ilastik software. c,d) TEM pictures of FAPI NCs superlattices.

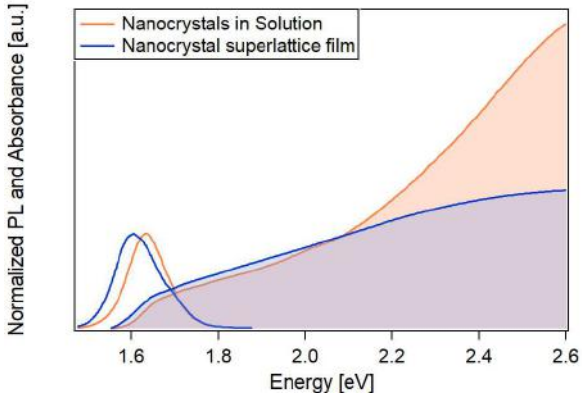

Figure B.8: Photoluminescence (solid lines) and absorption (filled areas) spectra of NCs in toluene dispersion and NCs superlattices.

is well described by two Gaussian peaks centered at 1.681 ± 0.004 eV and 1.603 ± 0.002 eV, corresponding to an energy separation $\Delta = 78 \pm 6$ meV. The full width at half maximum (FWHM) of the two peaks is 96 ± 2 meV and 103 ± 5 meV, respectively.

The absorbance spectrum hints at the presence of two excitonic-like resonances in the energy range between 1.6 and 1.8 eV, which are better resolved by 2DES. While an accurate analysis of the linear spectrum is hindered by the presence of broad and overlapping features, the data are compatible with the presence of two excitonic-like peaks described by the Elliott model [72]. For each of the two contributions, the absorption spectrum is described by an equation of the form

$$A_0\theta(\hbar\omega - E_g)\frac{\pi e^{\pi x}}{\sinh(\pi x)}\frac{1}{1 - b(\hbar\omega - E_g)} + A_0 R_{ex} 4\pi\delta(\hbar\omega - E_g + R_{ex}) \quad \text{(B.1)}$$

where E_g is the bandgap, R_{ex} is the exciton binding energy, A_0 is an amplitude parameter, b is a parameter taking into account the non-parabolicity of the bands, δ is the Dirac delta function and θ is the Heaviside step function [316, 241, 315]. Equation B.1 is then convoluted with a Gaussian to account for inhomogeneous broadening. According to the best fit (red solid line in Fig B.9b), the conduction band edge is located at 1.750 ± 0.007 eV, while the two peaks are centered at 1.65 ± 0.01 eV and 1.72 ± 0.01 eV and have a FWHM of 94 ± 5 meV and 90 ± 9 meV, respectively. The presence of two structures agrees with the 2D spectroscopy data discussed in the main text. Based on the 2DES spectra, these two structures can therefore be assigned to a trap state and an exciton state for the lower and higher energy peak, respectively.

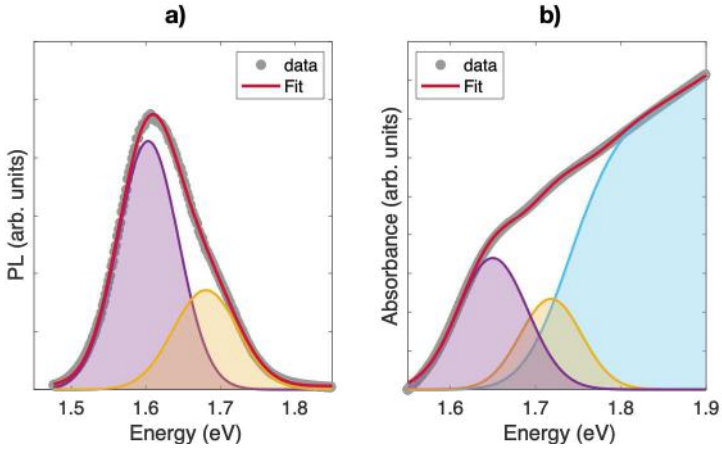

Figure B.9: Fit of photoluminescence (a) and absorption (b) spectra of NCs superlattice.

APPENDIX C

Pump-probe on $CsPbBr_3$ nanocube superlattices: differential fit analysis

This chapter has been adapted from the following manuscript:

Halide Perovskite Artificial Solids as a New Platform to Simulate Collective Phenomena in Doped Mott Insulators, A. Milloch, U. Filippi, P. Franceschini, M. Galvani, S. Mor, S. Pagliara, G. Ferrini, F. Banfi, M. Capone, D. Baranov, L. Manna, and C. Giannetti, *Nano Letters*, 2023, 23, 10617 - 10624, doi: 10.1021/acs.nanolett.3c03715

C.1 Equilibrium optical properties

Analysis of the pump-probe data by means of differential fitting of $\Delta R/R$ spectra requires a parametrization of the $CsPbBr_3$ optical constants at low temperature (T). We therefore build the real and imaginary parts of the low-T refractive index by employing a suitable Kramers-Krönig consistent model, where the relevant parameters are chosen in agreement with the energy values obtained from the experimental absorbance measured at room temperature (see Fig. B.2b in Appendix B.1) and with the temperature dependent trends reported in literature.

The real part of the optical conductivity, σ_1, is obtained as the sum of a sigmoid function, accounting for the conduction band edge, a Drude-Lorentz oscillator, describing the exciton resonance, and a background component modelled through a high-energy Drude-Lorentz oscillator (Fig. C.1a). The conduction band gap energy is red-shifted by ∼80 meV as compared to room temperature (Fig. B.2b in Appendix B.1) and the amplitude of the exciton peak is increased compared to the edge amplitude, consistently with the temperature dependence of $CsPbBr_3$ absorption spectra reported in literature [110, 252]. The exciton binding is fixed at 43 meV, in agreement with literature reports [225, 163] and experimental absorbance (Fig. B.2b in Appendix B.1). The imaginary part σ_2 is then computed from Kramers-Kroïig relations. The resulting real and imaginary parts of the refractive index (n and k, respectively) are plotted in Figure C.1b. We note that the results of the differential fitting procedure of pump-probe data are robust if small changes of the equilibrium dielectric function are introduced.

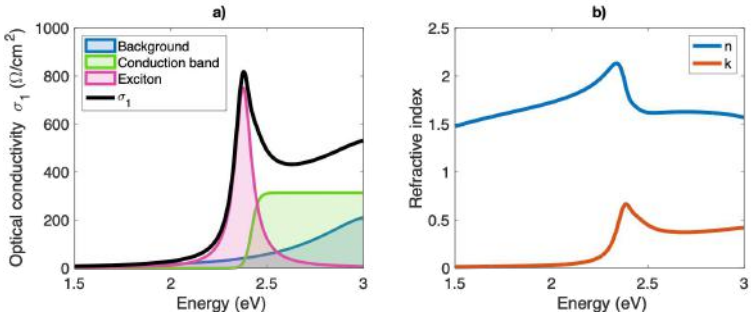

Figure C.1: a) Parametrized real part of the optical conductivity at low temperature (black line). Filled areas represent the different components included in σ_1. b) Real (n) and imaginary (k) parts of the parameterized low temperature refractive index.

C.2 $\Delta R/R$ fitting procedure and results

For each measured pump-probe time delay Δt between 4 ps and 130 ps, the spectrally resolved reflectivity variation $\Delta R/R$ is fitted with a function

$$\frac{\Delta R}{R} = \frac{R_{outeq} - R_{eq}}{R_{eq}} \tag{C.1}$$

where R_{eq} is the equilibrium reflectivity estimated as $((1-n)^2+k^2)/((1+n)^2+k^2)$, n and k being the real and imaginary parts of the refractive index plotted in Figure C.1b. R_{eq} is evaluated as the normal incidence bulk reflectivity because the light penetration depth in the photon energy range of interest is $\lesssim 1$ µm, which is smaller than the film overall thickness (on the order of ~ 10 µm). R_{outeq} is the out-of-equilibrium reflectivity, computed with the same procedure

employed for R_{eq} and containing the fit parameters. The free parameters for the differential fit are the out-of-equilibrium free-carriers edge energy position, the sigmoid edge width, the exciton energy and the exciton spectral weight, which represents the smallest subset of free parameters necessary to reproduce the out of equilibrium reflectivity at all fluences and all timescales. The data collected from NC superlattices require to include in the out-of-equilibrium optical conductivity also an additional feature at energy ∼2.36 eV, which is smaller then the exciton resonance. Since, at long time delays ($\Delta t \gtrsim 50$ ps), the pump-probe map in Figure 5.4b shows two distinct peaks between 2.30 eV and 2.37 eV, the experimental data is best described by modelling the new feature below band gap as a sum of two Drude-Lorentz oscillators centered at slightly different energies. This double-peak behaviour likely originates from local inhomogeneities of the samples within the photo-excited area, where superlattices of different lateral size or assembled from NCs of different size can be present and contribute to the measured signal. Figure C.2a and b show the the best differential fit at short (5 ps) and long (89 ps) time delays respectively, as reference examples. Fig. C.2c and d report the various components of the corresponding out-of-equilibrium optical conductivity (solid lines) obtained from the best fit to the data.

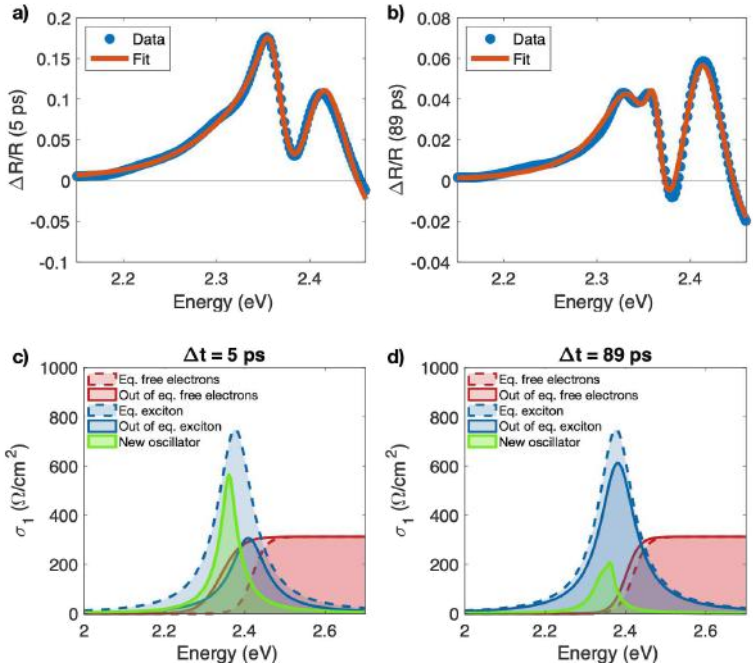

Figure C.2: Differential fit of $\Delta R/R$ data measured on NCs superlattices at 17 K with 230 μJ/cm^2 excitation fluence. a) and b) show the fitted spectra at 5 ps and 89 ps respectively. c) and d) report the equilibrium (dashed lines) and out of equilibrium (solid lines) components of the optical conductivity.

The output parameters of the fit performed at all time delays are displayed in Figure C.3, where the blue solid lines represent the values at equilibrium and the red markers are the out-of-equilibrium values extracted from the fit. The top row reports the free-carriers sigmoid edge parameters: the edge amplitude (Fig. C.3a) is kept constants at all Δt; the red-shift (Fig. C.3b) observed after pump excitation decays with two distinct dynamics, a fast one ($\sim$ 20 ps) and a lower one taking place over hundreds of ps timescale; the edge width displays a broadening in the first $\sim$ 30 ps. Interestingly, this kind of response for the position of the conduction band edge, surviving on a $\sim$ 100 ps timescale, is remarkably different from what usually reported for above-resonance excitation experiments in similar materials, where the large number of free carriers injected in the conduction band leads to a very fast band-gap renormalization followed by a band filling effect after $\sim$ 1 ps [8, 83, 224]. The second row in Fig. C.3 shows the dynamics of the parameters of the Drude-Lorentz oscillator relative to the excitonic line, namely the exciton energy (Fig. C.3d), the plasma frequency ω_p (Fig. C.3e) and the exciton width (Fig. C.3f). The exciton width does not show significant changes during the relaxation dynamics and is therefore kept constant at all Δt to increase the stability of the fitting procedure. The two bottom rows in Figure C.3 report the parameters relative to the Drude-Lorentz oscillators appearing out of equilibrium and associated to the emergence of the cooperative behaviour discussed in the main text. Whereas one single new oscillator is needed to qualitatively reproduce the spectral feature around 2.36 eV at short time delays, two distinct oscillators allow to fit the more structured response observed at long time delays. For consistency, we employed the same model with two new oscillators also at short time delays, where the effect of two distinguished components is covered by the free-carriers edge shift and therefore the error-bars of the associated parameters are larger.

It is relevant to point out that the details of the model employed to fit the $\Delta R/R$ have only a marginal effect on the overall result of the fitting procedure. In addition to what presented in Fig. C.3, we tested out other models that involved either only one new oscillator, no free-carriers edge width variation, a narrower edge width at equilibrium, or different starting points for the parameters in Fig. C.3g-l. Whatever the fit function employed, the extracted parameters and their relative dynamics display always compatible values and similar trends: the red-shift of the free-carriers edge decaying with two distinct dynamics, the blue-shift and the quench of the exciton recovering to the equilibrium values over $\sim$100 ps and the appearance of new oscillators that are red-shifted and narrower than the equilibrium excitonic peak.

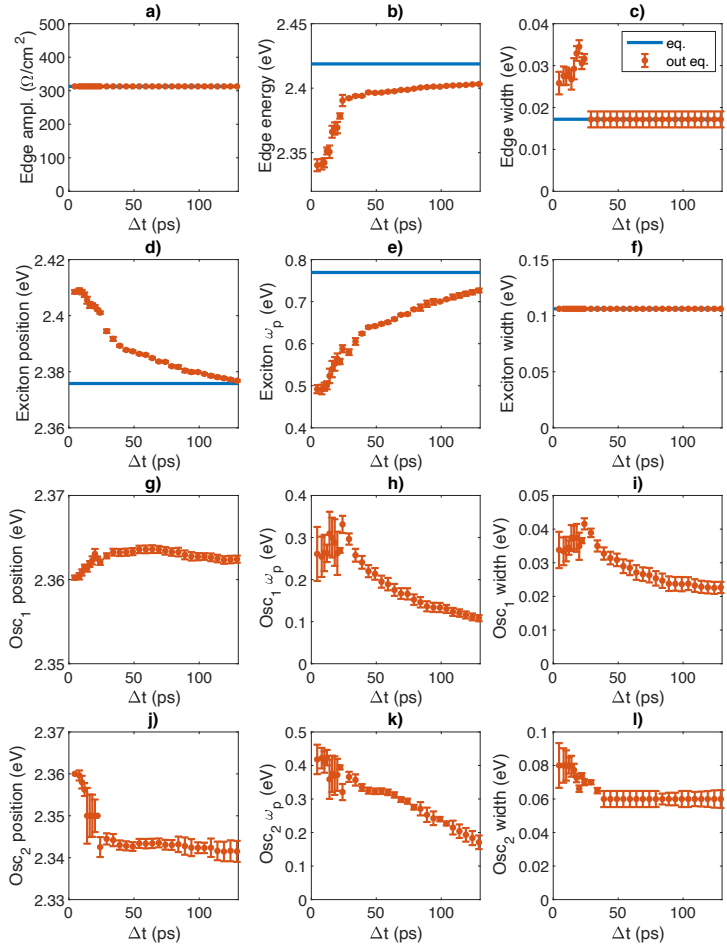

Figure C.3: $\Delta R/R$ fit output parameters for the superlattice NCs sample at 230 µJ/cm^2 excitation fluence. a), b) and c) are the free-carriers edge amplitude, center energy and width, respectively. d), e) and f) represent the exciton parameters: exciton energy, plasma frequency and width, respectively. g)-l) display the Drude-Lorentz model parameters for the new oscillators.

Starting from the differential fit model, we can calculate the total spectral weight introduced in Eq. 5.6:

$$SW_{tot} = \int_0^{+\infty} \sigma_{1,tot}(\omega) d\omega \tag{C.2}$$

which is, by definition, a conserved quantity depending on the total number of electrons in the system [308]. In particular, we obtain from the data the different contributions:

$$SW_{tot} = SW_{2.36eV} + SW_{exc} + SW_{free} \tag{C.3}$$

where $SW_{2.36eV}$ is the spectral weight of the photo-induced cooperative peak at 2.36 eV, SW_{exc} is the spectral weight of the excitonic peak already present in the equilibrium optical conductivity, and SW_{free} is the spectral weight associated to the direct across-gap transitions. Inspection of the spectral weight transfer between the exciton resonance and the free-carrier band is then performed by computing the spectral weight variation ΔSW, compared to equilibrium, of the different components coming into play. Figure C.4 reports ΔSW of each component, estimated as the integral of the optical conductivity σ_1 over the energy axis. We observe that the SW lost after photo-excitation by the exciton peak is re-distributed between the new oscillators and free-carrier states in conduction band. At $\Delta t = 5$ ps, for example, the photo-induced decrease of the excitonic spectral weight ($\Delta SW_{exc} \simeq$ -74 ΩeV/cm^2) is perfectly compensated by both the new peak at 2.36 eV ($\Delta SW_{2.36eV} \simeq 49$ ΩeV/cm^2) and by an increase of in-gap free electron states ($\Delta SW_{free} \simeq 25$ ΩeV/cm^2). Overall, the spectral weight is conserved at all time delays, as shown by the black markers in Figure C.4 representing the sum of all SW variation contributions, which is compatible with zero at all time delays.

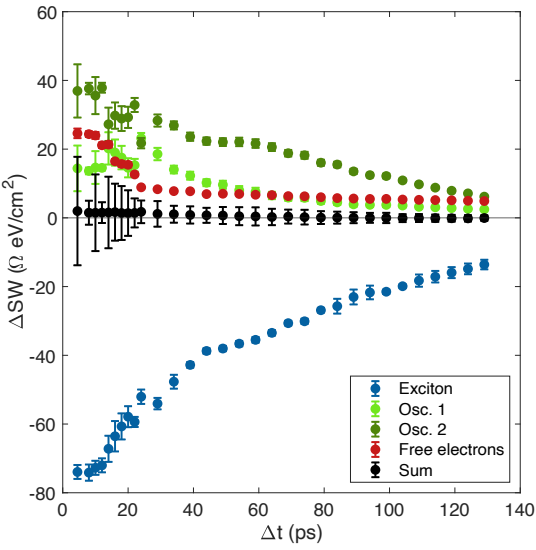

Figure C.4: Spectral weight variation of the exciton (blue), new oscillators (green), and conduction band (red) after pump excitation. Black points represent the sum of the four contributions, indicating SW conservation.

The same fitting procedure is applied to the data collected on the same superlattice sample with lower excitation fluence (30 µJ/cm^2), plotted in Figure C.5. The fit results are displayed in Figure C.6 for two time delays (5 ps and 89 ps) and in Figure C.7 (fit output parameters for all time delays). In this lower fluence excitation scheme the free-electron states edge red-shift is smaller and relaxes with a slow dynamics of 130 ps decay time. The exciton does not show any energy shift, but its spectral weight decreases and is transferred to new oscillators appearing out of equilibrium. Since the free-electrons edge amplitude and width as well as the exciton position and width do not show any significant variation during the relaxation dynamics, they are kept fixed to increase the fit stability.

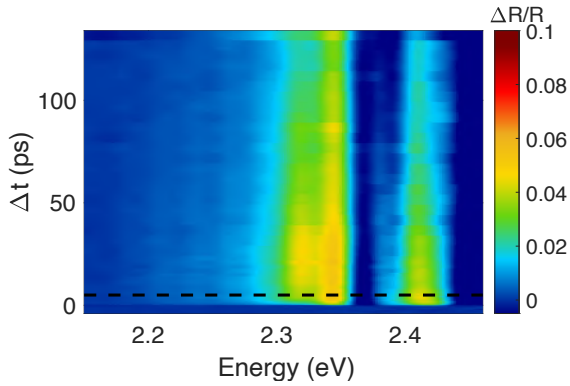

Figure C.5: Ultrafast transient reflectivity of $CsPbBr_3$ superlattice sample measured at 17 K and low excitation fluence (30 µJ/cm^2).

For the disordered NCs sample ($\Delta R/R$ data in Fig. 5.4a), the fit output is reported in Figures C.8 and C.9. In this case, no additional oscillator is needed to reproduce the out of equilibrium optical conductivity. After pump excitation, a red-shift of the free-carriers edge decaying over a $\sim$ 20 ps timescale is revealed, along with a broadening of the edge width and a decrease of the exciton spectral weight. No significant variation of the free-electrons edge amplitude and of the exciton position and width is observed.

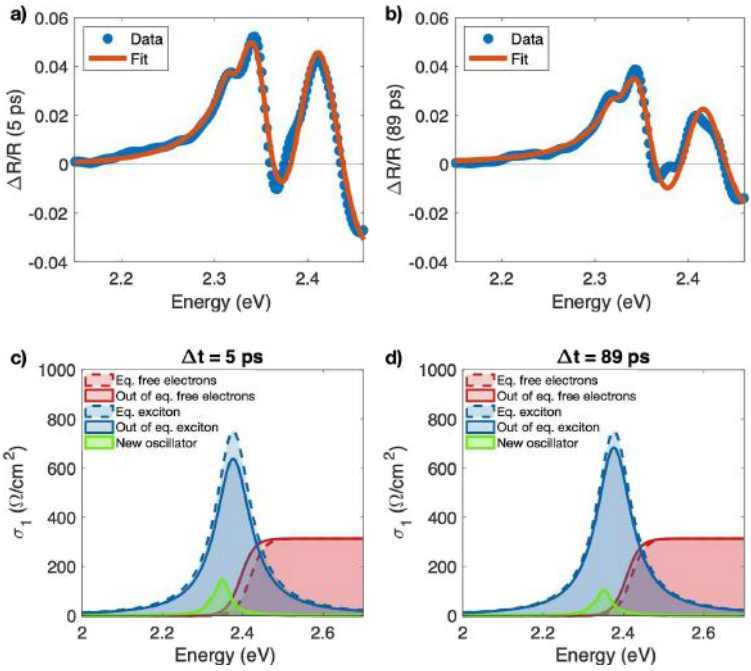

Figure C.6: Differential fit of $\Delta R/R$ data measured on NCs superlattices at 17 K with 30 μJ/cm^2 excitation fluence. a) and b) show the fitted spectra at 5 ps and 89 ps respectively. c) and d) report the equilibrium (dashed lines) and out of equilibrium (solid lines) components of the optical conductivity.

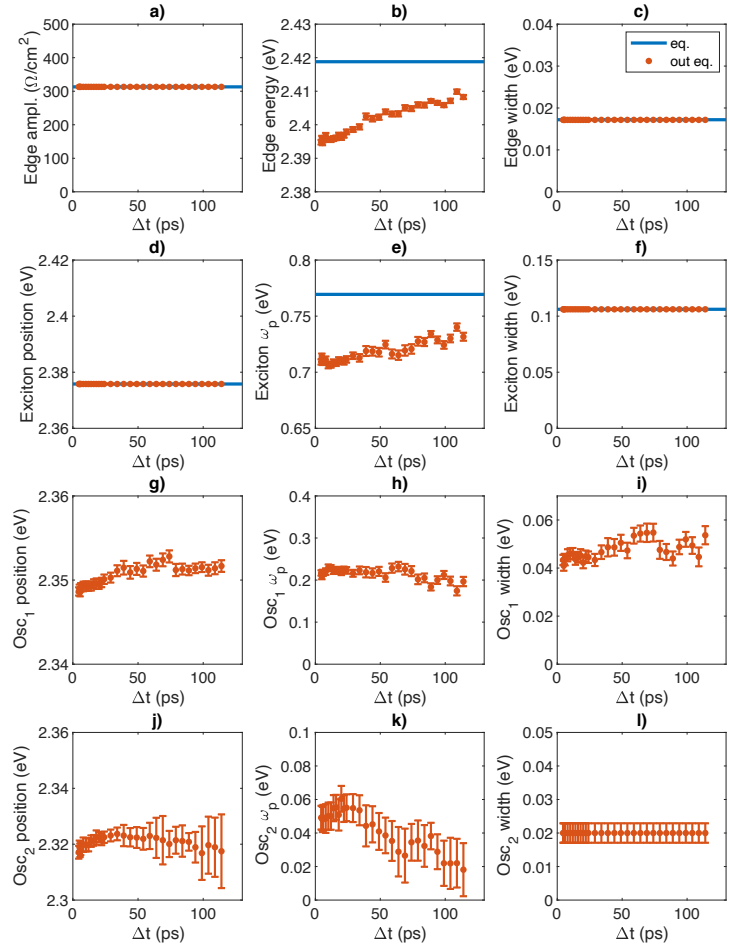

Figure C.7: $\Delta R/R$ fit output parameters for the superlattice NCs sample at 30 μJ/cm^2 excitation fluence. a), b) and c) are the free-carriers edge amplitude, center energy and width, respectively. d), e) and f) represent the exciton parameters: exciton energy, plasma frequency and width, respectively. g)-l) display the Drude-Lorentz model parameters for the new oscillators.

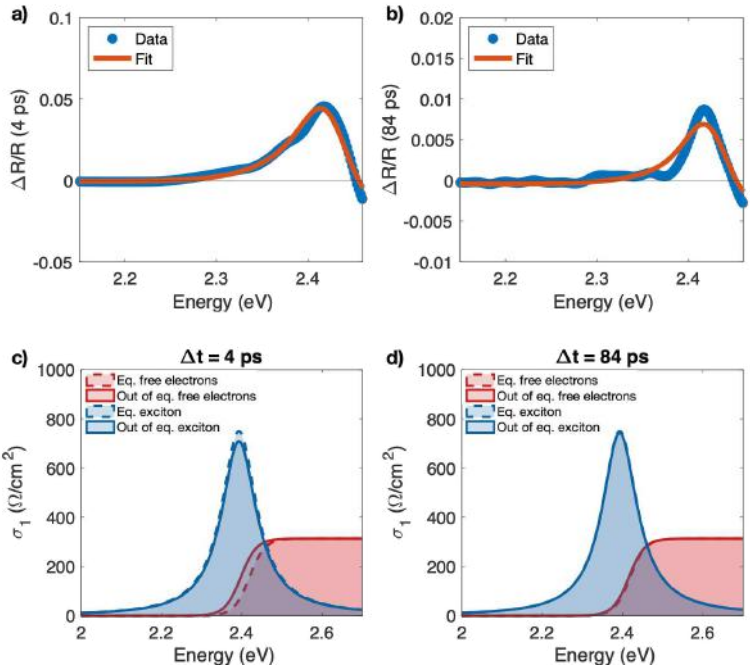

Figure C.8: Differential fit of $\Delta R/R$ data measured on disordered NCs at 17 K. a) and b) show the fitted spectra at 4 ps and 84 ps respectively. c) and d) report the equilibrium (dashed lines) and out of equilibrium (solid lines) components of the optical conductivity.

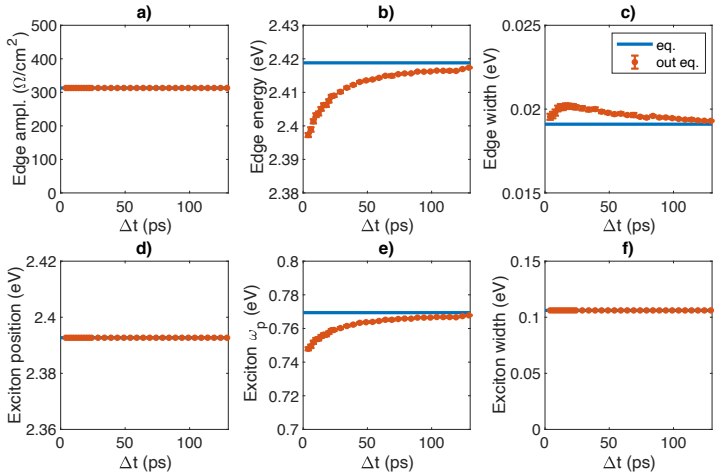

Figure C.9: $\Delta R/R$ fit output parameters for the disordered NCs sample. a), b) and c) are the free-carriers edge amplitude, center energy and width, respectively. d), e) and f) represent the exciton parameters: exciton energy, plasma frequency and width, respectively.

C.3 Exciton density estimate

In order to estimate the number of excitons generated by the pump pulse in each individual nanocube, we start from the equilibrium optical properties of $CsPbBr_3$ (Figure C.1) at the pump photon energy and calculate the reflectivity R, which results being $\approx 12\%$. Since the penetration depth is much smaller than the sample thickess, we assume that all the radiation that is not reflected is absorbed. The number of absorbed photons per unit area is then given by

$$N_{\gamma/area} = \frac{F}{\hbar\omega}(1 - R) \tag{C.4}$$

where $\hbar\omega$ is the photon energy and F is the incident fluence. The incident photons are absorbed within a thickness of 135 nm, which corresponds to the penetration depth l_p at the pump photon energy. The number of absorbed photons per unit volume is then estimated from

$$N_{\gamma/volume} = \frac{N_{\gamma/area}}{l_p}. \tag{C.5}$$

Lastly, the number of absorbed photons per nanocube can be obtained by taking into account the volume of each NC, modelled as a cube of $L = 8$ nm side:

$$N_{\gamma/NC} = N_{\gamma/volume} L^3. \tag{C.6}$$

We now assume that each absorbed photon produces an electronic excitation, of which 75% are electron-hole bound states and 25% are free carriers. These values are estimated from the contributions of exciton and band edge to the equilibrium optical conductivity at 17 K. Given the values of pump fluence employed in our experiment, we estimate to generate a number of excitons in each NC that can range between 0 and 25. Taking into account that the number of perovskite unit cells within each NC is L^3/a^3, $a = 5.83$ Å, this excitation regime corresponds to a photodoping level up to $\sim 1\%$.

APPENDIX D

2DES on FAPI nanocube superlattices: analysis and supplementary data

This chapter has been adapted from the following manuscript:

The fate of optical excitons in $FAPbI_3$ nanocube superlattices, A. Milloch, U. Filippi, P. Franceschini, S. Mor, S. Pagliara, G. Ferrini, F. V. A. Camargo, G. Cerullo, D. Baranov, L. Manna and C. Giannetti, *ACS Photonics*, 2024, 11, 9, 3511–3520, doi: 10.1021/acsphotonics.4c00105

D.1 2DES anti-diagonal profiles fitting

Lineshape analysis of the excitonic response in the 2D spectra are analyzed with the aim of investigating homogeneous broadening. The elongation of the excitonic peak along the diagonal indicates the presence of inhomogeneity in the system. Since the linewidth along diagonal and antidiagonal directions are of the same order of magnitude, the inhomogeneous and homogeneous broadening are not completely decoupled along diagonal and anti-diagonal respectively. In this case, a global lineshape analysis is needed to extract quantitative information about the homogeneous linewidth. We, therefore, follow the procedure outlined in Ref. 255 and fit the data by employing the diagonal and anti-diagonal lineshape functions derived in Chapter 2, Section 2.3.5 (Eq. 2.50-2.53).

The measured 2DES maps are sliced along the anti-diagonal and diagonal directions. The slices are centred on the maximum of the excitonic diagonal resonance in the 2D spectrum at short t_2 time delay. The asymmetry of the exciton peak in the 2D spectrum suggests the presence of two peaks, one centred on the diagonal (peak A) and one a few tens of meV above the diagonal (peak B). The presence of overlapping contributions hinders the performance of the global fitting, required by the approach presented above, for peak A and peak B separately. We therefore assume that the inhomogeneous broadening is the same for both features (peak A and peak B), i.e. $\sigma_A = \sigma_B$. Diagonal and anti-diagonal profiles are then fitted simultaneously: the diagonal one is fitted with $S_{A,\omega_0}(\omega')$ (sum of Eq. 2.51 and 2.53), describing the linshape of feature A along the diagonal direction; for the anti-diagonal direction, where two peaks are needed to fit the data, the linecuts are fitted with $I_A S_{A,\omega_0}(\omega) + I_B S_{B,\omega_0}(\omega)$, with I_i amplitude parameters, $S_{i,\omega_0}(\omega)$ given by the sum of Eq. 2.50 and 2.52, and the subscript $i = A, B$.
The fit is performed as described above for 2DES data at short time delays t_2, collected at temperatures between 30 K and 290 K. The fitted diagonal and anti-diagonal profiles are plotted in Figures D.1 and D.2, respectively. For the diagonal slices, the tail around 70 meV that is not reproduced by the fitting functions may suggest the presence of a weak response on the diagonal around 1.61 eV, as further discussed in the main text. Figure D.3 displays the obtained fit parameters parameters. For some temperatures the experiment was repeated twice; in these cases, the reported output parameters are the average values obtained from the two measurements.

The fluence-dependent data are analyzed with a similar approach. Since in this case we are mostly interested in estimating the amplitude of the two components rather than extracting the purely homogeneous linewidth, we fit only the anti-diagonal profiles by employing a sum of two Gaussians and a constant background as fit function. This choice results in a more robust fit for the fluence scan, due to the larger noise of the data collected at very low excitation intensity. Each component is described by a curve defined as

$$\frac{I_i}{\sqrt{2\pi}\sigma_i} \exp\left\{\left[-\frac{(x - x_{0,i})^2}{2\sigma_i^2}\right]\right\} \tag{D.1}$$

with I_i, $x_{0,i}$ and σ_i $(i = 1, 2)$ the fit free parameters, representing respectively the area, central energy and width (standard deviation) of each peak. The fit of fluence-dependent 2D spectra anti-diagonal profiles are plotted in Figure D.4 and the output parameters are displayed in Fig. D.5.

Similarly, the time-resolved 2D spectra anti-diagonal profiles are fitted with the sum of two Gaussian peaks and a constant background. From a first fit, we observe that the total spectral weight of the two components, given by $A_1 + A_2$, is constant over the scanned t_2 range. We, therefore, fix $A_1 + A_2$ to a constant value in order to improve fit quality and robustness. The results of the fitting procedure are displayed in figures D.6 and D.7.

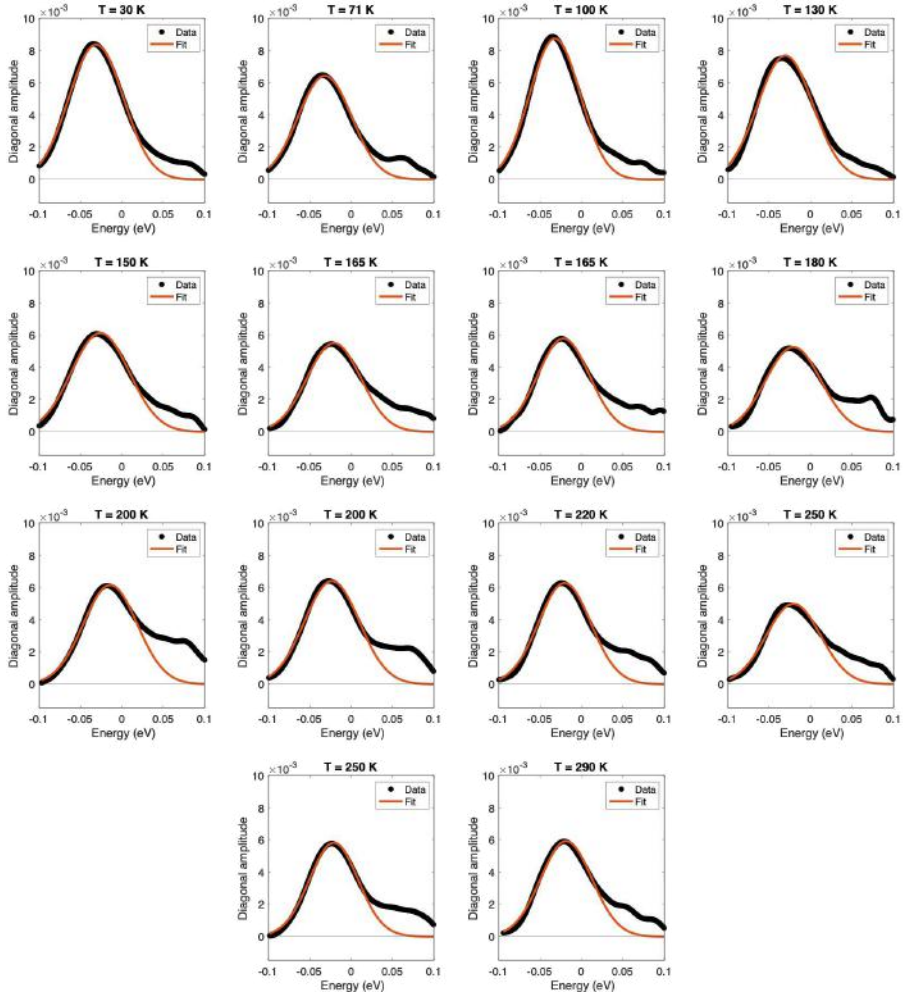

Figure D.1: a,b) Fit of the diagonal profiles of 2D spectra measured at short t_2 time delay ($t_2 = 0$) with $F = 175$ µJ/cm^2 at different temperatures. The curves are fitted with a function of the form $S^R_{\omega_0}(\omega') + S^{NR}_{\omega_0}(\omega')$ (sum of equations 2.51 and 2.53).

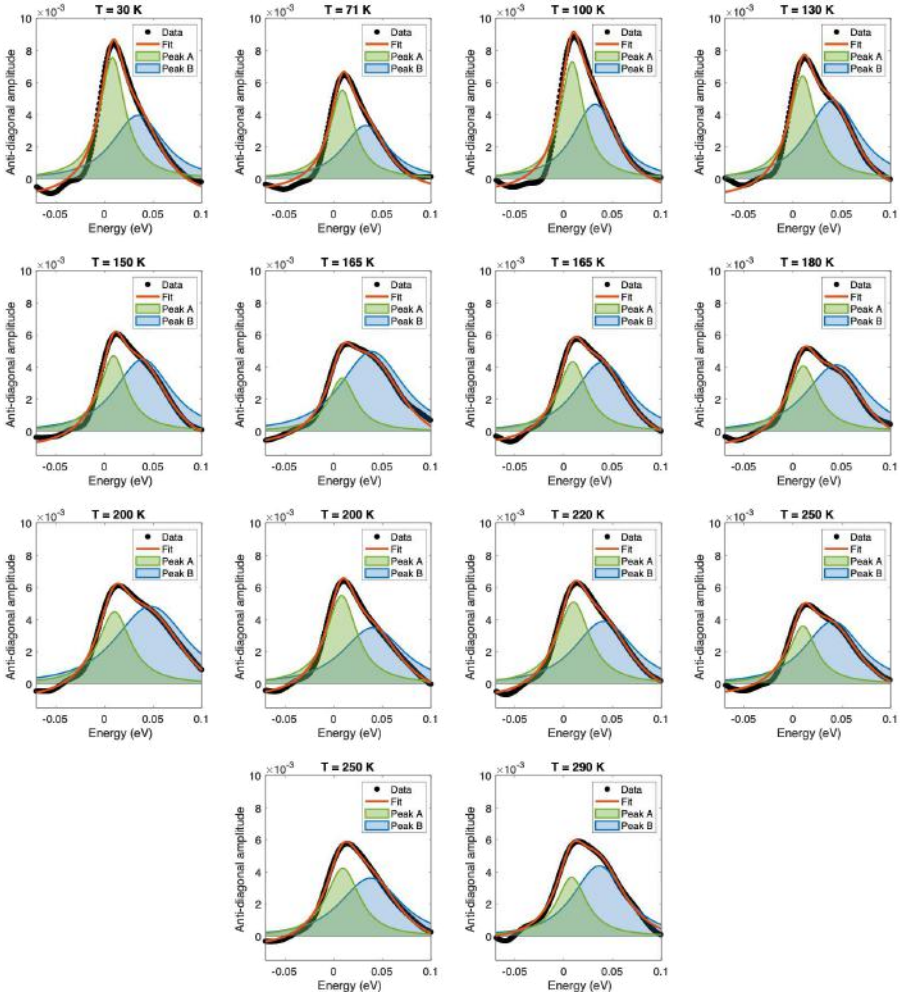

Figure D.2: Fit of the anti-diagonal profiles of 2D spectra measured at short t_2 time delay ($t_2 = 0$) with $F = 175$ μJ/cm^2 as a function of sample temperature. The curves are fitted with the sum of two peaks, each given by $S^R_{\omega_0}(\omega) + S^{NR}_{\omega_0}(\omega)$ (sum of equations 2.50 and 2.52), and a constant background.

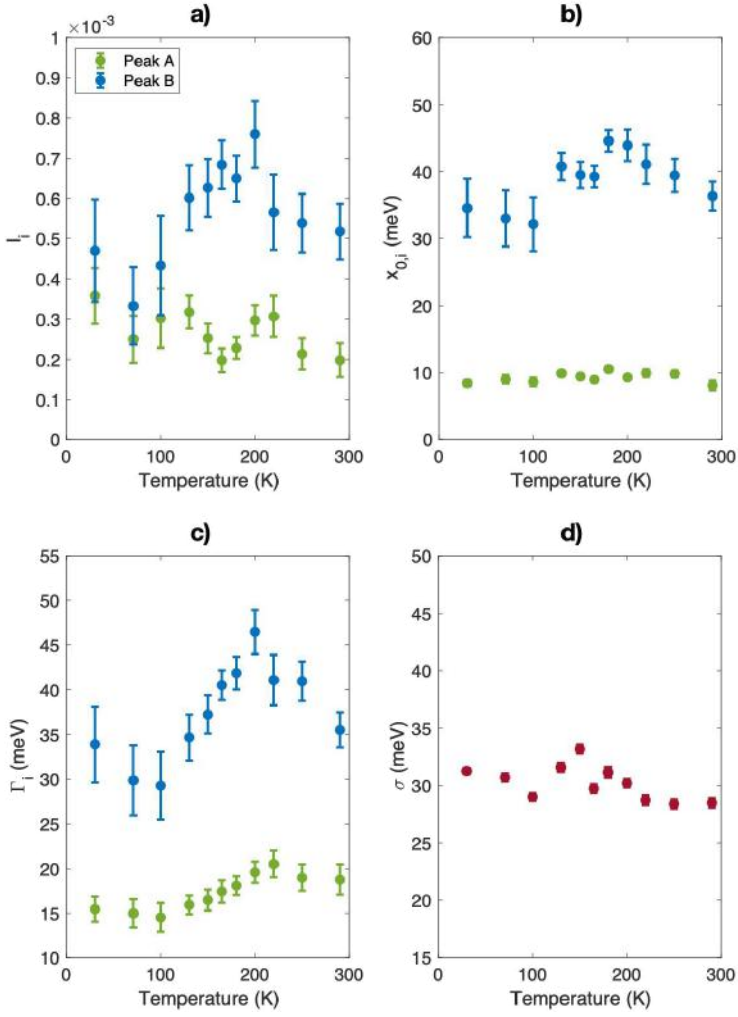

Figure D.3: Parameters obtained from the simultaneous fit of the diagonal and anti-diagonal profiles, as a function of sample temperature: a) amplitude parameters of peak A and peak B in the anti-diagonal slice, b) peak A and peak B central position along anti-diagonal direction, c) homogeneous widths of peak A and peak B and d) inhomogeneous broadening ($\sigma_A = \sigma_B$).

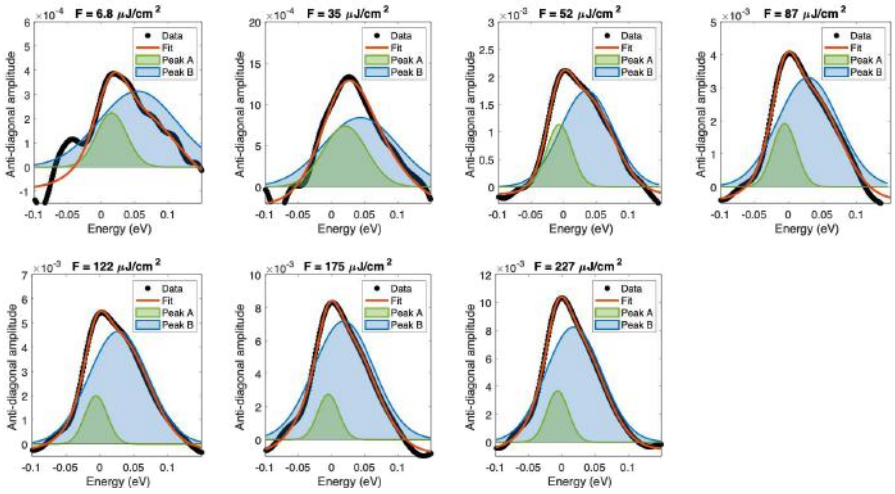

Figure D.4: Fit of the anti-diagonal profiles of 2D spectra measured at short t_2 time delay ($t_2 = 0$) and $T = 200$ K, as a function of pump fluence. The curves are fitted with the sum of two Gaussian functions (green and blue filled areas) and a constant background.

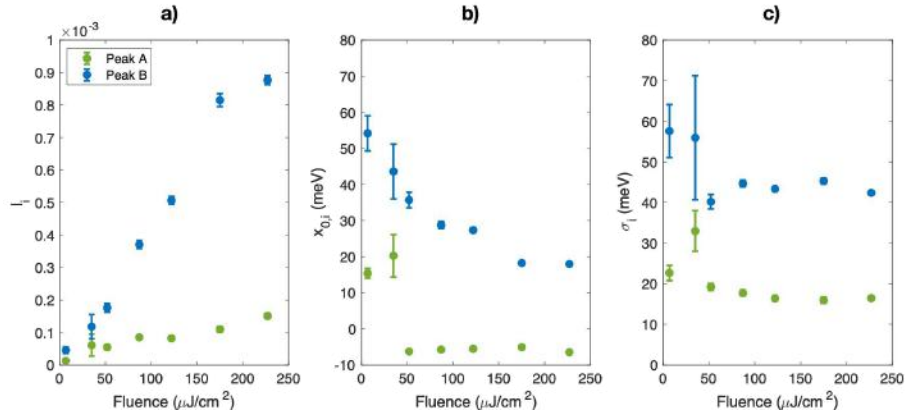

Figure D.5: Parameters of the two Gaussian peaks obtained from the fit of the anti-diagonal profiles as a function of sample temperature: a) amplitude, b) peak central position, c) width.

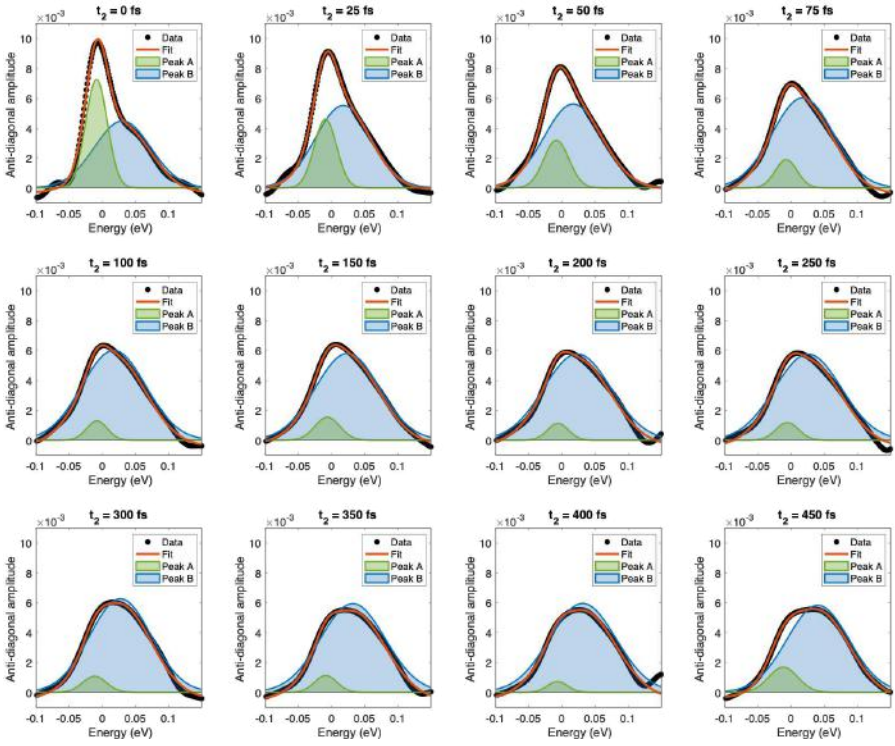

Figure D.6: Fit of the anti-diagonal profiles of 2D spectra measured as a function of t_2 time delay at $T = 200$ K with $F = 175$ μJ/cm^2. The curves are fitted with the sum of two Gaussian functions (green and blue filled areas) and a constant background.

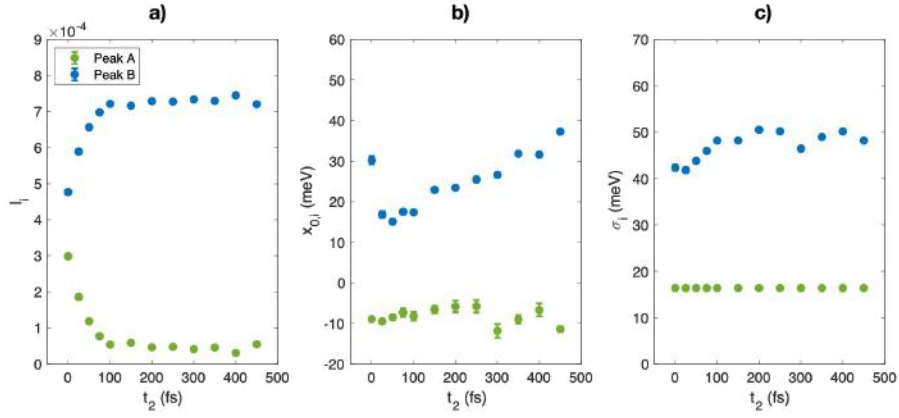

Figure D.7: Parameters of the two Gaussian peaks obtained from the fit of the anti-diagonal profiles as a function of t_2 time delay: a) amplitude, b) peak central position, c) width.

D.2 Exciton density

The number of excited excitons per nanocube can be estimated based on the experimental absorbance of the sample under investigation, the incoming energy per laser pulse, and the number of nanocubes present in the excited volume.
The measured absorbance A, reported in Figures B.8 and B.9b, is obtained from the sample transmission T_r according to $A = -\log_{10} T_r$. It therefore includes contributions from sample absorption, reflection and scattering. We neglect reflection and scattering effects and compute the sample absorption as $\alpha = 1 - T_r = 1 - 10^{-A}$, which results in an overestimate of the absorption. In this case, we obtain $\alpha \simeq 0.5$ in the photon energy range of the experiment.
The number of excited nanocubes is limited either by the penetration depth l_p of the material or by the sample thickness h. l_p can be estimated using the refractive index of bulk FAPI reported in literature [5], which returns $l_p \simeq 800$ nm in the 1.55-1.8 eV photon energy range of interest. The thickness of the sample is expected to be around 300-500 nm and thus turns out to be the limiting factor. Therefore, the number of nanocubes excited in an excitation area L^2, where L is nanocube edge size, will be h/L.
The number of absorbed photons per nanocube is thus given by

$$\langle N \rangle = \frac{F\alpha}{\hbar\omega_1} \frac{L^2}{h/L} \tag{D.2}$$

where F is the incoming pump fluence, $\hbar\omega_1$ is the pump photon energy. Based on the fitting of the sample absorbance, we expect that a large fraction of $\langle N \rangle$ will go into excitons rather than free carriers. Using $L = 10$ nm and $\alpha = 0.5$, we obtain $\langle N \rangle \sim 8 - 14$ (depending on the sample thickness) at the highest excitation fluence of 230 µJ/cm^2. While this value represents only a rough estimate, it provides a useful indication of the order of magnitude of $\langle N \rangle$ and shows that the number of excitons per nanocube varies between 1 and a few tens in the fluence range spanned in the 2D spectroscpy experiments.

D.3 Fluence dependent 2DES at $t_2 = 3$ ps

The fluence dependence of the off-diagonal structure in the 2D spectra is investigated from 2DES measurements performed at 21.3 K and $t_2 = 3$ ps. Integration of the signal in the squared region of interest (ROI) highlighted in Figure D.8a shows a linear behaviour of the intensity of the off-diagonal spectral feature with excitation intensity, as displayed in Figure D.8b.

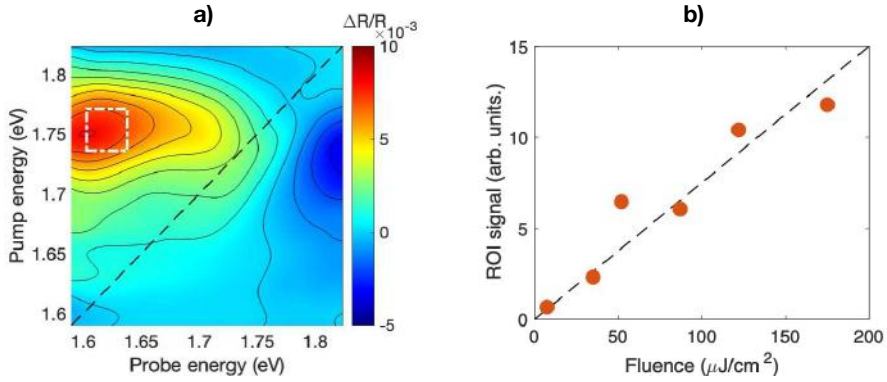

Figure D.8: a) 2D spectrum collected at $T = 21.3$ K, $t_2 = 3$ ps and $F = 175$ μJ/cm^2. The white dashed rectangle indicates the region of interest where the signal is integrated for all spectra acquired at the same temperature and t_2 delay, as a function of excitation intensity. b) The red dots display the fluence dependence of the 2DES signal integrated in the ROI highlighted in a), the black dashed line indicates the observed linear trend.

D.4 2DES in transmission geometry

2DES experiments in transmission geometry can be performed by employing samples deposited on a transparent glass substrate. We however find that, in the transmission configuration, there is stronger scattering of the pump beam, which affects the measured signal along the diagonal of the 2D spectrum. For this reason, the detailed experiments analysed in the main text are performed in reflection configuration.

For comparison, one 2DES experiment in transmission geometry is reported in Figure D.9. In this experimental configuration, the key features revealed from 2D spectroscopy are the same, although more noisy, as those observed in reflection geometry and discussed in the main text. Specifically, it is possible to observe an excitonic response centred on the spectrum diagonal and an off-diagonal feature emerging on a longer timescale.

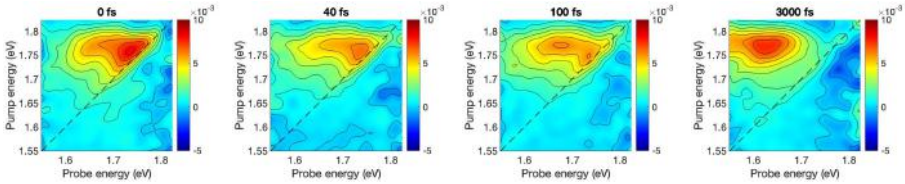

Figure D.9: 2D spectra measured in transmission geometry for a FAPI NC superlattice sample on a transparent substrate. The measurements are performed at $T = 23$ K and fluence 175 µJ/cm^2 excitation fluence for four different time delays t_2.

D.5 2DES on FAPI disordered nanocube film

Figure D.10 reports the 2DES spectrum measured for a sample composed of randomly oriented nanocrystals. In this case, the transient reflectivity signal was largely suppressed. The left panel shows the 2D spectrum of Fig. 6.3a, which was obtained for the superlattice sample ($T = 30$ K, $t_2 = 0$ fs, fluence F =175 µJ/cm^2), whereas the right panel displays the 2D spectrum acquired for randomly oriented nanocubes in equivalent experimental conditions ($T = 23$ K, $t_2 = 0$ fs, fluence F =175 µJ/cm^2). The extremely low signal of the disordered sample prevents any further analysis and investigation of the response in this system. The almost complete suppression of the signal in disordered samples however suggests some cooperative effect and calls for further investigation that is beyond the scope of the present work.

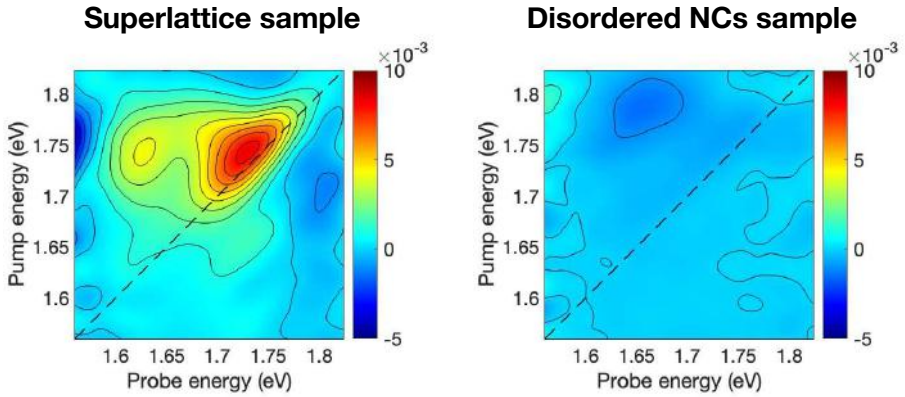

Figure D.10: 2D spectra collected for the nanocube superlattice sample (left panel) and disordered nanocube film (right panel) in the same experimental conditions, namely cryogenic temperature ($T = 30$ K for the superlattice sample and $T = 23$ K for the disordered sample), $t_2 = 0$ ps and $F = 175$ µJ/cm^2.

Bibliography

[1] Abreu, E., Gilbert Corder, S. N., Yun, S. J., Wang, S., Ramírez, J. G., West, K., Zhang, J., Kittiwatanakul, S., Schuller, I. K., Lu, J., et al. Ultrafast electron-lattice coupling dynamics in VO_2 and V_2O_3 thin films. *Physical Review B 96*, 9 (2017), 094309.

[2] Adda, C., Corraze, B., Stoliar, P., Diener, P., Tranchant, J., Filatre-Furcate, A., Fourmigué, M., Lorcy, D., Besland, M.-P., Janod, E., and Cario, L. Mott insulators: a large class of materials for Leaky Integrate and Fire (LIF) artificial neuron. *Journal of Applied Physics 124*, 15 (2018), 152124.

[3] Akkerman, Q. A., Martinez-Sarti, L., Goldoni, L., Imran, M., Baranov, D., Bolink, H. J., Palazon, F., and Manna, L. Molecular iodine for a general synthesis of binary and ternary inorganic and hybrid organic–inorganic iodide nanocrystals. *Chemistry of Materials 30*, 19 (2018), 6915–6921.

[4] Alfano, R. R. *The supercontinuum laser source: fundamentals with updated references*. Springer, 2006.

[5] Alonso, M. I., Charles, B., Francisco-López, A., Garriga, M., Weller, M. T., and Goñi, A. R. Spectroscopic ellipsometry study of $FA_xMA_{1-x}PbI_3$ hybrid perovskite single crystals. *Journal of Vacuum Science & Technology B 37*, 6 (2019).

[6] Altman, E., Brown, K. R., Carleo, G., Carr, L. D., Demler, E., Chin, C., DeMarco, B., Economou, S. E., Eriksson, M. A., Fu, K.-M. C., et al. Quantum simulators: architectures and opportunities. *PRX Quantum 2*, 1 (2021), 017003.

[7] Amaricci, A., Crippa, L., Scazzola, A., Petocchi, F., Mazza, G., de Medici, L., and Capone, M. EDIpack: a parallel exact diagonalization package for quantum impurity problems. *Computer Physics Communications 273* (2022), 108261.

[8] Aneesh, J., Swarnkar, A., Kumar Ravi, V., Sharma, R., Nag, A., and Adarsh, K. Ultrafast exciton dynamics in colloidal $CsPbBr_3$ perovskite nanocrystals: biexciton effect and auger recombination. *The Journal of Physical Chemistry C 121*, 8 (2017), 4734–4739.

[9] Archer, M. S., Roebuck, D. S. P., and Whitby, F. J. Magnetic susceptibility of vanadium dioxide. *Nature 174* (Oct 1954), 754.

[10] Asaba, T., Onishi, A., Kageyama, Y., Kiyosue, T., Ohtsuka, K., Suetsugu, S., Kohsaka, Y., Gaggl, T., Kasahara, Y., Murayama, H., Hashimoto, K., Tazai, R., Kontani, H., Ortiz, B. R., Wilson, S. D., Li, Q., Wen, H. H., Shibauchi, T., and Matsuda, Y. Evidence for an odd-parity nematic phase above the charge-density-wave transition in a kagome metal. *Nature Physics* (2024).

[11] Asenjo-Garcia, A., Moreno-Cardoner, M., Albrecht, A., Kimble, H. J., and Chang, D. E. Exponential improvement in photon storage fidelities using subradiance and "selective radiance" in atomic arrays. *Physical Review X 7* (Aug 2017), 031024.

[12] Attaccalite, C., and Fabrizio, M. Properties of Gutzwiller wave functions for multiband models. *Physical Review B 68* (Oct 2003), 155117.

[13] Babich, D., Tranchant, J., Adda, C., Corraze, B., Besland, M.-P., Warnicke, P., Bedau, D., Bertoncini, B., Mevellec, J.-Y., Humbert, B., Rupp, J., Hennen, T., Wouters, D., Llopis, R., Cario, L., and Janod, E. Lattice contraction induced by resistive switching in chromium-doped V_2O_3: a hallmark of Mott physics. *arXiv preprint arXiv:2105.05093* (2021).

[14] Baranov, D., Toso, S., Imran, M., and Manna, L. Investigation into the photoluminescence red shift in cesium lead bromide nanocrystal superlattices. *The Journal of Physical Chemistry Letters 10*, 3 (2019), 655–660.

[15] Basov, D., Averitt, R., and Hsieh, D. Towards properties on demand in quantum materials. *Nature Materials 16*, 11 (2017), 1077–1088.

[16] Bataller, A. W., Younts, R. A., Rustagi, A., Yu, Y., Ardekani, H., Kemper, A., Cao, L., and Gundogdu, K. Dense electron–hole plasma formation and ultralong charge lifetime in monolayer MoS_2 via material tuning. *Nano Letters 19*, 2 (2019), 1104–1111.

[17] Bernevig, B. A., Hughes, T. L., and Zhang, S.-C. Quantum spin Hall effect and topological phase transition in HgTe quantum wells. *Science 314*, 5806 (2006), 1757–1761.

[18] Biliroglu, M., Findik, G., Mendes, J., Seyitliyev, D., Lei, L., Dong, Q., Mehta, Y., Temnov, V. V., So, F., and Gundogdu, K. Room-temperature superfluorescence in hybrid perovskites and its origins. *Nature Photonics 16*, 4 (2022), 324–329.

[19] Blach, D. D., Lumsargis, V. A., Clark, D. E., Chuang, C., Wang, K., Dou, L., Schaller, R. D., Cao, J., Li, C. W., and Huang, L. Superradiance and exciton delocalization in perovskite quantum dot superlattices. *Nano Letters 22*, 19 (2022), 7811–7818.

[20] Bloch, I., Dalibard, J., and Nascimbene, S. Quantum simulations with ultracold quantum gases. *Nature Physics 8*, 4 (2012), 267–276.

[21] Bloch, I., Dalibard, J., and Zwerger, W. Many-body physics with ultracold gases. *Reviews of Modern Physics 80*, 3 (2008), 885.

[22] Bordet, P., Chaillout, C., Marezio, M., Huang, Q., Santoro, A., Cheong, S.-W., Takagi, H., Oglesby, C., and Batlogg, B. Structural aspects of the crystallographic-magnetic transition in $LaVO_3$ around 140 K. *Journal of Solid State Chemistry 106*, 2 (1993), 253–270.

[23] Boyd, R. W. *Nonlinear Optics, Third Edition*, 3rd ed. Academic Press, Inc., USA, 2008.

[24] Bradler, M., Baum, P., and Riedle, E. Femtosecond continuum generation in bulk laser host materials with sub-μJ pump pulses. *Applied Physics B 97* (2009), 561–574.

[25] Brahlek, M., Gupta, A. S., Lapano, J., Roth, J., Zhang, H.-T., Zhang, L., Haislmaier, R., and Engel-Herbert, R. Frontiers in the growth of complex oxide thin films: past, present, and future of hybrid MBE. *Advanced Functional Materials 28*, 9 (2018), 1702772.

[26] Bray, A. J. Theory of phase-ordering kinetics. *Advances in Physics 43*, 3 (1994), 357–459.

[27] Brennan, M. C., Toso, S., Pavlovetc, I. M., Zhukovskyi, M., Marras, S., Kuno, M., Manna, L., and Baranov, D. Superlattices are greener on the other side: how light transforms self-assembled mixed halide perovskite nanocrystals. *ACS Energy Letters 5*, 5 (2020), 1465–1473.

[28] Brida, D., Manzoni, C., and Cerullo, G. Phase-locked pulses for two-dimensional spectroscopy by a birefringent delay line. *Optics Letters 37*, 15 (2012), 3027–3029.

[29] Brinkman, W. F., and Rice, T. M. Electron-hole liquids in semiconductors. *Physical Review B 7* (Feb 1973), 1508–1523.

[30] Buluta, I., and Nori, F. Quantum simulators. *Science 326*, 5949 (2009), 108–111.

[31] Camargo, F. V., Nagahara, T., Feldmann, S., Richter, J. M., Friend, R. H., Cerullo, G., and Deschler, F. Dark subgap states in metal-halide perovskites revealed by coherent multidimensional spectroscopy. *Journal of the American Chemical Society 142*, 2 (2019), 777–782.

[32] Camargo, F. V. d. A., Grimmelsmann, L., Anderson, H. L., Meech, S. R., and Heisler, I. A. Resolving vibrational from electronic coherences in two-dimensional electronic spectroscopy: the role of the laser spectrum. *Physical Review Letters 118*, 3 (2017), 033001.

[33] Cao, Y., Fatemi, V., Demir, A., Fang, S., Tomarken, S. L., Luo, J. Y., Sanchez-Yamagishi, J. D., Watanabe, K., Taniguchi, T., Kaxiras, E., et al. Correlated insulator behaviour at half-filling in magic-angle graphene superlattices. *Nature 556*, 7699 (2018), 80–84.

[34] Cao, Y., Fatemi, V., Fang, S., Watanabe, K., Taniguchi, T., Kaxiras, E., and Jarillo-Herrero, P. Unconventional superconductivity in magic-angle graphene superlattices. *Nature 556*, 7699 (2018), 43–50.

[35] Capone, M., de' Medici, L., and Georges, A. Solving the dynamical mean-field theory at very low temperatures using the Lanczos exact diagonalization. *Physical Review B 76* (Dec 2007), 245116.

[36] Capone, M., Fabrizio, M., Castellani, C., and Tosatti, E. Strongly correlated superconductivity. *Science 296*, 5577 (2002), 2364–2366.

[37] Capone, M., Fabrizio, M., Castellani, C., and Tosatti, E. Colloquium: Modeling the unconventional superconducting properties of expanded A_3C_{60} fullerides. *Review of Modern Physics 81* (Jun 2009), 943–958.

[38] Carr, S., Fang, S., and Kaxiras, E. Electronic-structure methods for twisted moiré layers. *Nature Reviews Materials 5*, 10 (2020), 748–763.

[39] Castellani, C., Castro, C. D., Feinberg, D., and Ranninger, J. New model hamiltonian for the metal-insulator transition. *Physical Review Letters 43* (Dec 1979), 1957–1960.

[40] Castellani, C., Natoli, C., and Ranninger, J. Magnetic structure of V_2O_3 in the insulating phase. *Physical Review B 18*, 9 (1978), 4945.

[41] Cavalleri, A. Photo-induced superconductivity. *Contemporary Physics 59*, 1 (2018), 31–46.

[42] Chattopadhyay, S., Eckhardt, C. J., Kennes, D. M., Sentef, M. A., Shin, D., Rubio, A., Cavalleri, A., Demler, E. A., and Michael, M. H. Mechanisms for long-lived, photo-induced superconductivity. *arXiv preprint arXiv:2303.15355* (2023).

[43] Chen, C.-W., Choe, J., and Morosan, E. Charge density waves in strongly correlated electron systems. *Reports on Progress in Physics 79*, 8 (2016), 084505.

[44] Chen, Q., De Marco, N., Yang, Y. M., Song, T.-B., Chen, C.-C., Zhao, H., Hong, Z., Zhou, H., and Yang, Y. Under the spotlight: the organic–inorganic hybrid halide perovskite for optoelectronic applications. *Nano Today 10*, 3 (2015), 355–396.

[45] Chen, Y., Zhang, S., Ke, F., Ko, C., Lee, S., Liu, K., Chen, B., Ager, J. W., Jeanloz, R., Eyert, V., and Wu, J. Pressure-temperature phase diagram of vanadium dioxide. *Nano Letters 17*, 4 (2017), 2512–2516.

[46] Cheng, S., Lee, M.-H., Tran, R., Shi, Y., Li, X., Navarro, H., Adda, C., Meng, Q., Chen, L.-Q., Dynes, R., et al. Inherent stochasticity during insulator-metal transition in VO_2. *Proceedings of the National Academy of Sciences 118*, 37 (2021), e2105895118.

[47] Cheng, Y., Zong, A., Wu, L., Meng, Q., Xia, W., Qi, F., Zhu, P., Zou, X., Jiang, T., Guo, Y., van Wezel, J., Kogar, A., Zuerch, M. W., Zhang, J., Zhu, Y., and Xiang, D. Ultrafast formation of topological defects in a two-dimensional charge density wave. *Nature Physics 20*, 1 (2024), 54–60.

[48] Chernikov, A., Ruppert, C., Hill, H. M., Rigosi, A. F., and Heinz, T. F. Population inversion and giant bandgap renormalization in atomically thin WS_2 layers. *Nature Photonics 9*, 7 (2015), 466–470.

[49] Cherniukh, I., Rainò, G., Stöferle, T., Burian, M., Travesset, A., Naumenko, D., Amenitsch, H., Erni, R., Mahrt, R. F., Bodnarchuk, M. I., et al. Perovskite-type superlattices from lead halide perovskite nanocubes. *Nature 593*, 7860 (2021), 535–542.

[50] Chien, C.-C., Peotta, S., and Di Ventra, M. Quantum transport in ultracold atoms. *Nature Physics 11*, 12 (2015), 998–1004.

[51] Cho, K., Yamada, T., Tahara, H., Tadano, T., Suzuura, H., Saruyama, M., Sato, R., Teranishi, T., and Kanemitsu, Y. Luminescence fine structures in single lead halide perovskite nanocrystals: size dependence of the exciton–phonon coupling. *Nano Letters 21*, 17 (2021), 7206–7212.

[52] Cirac, J. I., and Zoller, P. Goals and opportunities in quantum simulation. *Nature Physics 8*, 4 (2012), 264–266.

[53] Clarke, D. G. Particle-hole bound states in Mott-Hubbard insulators. *Physical Review B 48*, 10 (1993), 7520.

[54] Collini, E. 2D electronic spectroscopic techniques for quantum technology applications. *The Journal of Physical Chemistry C 125*, 24 (2021), 13096–13108.

[55] Comanac, A., de' Medici, L., Capone, M., and Millis, A. J. Optical conductivity and the correlation strength of high-temperature copper-oxide superconductors. *Nature Physics 4*, 4 (2008), 287–290.

[56] Cong, K., Zhang, Q., Wang, Y., Noe, G. T., Belyanin, A., and Kono, J. Dicke superradiance in solids. *Journal of the Optical Society of America B 33*, 7 (Jul 2016), C80–C101.

[57] Cundiff, S. T., and Mukamel, S. Optical multidimensional coherent spectroscopy. *Physics Today 66*, 7 (2013), 44–49.

[58] da Silva Neto, E. H., Comin, R., He, F., Sutarto, R., Jiang, Y., Greene, R. L., Sawatzky, G. A., and Damascelli, A. Charge ordering in the electron-doped superconductor $Nd_{2-x}Ce_xCuO_4$. *Science 347*, 6219 (2015), 282–285.

[59] De La Torre, A., Kennes, D. M., Claassen, M., Gerber, S., McIver, J. W., and Sentef, M. A. Colloquium: Nonthermal pathways to ultrafast control in quantum materials. *Reviews of Modern Physics 93*, 4 (2021), 041002.

[60] De Raychaudhury, M., Pavarini, E., and Andersen, O. Orbital fluctuations in the different phases of $LaVO_3$ and YVO_3. *Physical Review Letters 99*, 12 (2007), 126402.

[61] Del Valle, J., Ramirez, J. G., Rozenberg, M. J., and Schuller, I. K. Challenges in materials and devices for resistive-switching-based neuromorphic computing. *Journal of Applied Physics 124*, 21 (2018), 211101.

[62] Del Valle, J., Salev, P., Tesler, F., Vargas, N. M., Kalcheim, Y., Wang, P., Trastoy, J., Lee, M.-H., Kassabian, G., Ramírez, J. G., et al. Subthreshold firing in Mott nanodevices. *Nature 569*, 7756 (2019), 388–392.

[63] Del Valle, J., Vargas, N. M., Rocco, R., Salev, P., Kalcheim, Y., Lapa, P. N., Adda, C., Lee, M.-H., Wang, P. Y., Fratino, L., et al. Spatiotemporal characterization of the field-induced insulator-to-metal transition. *Science 373*, 6557 (2021), 907–911.

[64] Dernier, P. D., and Marezio, M. Crystal structure of the low-temperature antiferromagnetic phase of V_2O_3. *Physical Review B 2* (Nov 1970), 3771–3776.

[65] Dey, A., Ye, J., De, A., Debroye, E., Ha, S. K., Bladt, E., Kshirsagar, A. S., Wang, Z., Yin, J., Wang, Y., et al. State of

the art and prospects for halide perovskite nanocrystals. *ACS Nano 15*, 7 (2021), 10775–10981.

[66] Dicke, R. H. Coherence in spontaneous radiation processes. *Physical Review 93*, 1 (1954), 99.

[67] Diener, P., Janod, E., Corraze, B., Querré, M., Adda, C., Guilloux-Viry, M., Cordier, S., Camjayi, A., Rozenberg, M., Besland, M., et al. How a dc electric field drives Mott insulators out of equilibrium. *Physical Review Letters 121*, 1 (2018), 016601.

[68] Dillemans, L., Smets, T., Lieten, R. R., Menghini, M., Su, C.-Y., and Locquet, J.-P. Evidence of the metal-insulator transition in ultrathin unstrained V_2O_3 thin films. *Applied Physics Letters 104*, 7 (02 2014), 071902.

[69] Diroll, B. T., Zhou, H., and Schaller, R. D. Low-temperature absorption, photoluminescence, and lifetime of $CsPbX_3$ (X= Cl, Br, I) nanocrystals. *Advanced Functional Materials 28*, 30 (2018), 1800945.

[70] Dostál, J., Fennel, F., Koch, F., Herbst, S., Würthner, F., and Brixner, T. Direct observation of exciton–exciton interactions. *Nature Communications 9*, 1 (2018), 2466.

[71] Eichberger, M., Schäfer, H., Krumova, M., Beyer, M., Demsar, J., Berger, H., Moriena, G., Sciaini, G., and Miller, R. D. Snapshots of cooperative atomic motions in the optical suppression of charge density waves. *Nature 468*, 7325 (2010), 799–802.

[72] Elliott, R. Intensity of optical absorption by excitons. *Physical Review 108*, 6 (1957), 1384.

[73] Fabini, D. H., Stoumpos, C. C., Laurita, G., Kaltzoglou, A., Kontos, A. G., Falaras, P., Kanatzidis, M. G., and Seshadri, R. Reentrant structural and optical properties and large positive thermal expansion in perovskite formamidinium lead iodide. *Angewandte Chemie 128*, 49 (2016), 15618–15622.

[74] Fang, H.-H., Protesescu, L., Balazs, D. M., Adjokatse, S., Kovalenko, M. V., and Loi, M. A. Exciton recombination in formamidinium lead triiodide: nanocrystals versus thin films. *Small 13*, 32 (2017), 1700673.

[75] Fang, H.-H., Wang, F., Adjokatse, S., Zhao, N., Even, J., and Antonietta Loi, M. Photoexcitation dynamics in solution-processed formamidinium lead iodide perovskite thin films for solar cell applications. *Light: Science & Applications 5*, 4 (2016), e16056–e16056.

[76] Fang, Z., and Nagaosa, N. Quantum versus Jahn-Teller orbital physics in YVO_3 and $LaVO_3$. *Physical Review Letters 93*, 17 (2004), 176404.

[77] Ferioli, G., Glicenstein, A., Henriet, L., Ferrier-Barbut, I., and Browaeys, A. Storage and release of subradiant excitations in a dense atomic cloud. *Physical Review X 11* (May 2021), 021031.

[78] Ferioli, G., Glicenstein, A., Robicheaux, F., Sutherland, R. T., Browaeys, A., and Ferrier-Barbut, I. Laser-driven superradiant ensembles of two-level atoms near Dicke regime. *Physical Review Letters 127* (Dec 2021), 243602.

[79] Ferreira, A., Paofai, S., Létoublon, A., Ollivier, J., Raymond, S., Hehlen, B., Rufflé, B., Cordier, S., Katan, C., Even, J., et al. Direct evidence of weakly dispersed and strongly anharmonic optical phonons in hybrid perovskites. *Communications Physics 3*, 1 (2020), 48.

[80] Fiebig, M., Miyano, K., Tomioka, Y., and Tokura, Y. Visualization of the local insulator-metal transition in $Pr_{0.7}Ca_{0.3}MnO_3$. *Science 280*, 5371 (1998), 1925–1928.

[81] Findik, G., Biliroglu, M., Seyitliyev, D., Mendes, J., Barrette, A., Ardekani, H., Lei, L., Dong, Q., So, F., and Gundogdu, K. High-temperature superfluorescence in methyl ammonium lead iodide. *Nature Photonics 15*, 9 (2021), 676–680.

[82] Fradkin, E., Kivelson, S. A., and Tranquada, J. M. Colloquium: Theory of intertwined orders in high temperature superconductors. *Reviews of Modern Physics 87*, 2 (2015), 457.

[83] Franceschini, P., Carletti, L., Pushkarev, A. P., Preda, F., Perri, A., Tognazzi, A., Ronchi, A., Ferrini, G., Pagliara, S., Banfi, F., et al. Tuning the ultrafast response of Fano resonances in halide perovskite nanoparticles. *ACS Nano 14*, 10 (2020), 13602–13610.

[84] Franceschini, P., Policht, V. R., Milloch, A., Ronchi, A., Mor, S., Mellaerts, S., Hsu, W.-F., Pagliara, S., Ferrini, G., Banfi, F., et al. Coherent control of the orbital occupation driving the insulator-to-metal Mott transition in V_2O_3. *Physical Review B 107*, 16 (2023), L161110.

[85] Frano, A., Blanco-Canosa, S., Keimer, B., and Birgeneau, R. J. Charge ordering in superconducting copper oxides. *Journal of Physics: Condensed Matter 32*, 37 (2020), 374005.

[86] Freeman, E., Stone, G., Shukla, N., Paik, H., Moyer, J. A., Cai, Z., Wen, H., Engel-Herbert, R., Schlom, D. G., Gopalan, V., et al. Nanoscale structural evolution of electrically driven insulator to metal transition in vanadium dioxide. *Applied Physics Letters 103*, 26 (2013).

[87] Freeney, S. E., Slot, M. R., Gardenier, T. S., Swart, I., and Vanmaekelbergh, D. Electronic quantum materials simulated with artificial model lattices. *ACS Nanoscience Au 2*, 3 (2022), 198–224.

[88] Fu, M., Tamarat, P., Huang, H., Even, J., Rogach, A. L., and Lounis, B. Neutral and charged exciton fine structure in single lead halide perovskite nanocrystals revealed by magneto-optical spectroscopy. *Nano Letters 17*, 5 (2017), 2895–2901.

[89] Fu, M., Tamarat, P., Trebbia, J.-B., Bodnarchuk, M. I., Kovalenko, M. V., Even, J., and Lounis, B. Unraveling exciton–phonon coupling in individual $FAPbI_3$ nanocrystals emitting near-infrared single photons. *Nature Communications 9*, 1 (2018), 3318.

[90] Fu, Y., Zhu, H., Chen, J., Hautzinger, M. P., Zhu, X.-Y., and Jin, S. Metal halide perovskite nanostructures for optoelectronic applications and the study of physical properties. *Nature Reviews Materials 4*, 3 (2019), 169–188.

[91] Fursina, A., Sofin, R., Shvets, I., and Natelson, D. Origin of hysteresis in resistive switching in magnetite is Joule heating. *Physical Review B 79*, 24 (2009), 245131.

[92] Fursina, A., Sofin, R., Shvets, I., and Natelson, D. Statistical distribution of the electric field-driven switching of the Verwey state in Fe_3O_4. *New Journal of Physics 14*, 1 (2012), 013019.

[93] Gandolfi, M., Celardo, G. L., Borgonovi, F., Ferrini, G., Avella, A., Banfi, F., and Giannetti, C. Emergent ultrafast phenomena in correlated oxides and heterostructures. *Physica Scripta 92*, 3 (2017), 034004.

[94] Gao, F. Y., Zhang, Z., Sun, Z., Ye, L., Cheng, Y.-H., Liu, Z.-J., Checkelsky, J. G., Baldini, E., and Nelson, K. A. Snapshots of a light-induced metastable hidden phase driven by the collapse of charge order. *Science Advances 8*, 29 (2022), eabp9076.

[95] Georges, A., Kotliar, G., Krauth, W., and Rozenberg, M. J. Dynamical mean-field theory of strongly correlated fermion systems and the limit of infinite dimensions. *Review of Modern Physics 68* (Jan 1996), 13–125.

[96] Ghazikhanian, N., Del Valle, J., Salev, P., El Hage, R., Kalcheim, Y., Adda, C., and Schuller, I. K. Resistive switching localization by selective focused ion beam irradiation. *Applied Physics Letters 123*, 12 (2023).

[97] Ghonge, S., Engel, D., Mattiotti, F., Celardo, G. L., Kuno, M., and Jankó, B. Enhanced robustness and dimensional crossover of superradiance in cuboidal nanocrystal superlattices. *Physical Review Research 5*, 2 (2023), 023068.

[98] Giannetti, C., Capone, M., Fausti, D., Fabrizio, M., Parmigiani, F., and Mihailovic, D. Ultrafast optical spectroscopy of strongly correlated materials and high-temperature superconductors: a non-equilibrium approach. *Advances in Physics 65*, 2 (2016), 58–238.

[99] Giannozzi, P., Baroni, S., Bonini, N., Calandra, M., Car, R., Cavazzoni, C., Ceresoli, D., Chiarotti, G. L., Cococcioni, M., Dabo, I., Corso, A. D., de Gironcoli, S., Fabris, S., Fratesi, G., Gebauer, R., Gerstmann, U., Gougoussis, C., Kokalj, A., Lazzeri, M., Martin-Samos, L., Marzari, N., Mauri, F., Mazzarello, R., Paolini, S., Pasquarello, A., Paulatto, L., Sbraccia, C., Scandolo, S., Sclauzero, G., Seitsonen, A. P., Smogunov, A., Umari, P., and Wentzcovitch, R. M. QUANTUM ESPRESSO: a modular and open-source software project for quantum simulations of materials. *Journal of Physics: Condensed Matter 21*, 39 (sep 2009), 395502.

[100] Gopalakrishnan, G., Ruzmetov, D., and Ramanathan, S. On the triggering mechanism for the metal-insulator transition in thin film VO_2 devices: electric field versus thermal effects. *Journal of Materials Science 44* (2009), 5345–5353.

[101] Gordon, R. J., Zhu, L., and Seideman, T. Coherent control of chemical reactions. *Accounts of Chemical Research 32*, 12 (1999), 1007–1016.

[102] Gramlich, M., Bohn, B. J., Tong, Y., Polavarapu, L., Feldmann, J., and Urban, A. S. Thickness-dependence of exciton–exciton annihilation in halide perovskite nanoplatelets. *The Journal of Physical Chemistry Letters 11*, 13 (2020), 5361–5366.

[103] Grandhi, G. K., Dhama, R., Viswanath, N. S. M., Lisitsyna, E. S., Al-Anesi, B., Dana, J., Sugathan, V., Caglayan, H., and Vivo, P. Role of self-trapped excitons in the broadband emission of lead-free perovskite-inspired Cu_2AgBiI_6. *The Journal of Physical Chemistry Letters 14*, 18 (2023), 4192–4199.

[104] Green, M. A., Ho-Baillie, A., and Snaith, H. J. The emergence of perovskite solar cells. *Nature Photonics 8*, 7 (2014), 506–514.

[105] Greif, D., Parsons, M. F., Mazurenko, A., Chiu, C. S., Blatt, S., Huber, F., Ji, G., and Greiner, M. Site-resolved imaging of a fermionic Mott insulator. *Science 351*, 6276 (2016), 953–957.

[106] Guénon, S., Scharinger, S., Wang, S., Ramírez, J., Koelle, D., Kleiner, R., and Schuller, I. K. Electrical breakdown in a V_2O_3 device at the insulator-to-metal transition. *Europhysics Letters 101*, 5 (2013), 57003.

[107] Guerci, D., Capone, M., and Fabrizio, M. Exciton Mott transition revisited. *Physical Review Materials 3*, 5 (2019), 054605.

[108] Guerin, W., Araújo, M. O., and Kaiser, R. Subradiance in a large cloud of cold atoms. *Physical Review Letters 116* (Feb 2016), 083601.

[109] Guiot, V., Cario, L., Janod, E., Corraze, B., Ta Phuoc, V., Rozenberg, M., Stoliar, P., Cren, T., and Roditchev, D. Avalanche breakdown in $GaTa_4Se_{8-x}Te_x$ narrow-gap Mott insulators. *Nature Communications 4*, 1 (2013), 1722.

[110] Guo, Y., Yaffe, O., Hull, T. D., Owen, J. S., Reichman, D. R., and Brus, L. E. Dynamic emission Stokes shift and liquid-like dielectric solvation of band edge carriers in lead-halide perovskites. *Nature Communications 10*, 1 (2019), 1–8.

[111] Hamm, P. *Principles of nonlinear optical spectroscopy: a practical approach or: Mukamel for dummies*. 2005.

[112] Hamm, P., and Zanni, M. *Concepts and methods of 2D infrared spectroscopy*. Cambridge University Press, 2011.

[113] Hansmann, P., Toschi, A., Sangiovanni, G., Saha-Dasgupta, T., Lupi, S., Marsi, M., and Held, K. Mott-hubbard transition in V_2O_3 revisited. *Physica Status Solidi B 250*, 7 (2013), 1251–1264.

[114] Haroche, S., and Kleppner, D. Cavity quantum electrodynamics. *Physics Today 42*, 1 (1989), 24–30.

[115] He, C., and Liu, X. The rise of halide perovskite semiconductors. *Light: Science & Applications 12*, 1 (2023), 15.

[116] Hellmann, S., Rohwer, T., Kalläne, M., Hanff, K., Sohrt, C., Stange, A., Carr, A., Murnane, M., Kapteyn, H., Kipp, L., et al. Time-domain classification of charge-density-wave insulators. *Nature Communications 3*, 1 (2012), 1069.

[117] Herz, L. M. Charge-carrier dynamics in organic-inorganic metal halide perovskites. *Annual Review of Physical Chemistry 67* (2016), 65–89.

[118] Hollander, M. J., Liu, Y., Lu, W.-J., Li, L.-J., Sun, Y.-P., Robinson, J. A., and Datta, S. Electrically driven reversible insulator-metal phase transition in $1T-TaS_2$. *Nano Letters 15*, 3 (2015), 1861–1866.

[119] Homm, P., Menghini, M., Seo, J. W., Peters, S., and Locquet, J. P. Room temperature Mott metal–insulator transition in V_2O_3 compounds induced via strain-engineering. *APL Materials 9*, 2 (02 2021), 021116.

[120] Horsch, P., Khaliullin, G., and Oleś, A. M. Dimerization versus orbital-moment ordering in a Mott insulator YVO_3. *Physical Review Letters 91*, 25 (2003), 257203.

[121] Horsch, P., Oleś, A. M., Feiner, L. F., and Khaliullin, G. Evolution of spin-orbital-lattice coupling in the RVO_3 perovskites. *Physical Review Letters 100*, 16 (2008), 167205.

[122] Horstmann, J. G., Böckmann, H., Wit, B., Kurtz, F., Storeck, G., and Ropers, C. Coherent control of a surface structural phase transition. *Nature 583*, 7815 (2020), 232–236.

[123] Hotta, T. Orbital ordering phenomena in d-and f-electron systems. *Reports on Progress in Physics 69*, 7 (2006), 2061.

[124] Hsu, W.-F., Mellaerts, S., Bellani, C., Homm, P., Uchida, N., Menghini, M., Houssa, M., Seo, J. W., and Locquet, J.-P. Raman spectroscopy and phonon dynamics in strained V_2O_3. *Physical Review Materials 7*, 7 (2023), 074606.

[125] Huang, X., Chen, L., Zhang, C., Qin, Z., Yu, B., Wang, X., and Xiao, M. Inhomogeneous biexciton binding in perovskite semiconductor nanocrystals measured with two-dimensional spectroscopy. *The Journal of Physical Chemistry Letters 11*, 23 (2020), 10173–10181.

[126] Ichikawa, H., Nozawa, S., Sato, T., Tomita, A., Ichiyanagi, K., Chollet, M., Guerin, L., Dean, N., Cavalleri, A., Adachi, S.-i., Arima, T.-h., Sawa, H., Ogimoto, Y., Nakamura, M., Tamaki, R., Miyano, K., and Koshihara, S.-y. Transient photoinduced hidden phase in a manganite. *Nature Materials 10*, 2 (2011), 101–105.

[127] Ielmini, D. Resistive switching memories based on metal oxides: mechanisms, reliability and scaling. *Semiconductor Science and Technology 31*, 6 (2016), 063002.

[128] Imada, M., Fujimori, A., and Tokura, Y. Metal-insulator transitions. *Review of Modern Physics 70* (Oct 1998), 1039–1263.

[129] Jagielski, J., Solari, S. F., Jordan, L., Scullion, D., Blülle, B., Li, Y.-T., Krumeich, F., Chiu, Y.-C., Ruhstaller, B., Santos, E. J., et al. Scalable photonic sources using two-dimensional lead halide perovskite superlattices. *Nature communications 11*, 1 (2020), 387.

[130] Janod, E., Tranchant, J., Corraze, B., Querré, M., Stoliar, P., Rozenberg, M., Cren, T., Roditchev, D., Phuoc, V. T., Besland, M.-P., et al. Resistive switching in Mott insulators and correlated systems. *Advanced Functional Materials 25*, 40 (2015), 6287–6305.

[131] Johnson, A. S., Moreno-Mencía, D., Amuah, E. B., Menghini, M., Locquet, J.-P., Giannetti, C., Pastor, E., and Wall, S. Ultrafast loss of lattice coherence in the light-induced structural phase transition of V_2O_3. *Physical Review Letters 129*, 25 (2022), 255701.

[132] Jördens, R., Strohmaier, N., Günter, K., Moritz, H., and Esslinger, T. A Mott insulator of fermionic atoms in an optical lattice. *Nature 455*, 7210 (2008), 204–207.

[133] Jung, S., Seok, B., Roh, C. j., Kim, Y., Kim, D., Lee, Y., Kang, S., Ishida, S., Shin, S., Eisaki, H., et al. Spontaneous breaking of mirror symmetry in a cuprate beyond critical doping. *Nature Physics* (2024), 1–6.

[134] Jurow, M. J., Lampe, T., Penzo, E., Kang, J., Koc, M. A., Zechel, T., Nett, Z., Brady, M., Wang, L.-W., Alivisatos, A. P., et al. Tunable anisotropic photon emission from self-organized $CsPbBr_3$ perovskite nanocrystals. *Nano Letters 17*, 7 (2017), 4534–4540.

[135] Kalcheim, Y., Camjayi, A., Del Valle, J., Salev, P., Rozenberg, M., and Schuller, I. K. Non-thermal resistive switching in Mott insulator nanowires. *Nature Communications 11*, 1 (2020), 2985.

[136] Kanemitsu, Y. Luminescence spectroscopy of lead-halide perovskites: materials properties and application as photovoltaic devices. *Journal of Materials Chemistry C 5*, 14 (2017), 3427–3437.

[137] Kanki, T., Kawatani, K., Takami, H., and Tanaka, H. Direct observation of giant metallic domain evolution driven by electric bias in VO_2 thin films on TiO_2 (001) substrate. *Applied Physics Letters 101*, 24 (2012).

[138] Keimer, B., Kivelson, S. A., Norman, M. R., Uchida, S., and Zaanen, J. From quantum matter to high-temperature superconductivity in copper oxides. *Nature 518*, 7538 (feb 2015), 179–186.

[139] Keimer, B., and Moore, J. E. The physics of quantum materials. *Nature Physics 13*, 11 (2017), 1045–1055.

[140] Kennes, D. M., Claassen, M., Xian, L., Georges, A., Millis, A. J., Hone, J., Dean, C. R., Basov, D., Pasupathy, A. N., and Rubio, A. Moiré heterostructures as a condensed-matter quantum simulator. *Nature Physics 17*, 2 (2021), 155–163.

[141] Khaliullin, G. Orbital order and fluctuations in Mott insulators. *Progress of Theoretical Physics Supplement 160* (2005), 155–202.

[142] Khaliullin, G., Horsch, P., and Oleś, A. M. Spin order due to orbital fluctuations: cubic vanadates. *Physical Review Letters 86*, 17 (2001), 3879.

[143] Kim, M. Signatures of spin-orbital states of t_{2g}^2 system in optical conductivity: RVO_3 (R= Y and La). *Physical Review B 97*, 15 (2018), 155141.

[144] Klimov, V. I. Optical nonlinearities and ultrafast carrier dynamics in semiconductor nanocrystals. *The Journal of Physical Chemistry B 104*, 26 (2000), 6112–6123.

[145] Koshihara, S., Ishikawa, T., Okimoto, Y., Onda, K., Fukaya, R., Hada, M., Hayashi, Y., Ishihara, S., and Luty, T. Challenges for developing photo-induced phase transition (PIPT) systems: from classical (incoherent) to quantum (coherent) control of PIPT dynamics. *Physics Reports 942* (2022), 1–61.

[146] Kotliar, G., and Vollhardt, D. Strongly correlated materials: insights from dynamical mean-field theory. *Physics Today 57*, 3 (2004), 53–59.

[147] Kovalenko, M. V., and Bodnarchuk, M. I. Lead halide perovskite nanocrystals: from discovery to self-assembly and applications. *Chimia 71*, 7-8 (2017), 461–470.

[148] Krieg, F., Sercel, P. C., Burian, M., Andrusiv, H., Bodnarchuk, M. I., Stoferle, T., Mahrt, R. F., Naumenko, D., Amenitsch, H., Rainò, G., et al. Monodisperse long-chain sulfobetaine-capped $CsPbBr_3$ nanocrystals and their superfluorescent assemblies. *ACS Central Science 7*, 1 (2020), 135–144.

[149] Kriete, B., Lüttig, J., Kunsel, T., Malỳ, P., Jansen, T. L., Knoester, J., Brixner, T., and Pshenichnikov, M. S. Interplay between structural hierarchy and exciton diffusion in artificial light harvesting. *Nature Communications 10*, 1 (2019), 4615.

[150] Kropf, C. M., Valli, A., Franceschini, P., Celardo, G. L., Capone, M., Giannetti, C., and Borgonovi, F. Towards high-temperature coherence-enhanced transport in heterostructures of a few atomic layers. *Physical Review B 100*, 3 (2019), 035126.

[151] Kumar, S., Strachan, J. P., and Williams, R. S. Chaotic dynamics in nanoscale NbO_2 Mott memristors for analogue computing. *Nature 548*, 7667 (2017), 318–321.

[152] Kuwamoto, H., Honig, J., and Appel, J. Electrical properties of the $(V_{1-x}Cr_x)_2O_3$ system. *Physical Review B 22*, 6 (1980), 2626.

[153] Lagoin, C., Bhattacharya, U., Grass, T., Chhajlany, R. W., Salamon, T., Baldwin, K., Pfeiffer, L., Lewenstein, M., Holzmann, M., and Dubin, F. Extended Bose-Hubbard model with dipolar excitons. *Nature 609*, 7927 (2022), 485–489.

[154] Lagoin, C., Suffit, S., Baldwin, K., Pfeiffer, L., and Dubin, F. Mott insulator of strongly interacting two-dimensional semiconductor excitons. *Nature Physics 18*, 2 (2022), 149–153.

[155] Lange, M., Guénon, S., Kalcheim, Y., Luibrand, T., Vargas, N. M., Schwebius, D., Kleiner, R., Schuller, I. K., and Koelle, D. Imaging of electrothermal filament formation in a Mott insulator. *Physical Review Applied 16*, 5 (2021), 054027.

[156] Laplace, Y., and Cavalleri, A. Josephson plasmonics in layered superconductors. *Advances in Physics: X 1*, 3 (2016), 387–411.

[157] Lee, J., Koteles, E. S., and Vassell, M. Luminescence linewidths of excitons in gaas quantum wells below 150 K. *Physical Review B 33*, 8 (1986), 5512.

[158] Lee, J. S., Lee, S., and Noh, T. W. Resistive switching phenomena: a review of statistical physics approaches. *Applied Physics Reviews 2*, 3 (08 2015), 031303.

[159] Lee, P. A., Nagaosa, N., and Wen, X.-G. Doping a Mott insulator: physics of high-temperature superconductivity. *Review of Modern Physics 78* (Jan 2006), 17–85.

[160] Lee, S.-H., Goh, J. S., and Cho, D. Origin of the insulating phase and first-order metal-insulator transition in 1T−TaS_2. *Physical Review Letters 122* (Mar 2019), 106404.

[161] Levchuk, I., Osvet, A., Tang, X., Brandl, M., Perea, J. D., Hoegl, F., Matt, G. J., Hock, R., Batentschuk, M., and Brabec, C. J. Brightly luminescent and color-tunable formamidinium lead halide perovskite $FAPbX_3$ (X= Cl, Br, I) colloidal nanocrystals. *Nano Letters 17*, 5 (2017), 2765–2770.

[162] Li, D., Sharma, A. A., Gala, D. K., Shukla, N., Paik, H., Datta, S., Schlom, D. G., Bain, J. A., and Skowronski, M. Joule heating-induced metal-insulator transition in epitaxial VO_2/TiO_2 devices. *ACS Applied Materials & Interfaces 8*, 20 (2016), 12908–12914.

[163] Li, J., Yuan, X., Jing, P., Li, J., Wei, M., Hua, J., Zhao, J., and Tian, L. Temperature-dependent photoluminescence of inorganic perovskite nanocrystal films. *RSC Advances 6*, 82 (2016), 78311–78316.

[164] Li, S., Luo, J., Liu, J., and Tang, J. Self-trapped excitons in all-inorganic halide perovskites: fundamentals, status, and potential applications. *The Journal of Physical Chemistry Letters 10*, 8 (2019), 1999–2007.

[165] Li, Y., Allegro, I., Kaiser, M., Malla, A. J., Richards, B. S., Lemmer, U., Paetzold, U. W., and Howard, I. A. Exciton versus free carrier emission: implications for photoluminescence efficiency and amplified spontaneous emission thresholds in quasi-2D and 3D perovskites. *Materials Today 49* (2021), 35–47.

[166] Li, Z., Goldoni, L., Wu, Y., Imran, M., Ivanov, Y. P., Divitini, G., Zito, J., Panneerselvam, I. R., Baranov, D., Infante, I., et al. Exogenous metal cations in the synthesis of $CsPbBr_3$ nanocrystals and their interplay with tertiary amines. *Journal of the American Chemical Society 146*, 30 (2024), 20636–20648.

[167] Liu, L., Zhao, R., Xiao, C., Zhang, F., Pevere, F., Shi, K., Huang, H., Zhong, H., and Sychugov, I. Size-dependent phase transition in perovskite nanocrystals. *The Journal of Physical Chemistry Letters 10*, 18 (2019), 5451–5457.

[168] Liu, M., Hwang, H. Y., Tao, H., Strikwerda, A. C., Fan, K., Keiser, G. R., Sternbach, A. J., West, K. G., Kittiwatanakul, S., Lu, J., et al. Terahertz-field-induced insulator-to-metal transition in vanadium dioxide metamaterial. *Nature 487*, 7407 (2012), 345–348.

[169] Liu, M., Pardo, B., Zhang, J., Qazilbash, M., Yun, S. J., Fei, Z., Shin, J.-H., Kim, H.-T., Basov, D., and Averitt, R. Photoinduced phase transitions by time-resolved far-infrared spectroscopy in V_2O_3. *Physical Review Letters 107*, 6 (2011), 066403.

[170] Liu, R., Si, L., Niu, W., Zhang, X., Chen, Z., Zhu, C., Zhuang, W., Chen, Y., Zhou, L., Zhang, C., Wang, P., Song, F., Tang, L., Xu, Y., Zhong, Z., Zhang, R., and Wang, X. Light-induced Mott-insulator-to-metal phase transition in ultrathin intermediate-spin ferromagnetic perovskite ruthenates. *Advanced Materials 35*, 12 (2023), 2211612.

[171] López, C. A., Abia, C., Alvarez-Galván, M. C., Hong, B.-K., Martínez-Huerta, M. V., Serrano-Sanchez, F., Carrascoso, F., Castellanos-Gomez, A., Fernandez-Diaz, M. T., and Alonso, J. A. Crystal structure features of $CsPbBr_3$ perovskite prepared by mechanochemical synthesis. *ACS Omega 5*, 11 (2020), 5931–5938.

[172] Lovinger, D., Brahlek, M., Kissin, P., Kennes, D., Millis, A., Engel-Herbert, R., and Averitt, R. Influence of spin and orbital fluctuations on Mott-Hubbard exciton dynamics in $LaVO_3$ thin films. *Physical Review B 102*, 11 (2020), 115143.

[173] Lu, X., Stepanov, P., Yang, W., Xie, M., Aamir, M. A., Das, I., Urgell, C., Watanabe, K., Taniguchi, T., Zhang, G., et al. Superconductors, orbital magnets and correlated states in magic-angle bilayer graphene. *Nature 574*, 7780 (2019), 653–657.

[174] Luibrand, T., Bercher, A., Rocco, R., Tahouni-Bonab, F., Varbaro, L., Rischau, C. W., Domínguez, C., Zhou, Y., Luo, W., Bag, S., et al. Characteristic length scales of the electrically induced insulator-to-metal transition. *Physical Review Research 5*, 1 (2023), 013108.

[175] Luo, J., Wang, X., Li, S., Liu, J., Guo, Y., Niu, G., Yao, L., Fu, Y., Gao, L., Dong, Q., et al. Efficient and stable emission of warm-white light from lead-free halide double perovskites. *Nature 563*, 7732 (2018), 541–545.

[176] Lupi, S., Baldassarre, L., Mansart, B., Perucchi, A., Barinov, A., Dudin, P., Papalazarou, E., Rodolakis, F., Rueff, J.-P., Itié, J.-P., et al. A microscopic view on the Mott transition in chromium-doped V_2O_3. *Nature Communications 1*, 1 (2010), 105.

[177] Maalej, A., Abid, Y., Kallel, A., Daoud, A., Lautié, A., and Romain, F. Phase transitions and crystal dynamics in the cubic perovskite $CH_3NH_3PbCl_3$. *Solid State Communications 103*, 5 (1997), 279–284.

[178] Madan, H., Jerry, M., Pogrebnyakov, A., Mayer, T., and Datta, S. Quantitative mapping of phase coexistence in Mott-Peierls insulator during electronic and thermally driven phase transition. *ACS Nano 9*, 2 (2015), 2009–2017.

[179] Maiuri, M., Garavelli, M., and Cerullo, G. Ultrafast spectroscopy: State of the art and open challenges. *Journal of the American Chemical Society 142*, 1 (2019), 3–15.

[180] Maklar, J., Sarkar, J., Dong, S., Gerasimenko, Y. A., Pincelli, T., Beaulieu, S., Kirchmann, P. S., Sobota, J. A., Yang, S., Leuenberger, D., et al. Coherent light control of a metastable hidden state. *Science Advances 9*, 47 (2023), eadi4661.

[181] Mansart, B., Boschetto, D., Sauvage, S., Rousse, A., and Marsi, M. Mott transition in Cr-doped V_2O_3 studied by ultrafast reflectivity: Electron correlation effects on the transient response. *Europhysics Letters 92*, 3 (2010), 37007.

[182] Manser, J. S., Christians, J. A., and Kamat, P. V. Intriguing optoelectronic properties of metal halide perovskites. *Chemical Reviews 116*, 21 (2016), 12956–13008.

[183] Manzoni, C., and Cerullo, G. Design criteria for ultrafast optical parametric amplifiers. *Journal of Optics 18*, 10 (2016), 103501.

[184] Masson, S. J., and Asenjo-Garcia, A. Universality of Dicke superradiance in arrays of quantum emitters. *Nature Communications 13*, 1 (2022), 2285.

[185] Masson, S. J., Ferrier-Barbut, I., Orozco, L. A., Browaeys, A., and Asenjo-Garcia, A. Many-body signatures of collective decay in atomic chains. *Physical Review Letters 125* (Dec 2020), 263601.

[186] Matsubara, Y., Ogihara, S., Itatani, J., Maeshima, N., Yonemitsu, K., Ishikawa, T., Okimoto, Y., Koshihara, S.-y., Hiramatsu, T., Nakano, Y., et al. Coherent dynamics of photoinduced phase formation in a strongly correlated organic crystal. *Physical Review B 89*, 16 (2014), 161102.

[187] Mattiotti, F., Kuno, M., Borgonovi, F., Jankó, B., and Celardo, G. L. Thermal decoherence of superradiance in lead halide perovskite nanocrystal superlattices. *Nano Letters 20*, 10 (2020), 7382–7388.

[188] Mattoni, G., Zubko, P., Maccherozzi, F., van der Torren, A. J., Boltje, D. B., Hadjimichael, M., Manca, N., Catalano, S., Gibert, M., Liu, Y., et al. Striped nanoscale phase separation at the metal–insulator transition of heteroepitaxial nickelates. *Nature Communications 7*, 1 (2016), 13141.

[189] Mazza, G., Amaricci, A., Capone, M., and Fabrizio, M. Field-driven mott gap collapse and resistive switch in correlated insulators. *Physical Review Letters 117*, 17 (2016), 176401.

[190] Mazza, G., and Georges, A. Superradiant quantum materials. *Physical Review Letters 122* (Jan 2019), 017401.

[191] McLeod, A. S., van Heumen, E., Ramirez, J. G., Wang, S., Saerbeck, T., Guenon, S., Goldflam, M., Anderegg, L., Kelly, P., Mueller, A., Liu, M. K., Schuller, I. K., and Basov, D. N. Nanotextured phase coexistence in the correlated insulator V_2O_3. *Nature Physics 13*, 1 (2017), 80–86.

[192] McLeod, A. S., Zhang, J., Gu, M. Q., Jin, F., Zhang, G., Post, K. W., Zhao, X. G., Millis, A. J., Wu, W. B., Rondinelli, J. M., Averitt, R. D., and Basov, D. N. Multi-messenger nanoprobes of hidden magnetism in a strained manganite. *Nature Materials 19*, 4 (2020), 397–404.

[193] McWhan, D., Menth, A., Remeika, J., Brinkman, W., and Rice, T. Metal-insulator transitions in pure and doped V_2O_3. *Physical Review B 7*, 5 (1973), 1920.

[194] McWhan, D., and Remeika, J. Metal-insulator transition in $(V_{1-x}Cr_x)_2O_3$. *Physical Review B 2*, 9 (1970), 3734.

[195] McWhan, D., Rice, T., and Remeika, J. Mott transition in Cr-doped V_2O_3. *Physical Review Letters 23*, 24 (1969), 1384.

[196] Meer, H., Gomonay, O., Schmitt, C., Ramos, R., Schnitzspan, L., Kronast, F., Mawass, M.-A., Valencia, S., Saitoh, E., Sinova, J., et al. Strain-induced shape anisotropy in antiferromagnetic structures. *Physical Review B 106*, 9 (2022), 094430.

[197] Mehonic, A., and Kenyon, A. J. Brain-inspired computing needs a master plan. *Nature 604*, 7905 (2022), 255–260.

[198] Milloch, A., Filippi, U., Franceschini, P., Galvani, M., Mor, S., Pagliara, S., Ferrini, G., Banfi, F., Capone, M., Baranov, D., Manna, L., and Giannetti, C. Halide perovskite artificial solids as a new platform to simulate collective phenomena in doped Mott insulators. *Nano Letters 23*, 22 (2023), 10617–10624.

[199] Milloch, A., Filippi, U., Franceschini, P., Mor, S., Pagliara, S., Ferrini, G., Camargo, F. V. A., Cerullo, G., Baranov, D., Manna, L., and Giannetti, C. Fate of optical excitons in $FAPbI_3$ nanocube superlattices. *ACS Photonics 11*, 9 (2024), 3511–3520.

[200] Milloch, A., and Giannetti, C. New order in the copper oxide phase diagram. *Nature Physics* (2024), 1–2.

[201] Mitrano, M., Lee, S., Husain, A. A., Delacretaz, L., Zhu, M., de la Peña Munoz, G., Sun, S. X.-L., Joe, Y. I., Reid, A. H., Wandel, S. F., et al. Ultrafast time-resolved x-ray scattering reveals diffusive charge order dynamics in $La_{2-x}Ba_xCuO_4$. *Science Advances 5*, 8 (2019), eaax3346.

[202] Miyasaka, S., Okimoto, Y., and Tokura, Y. Anisotropy of Mott-Hubbard gap transitions due to spin and orbital ordering in $LaVO_3$ and YVO_3. *Journal of the Physical Society of Japan 71*, 9 (2002), 2086–2089.

[203] Miyasaka, S., Okuda, T., and Tokura, Y. Critical Behavior of Metal-Insulator Transition in $La_{1-x}Sr_xVO_3$. *Physical Review Letters 85*, 25 (2000), 5388.

[204] Mizokawa, T., and Fujimori, A. Electronic structure and orbital ordering in perovskite-type 3d transition-metal oxides studied by Hartree-Fock band-structure calculations. *Physical Review B 54* (Aug 1996), 5368–5380.

[205] Mobilio, S., Boscherini, F., and Meneghini, C. *Synchrotron Radiation*. Springer Berlin, Heidelberg, 2016.

[206] Mott, N. F. The basis of the electron theory of metals, with special reference to the transition metals. *Proceedings of the Physical Society. Section A 62*, 7 (1949), 416.

[207] Mukamel, S. *Principles of Nonlinear Optical Spectroscopy*. Oxford series in optical and imaging sciences. Oxford University Press, 1995.

[208] Nagaoka, Y., Hills-Kimball, K., Tan, R., Li, R., Wang, Z., and Chen, O. Nanocube superlattices of cesium lead bromide perovskites and pressure-induced phase transformations at atomic and mesoscale levels. *Advanced Materials 29*, 18 (2017), 1606666.

[209] Nakamura, F., Sakaki, M., Yamanaka, Y., Tamaru, S., Suzuki, T., and Maeno, Y. Electric-field-induced metal maintained by current of the mott insulator Ca_2RuO_4. *Scientific Reports 3*, 1 (2013), 2536.

[210] Neukirch, A. J., Nie, W., Blancon, J.-C., Appavoo, K., Tsai, H., Sfeir, M. Y., Katan, C., Pedesseau, L., Even, J., Crochet, J. J., Gupta, G., Mohite, A. D., and Tretiak, S. Polaron Stabilization by Cooperative Lattice Distortion and Cation Rotations in Hybrid Perovskite Materials. *Nano Letters 16*, 6 (jun 2016), 3809–3816.

[211] Novelli, F., Fausti, D., Reul, J., Cilento, F., Van Loosdrecht, P. H., Nugroho, A. A., Palstra, T. T., Grüninger, M., and Parmigiani, F. Ultrafast optical spectroscopy of the lowest energy excitations in the Mott insulator compound YVO_3: Evidence for Hubbard-type excitons. *Physical Review B 86*, 16 (2012), 165135.

[212] O'Callahan, B. T., Jones, A. C., Hyung Park, J., Cobden, D. H., Atkin, J. M., and Raschke, M. B. Inhomogeneity of the ultrafast insulator-to-metal transition dynamics of VO_2. *Nature Communications 6*, 1 (2015), 6849.

[213] Palmieri, T., Baldini, E., Steinhoff, A., Akrap, A., Kollár, M., Horváth, E., Forró, L., Jahnke, F., and Chergui, M. Mahan excitons in room-temperature methylammonium lead bromide perovskites. *Nature Communications 11*, 1 (2020), 1–8.

[214] Park, J.-H., Tjeng, L., Tanaka, A., Allen, J., Chen, C., Metcalf, P., Honig, J., De Groot, F., and Sawatzky, G. Spin and orbital occupation and phase transitions in V_2O_3. *Physical Review B 61*, 17 (2000), 11506.

[215] Park, M., Kornienko, N., Reyes-Lillo, S. E., Lai, M., Neaton, J. B., Yang, P., and Mathies, R. A. Critical role of methylammonium librational motion in methylammonium lead iodide ($CH_3NH_3PbI_3$) perovskite photochemistry. *Nano Letters 17*, 7 (2017), 4151–4157.

[216] Pashaei Adl, H., Gorji, S., Muñoz-Matutano, G., Gualdrón-Reyes, A. F., Suárez, I., Chirvony, V. S., Mora-Seró, I., and Martínez-Pastor, J. P. Superradiance emission and its thermal decoherence in lead halide perovskites superlattices. *Advanced Optical Materials* (2023), 2202497.

[217] Pavarini, E., Biermann, S., Poteryaev, A., Lichtenstein, A. I., Georges, A., and Andersen, O. K. Mott transition and suppression of orbital fluctuations in orthorhombic $3d^1$ perovskites. *Physical Review Letters 92* (Apr 2004), 176403.

[218] Peli, S., Conte, S. D., Comin, R., Nembrini, N., Ronchi, A., Abrami, P., Banfi, F., Ferrini, G., Brida, D., Lupi, S., Fabrizio,

M., Damascelli, A., Capone, M., Cerullo, G., and Giannetti, C. Mottness at finite doping and charge instabilities in cuprates. *Nature Physics 13* (May 2017), 806–812.

[219] Perfetto, E., Marini, A., and Stefanucci, G. Self-consistent screening enhances the stability of the nonequilibrium excitonic insulator phase. *Physical Review B 102* (Aug 2020), 085203.

[220] Phuong, L. Q., Yamada, Y., Nagai, M., Maruyama, N., Wakamiya, A., and Kanemitsu, Y. Free carriers versus excitons in $CH_3NH_3PbI_3$ perovskite thin films at low temperatures: charge transfer from the orthorhombic phase to the tetragonal phase. *The Journal of Physical Chemistry Letters 7*, 13 (2016), 2316–2321.

[221] Pickett, M. D., Medeiros-Ribeiro, G., and Williams, R. S. A scalable neuristor built with Mott memristors. *Nature Materials 12*, 2 (2013), 114–117.

[222] Pofelski, A., Valencia, S., Kalcheim, Y., Salev, P., Rivera, A., Huang, C., Mawass, M. A., Kronast, F., Schuller, I. K., Zhu, Y., et al. Domain nucleation across the metal-insulator transition of self-strained V_2O_3 films. *arXiv preprint arXiv:2312.09051* (2023).

[223] Preda, F., Kumar, V., Crisafi, F., Del Valle, D. G. F., Cerullo, G., and Polli, D. Broadband pump-probe spectroscopy at 20-MHz modulation frequency. *Optics Letters 41*, 13 (2016), 2970–2973.

[224] Price, M. B., Butkus, J., Jellicoe, T. C., Sadhanala, A., Briane, A., Halpert, J. E., Broch, K., Hodgkiss, J. M., Friend, R. H., and Deschler, F. Hot-carrier cooling and photoinduced refractive index changes in organic–inorganic lead halide perovskites. *Nature Communications 6*, 1 (2015), 1–8.

[225] Protesescu, L., Yakunin, S., Bodnarchuk, M. I., Krieg, F., Caputo, R., Hendon, C. H., Yang, R. X., Walsh, A., and Kovalenko, M. V. Nanocrystals of cesium lead halide perovskites ($CsPbX_3$, X= Cl, Br, and I): novel optoelectronic materials showing bright emission with wide color gamut. *Nano Letters 15*, 6 (2015), 3692–3696.

[226] Qazilbash, M. M., Brehm, M., Chae, B.-G., Ho, P.-C., Andreev, G. O., Kim, B.-J., Yun, S. J., Balatsky, A. V., Maple, M. B., Keilmann, F., Kim, H.-T., and Basov, D. N. Mott transition in VO_2 revealed by infrared spectroscopy and nano-imaging. *Science 318*, 5857 (2007), 1750–1753.

[227] Qazilbash, M. M., Schafgans, A., Burch, K., Yun, S., Chae, B., Kim, B., Kim, H.-T., and Basov, D. Electrodynamics of the vanadium oxides VO_2 and V_2O_3. *Physical Review B 77*, 11 (2008), 115121.

[228] Qazilbash, M. M., Tripathi, A., Schafgans, A. A., Kim, B.-J., Kim, H.-T., Cai, Z., Holt, M. V., Maser, J. M., Keilmann, F., Shpyrko, O. G., and Basov, D. N. Nanoscale imaging of the electronic and structural transitions in vanadium dioxide. *Physical Review B 83* (Apr 2011), 165108.

[229] Quan, L. N., Rand, B. P., Friend, R. H., Mhaisalkar, S. G., Lee, T.-W., and Sargent, E. H. Perovskites for next-generation optical sources. *Chemical Reviews 119*, 12 (2019), 7444–7477.

[230] Quarti, C., Grancini, G., Mosconi, E., Bruno, P., Ball, J. M., Lee, M. M., Snaith, H. J., Petrozza, A., and De Angelis, F. The raman spectrum of the $CH_3NH_3PbI_3$ hybrid perovskite: interplay of theory and experiment. *The Journal of Physical Chemistry Letters 5*, 2 (2013), 279–284.

[231] Rabinovich, K. S., Yaresko, A. N., Dawson, R. D., Krautloher, M. J., Priessnitz, T., Mathis, Y.-L., Keimer, B., and Boris, A. V. Photoinduced phase switching at a Mott insulator-to-metal transition. *arXiv:2206.05005* (2022).

[232] Rainò, G., Becker, M. A., Bodnarchuk, M. I., Mahrt, R. F., Kovalenko, M. V., and Stöferle, T. Superfluorescence from lead halide perovskite quantum dot superlattices. *Nature 563*, 7733 (2018), 671–675.

[233] Rainò, G., Nedelcu, G., Protesescu, L., Bodnarchuk, M. I., Kovalenko, M. V., Mahrt, R. F., and Stoferle, T. Single cesium lead halide perovskite nanocrystals at low temperature: fast single-photon emission, reduced blinking, and exciton fine structure. *ACS Nano 10*, 2 (2016), 2485–2490.

[234] Ran, Y., Pei, Y., Zhou, Z., Wang, H., Sun, Y., Wang, Z., Hao, M., Zhao, J., Chen, J., and Yan, X. A review of Mott insulator in memristors: The materials, characteristics, applications for future computing systems and neuromorphic computing. *Nano Research 16*, 1 (2023), 1165–1182.

[235] Reul, J., Nugroho, A., Palstra, T., and Grüninger, M. Probing orbital fluctuations in RVO_3 (R= Y, Gd, or Ce) by ellipsometry. *Physical Review B 86*, 12 (2012), 125128.

[236] Ronchi, A., Franceschini, P., De Poli, A., Homm, P., Fitzpatrick, A., Maccherozzi, F., Ferrini, G., Banfi, F., Dhesi, S. S., Menghini, M., et al. Nanoscale self-organization and metastable non-thermal metallicity in Mott insulators. *Nature Communications 13*, 1 (2022), 3730.

[237] Ronchi, A., Franceschini, P., Homm, P., Gandolfi, M., Ferrini, G., Pagliara, S., Banfi, F., Menghini, M., Giannetti, C., et al. Light-assisted resistance collapse in a V_2O_3-based mott-insulator device. *Physical Review Applied 15*, 4 (2021), 044023.

[238] Ronchi, A., Homm, P., Menghini, M., Franceschini, P., Maccherozzi, F., Banfi, F., Ferrini, G., Cilento, F., Parmigiani, F., Dhesi, S. S., et al. Early-stage dynamics of metallic droplets embedded in the nanotextured Mott insulating phase of V_2O_3. *Physical Review B 100*, 7 (2019), 075111.

[239] Rozier, P., Ratuszna, A., and Galy, J. Comparative structural and electrical studies of V_2O_3 and $V_{2-x}Ni_xO_3$ ($0< x< 0.75$) solid solution. *Zeitschrift für Anorganische und Allgemeine Chemie 628*, 5 (2002), 1236–1242.

[240] Russo, M., McGhee, K. E., Virgili, T., Lidzey, D. G., Cerullo, G., and Maiuri, M. Dephasing processes in the molecular dye lumogen-f orange characterized by two-dimensional electronic spectroscopy. *Molecules 27*, 20 (2022), 7095.

[241] Saba, M., Cadelano, M., Marongiu, D., Chen, F., Sarritzu, V., Sestu, N., Figus, C., Aresti, M., Piras, R., Geddo Lehmann, A., et al. Correlated electron-hole plasma in organometal perovskites. *Nature Communications 5*, 1 (2014), 5049.

[242] Sachdev, S., and Keimer, B. Quantum criticality. *Physics Today 64*, 2 (2011), 29–35.

[243] Sakai, J., and Kurisu, M. Effect of pressure on the electric-field-induced resistance switching of VO_2 planar-type junctions. *Physical Review B 78*, 3 (2008), 033106.

[244] Salamon, M. B., and Jaime, M. The physics of manganites: Structure and transport. *Review of Modern Physics 73* (Aug 2001), 583–628.

[245] Sawa, A. Resistive switching in transition metal oxides. *Materials Today 11*, 6 (2008), 28–36.

[246] Sawada, H., Hamada, N., Terakura, K., and Asada, T. Orbital and spin orderings in YVO_3 and $LaVO_3$ in the generalized gradient approximation. *Physical Review B 53*, 19 (1996), 12742.

[247] Schlaus, A. P., Spencer, M. S., Miyata, K., Liu, F., Wang, X., Datta, I., Lipson, M., Pan, A., and Zhu, X.-Y. How lasing happens in $CsPbBr_3$ perovskite nanowires. *Nature Communications 10*, 1 (2019), 1–8.

[248] Sercel, P. C., Lyons, J. L., Bernstein, N., and Efros, A. L. Quasicubic model for metal halide perovskite nanocrystals. *The Journal of Chemical Physics 151*, 23 (2019), 234106.

[249] Serlin, M., Tschirhart, C., Polshyn, H., Zhang, Y., Zhu, J., Watanabe, K., Taniguchi, T., Balents, L., and Young, A. Intrinsic quantized anomalous hall effect in a moiré heterostructure. *Science 367*, 6480 (2020), 900–903.

[250] Shamsi, J., Urban, A. S., Imran, M., De Trizio, L., and Manna, L. Metal halide perovskite nanocrystals: synthesis, post-synthesis modifications, and their optical properties. *Chemical Reviews 119*, 5 (2019), 3296–3348.

[251] Sharpe, A. L., Fox, E. J., Barnard, A. W., Finney, J., Watanabe, K., Taniguchi, T., Kastner, M., and Goldhaber-Gordon, D. Emergent ferromagnetism near three-quarters filling in twisted bilayer graphene. *Science 365*, 6453 (2019), 605–608.

[252] Shcherbakov-Wu, W., Sercel, P. C., Krieg, F., Kovalenko, M. V., and Tisdale, W. A. Temperature-independent dielectric constant in $CsPbBr_3$ nanocrystals revealed by linear absorption spectroscopy. *The Journal of Physical Chemistry Letters 12*, 33 (2021), 8088–8095.

[253] Shimano, R., and Tsuji, N. Higgs mode in superconductors. *Annual Review of Condensed Matter Physics 11*, 1 (2020), 103–124.

[254] Shulenberger, K. E., Ashner, M. N., Ha, S. K., Krieg, F., Kovalenko, M. V., Tisdale, W. A., and Bawendi, M. G. Setting an upper bound to the biexciton binding energy in $CsPbBr_3$ perovskite nanocrystals. *The Journal of Physical Chemistry Letters 10*, 18 (2019), 5680–5686.

[255] Siemens, M. E., Moody, G., Li, H., Bristow, A. D., and Cundiff, S. T. Resonance lineshapes in two-dimensional fourier transform spectroscopy. *Optics Express 18*, 17 (2010), 17699–17708.

[256] Sierra, E., Masson, S. J., and Asenjo-Garcia, A. Dicke superradiance in ordered lattices: dimensionality matters. *Physical Review Research 4* (Jun 2022), 023207.

[257] Simon Mun, B., Yoon, J., Mo, S.-K., Chen, K., Tamura, N., Dejoie, C., Kunz, M., Liu, Z., Park, C., Moon, K., et al. Role of Joule heating effect and bulk-surface phases in voltage-driven metal-insulator transition in VO_2 crystal. *Applied Physics Letters 103*, 6 (2013).

[258] Smith, M. D., and Karunadasa, H. I. White-light emission from layered halide perovskites. *Accounts of Chemical Research 51*, 3 (2018), 619–627.

[259] Souza, I., Marzari, N., and Vanderbilt, D. Maximally localized Wannier functions for entangled energy bands. *Physical Review B 65* (Dec 2001), 035109.

[260] Stepanov, P., Das, I., Lu, X., Fahimniya, A., Watanabe, K., Taniguchi, T., Koppens, F. H., Lischner, J., Levitov, L., and Efetov, D. K. Untying the insulating and superconducting orders in magic-angle graphene. *Nature 583*, 7816 (2020), 375–378.

[261] Stojchevska, L., Vaskivskyi, I., Mertelj, T., Kusar, P., Svetin, D., Brazovskii, S., and Mihailovic, D. Ultrafast switching to a stable hidden quantum state in an electronic crystal. *Science 344*, 6180 (2014), 177–180.

[262] Stoliar, P., Cario, L., Janod, E., Corraze, B., Guillot-Deudon, C., Salmon-Bourmand, S., Guiot, V., Tranchant, J., and Rozenberg, M. Universal electric-field-driven resistive transition in narrow-gap Mott insulators. *Advanced Materials 25*, 23 (2013), 3222–3226.

[263] Stoliar, P., Rozenberg, M., Janod, E., Corraze, B., Tranchant, J., and Cario, L. Nonthermal and purely electronic resistive switching in a Mott memory. *Physical Review B 90*, 4 (2014), 045146.

[264] Stoliar, P., Tranchant, J., Corraze, B., Janod, E., Besland, M.-P., Tesler, F., Rozenberg, M., and Cario, L. A leaky-integrate-and-fire neuron analog realized with a Mott insulator. *Advanced Functional Materials 27*, 11 (2017), 1604740.

[265] Stranks, S. D., and Snaith, H. J. Metal-halide perovskites for photovoltaic and light-emitting devices. *Nature Nanotechnology 10*, 5 (2015), 391–402.

[266] Streltsov, A., Adesso, G., and Plenio, M. B. Colloquium: Quantum coherence as a resource. *Reviews of Modern Physics 89*, 4 (2017), 041003.

[267] Suen, C. T., Marković, I., Zonno, M., Zhdanovich, S., Jo, N.-H., Schmid, M., Hansmann, P., Pupuhal, P., Fürsich, K., Zimmerman, V., et al. Nature of the current-induced insulator-to-metal transition in Ca_2RuO_4 as revealed by transport-ARPES. *arXiv:2308.05803* (2023).

[268] Sun, K., Sun, S., Zhu, C., Tian, H., Yang, H., and Li, J. Hidden CDW states and insulator-to-metal transition after a pulsed femtosecond laser excitation in layered chalcogenide 1T-$TaS_{2-x}Se_x$. *Science Advances 4*, 7 (2018), eaas9660.

[269] Sun, Z., and Millis, A. J. Transient trapping into metastable states in systems with competing orders. *Physical Review X 10*, 2 (2020), 021028.

[270] Sundaram, S., and Mazur, E. Inducing and probing non-thermal transitions in semiconductors using femtosecond laser pulses. *Nature Materials 1*, 4 (2002), 217–224.

[271] Sutherland, B. R., and Sargent, E. H. Perovskite photonic sources. *Nature Photonics 10*, 5 (2016), 295–302.

[272] Tahara, H., Endo, M., Wakamiya, A., and Kanemitsu, Y. Experimental evidence of localized shallow states in orthorhombic phase of $CH_3NH_3PbI_3$ perovskite thin films revealed by photocurrent beat spectroscopy. *The Journal of Physical Chemistry C 120*, 10 (2016), 5347–5352.

[273] Takubo, N., Ogimoto, Y., Nakamura, M., Tamaru, H., Izumi, M., and Miyano, K. Persistent and reversible all-optical phase control in a manganite thin film. *Physical Review Letters 95* (Jun 2005), 017404.

[274] Tan, J., Li, D., Zhu, J., Han, N., Gong, Y., and Zhang, Y. Self-trapped excitons in soft semiconductors. *Nanoscale 14* (2022), 16394–16414.

[275] Tan, M., Chen, B., Zhang, Y., Ni, M., Wang, W., Zhang, H., Zhou, Q., Bao, Y., and Wang, Y. Temperature-dependent dynamic carrier process of $FAPbI_3$ nanocrystals' film. *The Journal of Physical Chemistry C 124*, 9 (2020), 5093–5098.

[276] Tang, Y., Poonia, D., Van Der Laan, M., Timmerman, D., Kinge, S., Siebbeles, L. D., and Schall, P. Electronic coupling of highly ordered perovskite nanocrystals in supercrystals. *ACS Applied Energy Materials 5*, 5 (2022), 5415–5422.

[277] Tesler, F., Adda, C., Tranchant, J., Corraze, B., Janod, E., Cario, L., Stoliar, P., and Rozenberg, M. Relaxation of a spiking Mott artificial neuron. *Physical Review Applied 10* (Nov 2018), 054001.

[278] Tocchio, L. F., Becca, F., and Gros, C. Backflow correlations in the Hubbard model: An efficient tool for the study of the metal-insulator transition and the large-U limit. *Physical Review B 83* (May 2011), 195138.

[279] Tokura, Y. Correlated-electron physics in transition-metal oxides. *Physics Today 56*, 7 (2003), 50–55.

[280] Tokura, Y. Critical features of colossal magnetoresistive manganites. *Reports on Progress in Physics 69*, 3 (2006), 797.

[281] Tokura, Y., Kawasaki, M., and Nagaosa, N. Emergent functions of quantum materials. *Nature Physics 13*, 11 (2017), 1056–1068.

[282] Tollerud, J. O., Cundiff, S. T., and Davis, J. A. Revealing and characterizing dark excitons through coherent multidimensional spectroscopy. *Physical Review Letters 117*, 9 (2016), 097401.

[283] Tollerud, J. O., and Davis, J. A. Coherent multi-dimensional spectroscopy: Experimental considerations, direct comparisons and new capabilities. *Progress in Quantum Electronics 55* (2017), 1–34.

[284] Tomimoto, S., Miyasaka, S., Ogasawara, T., Okamoto, H., and Tokura, Y. Ultrafast photoinduced melting of orbital order in $LaVO_3$. *Physical Review B 68*, 3 (2003), 035106.

[285] Tong, Y., Yao, E.-P., Manzi, A., Bladt, E., Wang, K., Döblinger, M., Bals, S., Müller-Buschbaum, P., Urban, A. S., Polavarapu, L., et al. Spontaneous self-assembly of perovskite nanocrystals into electronically coupled supercrystals: toward filling the green gap. *Advanced Materials 30*, 29 (2018), 1801117.

[286] Toso, S., Baranov, D., Altamura, D., Scattarella, F., Dahl, J., Wang, X., Marras, S., Alivisatos, A. P., Singer, A., Giannini, C., et al. Multilayer diffraction reveals that colloidal superlattices approach the structural perfection of single crystals. *ACS Nano 15*, 4 (2021), 6243–6256.

[287] Toso, S., Baranov, D., Filippi, U., Giannini, C., and Manna, L. Collective diffraction effects in perovskite nanocrystal superlattices. *Accounts of Chemical Research 56*, 1 (2022), 66–76.

[288] Toso, S., Baranov, D., Giannini, C., and Manna, L. Structure and surface passivation of ultrathin cesium lead halide nanoplatelets revealed by multilayer diffraction. *ACS Nano 15*, 12 (2021), 20341–20352.

[289] Toso, S., Baranov, D., Giannini, C., Marras, S., and Manna, L. Wide-angle X-ray diffraction evidence of structural coherence in $CsPbBr_3$ nanocrystal superlattices. *ACS Materials Letters 1*, 2 (2019), 272–276.

[290] Trebino, R., DeLong, K. W., Fittinghoff, D. N., Sweetser, J. N., Krumbügel, M. A., Richman, B. A., and Kane, D. J. Measuring ultrashort laser pulses in the time-frequency domain using frequency-resolved optical gating. *Review of Scientific Instruments 68*, 9 (1997), 3277–3295.

[291] Tung, L., Ivanov, A., Schefer, J., Lees, M. R., Balakrishnan, G., and Paul, D. M. Spin, orbital ordering, and magnetic dynamics of $LaVO_3$: magnetization, heat capacity, and neutron scattering studies. *Physical Review B 78*, 5 (2008), 054416.

[292] Ulrich, C., Khaliullin, G., Sirker, J., Reehuis, M., Ohl, M., Miyasaka, S., Tokura, Y., and Keimer, B. Magnetic neutron scattering study of YVO_3: evidence for an orbital Peierls state. *Physical Review Letters 91*, 25 (2003), 257202.

[293] Valensise, C. M., Giuseppi, A., Cerullo, G., and Polli, D. Deep reinforcement learning control of white-light continuum generation. *Optica 8*, 2 (2021), 239–242.

[294] Valmianski, I., Wang, P., Wang, S., Ramirez, J. G., Guénon, S., and Schuller, I. K. Origin of the current-driven breakdown in vanadium oxides: Thermal versus electronic. *Physical Review B 98*, 19 (2018), 195144.

[295] van der Burgt, J. S., Geuchies, J. J., van der Meer, B., Vanrompay, H., Zanaga, D., Zhang, Y., Albrecht, W., Petukhov, A. V., Filion, L., Bals, S., et al. Cuboidal supraparticles self-assembled from cubic $CsPbBr_3$ perovskite nanocrystals. *The Journal of Physical Chemistry C 122*, 27 (2018), 15706–15712.

[296] Vaskivskyi, I., Gospodaric, J., Brazovskii, S., Svetin, D., Sutar, P., Goreshnik, E., Mihailovic, I. A., Mertelj, T., and Mihailovic, D. Controlling the metal-to-insulator relaxation of the metastable hidden quantum state in 1T-TaS_2. *Science Advances 1*, 6 (2015), e1500168.

[297] Verma, A., Golež, D., Gorobtsov, O. Y., Kaj, K., Russell, R., Kaaret, J. Z., Lamb, E., Khalsa, G., Nair, H. P., Sun, Y., Bouck, R., Schreiber, N., Ruf, J. P., Ramaprasad, V., Kubota, Y., Togashi, T., Stoica, V. A., Padmanabhan, H., Freeland, J. W., Benedek, N. A., Shpyrko, O. G., Harter, J. W., Averitt, R. D., Schlom, D. G., Shen, K. M., Millis, A. J., and Singer, A. Picosecond volume expansion drives a later-time insulator-metal transition in a nano-textured Mott insulator. *Nature Physics 20*, 5 (2024), 807–814.

[298] Vogelgesang, S., Storeck, G., Horstmann, J., Diekmann, T., Sivis, M., Schramm, S., Rossnagel, K., Schäfer, S., and Ropers, C. Phase ordering of charge density waves traced by ultrafast low-energy electron diffraction. *Nature Physics 14*, 2 (2018), 184–190.

[299] Walther, H., Varcoe, B. T., Englert, B.-G., and Becker, T. Cavity quantum electrodynamics. *Reports on Progress in Physics 69*, 5 (2006), 1325.

[300] Wandel, S., Boschini, F., da Silva Neto, E. H., Shen, L., Na, M. X., Zohar, S., Wang, Y., Welch, S. B., Seaberg, M. H., Koralek, J. D., Dakovski, G. L., Hettel, W., Lin, M.-F., Moeller, S. P., Schlotter, W. F., Reid, A. H., Minitti, M. P., Boyle, T., He, F., Sutarto, R., Liang, R., Bonn, D., Hardy, W., Kaindl, R. A., Hawthorn, D. G., Lee, J.-S., Kemper, A. F., Damascelli, A., Giannetti, C., Turner, J. J., and Coslovich, G. Enhanced charge density wave coherence in a light-quenched, high-temperature superconductor. *Science 376*, 6595 (2022), 860–864.

[301] Wang, J. X., and Kais, S. Finite-size scaling for Mott metal-insulator transition on a half filled nonpartite lattice. *Physical Review B 66* (Aug 2002), 081101.

[302] Wang, Y., Kang, K.-M., Kim, M., Lee, H.-S., Waser, R., Wouters, D., Dittmann, R., Yang, J. J., and Park, H.-H. Mott-transition-based RRAM. *Materials Today 28* (2019), 63–80.

[303] Wang, Z., Wu, H., Burr, G. W., Hwang, C. S., Wang, K. L., Xia, Q., and Yang, J. J. Resistive switching materials for information processing. *Nature Reviews Materials 5*, 3 (2020), 173–195.

[304] Waser, R., and Aono, M. Nanoionics-based resistive switching memories. *Nature Materials 6*, 11 (2007), 833–840.

[305] Weber, O. J., Ghosh, D., Gaines, S., Henry, P. F., Walker, A. B., Islam, M. S., and Weller, M. T. Phase behavior and polymorphism of formamidinium lead iodide. *Chemistry of Materials 30*, 11 (2018), 3768–3778.

[306] Wegkamp, D., Herzog, M., Xian, L., Gatti, M., Cudazzo, P., McGahan, C. L., Marvel, R. E., Haglund, R. F., Rubio, A., Wolf, M., and Stähler, J. Instantaneous band gap collapse in photoexcited monoclinic VO_2 due to photocarrier doping. *Physical Review Letters 113* (Nov 2014), 216401.

[307] Werner, P., and Millis, A. J. High-spin to low-spin and orbital polarization transitions in multiorbital Mott systems. *Physical Review Letters 99* (Sep 2007), 126405.

[308] Wooten, F. *Optical Properties of Solids*. Academic Press, 1972.

[309] Wouters, D. J., Menzel, S., Rupp, J. A. J., Hennen, T., and Waser, R. On the universality of the I-V switching characteristics in non-volatile and volatile resistive switching oxides. *Faraday Discussions 213* (2019), 183–196.

[310] Wright, A. D., Milot, R. L., Eperon, G. E., Snaith, H. J., Johnston, M. B., and Herz, L. M. Band-tail recombination in hybrid lead iodide perovskite. *Advanced Functional Materials 27*, 29 (2017), 1700860.

[311] Wróbel, P., and Eder, R. Excitons in Mott insulators. *Physical Review B 66*, 3 (2002), 035111.

[312] Yamada, Y., and Kanemitsu, Y. Electron-phonon interactions in halide perovskites. *NPG Asia Materials 14*, 1 (2022), 48.

[313] Yamada, Y., Nakamura, T., Endo, M., Wakamiya, A., and Kanemitsu, Y. Photocarrier recombination dynamics in perovskite $CH_3NH_3PbI_3$ for solar cell applications. *Journal of the American Chemical Society 136*, 33 (2014), 11610–11613.

[314] Yamamoto, A., Miyajima, K., Goto, T., Ju Ko, H., and Yao, T. Biexciton luminescence in high-quality ZnO epitaxial thin films. *Journal of Applied Physics 90*, 10 (2001), 4973–4976.

[315] Yang, Y., Yan, Y., Yang, M., Choi, S., Zhu, K., Luther, J. M., and Beard, M. C. Low surface recombination velocity in solution-grown $CH_3NH_3PbBr_3$ perovskite single crystal. *Nature Communications 6*, 1 (2015), 7961.

[316] Yang, Y., Yang, M., Zhu, K., Johnson, J. C., Berry, J. J., Van De Lagemaat, J., and Beard, M. C. Large polarization-dependent exciton optical stark effect in lead iodide perovskites. *Nature Communications 7*, 1 (2016), 12613.

[317] Yang, Z., Ko, C., and Ramanathan, S. Oxide electronics utilizing ultrafast metal-insulator transitions. *Annual Review of Materials Research 41* (2011), 337–367.

[318] Yankowitz, M., Chen, S., Polshyn, H., Zhang, Y., Watanabe, K., Taniguchi, T., Graf, D., Young, A. F., and Dean, C. R. Tuning superconductivity in twisted bilayer graphene. *Science 363*, 6431 (2019), 1059–1064.

[319] Yazdani, N., Bodnarchuk, M. I., Bertolotti, F., Masciocchi, N., Fureraj, I., Guzelturk, B., Cotts, B. L., Zajac, M., Rainò, G., Jansen, M., et al. Coupling to octahedral tilts in halide perovskite nanocrystals induces phonon-mediated attractive interactions between excitons. *Nature Physics 20* (2024), 47–53.

[320] Yoshida, M., Suzuki, R., Zhang, Y., Nakano, M., and Iwasa, Y. Memristive phase switching in two-dimensional $1T^{-}TaS_2$ crystals. *Science Advances 1*, 9 (2015), e1500606.

[321] Yoshida, R., Yamamoto, T., Ishida, Y., Nagao, H., Otsuka, T., Saeki, K., Muraoka, Y., Eguchi, R., Ishizaka, K., Kiss, T., Watanabe, S., Kanai, T., Itatani, J., and Shin, S. Ultrafast photoinduced transition of an insulating VO_2 thin film into a nonrutile metallic state. *Physical Review B 89* (May 2014), 205114.

[322] You, Y., Zhang, X.-X., Berkelbach, T. C., Hybertsen, M. S., Reichman, D. R., and Heinz, T. F. Observation of biexcitons in monolayer WSe_2. *Nature Physics 11*, 6 (2015), 477–481.

[323] Yu, Y., Bataller, A. W., Younts, R., Yu, Y., Li, G., Puretzky, A. A., Geohegan, D. B., Gundogdu, K., and Cao, L. Room-temperature electron–hole liquid in monolayer MoS_2. *ACS Nano 13*, 9 (2019), 10351–10358.

[324] Yuan, F., Wu, Z., Dong, H., Xi, J., Xi, K., Divitini, G., Jiao, B., Hou, X., Wang, S., and Gong, Q. High stability and ultralow

threshold amplified spontaneous emission from formamidinium lead halide perovskite films. *The Journal of Physical Chemistry C 121*, 28 (2017), 15318–15325.

[325] Yusupov, R., Mihailovic, D., Colin, C., Blake, G., and Palstra, T. T. Critical phenomena and femtosecond ordering dynamics associated with electronic and spin-ordered phases in YVO_3 and $GdVO_3$. *Physical Review B 81*, 7 (2010), 075103.

[326] Zhang, H.-T., Brahlek, M., Ji, X., Lei, S., Lapano, J., Freeland, J. W., Gopalan, V., and Engel-Herbert, R. High-quality $LaVO_3$ films as solar energy conversion material. *ACS Applied Materials & Interfaces 9*, 14 (2017), 12556–12562.

[327] Zhang, J., and Averitt, R. D. Dynamics and control in complex transition metal oxides. *Annual Review of Materials Research 44* (2014), 19–43.

[328] Zhang, J., Tan, X., Liu, M., Teitelbaum, S. W., Post, K. W., Jin, F., Nelson, K., Basov, D. N., Wu, W., and Averitt, R. D. Cooperative photoinduced metastable phase control in strained manganite films. *Nature Materials 15*, 9 (2016), 956–960.

[329] Zhang, S., Jin, L., Lu, Y., Zhang, L., Yang, J., Zhao, Q., Sun, D., Thompson, J. J., Yuan, B., Ma, K., et al. Moiré superlattices in twisted two-dimensional halide perovskites. *Nature Materials* (2024), 1–8.

[330] Zhang, X., Zhuo, Y., Luo, Q., Wu, Z., Midya, R., Wang, Z., Song, W., Wang, R., Upadhyay, N. K., Fang, Y., Kiani, F., Rao, M., Yang, Y., Xia, Q., Liu, Q., Liu, M., and Yang, J. J. An artificial spiking afferent nerve based on Mott memristors for neurorobotics. *Nature Communications 11*, 1 (2020), 51.

[331] Zhang, X.-J., Koch, E., and Pavarini, E. $LaVO_3$: a true Kugel-Khomskii system. *Physical Review B 106* (Sep 2022), 115110.

[332] Zhou, C., Zhong, Y., Dong, H., Zheng, W., Tan, J., Jie, Q., Pan, A., Zhang, L., and Xie, W. Cooperative excitonic quantum ensemble in perovskite-assembly superlattice microcavities. *Nature Communications 11*, 1 (2020), 1–7.

[333] Zhou, Y., and Ramanathan, S. Mott Memory and Neuromorphic Devices. *Proceedings of the IEEE 103*, 8 (2015), 1289–1310.

[334] Zhu, H., Miyata, K., Fu, Y., Wang, J., Joshi, P. P., Niesner, D., Williams, K. W., Jin, S., and Zhu, X.-Y. Screening in crystalline liquids protects energetic carriers in hybrid perovskites. *Science 353*, 6306 (2016), 1409–1413.

[335] Zhu, Y., Hoffman, J., Rowland, C. E., Park, H., Walko, D. A., Freeland, J. W., Ryan, P. J., Schaller, R. D., Bhattacharya, A., and Wen, H. Unconventional slowing down of electronic recovery in photoexcited charge-ordered $La_{1/3}Sr_{2/3}FeO_3$. *Nature Communications 9*, 1 (2018), 1799.

[336] Zimmers, A., Aigouy, L., Mortier, M., Sharoni, A., Wang, S., West, K., Ramirez, J., and Schuller, I. K. Role of thermal heating on the voltage induced insulator-metal transition in VO_2. *Physical Review Letters 110*, 5 (2013), 056601.

[337] Zong, A., Dolgirev, P. E., Kogar, A., Ergeçen, E., Yilmaz, M. B., Bie, Y.-Q., Rohwer, T., Tung, I.-C., Straquadine, J., Wang, X., et al. Dynamical slowing-down in an ultrafast photoinduced phase transition. *Physical Review Letters 123*, 9 (2019), 097601.

[338] Zong, A., Kogar, A., Bie, Y.-Q., Rohwer, T., Lee, C., Baldini, E., Ergeçen, E., Yilmaz, M. B., Freelon, B., Sie, E. J., et al. Evidence for topological defects in a photoinduced phase transition. *Nature Physics 15*, 1 (2019), 27–31.

Statement on the use of Generative AI

I did not use generative AI assistance tools during the research/writing process of my thesis, except for mere language assistance. The text/code/images in this thesis are my own (unless otherwise specified) and generative AI has only been used in accordance with the KU Leuven guidelines and appropriate references have been added. I have reviewed and edited the content as needed and I take full responsibility for the content of the thesis.

List of publications

A. Milloch, I. Figueruelo-Campanero, W.-F. Hsu, S. Mor, S. Mellaerts, F. Maccherozzi, L. Ishibe Veiga, S. Dhesi, M. Spera, J. W. Seo, J.P. Locquet, M. Fabrizio, M. Menghini, and C. Giannetti, Mott resistive switching initiated by topological defects, *Nature Communications*, 15:9411, DOI: 10.1038/s41467-024-53726-z (2024)

A. Milloch, U. Filippi, P. Franceschini, S. Mor, S. Pagliara, G. Ferrini, F. Camargo, G. Cerullo, D. Baranov, L. Manna, and Claudio Giannetti, The fate of optical excitons in $FAPbI_3$ nanocube superlattices, *ACS Photonics*, 11, 9, 3511–3520, DOI: 10.1021/acsphotonics.4c00105 (2024)

A. Milloch, M. Fabrizio and C. Giannetti, Mott materials: unsuccessful metals with a bright future, *npj Spintronics*, 2:49, DOI: 10.1038/s44306-024-00047-y (2024)

A. Milloch and C. Giannetti, New order in the copper oxide phase diagram, *Nature Physics, News & views*, DOI: 10.1038/s41567-024-02602-0 (2024)

D. Soranzio, D. Puntel, M. Tuniz, P. E. Majchrzak, **A. Milloch**, N. M. Olsen, W. Bronsch, B. S. Jessen, D. Fainozzi, J. S. Pelli Cresi, D. De Angelis, L. Foglia, R. Mincigrucci, X. Zhu, C. R. Dean, S. Ulstrup, F. Banfi, C. Giannetti, F. Parmigiani, F. Bencivenga, and F. Cilento, Impact of MoS_2 Monolayers on the Thermoelastic Response of Silicon Heterostructures, *ACS Applied Nano Materials*, 7, 13, 15317–15324, DOI: 10.1021/acsanm.4c02096 (2024)

A. Milloch, U. Filippi, P. Franceschini, M. Galvani, S. Mor, S. Pagliara, G. Ferrini, F. Banfi, M. Capone, D. Baranov, L. Manna and Claudio Giannetti, Halide Perovskite Artificial Solids as a New Platform to Simulate Collective Phenomena in Doped Mott Insulators, *Nano Letters*, 23, 10617-10624, DOI: 10.1021/acs.nanolett.3c03715 (2023)

P. Franceschini, V. R. Policht, **A. Milloch**, A. Ronchi, S. Mor, S. Mellaerts, W.-F. Hsu, S. Pagliara, G. Ferrini, F. Banfi, M. Fabrizio, M. Menghini, J.-P. Locquet, S. Dal Conte, G. Cerullo, and C. Giannetti, Coherent control of the orbital occupation driving

the insulator-to-metal Mott transition in V_2O_3, *Physical Review B* 107, L161110, DOI: 10.1103/PhysRevB.107.L161110 (2023)

L. Foglia, R. Mincigrucci, A.A. Maznev, G. Baldi, F. Capotondi, F. Caporaletti, R. Comin, D. De Angelis, R.A. Duncan, D. Fainozzi, G. Kurdi, J. Li, A. Martinelli, C. Masciovecchio, G. Monaco, **A. Milloch**, K.A. Nelson, C.A. Occhialini, M. Pancaldi, E. Pedersoli, J.S. Pelli-Cresi, A. Simoncig, F. Travasso, B. Wehinger, M. Zanatta and F. Bencivenga, Extreme ultraviolet transient gratings: A tool for nanoscale photoacoustics, *Photoacoustics*, 29, 100453, DOI: 10.1016/j.pacs.2023.100453 (2023)

A. Milloch, R. Mincigrucci, F. Capotondi, D. De Angelis, L. Foglia, G. Kurdi, D. Naumenko, E. Pedersoli, J. S. Pelli-Cresi, A. Simoncig, B. Wehinger, C. Masciovecchio, and F. Bencivenga, Nanoscale Thermoelasticity in Silicon Nitride Membranes: Implications for Thermal Management, *ACS Applied Nano Materials*, 4, 10, 10519–10527, DOI: 10.1021/acsanm.1c02034 (2021)

FACOLTÀ DI SCIENZE MATEMATICHE, FISICHE E NATURALI
DIPARTIMENTO DI MATEMATICA E FISICA
Via della Garzetta 48
25133 Brescia
alessandra.milloch@unicatt.it

FACULTY OF SCIENCE
DEPARTMENT OF PHYSICS AND ASTRONOMY
Celestijnenlaan 200D box 2417
B-3001 Leuven
alessandra.milloch@kuleuven.be